EPFL

New insights into rodent brain microstructure and metabolism in hepatic encephalopathy

Jessie Julie MOSSO

École
polytechnique
fédérale
de Lausanne

2023

Acknowledgements

There is one name in the front page of this thesis manuscript, but many other names without who this journey would have not been possible. I would like to express my gratitude to all the people that I have met during these 4 years and before, to the ones who have guided and supported me, who have helped me grow and improve, and to the ones who have inspired me both scientifically and personally.

Cristina, we have travelled a long way together, 4 years, a pandemic and >50 exhausting denoising powerpoints, but we made it. Thank you for offering me a lucky research experience in Switzerland, joining your group was an incredible chance for me, topped up by the EU project which opened many opportunities and perspectives, both scientifically and personally. Thank you for teaching me everything I know about rigorous MRS acquisition-processing-fitting-modelling-paperwriting with great enthusiasm, for guiding me into enriching scientific projects, for challenging me (trying for 3 years to get a decent shim in cerebellum, while you and everyone else knew it was almost impossible), for teaching me that there is no mistake except the one of not asking for help, and for giving me freedom to explore my own ideas and always be trustful and supportive, which was extremely important for me. Thank you for offering me to work on side projects with Bernard and Ileana at the beginning of my thesis (to go to ISMRM, but then covid...), thank you for pushing me to work hard, and write papers without having solved all the questions in the field (in the world). You have always been available for a discussion anytime and have provided fast feedback despite your busy schedule, also very precious in a PhD journey. Thank you for fighting for us to be recognized at all levels and to be acknowledged for our contributions. Thank you for bringing us to international conferences, for introducing us to your numerous collaborators, and for teaching me your ways of creating and handling fruitful collaborations. Thank you for always trying to protect us from additional concerns as much as you could, allowing us to work in the best possible conditions, this was never left unnoticed. Thank you for being supportive of my personal fights (Invisible Women was the most perfect gift of all), and for sharing yours with so much honesty. Thank you Cristina, you are an exceptional supervisor and mentor, you empowered me in so many ways.

inspiring. Countless times did I come across a topic that was not clear to me, until I listened to one of your talks and realized in the middle: "of course, this is it", so clearly expressed. Thank you for supporting me all along.

Julien, thank you for helping us initially with the sequence in Lausanne, for hosting me in secondment in your lab, for the numerous interesting discussions, and for setting so high standards in the field of diffusion and MRS.

Roland, thank you for hosting me during my secondment in Bern. At the time, I knew you only by reputation, which was impressive. From these months spent in your lab, I will remember the extreme patience with which you were answering our questions (even many times the same one... you created the worst tool for that, FiTAID), you being still so close to science and technical aspects, after all these years. Thank you for sharing your knowledge passionately and teaching us rigorous thinking, for initiating me to Siemens scanning one afternoon, for our continuing projects and for your honest career advises. You also set a standard of having the honesty and strength to navigate opposing established scientific trends, which I admire a lot.

I would like to thank my jury committee, *Marco, Jamie, Valerio*, for their careful reading of this manuscript, and great (and challenging) inputs during the defense. A special thank you to everyone who carefully read parts of my thesis, and helped me improve the quality of the manuscript: *Cristina, Bernard, Ileana, Kasia, Emma, Sarah, Philippe*, and *Thanh* for helping me with the formatting.

Thank you to the CIBM and LIFMET administrations for access to great infrastructures and a special thank you to *Lillian, Tanja, Sarah, Nathalie* and *Anh* for your support.

Nasreen, thank you for lightning up our offices with your kind words and attentions. Mornings were a bit less difficult after meeting you.

Thank you *Vladimir* and *Ivan* for sharing your knowledge about basic NMR and sequence development, a chance for me to be learning from world experts.

To *Guillaume, Mickael, Michael and David*, thank you for trusting us with your master internships. The experience was for me very rich, I was impressed by your ability to come up with brilliant ideas even outside the field you were trained on. You have been true peers, and helped me a lot with the projects, thank you all very much.

I would also like to thank my previous research supervisors, *Daniel* and *Myriam*, who opened

Kus, kuskus, markuuuus, cocododeldo (how do we even write this? Cocorico of la grande nation, much better). Over these years, you have been the constant rock, the one I was looking for when I needed someone to help me smile. You have sometimes stressed me out a bit (time to press the button now!!), but you would definitely not be Mark otherwise. I have loved all these moments by your side, our beers, our nights out, especially the ones when you sacrificed your integrity to go to Jaggers instead of boom boom boom D, our ski trips, restaurants, celebrations of all kinds. Thank you for being so friendly and supportive also during the writing phase of my PhD, your silent hugs, your escort to the exam room with Toni and Emma, our shouting in the street, you made me feel nothing could go wrong, it was very precious, you are a wonderful friend.

Thanh, very special Thanh, you have helped me and saved me so many times that I would need another thesis to list them all: my computer two times, my watch, my thesis, my figure alignment, my abstracts, the 14T and so on and on. It is hard to describe to someone how knowledgeable you are literally on everything. I was lucky to have you as my friend during these years, you have supported me all along, have made my life so easy and so fun, even in the most intense and difficult moments. Thank you for our shared lunches for all these years (especially the carrots), our diners and events together outside the lab, and for having been so kind to me all along.

Emma, my new office mate, I already love every moment we have been sharing in this (tiny) space, the new design, the plants and the conversations. Thank you for always being here for me, for the personal discussions we had here and in Paris (the full, not-so-straight weekend was magical, Nina, crepe crème de marron to be redone definitely, thank you again), you make me feel safe, understood and at home. Thank you for the nights at your place, the ski together, for bearing with the moody me and for your great support also during the writing phase and the day of the exam, and for the most prefect gift on submission day!

To my Swiss-French friends, *Sarah* and *Florian*-test1234, we have experienced different places together (even very remote ones... St-Triphon), all the variations of our favourite moody free anarchist Florian that I love, everytime was so fun, with the same feeling of happiness shared with true friends. Thank you also for the honest discussions, the time spent together is a precious memory I will keep from my Swiss stay.

To *Toni*, *Fran* and *Nikos*, I have so much fun by your side, you are beautiful people, it is so clear, so bright, thank you for being part of my life. *Toni*, thank you for your escort to the exam, very precious moment that I will not forget.

Acknowledgements

To *Songi, Emmanuelle, Veronika, Radek, Yujian*, and all the members of the CIBM and LIFMET, thank you for making the everyday life in the lab very happy. *Songi*, thank you for introducing me to the most fancy places in Lausanne!

Thank you to the INSPiRE-MED consortium, which was a great chance to me part of. To my INSPiRE-MED friends, listing your names one last time in the order of the ESR numbers (because why should we have a name?): *Rudy, Zoona, Lurii, Luigi, Berardino, Dimitri, Ana, Elina, Pooya, Gulnur, Amir, Mladen, Federico, Kyung Min*, thank you so much, I have discovered true friends in you and the time spent together constitutes some of the most precious memories I have from my PhD. You gave to this journey another layer of immense and endless joy, every meeting was wonderful, everywhere, making me so eager to meet you all again (for science updates of course). My *Elina*-rabbit friend, I love you so much, I think about Fofo every night before going to bed (I hope she is well and living a peaceful life), you are such a beautiful person, genuinely interested in the most strange, unusual parts of people, you navigate with so much honesty in your life and I feel extremely lucky that we have met. I had so much fun, countless hours of laughs and jokes and good beers and dance nights (you being so persuasive when asking for Steve's 70s rock song), and happiness and looking for small Ben and rabbit faces, your love and support have helped me all along and I am sure that Domicic was right, no separation ever for us. *Rudy*, the glue of our group, thank you so much for holding us together, you are a beautiful person, I miss you a lot here in Switzerland and I wish we can meet again soon. *Luigi*, my dearest friend who in extremis came for a secondment in Lausanne, two weeks where we had so much fun, it was precious to have you here.

Simone, a bit in between my INSPiRE-MED mates and my lab mates, thank you for the amazing Aar boat trip, and the perfect combination of work-beers in Bern!

Je continue ces remerciements avec ceux adressés à ma famille. Merci d'avoir été toujours là, chaque jour, jusqu'au bout de cette thèse, de m'avoir toujours soutenue inconditionnellement malgré les longues semaines de silence et la distance. A ma famille *ESPCI*, vous revoir, vous entendre, penser à vous souvent remplissait les ressources les plus fondamentales de mon existence. A ma famille *Duby*, je vous ai retrouvés dans ces derniers mois de thèse pour deux très heureux évènements (et une visite en vélo avec un pied presque cassé), qui m'ont rappelé toutes ces années merveilleuses que nous avons vécues ensemble, merci d'être toujours là. A ma famille *Philippe*, merci pour tout, ton écoute, ton aide et ton soutien indéfectibles, tu me donnes à voir la beauté dans les endroits où je pensais qu'elle n'existait pas, et dans ceux où je pensais que je la voyais déjà. A ma famille *Mathilde, Juliette* et *Lucas*, vous avec qui j'ai grandi, vous qui me soutenez inconditionnellement depuis toutes ces années, merci infiniment, vous êtes sans cesse dans mes pensées, dans un poème, une lettre que je relis, un souvenir que je revisite, un spectacle ou un paysage qui me fait penser à vous, vous rendez ma

vie si heureuse. A ma famille *Lucille, Clotilde, Julien, Vincent*, merci d'avoir agrandi ma famille d'une si belle façon. A ma famille *Lou, Éric, Éric, Hervé, Quentin, Mathilde, Mireille, Alain*, vous m'avez toujours aimée, encouragée et soutenue dans chacun de mes choix, et ce depuis très longtemps, je suis ici en train d'écrire ces mots grâce à vous. Merci de m'avoir offert une vie privilégiée qui a rendu tous ces choix, et finalement cette thèse, possibles.

I would like to finish this list by thanking the organizers of the workshop "Sex as a biological variable", held in June 2022 in Bern, *Hanno Würbel* and *Ivana Jaric*, as well as the members of the *Réseau Romand de mentoring pour femmes*, including the other mentees, the organizers and *Selma Aybek*, for sharing your experiences. You gave me clues to understand that we have all the rights to be angry, and that if we are given a voice, it should be our duty to speak up for those who were not given that chance and to fight for our definition of equality.

Lausanne, November 23, 2023

Abstract

Type C hepatic encephalopathy (HE) is a severe neuropsychiatric complication of chronic liver disease, for which the prognosis is poor in the absence of liver transplantation. Cirrhosis in type C HE leads to a toxic accumulation of ammonia in the blood, which will eventually travel to the brain and adversely affect its structure and function. However, the biochemical mechanisms underpinning neurological and cognitive dysfunctions are intertwined and still incompletely understood.

First, **it remains unclear how brain cells morphology is affected** by the ammonia-induced glutamine increase and osmotic stress in HE. In the bile-duct ligated (BDL) rat model of type C HE, alterations of neurons and astrocytes' shape have been observed ex vivo by histology, but these observations were until now not replicated in vivo. Magnetic resonance (MR) spectroscopy (MRS) at ultra-high field is a powerful tool to probe metabolism in vivo, and can, with the insertion of diffusion gradients, in addition be sensitized to probe cell-specific microstructure.

In this thesis, diffusion-weighted MR spectroscopy (dMRS) and imaging (dMRI) experiments were conducted at 14.1T in the developing brain of the BDL rat model of type C HE. The acquisition was optimized to measure the cerebellum, a challenging brain region due to motion and the presence of fat, but of particular vulnerability in HE. Analysed jointly through cell-specific biophysical modelling, **dMRS and dMRI probed faster metabolite diffusivities and faster intra-neurite/intra-axon water diffusivity in cerebellar white and grey matter of BDL rats** compared to control rats. These observations point towards **an alteration of cell density and/or of neurite network complexity** and reorient the debate from the restrictive hypothesis of astrocytes swelling to the wider one of **multi-cellular microstructure alterations in type C HE**.

The dMRS acquisition was further optimized with the implementation of a new sequence, DW-SPECIAL. The latter **improved the detection and subsequent estimation of the diffusion properties of strongly J-coupled metabolites** such as glutamine, of particular interest in the study of HE.

A post-processing denoising technique based on the Marchenko Pastur principal component analysis method (MP-PCA) was also tested on simulated, rodent and human dMRS data. **MP-**

Abstract

PCA denoising yielded both valuable and adverse features specific to the nature of the input data, an effect for which a detailed description was provided and which should be carefully considered.

Second, **conflicting results on brain energy metabolism alterations in type C HE** have been previously reported. Positron emission tomography (PET) is an imaging modality that enables the study of glucose uptake, following the conversion of fluorodeoxyglucose (FDG) in the first steps of the glycolysis in vivo.
In this thesis, a new preclinical FDG PET methodology was implemented to compute quantitative 3D maps of the regional cerebral metabolic rate of glucose (CMR_{glc}) from a labelling steady-state PET image of the brain and an image-derived input function. **A 2-fold lower CMR_{glc} brain glucose uptake was observed in the hippocampus and cerebellum of the BDL rats**. Combined with MRS, it provided for the first time **local and quantitative information on both brain glucose uptake and neurometabolic profile alterations** in a rat model of type C HE. The quantitative approach also showed its strength when comparing groups of animals with divergent physiology.

Résumé

L'encéphalopathie hépatique (EH) de type C est une complication neurodégénérative grave de la maladie hépatique chronique, pour laquelle le pronostic est mauvais en l'absence d'une transplantation du foie. La cirrhose à l'origine de l'EH de type C provoque une accumulation toxique d'ammoniac dans le sang, qui finira par atteindre le cerveau et avoir des conséquences délétères sur sa structure et ses fonctions. Cependant, les mécanismes biochimiques à la base des dysfonctionnements neurologiques et cognitifs sont étroitement liés et restent mal compris encore à ce jour.

Tout d'abord, **les conséquences sur la morphologie des cellules cérébrales de l'augmentation de la glutamine et du stress osmotique induite par l'ammoniac dans l'EH sont mal connues**. Dans le modèle de rat ligaturé des voies biliaires (LVB) de l'EH de type C, les données histologiques ex vivo ont mis en évidence des modifications de la forme des neurones et des astrocytes, mais ces observations n'ont jusqu'à présent jamais été confirmées in vivo. La spectroscopie de résonance magnétique (SRM) à haut champ magnétique est un outil puissant permettant de mesurer le métabolisme in vivo et offrant aussi, grâce à l'ajout de gradients de diffusion, la possibilité de caractériser la microstructure spécifique à chaque type de cellule.

Dans cette thèse, des expériences de spectroscopie et d'imagerie de résonance magnétique pondérée en diffusion (SRMd et IRMd) ont été menées à 14.1T dans le cerveau en développement du modèle de rat LVB de l'EH de type C. L'acquisition a été optimisée pour mesurer le cervelet, une région cérébrale présentant des difficultés méthodologiques en raison du mouvement et de la présence de gras, et particulièrement affectée dans l'EH. Les résultats de SRMd et IRMd ont été analysés conjointement avec des modèles biophysiques spécifiques à la matière grise ou blanche et à chaque type de cellule. Ils ont mis en évidence que **les diffusivités des métabolites et de l'eau dans les neurites et axones de la matière blanche et grise du cervelet des rats LVB étaient plus rapides** que celles chez les rats contrôles. Ces observations suggèrent que **la densité cellulaire et/ou que la complexité du réseau de neurites est altérée**, réorientant ainsi le débat d'une hypothèse trop restrictive du gonflement des astrocytes vers une hypothèse plus large **d'altérations multi-cellulaires de la microstructure dans l'EH**. L'acquisition SRMd a été optimisée dans un second temps avec le développement d'une nou-

velle séquence, nommée DW-SPECIAL. **Cette dernière a amélioré la détection et l'estimation des propriétés de diffusion des métabolites avec des constantes de couplage scalaire élevées**, tels que la glutamine, particulièrement importante dans l'étude de l'EH. Une technique de débruitage basée sur la méthode d'analyse en composantes principales de Marchenko Pastur (MP-ACP) a également été testée sur des données de SRMd simulées, de rongeurs et d'humains. **Le débruitage MP-ACP a abouti à certaines caractéristiques favorables et certaines défavorables, dépendant fortement de la nature des données d'entrée**, un effet pour lequel une description détaillée a été fournie dans cette thèse et qui doit être rigoureusement pris en compte.

Par ailleurs, de précédentes études ont mis en évidence des **résultats contradictoires en ce qui concerne les possibles altérations du métabolisme énergétique cérébral dans l'EH de type C**. La tomographie par émission de positons (TEP) est une modalité d'imagerie qui permet d'étudier la consommation du glucose par les cellules, en suivant le devenir de son analogue, le radiotraceur fluorodésoxyglucose (FDG), dans les premières étapes de la glycolyse in vivo. Dans cette thèse, une nouvelle méthodologie préclinique de TEP au FDG a été proposée afin de quantitativement cartographier en 3D le taux local de consommation de glucose dans le cerveau (CMR_{glc}). Ces cartes ont été obtenues à partir d'une image TEP du cerveau à l'état d'équilibre et d'une fonction d'entrée mesurée aussi directement sur l'image TEP. **Un taux CMR_{glc} deux fois inférieur a été observé dans l'hippocampe et le cervelet des rats LVB**. Pour la première fois, l'imagerie TEP a fourni ici des **informations locales et quantitatives sur la consommation cérébrale du glucose dans un modèle de rat de l'EH de type C, en complément des altérations métaboliques mesurées par SRM.** L'approche quantitative proposée dans cette thèse s'est également révélée indispensable lors de la comparaison de groupes d'animaux présentant de grandes différentes physiologiques, tel que dans notre étude.

Mots-clés : spectroscopie par résonance magnétique, résonance magnétique pondérée en diffusion, encéphalopathie hépatique de type C, cerveau de rongeur, cerveau en développement, métabolites avec un couplage scalaire élevé, tomographie par émission de positons au ^{18}F-fluorodésoxyglucose, analyse en composantes principales

Outline

The phenomenon of nuclear magnetic resonance (MR) enables the investigation of the nuclear structure of organic compounds and by inference their properties and surroundings. Applied in vivo, MR offers a versatile, non-invasive and non-ionizing medical imaging tool to investigate soft tissues at the millimetre or sub-millimetre scales. Different modalities reflecting various tissue properties have been developed: diffusion-weighted magnetic resonance imaging (MRI) to probe microstructure, functional MRI to probe brain function at rest and during functional activity, T_1 and T_2-weighted MRI to enhance contrast of different tissues compared to proton density, or magnetic resonance spectroscopy (MRS) to probe metabolism, to name a few. Positron emission tomography (PET) is a less versatile, ionizing but very sensitive medical imaging technique. It relies on the measurement of the β-decay of radioisotopes, competing with endogenous molecules of interest for binding or metabolic conversion.

Yet, a **synergetic combination of these modalities** is often required as none of them alone provides sufficient insight into complex pathological conditions.

The overall objective of this thesis was to develop and implement advanced MR and PET methodologies in a rat model of hepatic encephalopathy (HE) to extend our current understanding of the pathophysiology of the disease. More specifically, the focus was set on the questions of **microstructure** and **energy metabolism alterations** probed with **diffusion-weighted MR** and ^{18}**F-FDG PET**, respectively. On the methodological standpoint, we will show how the information derived from **the current methodologies**, namely the standardized uptake value (SUV) in PET studies and of the non-cell specific information from diffusion-weighted MRI, **would have failed to provide such insights into the disease mechanisms.**

Part 1 will first introduce some general concepts relevant to the development of this thesis. **Chapter 1** will first introduce MR and **Chapter 2** diffusion-weighted MR, spanning from basic theory to experimental considerations and modelling. These two chapters aimed at highlighting and addressing some of the questions that appeared fundamental in my journey towards a better understanding of MR, such as: *How satisfactory are the classical descriptions of the MR phenomena and how unsatisfactory (for the classical human brain) are the quantum*

descriptions? What survives voxel averaging? What limits the sensitivity of a measurement to a parameter of interest?, to list a few. To that aim, some sections in **Chapter 1** will start with a question in italics.

Chapter 3 will introduce the known biochemical mechanisms underpinning hepatic encephalopathy at the preclinical and clinical levels. Some remaining unknowns in the pathophysiology of HE will be discussed, together with the potential of new methodologies to fill in these gaps.

Part 2 will present the study of microstructure in HE measured with diffusion-weighted MR, and is divided into three chapters.

Chapter 4 will focus on the implementation of diffusion-weighted MRS and MRI in the cerebellum of a rat model of hepatic encephalopathy. The chapter starts with a preliminary study in adult rats, from which conclusions are drawn to improve the methodology for the second study, performed in young rats to study longitudinally the developing brain. Diffusion results were linked to the brain microstructural alterations observed by histology.

Chapter 5 will present the design, implementation and validation of a new diffusion-weighted MR sequence that improves the detection of J-coupled metabolites. This sequence was designed to circumvent the limitations of the gold-standard diffusion-weighted MRS sequence used in **Chapter 4**.

Chapter 6 will describe a post-processing method based on the Marchenko-Pastur principal component analysis (MP-PCA) for the denoising of diffusion-weighted MRS data. The consequences of the method on the properties of the input data and on the resulting estimated parameters in terms of accuracy and precision will be described, based on simulations, in vivo rodent and human diffusion-weighted MRS data. This chapter constitutes an attempt to improve dMRS measurements at the post-processing stage, while **Chapter 5** aimed at improvement dMRS measurements at the acquisition stage.

Part 3 will present the study of energy metabolism in HE measured with PET, and contains only one chapter.

Chapter 7 will present the implementation of ^{18}F-fluorodeoxyglucose (FDG) PET in a rat model of hepatic encephalopathy HE, combined with single-voxel MRS. We will address both the implication of our results on the still-debated question of energy metabolism alteration in HE, and present a new methodology that unequivocally quantifies glucose uptake also in conditions of altered systemic metabolism.

The Matlab codes used to generate the figures in this thesis will be made available here: https://github.com/jessie-mosso/.

Contents

Contents

Contents

List of Figures

List of Tables

List of Abbreviations

AD	axial diffusivity
ADC	apparent diffusion coefficient
ADP	adenosine diphosphate
AIF	arterial input function
Ala	alanine
ALF	acute liver failure
ALT/GPT	alanine aminotransferase
AMARES	advanced method for accurate, robust, and efficient spectral fitting
Asc	ascorbate
Asp	aspartate
AST/GOT	aspartate aminotransferase
ATP	adenosine triphosphate
BBB	blood-brain barrier
BDL	bile duct ligation
bHB	β-hydroxybutyrate
BPP	Bloembergen-Purcell-Pound
CBF	cerebral blood flow
CHESS	chemical shift selective
CLD	chronic liver disease
CM	classical mechanics
CMR$_{glc}$	glucose cerebral metabolic rate
CNS	central nervous system
CPMG	Carr-Purcell-Meiboom-Gill
Cr	creatine
CRLB	Cramer-Rao lower bounds
CSD	chemical shift displacement
DDE	double-diffusion encoding
dMRI	diffusion-weighted MRI
dMRS	diffusion-weighted MRS
dn	denoising/denoised
DNP	dynamic nuclear polarization
DTI	diffusion tensor imaging
ES	extracellular space
ESFU	estimated spectral fit uncertainty
FA	fractional anisotropy

List of Abbreviations

FASTMAP	fast automatic shimming technique by mapping along the projections
^{18}F-FDG	^{18}F-fluorodeoxyglucose
FDG-6P	FDG 6-phosphate
FID	free induction decay
FLASH	fast low angle shot
FOV	field of view
FT	Fourier transformation
FWHM	full width at half maximum
GABA	gamma-aminobutyric acid
GFAP	glial fibrillary acidic protein
Glc	glucose
Gln	glutamine
Glu	glutamate
Glx	glutamine+glutamate
GM	grey matter
GPC	glycerophosphocholine
GS	glutamine synthetase
GSH	glutathione
HE	hepatic encephalopathy
HS	hyperbolic secant
IDIF	image-derived input function
(m)Ins	myo-inositol
IHC	Immunohistochemistry
(d)IR	(double) inversion recovery
ISIS	image-selected in vivo spectroscopy
jMRUI	java based magnetic resonance user interface
K_{app}	apparent kurtosis
Lac	lactate
LASER	Localization by Adiabatic Selective Refocusing
LC	Lumped Constant
LC Model	linear combination of model spectra of metabolites
MD	mean diffusivity
MFG	magnetic field gradients
MIP	maximum intensity projection
MLEM	maximum likelihood expectation maximization
MM	mobile macromolecules
MP	Marchenko-Pastur
MR	magnetic resonance
MRI	magnetic resonance imaging
MRS	magnetic resonance spectroscopy
MRSI	magnetic resonance spectroscopic imaging
MS	multiple sclerosis
NAA	N-acetyl aspartate
NAAG	N-acetylaspartylglutamate
NfL	neurofilament light chain
NLLS	non-linear least squares
NMR	nuclear magnetic resonance
NS	number of shots

ODF	orientation dispersion function
OS	oxidative stress
OVS	outer volume suppression
PCA	principal component analysis
PCho	phosphocholine
PCr	phosphocreatine
PE	phosphorylethanolamine
PET	positron emission tomography
PJ	Purkinje neurons
ppm	parts per million
PRESS	point resolved spectroscopy
PSS	portosystemic shunting
QM	quantum mechanics
RD	radial diffusivity
RF	radiofrequency
RMSE	root mean squared error
RNS	reactive nitrogen species
ROS	reactive oxygen species
SADLOVE	single-shot adiabatic localized volume excitation
SANDI	soma and neurite density imaging
SAR	specific absorption rate
Scyllo	scyllo-inositol
SD	standard deviation
SE	spin echo
SGP	short gradient pulse
SM	standard model
SNR	signal-to-noise ratio
SPECIAL	spin echo, full intensity aquired localized spectroscopy
SPECT	single photon emission computed tomography
STE	stimulated echo
STEAM	stimulated echo pulse sequence
SUV	standardized uptake value
SVD	singular value decomposition
sw	sliding window
SW	spectral width
Tau	taurine
tCho	total choline
tCr	total creatine
TE	echo time
TGV	total generalized variation
TM	mixing time
TMS	tetramethyl silane
TR	repetition time
VAPOR	variable pulse power and optimized relaxation delay
VOI	volume of interest
WM	white matter
WMTI	white matter tract integrity
WS	water suppression

General concepts Part I

1 Nuclear Magnetic Resonance (NMR)

The aims of this chapter are two-fold: first, to present the general nuclear magnetic resonance concepts relevant to the development of this thesis work and second, to address some of the aspects that remained challenging to me for a long time (and for some, that still are).

This chapter will also highlight the good agreement between the classical and quantum mechanical representations of the magnetic resonance (MR) phenomenon for an ensemble of spins-1/2, as shown by Feynman *et al.* [1]. It was written with the help of the following books: *Spin Dynamics* by Malcolm H. Levitt [2], *Understanding NMR spectroscopy* by James Keeler [3], *Principles of Nuclear Magnetic Resonance Microscopy* by Paul T. Callaghan [4], *In vivo NMR Spectroscopy: Principles and Techniques* by Robin A. de Graaf [5] and *The Principles of Nuclear Magnetism* by Anatole Abragam [6].

The term *spin* will be abusively used to describe the property ("the intrinsic property of a nucleus") and the object ("ensemble of spins-1/2"). The statements and derivations below will focus on a system of spins-1/2 with a gyromagnetic ratio $\gamma > 0$.

1.1   One spin

Why do we talk about angular momentum and magnetic moment as quantities of classical physics in relation to the atomic nucleus?

Nuclear magnetic resonance (NMR) relies on the fundamental property of nuclear (para) magnetism arising from nuclear spin. Nuclear magnetism reflects the capacity of atomic nuclei to interact with magnetic fields. It is weak compared to electronic magnetism, the latter being responsible for the macroscopic magnetic behavior of objects, nevertheless nuclear magnetism allows one to study the internal structure of molecules with NMR.

1.1.1 Rotational angular momentum versus spin angular momentum

In the classical mechanics (CM) description, a rotating object acquires a rotational angular momentum. This angular momentum has an analogy in the quantum mechanics (QM) description, where its norm is quantized and its energy levels are degenerate in an environment isotropic for rotations.

The spin, however, has no classical equivalent and does not arise from a rotation of the nucleus *per se*. It is an intrinsic property of the nucleus and is associated with a (spin) angular momentum. The concept of rotation for a spin-1/2 had been challenged by the observation that a 2π-rotation of the wavefunction does not produce identity [7]. However, the intrinsic spin angular momentum follows the same QM quantification rules as the angular momentum of rotating molecules. In particular:

- The total intrinsic spin angular momentum of an atomic nucleus **P** depends on the combination of the spin angular momenta of its protons and neutrons I_{tot} and its norm is quantized:

$$\|\mathbf{P}\| = \sqrt{I_{\text{tot}}(I_{\text{tot}} + 1)}\hbar \tag{1.1}$$

  where I_{tot} can be an integer or a half integer depending on the number of protons and neutrons. The ground state nuclear spin I is the value of I_{tot} associated with the lowest energy, which is in general not trivial to guess. Protons, neutrons and electrons have a spin-1/2. Hydrogen (protium hydrogen, ^{1}H), the atom the most commonly used in NMR applications, has one proton, therefore $I_{\text{tot}} = \frac{1}{2}$. In that case, there is only one possibility for the value of the ground state spin number: $I = \frac{1}{2}$.

- A magnetic moment $\boldsymbol{\mu}$ is associated with all nonzero total intrinsic spin angular momentum **P**:

$$\boldsymbol{\mu} = \gamma \mathbf{P} \tag{1.2}$$

  where γ is the gyromagnetic ratio.

Without an external magnetic field (i.e. in an isotropic environment for magnetism), the ground state has $M_I = 2 \times I + 1$ levels which are degenerate.

1.2 Interaction of one spin-1/2 with a magnetic field

How wrong is the vector representation of one spin?

1.2.1   Quantum description

In the presence of a external magnetic field $\mathbf{B_0} = B_0\hat{\mathbf{z}}$, the M_I levels of one spin are split by the nuclear Zeeman effect into sub-levels from $m = -I$ to $m = +I$ in steps of one, which is for ^{1}H, $M_I = 2$. These two M_I states imply that the z-projection of the total intrinsic spin angular momentum μ_z and its corresponding energy are quantized ($\mu_z = \gamma\hbar m$ (along $+\hat{\mathbf{z}}$) and $E = -\mu_z\hat{\mathbf{z}}\mathbf{B_0}$). These two states are denoted as spin-up or α-state and spin-down or β-state, the α-state corresponding to μ_z aligned with $\mathbf{B_0}$ minimizes the energy E:

$$\boldsymbol{\mu_\alpha} = \frac{1}{2}\gamma\hbar\hat{\mathbf{z}} \quad \text{with} \quad E_\alpha = -\frac{1}{2}\gamma\hbar B_0 \quad \text{and} \quad \boldsymbol{\mu_\beta} = -\frac{1}{2}\gamma\hbar\hat{\mathbf{z}} \quad \text{with} \quad E_\beta = \frac{1}{2}\gamma\hbar B_0 \tag{1.3}$$

The α and β-states are the eigenstates of the operator $\hat{I}_z$ describing the z-projection of the total intrinsic spin angular momentum of an isolated spin-1/2. At a given time, the wavefunction of a isolated spin-1/2 ψ can be any linear combination (mixed state) of these two eigenstates, associated with some intrinsic quantum uncertainty:

$$|\psi\rangle = c_\alpha|\alpha\rangle + c_\beta|\beta\rangle \tag{1.4}$$

with

$$\hat{I}_z|\alpha\rangle = \frac{1}{2}\hbar|\alpha\rangle \quad \text{and} \quad \hat{I}_z|\beta\rangle = -\frac{1}{2}\hbar|\beta\rangle \tag{1.5}$$

The two possible outcomes of the measurement of this wavefunction by $\hat{I}_z$ are the eigenstates: $|\alpha\rangle$ or $|\beta\rangle$ and the probability of observing the $|\alpha\rangle$ is proportional to $\overline{c_\alpha}c_\alpha$ as developed in section 1.3.1.

1.2.2   Classical description

The vector representation of an individual spin is troublesome since, from the QM perspective, it is in a mixed state (which is not a vectorial sum of the two states $|\alpha\rangle$ or $|\beta\rangle$) and the projections of the total intrinsic spin angular moment cannot be known *simultaneously* according to Heisenberg uncertainty principle. The rules of classical mechanics governing rotations are not readily applicable to individual spins.

1.3   An ensemble of isolated spins-1/2 in a magnetic field - macroscopic magnetization

How is the steady-state with an equilibrium magnetization reached?

1.3.1 Quantum description

As seen above, a single spin-1/2 wavefunction is given by $|\psi\rangle = c_\alpha |\alpha\rangle + c_\beta |\beta\rangle$ and its observation is described by probabilities. The quantum uncertainty vanishes when a large ensemble is considered, and the expectation value $\langle\psi|\hat{I}_z|\psi\rangle$, i.e. the average observation over a large number of measurements of the z-component of the angular momentum (represented by the operator $\hat{I}_z$) for the same wavefunction $|\psi\rangle$, is given by:

$$\langle\psi|\hat{I}_z|\psi\rangle = \left(\overline{c_\alpha}\langle\alpha| + \overline{c_\beta}\langle\beta|\right)\hat{I}_z\left(c_\alpha|\alpha\rangle + c_\beta|\beta\rangle\right) \tag{1.6}$$

where $\overline{c_\alpha}$ is the complex conjugate of c_α. Using equations 1.5 and the fact that $|\alpha\rangle$ and $|\beta\rangle$ are normalized and orthogonal to each other, we have:

$$\langle\psi|\hat{I}_z|\psi\rangle = \frac{1}{2}\hbar\overline{c_\alpha}c_\alpha - \frac{1}{2}\hbar\overline{c_\beta}c_\beta \tag{1.7}$$

The magnetization M_z is related to the ensemble average, denoted $\left\langle\ \right\rangle_{ens}$, of the expectation value of $\hat{I}_z$ by:

$$M_z = \gamma N\left\langle\langle\psi|\hat{I}_z|\psi\rangle\right\rangle_{ens} = \frac{1}{2}\gamma\hbar N\left(\left\langle\overline{c_\alpha}c_\alpha\right\rangle_{ens} - \left\langle\overline{c_\beta}c_\beta\right\rangle_{ens}\right) \tag{1.8}$$

where N is the total number of spins, $\left\langle\overline{c_\alpha}c_\alpha\right\rangle_{ens}$ the probability of population of the α-state at the ensemble level (i.e. $N\left\langle\overline{c_\alpha}c_\alpha\right\rangle_{ens} = n_\alpha$, the population of the α-state) and $\left\langle\overline{c_\beta}c_\beta\right\rangle_{ens}$ the probability of population of the β-state at the ensemble level (i.e. $N\left\langle\overline{c_\beta}c_\beta\right\rangle_{ens} = n_\beta$, the population of the β-state). Introducing n_α and n_β in equation 1.8, we have:

$$M_z = \frac{1}{2}\gamma\hbar\left(n_\alpha - n_\beta\right) \tag{1.9}$$

For the components of the transverse magnetization, we have similarly:

$$M_x = \gamma N\left\langle\langle\psi|\hat{I}_x|\psi\rangle\right\rangle_{ens} \quad\text{and}\quad M_y = \gamma N\left\langle\langle\psi|\hat{I}_y|\psi\rangle\right\rangle_{ens} \tag{1.10}$$

where

$$\hat{I}_x|\alpha\rangle = \frac{1}{2}\hbar|\beta\rangle \quad\text{and}\quad \hat{I}_x|\beta\rangle = \frac{1}{2}\hbar|\alpha\rangle \tag{1.11}$$

and

$$\hat{I}_y|\alpha\rangle = \frac{1}{2}i\hbar|\beta\rangle \quad\text{and}\quad \hat{I}_y|\beta\rangle = -\frac{1}{2}i\hbar|\alpha\rangle \tag{1.12}$$

Using the complex notation for $c_\alpha = r_\alpha \exp(i\phi_\alpha)$, $\overline{c_\alpha} = r_\alpha \exp(-i\phi_\alpha)$, $c_\beta = r_\beta \exp(i\phi_\beta)$, $\overline{c_\beta} = r_\beta \exp(-i\phi_\beta)$, we get:

$$M_x = \frac{1}{2}\gamma\hbar N \left\langle \overline{c_\beta}c_\alpha + \overline{c_\alpha}c_\beta \right\rangle_{ens} = \gamma\hbar N \left\langle r_\alpha r_\beta \cos(\phi_\beta - \phi_\alpha) \right\rangle_{ens} \tag{1.13}$$

and:

$$M_y = \frac{1}{2}i\gamma\hbar N \left\langle \overline{c_\beta}c_\alpha - \overline{c_\alpha}c_\beta \right\rangle_{ens} = \gamma\hbar N \left\langle r_\alpha r_\beta \sin(\phi_\beta - \phi_\alpha) \right\rangle_{ens} \tag{1.14}$$

At equilibrium, the phases ϕ_α and ϕ_β of the individual spins are randomly distributed so the ensemble averages of the sine and cosine functions average out to 0 and thus $M_x = 0$ and $M_y = 0$.

1.3.2   Classical description

When a field $\mathbf{B_0}$ is applied, because of thermal fluctuations and motions of surrounding molecules creating varying magnetic fields (T_1 relaxation, which will be explored in section 1.6), the individual magnetic moments $\boldsymbol{\mu}$ will tend to wander and align preferentially in the direction along the field, i.e. with the lowest energy. This preferential alignment leads to a population distribution between the α and β-states, governed by the Maxwell-Boltzmann distribution:

$$\frac{n_\alpha}{n_\beta} = \exp\left(\frac{\Delta E}{k_B T}\right) = \exp\left(\frac{\gamma\hbar B_0}{k_B T}\right) \tag{1.15}$$

This expression can be linearized given $\gamma\hbar B_0 \ll k_B T$ and $n_\beta \approx \frac{n_\alpha + n_\beta}{2} \approx \frac{N}{2}$ and becomes:

$$n_\alpha - n_\beta \approx \frac{N\gamma\hbar B_0}{2k_B T} \tag{1.16}$$

At thermal equilibrium, the total magnetization M_0 is proportional to this difference in population of energy states $M_0 = \sum \mu_z = (n_\alpha - n_\beta)\gamma\frac{\hbar}{2}$ (equation 1.9), so:

$$M_0 \approx \frac{N\gamma^2\hbar^2 B_0}{4k_B T} \tag{1.17}$$

1.3.3   Factors influencing M_0

The signal (i.e. sensitivity) of an MR experiment is proportional to M_0. From this equation, we see that M_0 is proportional to:

- N, the total number of spins of interest in the sample. N is a combination of the net amount of the spins in the sample and of the fraction of the MR observable isotopes

in this total amount. In vivo magnetic resonance imaging (MRI) is more sensitive than X-nuclei MR because it measures the spin-1/2 of the protons of the water molecules: the body is made of approximately 60% water and ^{1}H has a high natural abundance (99.98%). As a comparison, ^{13}C, the MR observable and stable carbon isotope has a natural abundance of 1.1%.

- γ^2, the square of the gyromagnetic ratio of the spin of interest. It represents the strength of interaction of a spin with a magnetic field. $\gamma_{^1H} \approx 4\gamma_{^{13}C}$, making the ^{1}H a more sensitive candidate than ^{13}C ($\gamma_{^1H} = 267.515 \ 10^6$rad/s/T and $\frac{\gamma_{^1H}}{2\pi} = 42.576$ MHz/T).

- B_0, the strength of the main magnetic field. This explains the desire to reach higher magnetic fields to improve the sensitivity of the measurement. Increasing the magnetic field has another important effect: it increases the spectral separation of overlapping metabolites and therefore improves their quantification (section 1.7.1). However, a higher B_0 also leads to shorter T$_2$ relaxation times i.e. broader lineshapes in frequency domain.

and inversely proportional to:

- T, the sample temperature. In vivo, it is in general not possible to decrease the temperature of the sample to improve sensitivity, but it benefits other methods such as dynamic nuclear polarization (DNP) where the polarization is performed at a few kelvins prior to the in vivo experiment. However, as we mentioned above, the establishment of the thermal equilibrium polarization relies on thermal fluctuations of the molecules leading to a preferential realignment towards B_0. In DNP, the polarization is strong but the T_1 relaxation process is slow.

1.4   Excitation - effect of a radio-frequency pulse

Is there something wrong with the representation of energy levels populated by isolated spins up and spins down?
If a radio-frequency excitation equilibrates the energy levels in the case of a spin-1/2, we expect M_z=0, but how is M_{xy} created?

1.4.1   Classical description

At thermal equilibrium, the macroscopic magnetization is undetectable and aligned with **B$_0$**. As soon as the macroscopic magnetisation **M** is tilted away from the **B$_0$** axis, it will start precessing about **B$_0$** at a frequency given by the energy difference between the two states

$\Delta E = \gamma \hbar B_0$:

$$\frac{d\boldsymbol{M}}{dt} = -\gamma \mathbf{B_0} \times \boldsymbol{M} \tag{1.18}$$

where $\boldsymbol{\omega_0}$ is called the Larmor frequency:

$$\boldsymbol{\omega_0} = -\gamma \mathbf{B_0} \tag{1.19}$$

For a positive γ, the Larmor frequency is negative and the rotation is clock-wise (left-hand rule).

The macroscopic magnetisation **M** is tilted away from the $\mathbf{B_0}$ axis by a radio-frequency (RF) pulse. It is an additional oscillating magnetic field produced by an RF coil, used to perturb the system out of thermal equilibrium. As a result, a magnetisation in the xy-plane is created, and a signal can be detected through magnetic induction of the precessing magnetization in the same or another RF coil.

The amplitude of the RF field B_1 is small compared to B_0, it is applied on an axis perpendicular to the axis of $\mathbf{B_0}$ and at a frequency ω_{RF} close to the Larmor frequency ω_0 for conventional (non-frequency modulated) pulses.

When accounting for the additional RF field, equation 1.18 takes a more general form:

$$\frac{d\boldsymbol{M}}{dt} = -\gamma \mathbf{B}_{\text{eff}} \times \boldsymbol{M} \tag{1.20}$$

where $\mathbf{B}_{\text{eff}}$ accounts for the contributions of all the magnetic fields at the position of the considered magnetization. Typically, $\mathbf{B}_{\text{eff}}$ has a contribution from the main magnetic field $\mathbf{B_0}$ along z and from the additional RF field $\mathbf{B_1}$ in the xy-plane. The macroscopic magnetization **M** will precess about the axis of $\mathbf{B}_{\text{eff}}$.

1.4.2 Back to the quantum description?

From the QM description, the transmission of a RF wave whose energy equals the energy gap between the two eigenstates will create a transition of spins from one state to another. From that concept, it is clear that we can cancel out M_z by equalizing the populations of the two states. However, it remains unclear how a net xy-magnetization will be created. An explanation can be found in the expression of the time-dependent Schrödinger equation at the ensemble level.

During an RF pulse, the time evolution of the coefficient c_α and c_β (and thus of n_α and n_β) is described by the time-dependent Schrödinger equation. If an on-resonance RF pulse (see section 1.5.4) is applied along the x-axis (with an amplitude $\omega_1 = \gamma B_1$) in the rotating frame (which will be introduced later in section 1.5.3), the differential equations describing the

evolution of c_α and c_β with time are:

$$\frac{dc_\alpha(t)}{dt} = -\frac{1}{2}i\omega_1 c_\beta(t)$$
$$\frac{dc_\beta(t)}{dt} = -\frac{1}{2}i\omega_1 c_\alpha(t) \tag{1.21}$$

These are coupled differential equations: an RF pulse creates an interchange of c_α and c_β over time at a rate γB_1. The solutions of the equations 1.21 are:

$$c_\alpha(t) = \cos\left(\frac{\omega_1 t}{2}\right)c_\alpha(0) - i\sin\left(\frac{\omega_1 t}{2}\right)c_\beta(0)$$
$$c_\beta(t) = \cos\left(\frac{\omega_1 t}{2}\right)c_\beta(0) - i\sin\left(\frac{\omega_1 t}{2}\right)c_\alpha(0) \tag{1.22}$$

We can now compute the evolution of the y-magnetization during an RF pulse on x with the time-dependent expressions of c_α and c_β:

$$M_y(t) = \frac{1}{2}i\gamma\hbar N\left(\left\langle \overline{c_\beta(t)}c_\alpha(t) - \overline{c_\alpha(t)}c_\beta(t) \right\rangle_{ens}\right) \tag{1.23}$$

Substituting the expressions 1.22 in the above expression, we have:

$$M_y(t) = -\frac{1}{2}i\gamma\hbar N\left(\left\langle \overline{c_\alpha(0)}c_\beta(0) \right\rangle_{ens} - \left\langle \overline{c_\beta(0)}c_\alpha(0) \right\rangle_{ens}\right)\cos(\omega_1 t)$$
$$-\frac{1}{2}\gamma\hbar N\left(\left\langle \overline{c_\alpha(0)}c_\alpha(0) \right\rangle_{ens} - \left\langle \overline{c_\beta(0)}c_\beta(0) \right\rangle_{ens}\right)\sin(\omega_1 t) \tag{1.24}$$

The terms $\left\langle \overline{c_\alpha(0)}c_\beta(0) \right\rangle_{ens}$ and $\left\langle \overline{c_\beta(0)}c_\alpha(0) \right\rangle_{ens}$ are the coherence terms (off-diagonal elements of the density operator). At time 0, they vanish to 0 as described in section 1.3.1. The terms $\left\langle \overline{c_\alpha(0)}c_\alpha(0) \right\rangle_{ens}$ and $\left\langle \overline{c_\beta(0)}c_\beta(0) \right\rangle_{ens}$ are the population terms (diagonal elements of the density operator). At time 0, they express the difference in population of the two states as described in section 1.3.1 and do not vanish to 0. The expression 1.24 becomes:

$$M_y(t) = -\frac{1}{2}\gamma\hbar\left(n_\alpha(0) - n_\beta(0)\right)\sin(\omega_1 t) = -M_z(0)\sin(\omega_1 t) \tag{1.25}$$

The same reasoning holds for M_z. The z-magnetization based on the time-dependent solutions of the Schrödinger equation is:

$$M_z(t) = \frac{1}{2}\gamma\hbar N\left(\left\langle \overline{c_\alpha(t)}c_\alpha(t) - \overline{c_\beta(t)}c_\beta(t) \right\rangle_{ens}\right) \tag{1.26}$$

Substituting the expressions 1.22 in the above expression, we have:

$$
\begin{aligned}
M_z(t) = \frac{1}{2}\gamma\hbar N &\left(\left\langle \overline{c_\alpha(0)}c_\alpha(0) \right\rangle_{ens} - \left\langle \overline{c_\beta(0)}c_\beta(0) \right\rangle_{ens} \right) \cos(\omega_1 t) \\
&+ \frac{1}{2}i\gamma\hbar N \left(\left\langle \overline{c_\beta(0)}c_\alpha(0) \right\rangle_{ens} - \left\langle \overline{c_\alpha(0)}c_\beta(0) \right\rangle_{ens} \right) \sin(\omega_1 t)
\end{aligned}
\tag{1.27}
$$

and therefore:

$$
M_z(t) = \frac{1}{2}\gamma\hbar \left(n_\alpha(0) - n_\beta(0) \right) \cos(\omega_1 t) = M_z(0)\cos(\omega_1 t)
\tag{1.28}
$$

Overall, from the QM perspective, the RF pulse mixes the coefficients c_α and c_β with time, and doing so, the difference in population of M_z at $t = 0$ is transferred to M_y at time $t > 0$ to generate a coherent (observable) y-magnetization, which comes down to a rotation around the x-axis, of angle $\theta = \omega_1 t$ ($M_z(t) = M_z(0)\cos(\omega_1 t)$ and $M_y(t) = -M_z(0)\sin(\omega_1 t)$).

Some comments on the representations:

1- the representation of isolated spins either as vectors, or as being in either one of the two states are misleading. CM laws and representations do not apply to individual spins and only their measurement will result in either the spin up or the spin down state.

2- the representation of an ensemble of isolated spins as a collection of spins being distributed among the two states is misleading as the measurement of the macroscopic magnetization is not forcing the individual spins into their eigenstates. Only a representation of population differences involving n_α and n_β is meaningful.

3- an RF excitation does not create phase coherence by aligning the phases of the individual spins in the xy-plane. Instead, an RF excitation converts a difference in population into an xy-plane coherence at the ensemble level.

1.5 Radio-frequency pulses

1.5.1 Transmission

In this thesis work, a surface coil with two loops in quadrature was used as a transmit/receive RF coil for all the in vivo acquisitions, as recommended for localized magnetic resonance spectroscopy (MRS) in rodents [8]. Surface coils benefit from a smaller power requirement in transmit mode and a better sensitivity in receive mode than volume coils, but suffer from spatially-inhomogeneous excitation and reception. To circumvent this problem (on the transmit side), adiabatic pulses can be used, as it was done for most of the sequences presented in this PhD.

The RF field created by a single-loop RF coil is linearly-polarized (i.e. the polarization axis is

time-independent). For example, for a square RF pulse (section 1.5.4) of constant amplitude $B_{1,\max} = \frac{\omega_{1,\max}}{\gamma}$ and frequency ω_{RF} around the z-axis, applied on the x-axis, the RF field can be seen as the sum of two circularly-polarized fields rotating at $\omega_{RF} < 0$ and $-\omega_{RF} > 0$ of half the amplitude. We have:

$$
\begin{aligned}
B_1(t)\hat{\mathbf{x}} &= B_{1,\max} \cos(|\omega_{RF}|t)\hat{\mathbf{x}} \\
&= \frac{B_{1,\max}}{2}\left(\cos(|\omega_{RF}|t)\hat{\mathbf{x}} + \sin(|\omega_{RF}|t)\hat{\mathbf{y}}\right) \\
&+ \frac{B_{1,\max}}{2}\left(\cos(|\omega_{RF}|t)\hat{\mathbf{x}} - \sin(|\omega_{RF}|t)\hat{\mathbf{y}}\right)
\end{aligned}
\tag{1.29}
$$

The component of the RF field which rotates at a frequency of opposite sign to the Larmor frequency ω_0 (counter-rotating field at $-\omega_{RF} > 0$, here: $B_{1,\max}\left(\cos(|\omega_{RF}|t)\hat{\mathbf{x}} + \sin(|\omega_{RF}|t)\hat{\mathbf{y}}\right)$, creating a clock-wise rotation) is fast time-dependent. It creates a small shift in the resonant frequency and a tilt of the polarization axis known as Bloch–Siegert shifts [9]. In practice, this effect can be ignored as long as $B_{1,\max} \ll B_0$ ($B_{1,\max}$ on the order of a few μT, B_0 on the order of a few Tesla).

Because half of the transmit power in the coil is used to generate a counter-rotating field B_1 that does not change the population of the two spin-1/2 states (but does produce heat), linearly polarized coils are not very efficient. To create a circularly-polarized field with an amplitude $B_{1,\max}$ (instead of $\frac{B_{1,\max}}{2}$), we use a coil made up of two single loops, positioned in geometric quadrature (ideally with their polarization axes at 90°), with which we get:

$$
\begin{aligned}
&B_{1,\max}\cos(|\omega_{RF}|t)\hat{\mathbf{x}} + B_{1,\max}\cos(|\omega_{RF}|t + \frac{\pi}{2})\hat{\mathbf{y}} \\
&= B_{1,\max}\cos(|\omega_{RF}|t)\hat{\mathbf{x}} - B_{1,\max}\sin(|\omega_{RF}|t)\hat{\mathbf{y}} \\
&= B_{1,\max}(\cos(|\omega_{RF}|t)\hat{\mathbf{x}} - \sin(|\omega_{RF}|t)\hat{\mathbf{y}})
\end{aligned}
\tag{1.30}
$$

When the RF pulse is amplitude modulated but not frequency-modulated (conventional pulses, section 1.5.4), ω_{RF} is the carrier frequency of the pulse and is generally applied in the middle of the metabolite spectrum to limit the chemical shift displacement artefacts (section 1.8.2).

1.5.2 Reception

The same quadrature surface coil is used for reception of the MR signal. Each loop records a complex signal, S_1 and S_2, combined (in our case, directly on the MR scanner) into S_{tot} by complex summation with an optimized phase calibrated for each scan:

$$\begin{pmatrix} \Re(S_{\text{tot}}) \\ \Im(S_{\text{tot}}) \end{pmatrix} = A_1 R(\phi_1) \begin{pmatrix} \Re(S_1) \\ \Im(S_1) \end{pmatrix} + A_2 R(\phi_2) \begin{pmatrix} \Re(S_2) \\ \Im(S_2) \end{pmatrix} \quad (1.31)$$

where A_1 and A_2 are the scaling factors of the coil loops 1 and 2, ϕ_1 and ϕ_2 their phases, R the 2D rotation matrix, $\Re$ and $\Im$ the real and imaginary parts of the complex signal from the coil loop 1 S_1, from the coil loop 2 S_2, or from the combined signal S_{tot}. Each loop records a complex signal (i.e sensitive to the phase information) because the signal is sampled twice in a dwell time interval with a 90° software phase shift. In the case of perfect quadrature, each loop receives the same signal but a independent white noise (coming from the hardware and/or from the sample), quadrature detection improves the SNR by $\sqrt{2}$.

The receiver central frequency is generally set at the center of the spectrum or on the water signal.

1.5.3   Effective field and rotating frame

The general expression of a conventional RF pulse applied on the x-axis is:

$$B_1(t)\hat{\mathbf{x}} = B_{1,\text{env}}(t)\cos(\omega_{RF}t + \Phi_0)\hat{\mathbf{x}} \quad (1.32)$$

where $B_{1,\text{env}}$ is the pulse envelope that can vary with time, ω_{RF} its carrier frequency and Φ_0 its initial phase. Without loss of generality, we will assume $\Phi_0 = 0$ in this section.

We can now write the expression of $\mathbf{B}_{\text{eff}}$ in equation 1.20 with the contributions of $\mathbf{B_0}$ and $\mathbf{B_1}$:

$$\mathbf{B}_{\text{eff}}(t) = B_{1,\text{env}}(t)\cos\left(\omega_{RF}t\right)\hat{\boldsymbol{x}} + \left(\frac{\omega}{\gamma}\right)\hat{\boldsymbol{z}} \quad (1.33)$$

where ω is the resonance frequency of the compound of interest.
ω can differ from the Larmor frequency ω_0 for several reasons. First of all, the direct environment of the resonance of interest creates some shielding or deshielding that will slightly change its Larmor frequency, known an chemical shift (in the order of a few ppm, i.e. a few hundred Hz). This effect will be discussed in section 1.7.1. Second of all, some magnetic field gradients can be applied so that the field experienced by a spin, and consequently its frequency, are greatly changed, depending on its position (in the order of a few kHz). This is used to do slice-selection in localized MRS, as developed in section 1.8.

$$\frac{\omega}{\gamma} = -\mathbf{G}.\mathbf{r} - B_0(1 - \sigma) \quad (1.34)$$

where **G** is the amplitude of the gradient, **r** the position and σ the shielding constant.

The rotating frame has been introduced as a thought process to simplify the representation of the rotations, especially the ones created by $\mathbf{B_1}$. It removes the dependence in $\cos(\omega_{RF} t)$ from the Hamiltonian. We have:

$$\mathbf{B}_{\text{eff}}(t) = B_{1,\text{env}}(t)\left(\cos\left((\omega_{RF} - \omega_{\text{rot}})t\right)\hat{\boldsymbol{x}}' - \sin\left((\omega_{RF} - \omega_{\text{rot}})t\right)\hat{\boldsymbol{y}}'\right) + \left(\frac{\omega}{\gamma} - \frac{\omega_{\text{rot}}}{\gamma}\right)\hat{\boldsymbol{z}} \qquad (1.35)$$

where ω_{rot} is the frequency of the rotating frame and where $\hat{\boldsymbol{x}}'$ is the axis $\hat{\boldsymbol{x}}$ that rotate at ω_{rot} around B_0 in the laboratory frame. Note here that the factor $\frac{1}{2}$ due to the discarded counter-rotating field has been omitted. We will chose $\omega_{\text{rot}} = \omega_{RF}$ during an RF pulse. If we define the offset as $\Omega = \omega - \omega_{RF}$, $\mathbf{B}_{\text{eff}}$ becomes in the rotating frame:

$$\mathbf{B}_{\text{eff}}(t) = B_{1,\text{env}}(t)\hat{\boldsymbol{x}}' + \left(\frac{\Omega}{\gamma}\right)\hat{\boldsymbol{z}} \qquad (1.36)$$

where $\hat{\boldsymbol{x}}'$ is the axis $\hat{x}$ that rotate with ω_{rot} in the laboratory frame.

The magnetization **M** will therefore precess around an effective field tilted from the xy-plane due to the offset Ω, to an extent that depends on the ratio of the $\hat{\boldsymbol{x}}'$ and $\hat{\boldsymbol{z}}$ components, i.e. $\frac{\Omega}{\omega_{1,\text{env}}}$ (**Figure 1.1**).
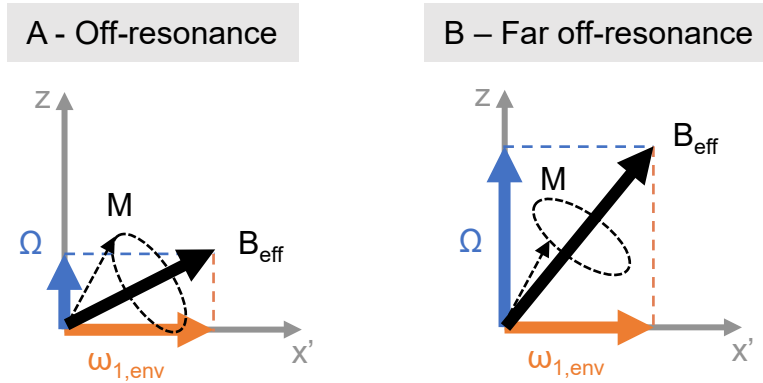
Figure 1.1: Axis of rotation of the effective field B_{eff}, for off-resonance (**A**) and far off-resonance (**B**) excitations. The axis is tilted away from the xy-plane by an amount depending on the offset Ω and the amplitude of the RF field $\omega_{1,\text{env}}$.

In the next sections, conventional and adiabatic pulses, the only ones used in this thesis, will be presented. Other types of pulse exist (frequency-modulated but non-adiabatic pulses, pulses combined with modulating gradients) but will not be presented here.

1.5.4 Conventional pulses

The ratio $\frac{\Omega}{\omega_{1,\text{env}}}$ defines the nature of the RF pulse as follows:

On resonance pulses, $\Omega = 0$ and Φ is constant: when the pulse is applied exactly on resonance for a compound rotating at ω_0, i.e. $\omega_{RF} = \omega_0$ and $\Omega = 0$, the effective field becomes:

$$\mathbf{B}_{\text{eff}}(t) = B_{1,\text{env}}(t)\hat{\boldsymbol{x}}' \tag{1.37}$$

Solving equation 1.20 with the above expression of $\mathbf{B}_{\text{eff}}$, we see that the RF pulse creates a rotation around the $\hat{x}'$-axis, described by the flip angle:

$$\theta = \int_0^{\tau_p} \gamma B_{1,\text{env}}(t)dt \tag{1.38}$$

where τ_p is the pulse duration. In practise, the condition $\Omega = 0$ cannot be satisfied for all the nuclei that have different chemical environments, i.e. chemical shifts.

Hard pulses, $\Omega^j \ll \omega_{1,\text{env}}$ and Φ is constant: this is the hard pulse condition, stating that for most nuclei j under investigation, the on-resonance condition is met (for most j, $\Omega^j \approx 0$). In practice, this is possible only when no gradients are applied, i.e. for non localized MRS where the term **G.r** in the expression 1.34 is zero.

The pulse duration τ_p is inversely proportional to its bandwidth $\Delta\Omega$ (i.e. the frequency range it will act upon with intended tilting effect): a pulse can be made shorter to affect a wider range of frequencies, or longer to affect a narrower range of frequencies.

Soft pulses, $\Omega \approx \omega_{1,\text{env}}$ and Φ is constant: when a gradient is applied to select a slice in localized MRS (section 1.8), a large range of offset Ω have to be excited by the RF pulse and the condition $\Omega^j \ll \omega_{1,\text{env}}$ is not met anymore for all the positions. The effective field is tilted from the x'-axis and its amplitude is given by:

$$B_{\text{eff}}(t) = \sqrt{B_{1,\text{env}}(t)^2 + \frac{\Omega^2}{\gamma}} \tag{1.39}$$

For soft pulses, because B_{eff} is not aligned with the x'-axis, the tilting motion brings the magnetization out of the plane perpendicular to B_1. Depending on the value of Ω, the magnetisation may not cross the xy-plane anymore (off resonance effects, **Figure 1.1**).

1.5.5 Adiabatic pulses

In the case of adiabatic pulses, the phase of the pulse is not constant: they are phase (or frequency)-modulated. In equation 1.32, Φ will change with time:

$$B_1(t)\hat{\mathbf{x}} = B_{1,\text{env}}(t)\cos(\omega_{RF}t + \Phi(t))\hat{\mathbf{x}} \tag{1.40}$$

where ω_{RF} is the RF carrier frequency and:

$$\Phi(t) = \int_0^t (\omega_{\text{mod}}(t') - \omega_{RF})dt' + \Phi_0 \tag{1.41}$$

or defining $\Phi_{RF}(t) = \omega_{RF}t + \Phi(t)$:

$$\Phi_{RF}(t) = \int_0^t \omega_{\text{mod}}(t')dt' + \Phi_0 \tag{1.42}$$

Ω is redefined as:

$$\Omega(t) = \omega - \omega_{\text{mod}}(t) \tag{1.43}$$

where ω is the resonance frequency of the compound of interest and ω_{mod} the RF modulation. Ω changes with time and different resonance frequencies will be affected at different times.

$$B_{\text{eff}}(t) = \sqrt{B_{1,\text{env}}(t)^2 + \frac{\Omega(t)^2}{\gamma}} \tag{1.44}$$

The adiabatic condition states that the change of orientation of B_{eff} should be small compared to the amplitude of B_{eff} for the magnetization $\boldsymbol{M}$ to follow the effective field (or its perpendicular plane) at all times. In other words, if we define α as the angle between B_{eff} and the z-axis, using 1.44:

$$\alpha(t) = \arctan\left(\frac{\gamma B_{1,\text{env}}(t)}{\Omega(t)}\right) \tag{1.45}$$

and thus:

$$\left|\frac{d\alpha}{\gamma dt}\right| \ll |B_{\text{eff}}(t)| \tag{1.46}$$

One of the most common adiabatic pulses is the hyperbolic secant (HS) pulse HS1. Its amplitude modulation $B_{1,\text{env}}(t)$ and frequency modulation $\omega_{\text{mod}}(t) - \omega_{RF}$ over time are:

$$B_{1,\text{env}}(t) = B_{1,\text{max}}\,\text{sech}\left(\beta\left(\frac{2t}{\tau_p} - 1\right)\right) \tag{1.47}$$

$$\omega_{\text{mod}}(t) - \omega_{RF} = A\tanh\left(\beta\left(1 - \frac{2t}{\tau_p}\right)\right) \tag{1.48}$$

where $B_{1,\max}$ is the peak amplitude of the pulse in Tesla, β is a cutoff constant typically chosen as $\mathrm{sech}(\beta) = 0.01$, τ_p is the pulse duration in seconds, and t varies between 0 and τ_p, ω_{RF} the central frequency of the pulse, A the amplitude of the frequency modulation in rad/s, which goes from -A to +A, following the conventions of Garwood at al. [10]. The R value is defined as $\mathrm{R} = \tau_p \times \frac{A}{\pi}$. The HS1 shape is shown in **Figure 1.2**.
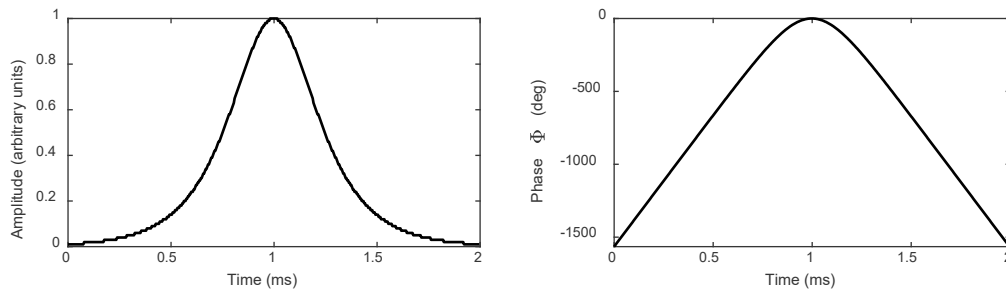
Figure 1.2: Amplitude (left) and phase (right) modulation profiles of an adiabatic hyperbolic secant pulse HS1-R20, defined by equations 1.48 with $\mathrm{R} = \tau_p \times \frac{A}{\pi} = 20$. $\tau_p = 2$ ms is the pulse duration and $\frac{A}{\pi} = 10$ kHz is the pulse bandwidth. $\mathrm{sech}(\beta) = 0.01$.

Adiabatic pulses are beneficial for their sharp selection profiles as illustrated in **Figure 1.5** and limited sensitivity to B_1 inhomogeneities. However, when applied as refocusing pulses in the xy-plane, they lead to the creation of a quadrature phase that cannot be rewinded with linear gradients. Adiabatic refocusing pulses thus have to be applied in pairs, which prolongs the echo time (TE).

The HS1-R20 pulses will be used in the implementation of the diffusion-weighted MRS sequences presented in this thesis.

1.5.6   Power calibration on Bruker systems

Some elements in this section are specific to the workflow in Bruker Paravision. Power calibration of non-conventional pulses is an essential element of sequence programming and the strategies presented in this section were used throughout the thesis. Solving the Bloch equations in 1.20 (without relaxation) for a rotation of **M** around an arbitrary axis given by the orientation of $\mathbf{B}_{\mathrm{eff}}$ allows one to follow the evolution of the components of the magnetization vector as a function of the offset. Numerical solutions of the Bloch equations can be found in many ways [11], the methods based on the quaternions used here being computationally efficient when relaxation is omitted [12]. For each frequency isochromat, the final magnetization components at the end of the RF pulse for a square pulse and for a HS1-R20 pulse are shown in **Figures 1.3** and **1.4**, respectively.
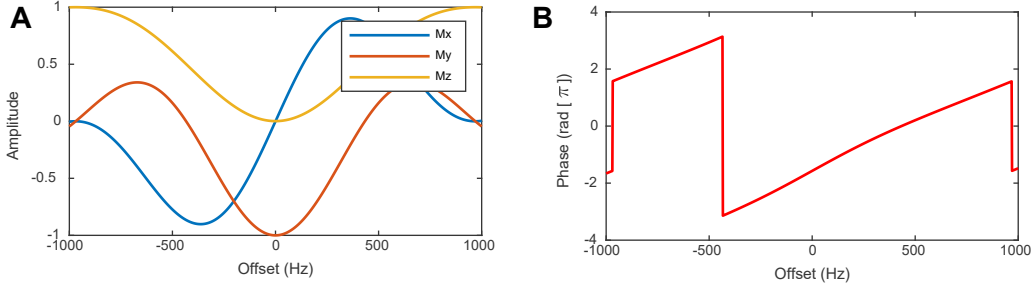
Figure 1.3: Offset-dependent response of the RF pulse for the magnetization in the rotating frame during a square 90° pulse on $\hat{x}'$ ($\tau_p = 1$ ms) with the initial conditions: $M_{x'} = M_{y'} = 0$ and $M_z = 1$. **A**: $M_{x'}$, $M_{y'}$ and M_z for a peak amplitude $\frac{\gamma B_{1,\max}}{2\pi} = 250$ Hz, computed with equation 1.49. **B**: phase $\psi = \text{angle}(M_{x'}; M_{y'})$ (*atan2* in Matlab), linear with the offset around $\Omega = 0$.
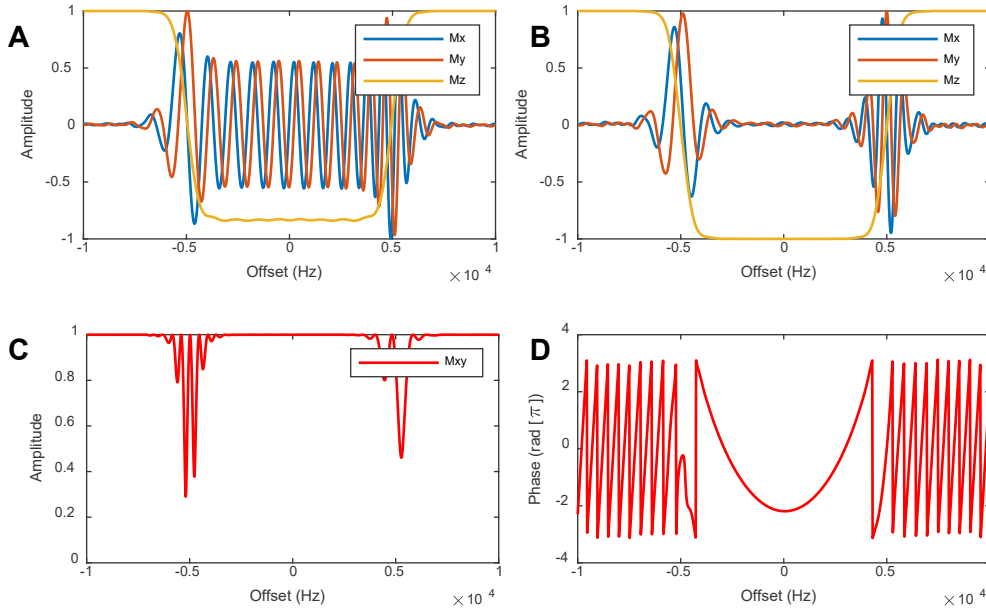
Figure 1.4: Offset-dependent response of the RF pulse for the magnetization in the rotating frame during a HS1-R20 180° pulse ($\tau_p = 2$ ms, $R = \frac{A\tau_p}{\pi} = 20$, i.e. $\frac{A}{\pi} = 10$ kHz bandwidth [10]), with the initial conditions: $M_x' = M_y' = 0$ and $M_z = 1$ for **A** and **B**, and: $M_z = M_y' = 0$ and $M_x' = 1$ for **C** and **D**. **A**: M_x', M_y' and M_z' for $\frac{\gamma B_1}{2\pi} = 2500$ Hz peak amplitude, insufficient to produce a full inversion. **B**: M_x', M_y' and M_z for $\frac{\gamma B_1}{2\pi} = 4500$ Hz peak amplitude, sufficient to produce a full inversion. **C**: $|M_{xy}| = \sqrt{M_x^2 + M_y^2}$, producing a good refocusing for an offset range of ≈ 10 kHz. **D**: phase $\psi = \text{angle}(M_{x'}; M_{y'})$ (*atan2* in Matlab), quadratic with the offset around $\Omega = 0$. Profiles in panels **C** and **D** are computed with the optimized peak amplitude found in panel **B**.
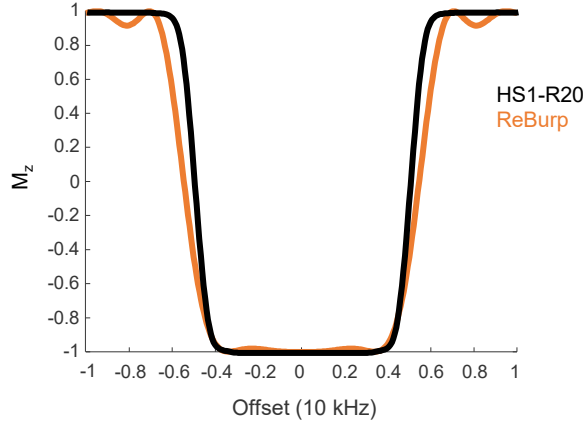
Figure 1.5: Comparison of the inversion profiles for an adiabatic (HS1-R20) and a conventional 180° pulse (ReBurp), for a nominal bandwidth of 10 kHz. Simulation parameters, adjusted to produce a 10 kHz bandwidth for each pulse: HS1-R20: 2 ms, $\frac{\gamma B_1}{2\pi}$ = 4500 Hz peak amplitude, $R = \frac{A\tau_p}{\pi} = 20$, i.e. $\frac{A}{\pi}$ = 10 kHz bandwidth. ReBurp: 500 μs, $\frac{\gamma B_1}{2\pi}$ = 12.5 kHz peak amplitude, $\frac{A}{\pi}$ = 10 kHz bandwidth.

Figure 1.5 shows the inversion profiles of an adiabatic HS1-R20 pulse and of a conventional 180° RF pulse (ReBurp shape, known for its good inversion profile [13]), where the pulse parameters have been adjusted so that each of them produces a bandwidth of 10 kHz. The adiabatic pulse shows a sharper selection profile and fewer unwanted side lobes. The conventional pulse is shorter but requires ≈ 3 times as much peak amplitude to achieve the same 10 kHz bandwidth as the conventional pulse. Although not visible here, the specific absorption rate (SAR) creating adverse effects and possible heating of the subject is proportional to the averaged power (over TR) and not the peak power, for which adiabatic pulses are less advantageous because they are often longer. Another interesting property of the adiabatic pulse is that it is insensitive to B_1 inhomogeneities. As soon as sufficient power is provided, the inversion reaches a stable plateau as shown in **Figure 1.6**.

The amplitude calibration of RF pulses can be done theoretically for conventional pulses following:

$$\frac{\gamma B_{1,\text{max}}}{2\pi} = \frac{\theta}{360} \frac{1}{\tau_p} \frac{1}{S_{\text{int}}} \tag{1.49}$$

where $\frac{\gamma B_{1,\text{max}}}{2\pi}$ is the amplitude in Hz, θ is the flip angle in degrees, τ_p the duration of the pulse in seconds, and S_{int} the shape integration factor of the pulse, which is $S_{\text{int}} = \frac{\sum_i \text{amplitude}_i}{N}$ with N the length of the time-evolution of the pulse shape and where the amplitudes are normalized to 1. $\frac{\gamma B_{1,\text{max}}}{2\pi}$ is linked to the power in Watts by:
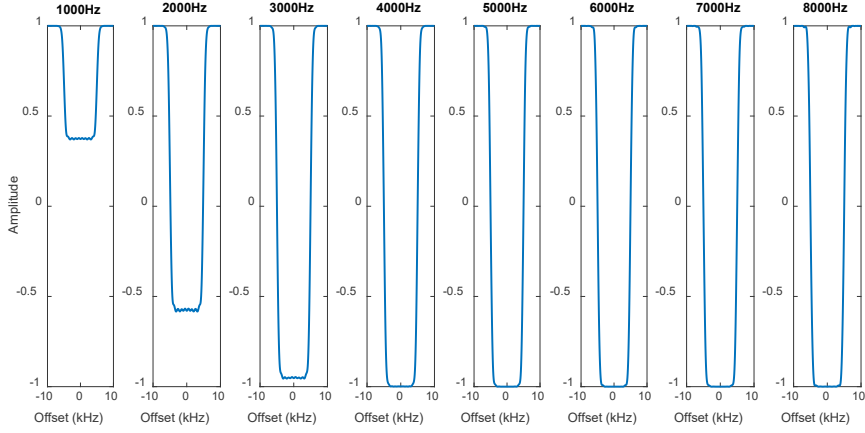
Figure 1.6: Evolution of the inversion profiles for an adiabatic (HS1-R20) as a function of $\frac{\gamma B_1}{2\pi}$, varying from 1000 to 8000 Hz, with the same simulation parameters as in **Figure 1.5**. For any $\frac{\gamma B_1}{2\pi} > 4000$ Hz, the magnetization is well inverted.

$$P_W = P_{W,\text{ref}}\left(\frac{\theta}{90}\frac{1\,\text{ms}}{\tau_{p,\text{ms}}}\frac{1}{S_{\text{int}}}\right)^2 = P_{W,\text{ref}}\left(\frac{\gamma B_{1,\text{max}}}{2\pi}\frac{4}{1000}\right)^2 \tag{1.50}$$

where $P_{W,\text{ref}}$ is the reference power in Watts and $\tau_{p,\text{ms}}$ the duration of the pulse in ms. Typically, on Bruker systems and using a surface coil, the reference power is measured at the beginning of each acquisition by positioning a slab at the depth of voxel or of the region of interest. The reference power will be the power necessary to achieve excitation with a 90° square pulse of 1 ms in that slab. For B_1-inhomogeneous excitations (typically with surface coil), this value will depend on the depth of the slab (the deeper the slab the higher the reference power). The reference power is then used for calibration of all the other non-adiabatic pulses. For adiabatic pulses, equation 1.49 is not valid anymore and the power of the pulse needs to be determined differently: $\frac{\gamma B_{1,\text{max}}}{2\pi}$ should be such that the simulations provide a good inversion profile. The corresponding minimum required power in Watts can be retrieved from the equation 1.50 using the reference power of each acquisition. This power will then be increased to be above the minimum threshold for good inversion. For example, for the HS1-R20 pulse: a typical reference power obtained with the surface coil for a 250 g rat is 0.03 W, the minimum value of $\frac{\gamma B_{1,\text{max}}}{2\pi}$ for a good inversion is 4000 Hz, so with equation 1.50, we have: $0.03 \times (4000 \times \frac{4}{1000})^2 = 7.7\ W$. We will then use a power above this minimum power, improving the tolerance of the pulse to B_1 inhomogeneities.

1.6   Relaxation

Can we predict what part of the Hamiltonian leads to coherent evolution and what part to relaxation?

The phenomenon of spontaneous emission of energy is negligible in MR, the transitions are governed by stimulated emissions (RF) and relaxation. In the case of relaxation, energy is dissipated through:

- spin-lattice interactions, governing longitudinal T_1 relaxation, where M_z goes back to M_0 through energy transfer from the spins to the thermal reservoir (lattice)

- spin-spin interactions, governing transverse T_2 relaxation, where M_{xy} goes back to 0 through a loss of phase coherence caused by different local spin-spin interactions

At the molecular level, the relaxation phenomenon in pure substances is explained by the Bloembergen-Purcell-Pound (BPP) theory of relaxation [14], and governed by the spins tumbling motion (characterized by a correlation time τ_c). T_1 and T_2 are phenomenological constants where spatial dependences have been averaged over the voxel.

The T_1 constants can be measured with inversion recovery or saturation recovery sequences, where the magnetization is first inverted or saturated and then measured at different times during its recovery process. The T_2 constants can be measured with a Carr-Purcell-Meiboom-Gill (CPMG) sequence.

The phenomenological Bloch equations describe the evolution of the magnetization at the ensemble level, with respect to relaxation:

$$\frac{d\mathbf{M}}{dt}\bigg|_{rot} = -\gamma \mathbf{B}_{\text{eff}} \times \mathbf{M} - \frac{M_x \hat{\boldsymbol{x}}' + M_y \hat{\boldsymbol{y}}'}{T_2} - \frac{M_z - M_0}{T_1}\hat{\boldsymbol{z}} \tag{1.51}$$

When the magnetic field experienced by the sample is inhomogeneous, the effective relaxation in the plane is governed by T_2^*, which is smaller than T_2:

$$\frac{1}{T_2^*} = \frac{1}{T_2} + \frac{1}{T_2^+} \tag{1.52}$$

where T_2^+ represents the loss of phase coherence created by local B_0 field inhomogeneities, approximated here to be also of Lorentzian shape but which is not always the case. The solution of this equation for M_{xy} is, ignoring the effect of J-evolution and the effet of RF pulses:

$$M_{xy}(t) = M_{xy}(0)\exp(i\Omega_r t)\exp\left(\frac{-t}{T_2^*}\right) \tag{1.53}$$

where $M_{xy}(0)$ is the initial value of the magnetization, Ω_r is the frequency offset of the compound of interest with respect to the receiver central frequency (which is a priori different from the Ω defined in section 1.5, which was the frequency offset of the compound of interest with respect to the RF carrier frequency). This complex time-domain signal M_{xy} is called the free induction decay (FID). The signal we visualize is the Fourier Transform of equation 1.53:

$$S(\omega) = \text{FT}\left\{M_{xy}\right\} = A(\omega) + iD(\omega) \tag{1.54}$$

where ω is the frequency variable, A is the absorption and D the dispersion parts such that:

$$A(\omega) = M_0 \frac{\frac{1}{T_2^*}}{\left(\frac{1}{T_2^*}\right)^2 + (\omega - \Omega_r)^2} \tag{1.55}$$

and:

$$D(\omega) = -M_0 \frac{(\omega - \Omega_r)}{\left(\frac{1}{T_2^*}\right)^2 + (\omega - \Omega_r)^2} \tag{1.56}$$

If the signal is well phased, the real part of the spectrum is the absorption lineshape and the imaginary part the dispersion lineshape. If the signal is not well phased ($M_{xy}(t) = M_0\exp(i\Omega_r t)\exp\left(\frac{-t}{T_2^*}\right)\exp(i\phi)$), the real and imaginary parts of S(ω) are a combination of the absorption and dispersion lineshapes: $S(\omega) = R(\omega) + iI(\omega)$ where $R(\omega) = A(\omega)\cos\phi - iD(\omega)\sin\phi$ and $I(\omega) = A(\omega)\sin\phi + iD(\omega)\cos\phi$. The full width half maximum (FWHM) for a Lorentzian shape is given by:

$$\text{FWHM} = \frac{1}{\pi T_2^*} \tag{1.57}$$

and the integral of the spectrum is by definition the first point of the FID:

$$M_{xy}(0) = \int_{-\infty}^{+\infty} \tilde{M}_{xy}(\omega)d\omega \tag{1.58}$$

1.7   Spin interactions

The secular approximation and motional averaging lead to a simplification of the Hamiltonian terms predicting the NMR interactions [2].
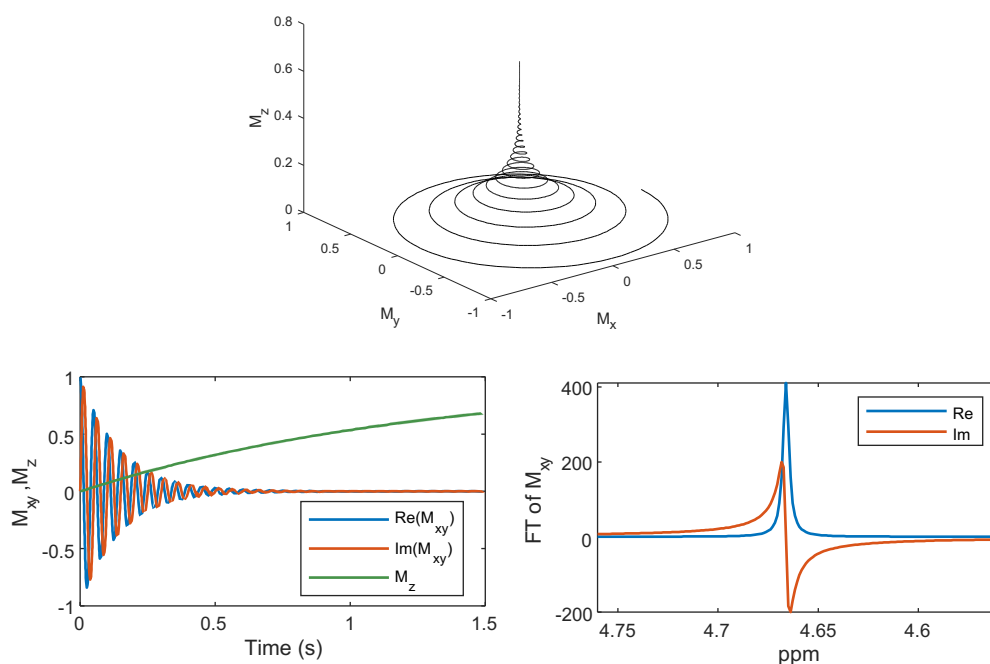
Figure 1.7: Evolution of the magnetization during the acquisition under relaxation and offset after a 90° pulse. Top: 3D representation of M in the time domain, Bottom: 2D representation of **M** in the time domain (left) and its corresponding frequency domain representation (right). Simulation parameters: $M_{xy}(0) = 1$, $T_1 = 1.3$ s, $T_2^* = 150$ ms, $\Omega_r = 2\pi \times 20$ rad/s, $\frac{\gamma B_0}{2\pi} = 600$ MHz, receiver central frequency: 4.7 ppm.

- The secular approximation arises because the Hamiltonian is in general dominated by the large interaction with the external magnetic field, masking some slowly time-varying contributions of other interactions (details of the simplifications for the case of chemical shift or scalar coupling are given in ref [2], *Appendix A6*).

- Motional averaging (as it occurs in isotropic liquids) implies that some interactions average out to zero due to motion and only the motion-invariant terms survive (having a non-zero mean).

The elements of the Hamiltonian that survive these two steps lead to a coherent evolution, and the elements discarded during either one of these two steps lead to relaxation.

In isotropic liquids of spins-1/2, **dipolar interactions** average out to 0 by motional averaging and only lead to relaxation. The **chemical shift** Hamiltonian has a non-zero mean that survives these two steps: only the diagonal element in the direction of B_0 of the tensor $\boldsymbol{\sigma}$ is preserved after the secular approximation, and replaced by the rotational invariant $\sigma = \frac{Tr(\boldsymbol{\sigma})}{3}$

after motional averaging leading to:

$$H_{cs} = -\gamma \hbar \sigma B_0 \tag{1.59}$$

For the **weak scalar coupling (or J-coupling) interactions**, i.e. when $|\omega_2 - \omega_1| \gg \pi J_{12}$, only the $I_{1z}I_{2z}$ term survives after secular approximation and motional average approximations ($J = \frac{Tr(\mathbf{J})}{3}$) leading to:

$$H_J = \pi \hbar J 2 I_{1z} I_{2z} \tag{1.60}$$

Other interactions exist but are small or inexistent for spins-1/2 in most frequent cases.

1.7.1 Chemical shift

The resonance frequency of a nucleus depends on its environment. The electrons rotating on atomic orbitals create a small additional local magnetic field and the resulting field felt by the nucleus is shifted compared to the Larmor frequency $\omega_0 = -\gamma B_0$ by:

$$\omega^j = -\gamma B_0 (1 - \sigma^j) \tag{1.61}$$

where σ^j the shielding constant. A compound is chosen as reference, in general TMS for ^{1}H MRS: it has one single heavily shielded resonance. For any other compound j, we have:

$$\omega^j = \omega^{\text{ref}} (1 + \delta^j) \tag{1.62}$$

where δ^j expresses the deshielding compared to the reference compound. ω^j is more negative than ω^{ref} for a positive γ and a positive δ^j (**Figure 1.8**). For example water is deshielded (towards decreasing frequencies, left side of the spectrum) compared to the TMS because the oxygen is electronegative and attracts the electron cloud.

The chemical shift is then defined, in parts per million, as:

$$\delta^j{}_{\text{ppm}} = 10^6 \frac{\omega^j - \omega^{\text{ref}}}{\omega^{\text{ref}}} \tag{1.63}$$

The chemical shift scale renders the metabolites position independent of the field strength. Increasing B_0 increases the spectral separation of metabolites and facilitates their quantification.
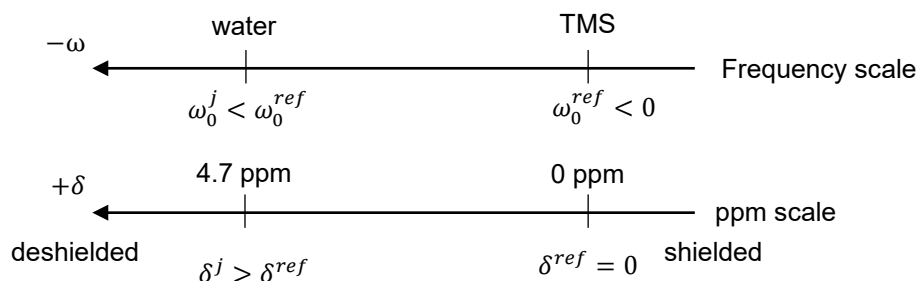
Figure 1.8: Relation between the frequency scale and the ppm scale for the reference compound (TMS) and water

1.7.2 Scalar coupling

Scalar coupling arises from spin interactions through chemical bonds that create new levels of energies. It creates a modulation of the signal during the echo time and during the acquisition of form $\cos(\pi J t)$, where J is the coupling constant. This leads to a splitting of the spectral peaks as shown in **Figure 1.9**, analogous to **Figure 1.7** but including this time the effect of scalar coupling.
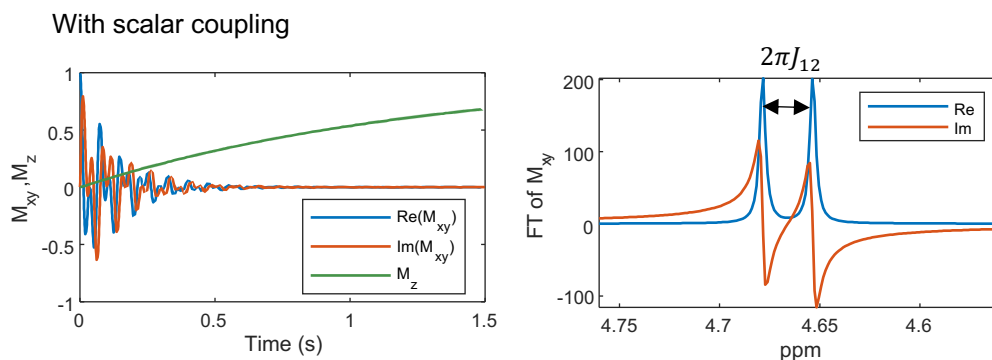
Figure 1.9: Evolution of the magnetization during the acquisition under relaxation, offset and J-coupling after a 90° pulse. 2D representation of **M** in the time domain (left) and its corresponding frequency domain representation (right). The FID is modulated by $\cos(\pi J_{12} t)$, i.e., $M_{xy} = M_{xy}(0) \exp(i\Omega_r t) \exp\left(-\frac{t}{T_2^*}\right) \cos(\pi J_{12} t)$. Simulation parameters: $M_{xy}(0) = 1$, $T_1 = 1.3$ s, $T_2^* = 150$ ms, $\Omega_r = 2\pi \times 20$ rad/s, $B_0 = 600$ MHz, receiver central frequency: 4.7 ppm, $J_{12} = 15$ Hz.

The product operator formalism is well suited to represent coherent evolution, created for example by the chemical shift or frequency offsets creates by gradients, B_0 inhomogeneities and J-coupling during standard MR sequences.

In particular, if we consider a system of two spins with their respective offsets and coupled by a constant J_{12}, the Hamiltonian of the system is:

$$\hat{H}_{2spins} = \Omega_1 \hat{I}_{1z} + \Omega_2 \hat{I}_{2z} + 2\pi J_{12} \hat{I}_{1z} \hat{I}_{2z} \tag{1.64}$$

where $\Omega_1 \hat{I}_{1z}$ is the Hamiltonian associated to the offset of spin 1, $\Omega_2 \hat{I}_{2z}$ the Hamiltonian associated to the offset of spin 2 and $2\pi J_{12} \hat{I}_{1z} \hat{I}_{2z}$ the Hamiltonian associated to the J-coupling.

We will show that the offset (including the chemical shift and the phase dispersion created by B_0 inhomogeneities) are refocused by a spin echo, but not the J-evolution.

This is an important concept because the J-evolution is often the main source of signal loss in standard MRS sequences (together with T_2 relaxation but whose induced loss is intrinsically irreversible).

The offset and the J-coupling evolutions can be treated separately. Let's show first that the chemical shift offset is refocused for a single isolated spin with a spin echo (with the convention $\omega_1 = +\gamma B_1$).

$$\hat{I}_{1z} \xrightarrow{\frac{\pi}{2}\hat{I}_y} \hat{I}_{1x} \xrightarrow{\Omega_1 \tau \hat{I}_{1z}} \cos(\Omega_1\tau)\hat{I}_{1x} + \sin(\Omega_1\tau)\hat{I}_{1y} \xrightarrow{\pi\hat{I}_x} \cos(\Omega_1\tau)\hat{I}_{1x} - \sin(\Omega_1\tau)\hat{I}_{1y}$$

$$\xrightarrow{\Omega_1 \tau \hat{I}_{1z}} \cos(\Omega_1\tau)\left(\cos(\Omega_1\tau)\hat{I}_{1x} + \sin(\Omega_1\tau)\hat{I}_{1y}\right) - \sin(\Omega_1\tau)\left(\cos(\Omega_1\tau)\hat{I}_{1y} - \sin(\Omega_1\tau)\hat{I}_{1x}\right)$$

$$= \hat{I}_{1x}$$

$$\tag{1.65}$$

Let's now show that the phase dispersion created by B_0 inhomogeneities for an ensemble of spins is refocused with a spin echo.

$$\hat{I}_{1z} \xrightarrow{\frac{\pi}{2}\hat{I}_y} \hat{I}_{1x} \xrightarrow{\Delta\Omega_1 \tau \hat{I}_{1z}} \cos(\Delta\Omega_1\tau)\hat{I}_{1x} + \sin(\Delta\Omega_1\tau)\hat{I}_{1y} \xrightarrow{\pi\hat{I}_x} \cos(\Delta\Omega_1\tau)\hat{I}_{1x} - \sin(\Delta\Omega_1\tau)\hat{I}_{1y}$$

$$\xrightarrow{\Delta\Omega_1 \tau \hat{I}_{1z}} \cos(\Delta\Omega_1\tau)\left(\cos(\Delta\Omega_1\tau)\hat{I}_{1x} + \sin(\Delta\Omega_1\tau)\hat{I}_{1y}\right) - \sin(\Delta\Omega_1\tau)\left(\cos(\Delta\Omega_1\tau)\hat{I}_{1y} - \sin(\Delta\Omega_1\tau)\hat{I}_{1x}\right)$$

$$= \overline{\cos^2(\Delta\Omega_1\tau)}\hat{I}_{1x} + \overline{\sin^2(\Delta\Omega_1\tau)}\hat{I}_{1x} = \hat{I}_{1x}$$

$$\tag{1.66}$$

Chemical shifts or B_0 inhomogeneities are undistinguishable in the above derivations and are both refocused with a SE.

Let's now show that the J-evolution is not refocused and creates a modulation of the magneti-

zation:

$$
\hat{I}_{1z} \xrightarrow{\frac{\pi}{2}\hat{I}_y} \hat{I}_{1x} \xrightarrow{2\pi J_{12}\tau\hat{I}_{1z}\hat{I}_{2z}} \cos(\pi J_{12}\tau)\hat{I}_{1x} + \sin(\pi J_{12}\tau)2\hat{I}_{1y}\hat{I}_{2z}
$$

$$
\xrightarrow{\pi\hat{I}_x} \cos(\pi J_{12}\tau)\hat{I}_{1x} + \sin(\pi J_{12}\tau)2\hat{I}_{1y}\hat{I}_{2z}
$$

$$
\xrightarrow{2\pi J_{12}\tau\hat{I}_{1z}\hat{I}_{2z}} \cos(\pi J_{12}\tau)\left(\cos(\pi J_{12}\tau)\hat{I}_{1x} + \sin(\pi J_{12}\tau)2\hat{I}_{1y}\hat{I}_{2z}\right) \tag{1.67}
$$

$$
+ \sin(\pi J_{12}\tau)\left(\cos(\pi J_{12}\tau)2\hat{I}_{1y}\hat{I}_{2z} - \sin(\pi J_{12}\tau)\hat{I}_{1x}\right)
$$

$$
= \left(\cos(\pi J_{12}\tau)^2 - \sin(\pi J_{12}\tau)^2\right)\hat{I}_{1x} + 2\cos(\pi J_{12}\tau)\sin(\pi J_{12}\tau)2\hat{I}_{1y}\hat{I}_{2z}
$$

In the end we have for $\hat{I}_{1x}$:

$$
\hat{I}_{1z} \xrightarrow{\text{J-evolution in a SE}} \cos(2\pi J_{12}\tau)\hat{I}_{1x} + \sin(2\pi J_{12}\tau)2\hat{I}_{1y}\hat{I}_{2z} \tag{1.68}
$$

From this equation, we see that, at the time of the echo (very beginning of the acquisition), the in-phase term $\hat{I}_{1x}$, proportional to observable M_x, is ponderated by the cosine of the J-evolution: $\cos(2\pi J_{12}\tau)$, where 2τ is the echo time. The anti-phase term $2\hat{I}_{1y}\hat{I}_{2z}$ is not observable as is but will evolve in an observable $\hat{I}_{1x}$ term during the acquisition time.

Overall, the J-evolution is not refocused by a spin echo. It is thus important to minimize the TE of MRS sequences to limit the loss by J-evolution. As an example, we can compare the effect of a loss by T_2-relaxation (also not refocused) with the loss by J-evolution. For a spin echo sequence with a TE of 30 ms, a T_2 of 150 ms (typical value at 14.1T), a coupling of $J = 10$ Hz, we have: $\exp(-TE/T_2) = 0.82$ and $\cos(\pi JTE) = 0.59$, thus a stronger penalty due to J-evolution than T_2 relaxation. In practice, the application of a train of adiabatic pulses reduces the apparent T_2 and J-evolution compared to a sequence with the same echo time but free precession [15, 16], but their description is more difficult.

The observation (theoretically and with simulations) of the strong loss by J-evolution during the long echo time of the STE-LASER sequence triggered the idea to propose an alternative sequence with a shorter echo time.

For a stimulated echo (succession of 3 90° pulses, here on y), the multiple-quantum contribution from the multiple-coherence term $2\hat{I}_{1y}\hat{I}_{2x}$ is removed during the mixing time my homonuclear spoiling (the zero quantum coherence contribution remains but we will assume here that it is small) and we have at the end:

$$
\hat{I}_{1z} \xrightarrow{\text{J-evolution in a STE}} -\cos(\pi J_{12}\tau)^2\hat{I}_{1x} - \cos(\pi J_{12}\tau)\sin(\pi J_{12}\tau)2\hat{I}_{1y}\hat{I}_{2z} \tag{1.69}
$$

Here, at the time of the echo, the observable term $\hat{I}_{1x}$ is proportional to $\cos(\pi J_{12}\tau)^2$, where 2τ is the echo time.

1.8 MR spectroscopy

In vivo MRS allows one to measure the local content of metabolites from a tissue, exploiting the chemical shift differences between the resonances of each metabolite. In the brain for example, MRS provides valuable information on a variety of brain functions, probing metabolites involved in neurotransmission, osmoregulation, or energy metabolism.

The general principles of 1D NMR described above still hold but there is in addition the desire to record the NMR signal from a specific region of the sample only. To select a volume, linearly-varying magnetic field gradients are used because they render the frequency position-dependent:

$$\omega(\boldsymbol{r}) = \omega_j - \gamma \mathbf{G}.\mathbf{r} = -\gamma B_0(1 - \sigma^j) - \gamma \mathbf{G}.\mathbf{r} \tag{1.70}$$

where ω_j is the chemically-shifted Larmor frequency of the compound j defined in equation 1.61, $\mathbf{G}$ the gradient and $\mathbf{r}$ the position of the compound j. In practise, the frequency shift introduced by the gradients is much greater than the one caused by the different chemical environments (chemical shift).

If a gradient of magnetic field is applied on the z-direction, the frequency will depend on the z-coordinate. Now, if an RF pulse, whose frequency response is defined by a central frequency ω_{RF} and a bandwidth $\Delta\omega_{RF}$ is applied simultaneously with the gradient, the frequencies approximately ranging from $\omega_{RF} - \frac{\Delta\omega_{RF}}{2}$ and $\omega_{RF} + \frac{\Delta\omega_{RF}}{2}$ will be affected by the RF pulse. Because of the gradient G_z, these frequencies correspond to a range of z-coordinates, from $z_{sl} - \frac{\Delta z}{2}$ to $z_{sl} + \frac{\Delta z}{2}$. Only the regions of the sample with these coordinates will be affected, i.e. in a slice perpendicular to the z-axis centred around z_{sl} with a thickness Δz (**Figure 1.10**). The size Δz of the selected region is fixed by the pulse bandwidth and by the gradient amplitude:

$$\Delta z = \frac{2\pi\Delta\omega_{RF}}{\gamma G_z} \tag{1.71}$$

centred around:

$$z_{sl} = \frac{\omega_{RF} - \omega_{RF,zsl=0}}{\gamma G_z} \tag{1.72}$$

where G_z is the value of the gradient required to select the desired slice Δz, ω_{RF} is the frequency offset with respect to the water frequency and $\omega_{RF,zsl=0}$ the offset created due to the chemical shift when no gradient is applied. This is the principle of slice-selection in MRS. By applying a gradient and an RF pulse successively along three perpendicular directions, a 3D volume can be selected as shown in **Figure 1.10**.
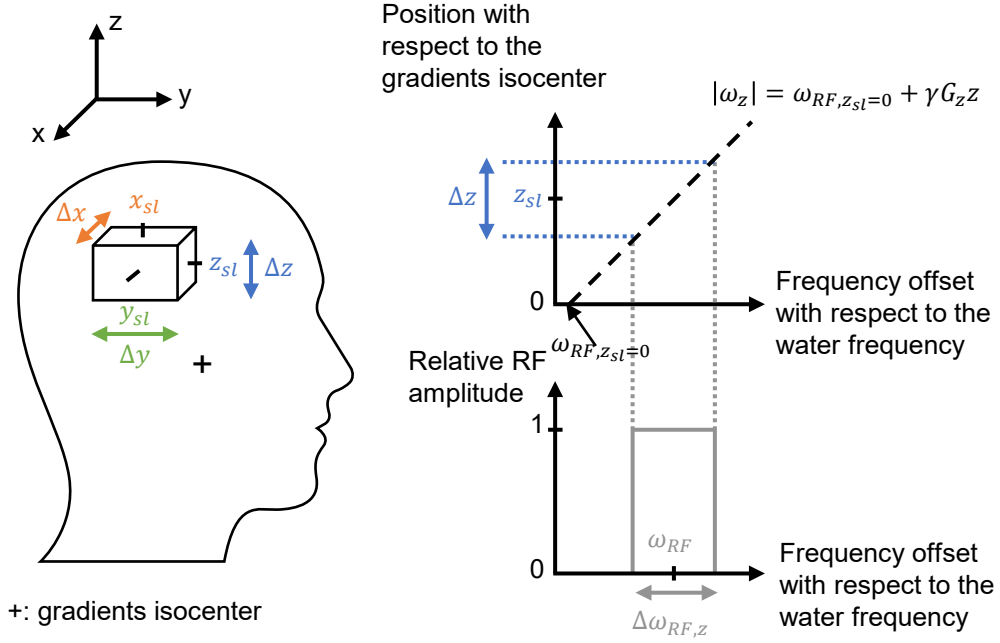
Figure 1.10: Principe of volume selection in MRS, consisting of successive slice selections in all 3 directions. Here ω_{RF} is the RF pulse carrier frequency, in general shifted to the centre of the metabolite spectrum to limit chemical shift displacement artefacts (designated here by $\omega_{RF,zsl=0}$, when no gradient is applied). $\Delta\omega_{RF,z}$ is the bandwidth of the RF pulse, z_{sl} the central position of the slice and Δz the size of the slice.

1.8.1 MRS sequences

This 3D volume selection can be achieved by several combinations of RF pulses and gradients. The most widespread single-voxel MRS sequences are illustrated in **Figure 1.11**.

The STEAM sequence [17] consists of 3 slice-selective 90° pulses and a stimulated echo is measured. It benefits a the short minimum echo time and the 90° pulses are well suited for high fields because they allow a good volume selection (high bandwidth for limited power as compared to 180° pulses) but half of the magnetization is lost. We can understand the loss of half of the magnetization with the product operator formalism (neglecting J-evolution):

$$\hat{I}_z \xrightarrow{\frac{\pi}{2}\hat{I}_x} -\hat{I}_y \xrightarrow{\Omega\tau\hat{I}_z} -\cos(\Omega\tau)\hat{I}_y + \sin(\Omega\tau)\hat{I}_x \xrightarrow{\frac{\pi}{2}\hat{I}_x} -\cos(\Omega\tau)\hat{I}_z + \sin(\Omega\tau)\hat{I}_x$$

$$\xrightarrow{\text{homonuclear spoiling}} -\cos(\Omega\tau)\hat{I}_z \xrightarrow{\frac{\pi}{2}\hat{I}_x} \cos(\Omega\tau)\hat{I}_y \xrightarrow{\Omega\tau\hat{I}_z} \cos(\Omega\tau)\left(\cos(\Omega\tau)\hat{I}_y - \sin(\Omega\tau)\hat{I}_x\right)$$

$$\rightarrow \overline{\cos^2(\Omega\tau)}\hat{I}_y - \overline{\cos(\Omega\tau)\sin(\Omega\tau)}\hat{I}_x \rightarrow \frac{1}{2}\hat{I}_y$$

$$(1.73)$$
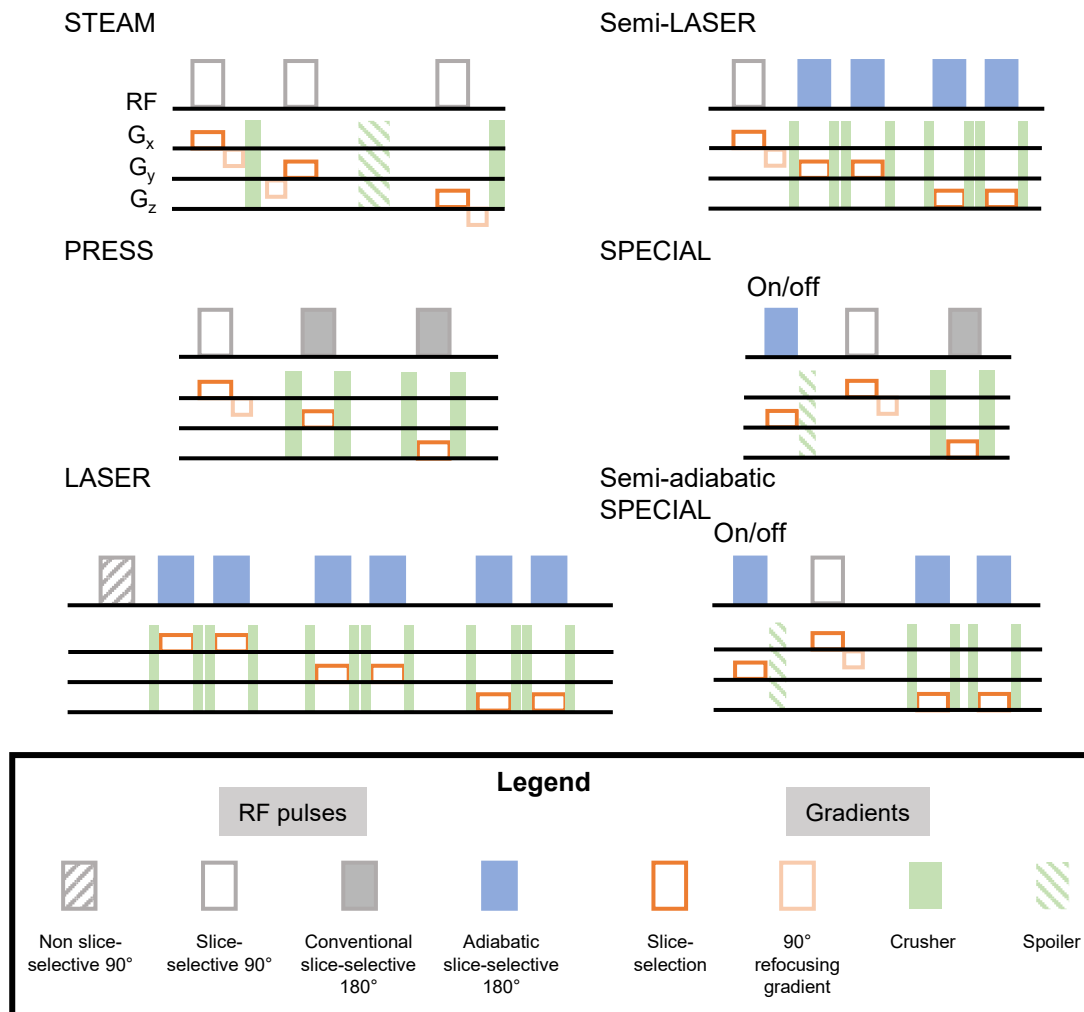
Figure 1.11: Schematic representation of the most used MRS sequences. RF: grey-empty: slice-selective 90° pulses, grey-dashed: non slice-selective 90° pulses, grey-full: conventional slice-selective 180° pulses, blue: adiabatic slice-selective 180° pulses. Gradients: orange: slice selection gradients, light orange: refocusing gradients for the slice selective 90° pulses (see section 1.8.3), green-full: crusher gradients, green-light: spoiler gradients. *On/off* indicates that the pulse is applied once every two shots (ISIS scheme).

where Ω includes the effect of chemical shift, B_0 inhomogeneities and gradients. The overline indicates averaging of a uniform distribution of $\Omega\tau$ and gives $\frac{1}{2}$ for the squared cosine.

The PRESS sequence [18] preserves the full magnetization but utilizes non adiabatic 180° pulses which are sensitive to B_1 inhomogeneities and provide a worse selection profile for higher peak power requirements than adiabatic pulses (see Reburp versus HS1-R20 profiles, **Figure 1.5**) or 90° pulses such as in STEAM. Low-bandwidth 180° RF pulses lead to higher chemical shift displacement artefacts (section 1.8.2) and minimal achievable echo times are

longer than in STEAM.

The LASER sequence [10] (initially SADLOVE [19]) uses a non-selective excitation and 6 adiabatic 180° pulses for localization in the 3 directions. The pairs are necessary to refocus the quadratic phase caused by adiabatic pulses. It benefits from sharp voxel selection properties, limited chemical shift displacement (CSD) artefacts (see details in section 1.8.2) due to high RF bandwidth achieved with limited RF power, and limited sensitivity to B_1 inhomogeneities. However, it suffers from long echo times, thus more loss by J-evolution and T_2. The non-selective excitation may also refocus unwanted outer volume signals. It also suffers from a high specific absorption rate (SAR), proportional to the average RF power, which limits its clinical translation [20, 8]. Its semi-adiabatic counterpart (semi-LASER) uses a slice-selective 90° instead of the first pair of adiabatic and thus reduces the echo time, while maintaining the good properties given by the adiabatic pulses for the other directions. Consequently, it is less SAR-demanding than the LASER sequence and limits the appearance of spurious echoes from outside the VOI because the first pulse is now slice-selective.

The SPECIAL sequence [21] consists of a slice-selective adiabatic 180° pulse on/off as for an 1D ISIS module, followed by a slice-selective 90°-180° spin echo. It is a two shot sequence and can be sensitive to motion, but allows to reach shorter echo times and thus enables a good quantification of the metabolites. The semi-adiabatic SPECIAL is its counterpart where the last 180° pulse has been replaced by a pair of adiabatic pulses to benefit from their advantages listed above. However, it prolongs the echo time. **The SPECIAL localization will be used as an alternative to the LASER localization for the diffusion-weighted MRS sequence developed in this thesis.**

1.8.2 Chemical shift displacement artefacts

As seen in equation 1.72, the exact position of the voxel will depend on the chemical shift. As a consequence, a different voxel will be selected for each resonance frequency, and thus for each metabolite and for the water. This is known as chemical displacement artefact (CSD).

In the case where all three slice-selective pulses have the same bandwidth, it is defined as (in %):

$$\text{Overlap}_\% = \left(1 - \frac{\Delta f_{\text{met,Hz}}}{RF_{BW}}\right)^3 \times 100 \qquad (1.74)$$

where $\Delta f_{\text{met,Hz}}$ is the frequency difference between the compound of interest and the RF carrier frequency in Hz, and RF_{BW} the bandwidth of the RF pulses selecting the voxel, assuming $RF_{BW} > \Delta f_{\text{met,Hz}}$ which is always the case in practise. For example, if the RF carrier frequency in centered on the water peak at 4.7 ppm, the difference with the macromolecule peak at 0.9 ppm at 14T is 2280 Hz. With a $RF_{BW} = 10$ kHz, there is 46% overlap between the water

(the voxel we positioned on the anatomical image) and the macromolecule voxel and all the metabolite voxels are shifted towards the same direction for a given gradient polarity. If the RF carrier frequency in centered instead in the middle of the metabolite spectrum around 3 ppm, the difference with the macromolecule peak at 0.9 ppm at 14T is now 1260 Hz, the overlap is 67% between the voxel corresponding to the resonance in the middle of the spectrum and the MM resonance, and the metabolite voxels are shifted towards both the positive and the negative directions for a given gradient polarity. This effect is even more important at high fields since the spread of frequencies if proportional to B_0. We thus try to have high RF bandwidths.

1.8.3 Refocusing factor for a slice-selective 90° pulse

In the design of an MR sequence, a slice-refocusing gradient lobe is necessary after a slice-selective 90° RF pulse to refocus the different phases acquired by the spins depending on their position in the slice. For many excitation pulses, this phase is linear with the offset (contrary to quadratic for adiabatic pulses), which can then be refocused by an additional gradient of inverse polarity and of area equal to a fraction α of the slice-selection gradient.

The simulations of the effect of an RF pulse presented in section 1.5.6 for power calibration can also be used to estimate the refocusing factor α. The area of the slice-selection gradient $A_{G_{\mathrm{sl}}}$ and of the slice-refocusing lobe $A_{G_{\mathrm{slrefoc}}}$ are linked by:

$$A_{G_{\mathrm{slrefoc}}} = \alpha A_{G_{\mathrm{sl}}} \tag{1.75}$$

with $0 < \alpha < 1$ and:

$$\alpha = \frac{|\Delta\psi_{\mathrm{rad}}|}{\Delta f \times 2\pi \times \tau_p} \tag{1.76}$$

where $\Delta\psi_{\mathrm{rad}}$ is the phase range in radians of M_{xy} created by the pulse over a range of frequencies Δf in Hz, and τ_p the duration of the RF pulse in seconds.

$\frac{|\Delta\psi_{\mathrm{rad}}|}{\Delta f}$ can be measured from the Bloch simulations of the pulse frequency response (e.g. **Figure 1.3**), as the slope of the phase as a function of the offset around 0 Hz (**Figure 1.12**, zoom from **Figure 1.3**).

With the small flip angle approximation (i.e. $M_z(t) \approx M_0$) [22], the Bloch equations can be uncoupled and the slice profile is approximated by the Fourier transform of the time-dependent pulse envelop $B_{1,\mathrm{env}}(t)$:

$$M_{xy}(t) \approx \gamma M_0 \int_0^t B_{1,\mathrm{env}}(t') \exp(-i\omega t') dt' \tag{1.77}$$

For the square 90° pulse of **Figure 1.3**, with amplitude $B_{1,\mathrm{env}}(t) = B_{1,\mathrm{max}} = A$ and duration τ_p, $H(f) = \int_0^t B_{1,\mathrm{env}}(t')\exp(-i\omega t')dt'$ is:

$$H(f) = \int_0^{\tau_p} A\exp(-i2\pi f t)dt = \frac{A}{\pi f}|\sin(2\pi f\frac{\tau_p}{2})|\exp(i\psi) \tag{1.78}$$

with

$$\psi = \arctan\left(\frac{\cos\left(2\pi f\tau_p\right)-1}{\sin\left(2\pi f\tau_p\right)}\right) = -\pi f\tau_p \tag{1.79}$$

so

$$\Delta\psi = -\pi\Delta f\tau_p \tag{1.80}$$

With this approximation, $\alpha = 0.5$. If we compute instead the refocusing factor based on the solutions of the Bloch simulations without the FT approximation, we get $\alpha = 0.637$, which is the correct value for a square 90° pulse. With this example, we see that the FT approximation of the profile is not well suited to compute the refocusing factor of a 90° pulse. The comparison is detailed in **Figure 1.12**. This factor α is not only involved in the scaling of the refocusing gradient but also in the timing calculation of the sequence: if improperly computed, it will lead to a loss of signal or to a first order phase due to an unbalanced delay.

Because $\alpha = 0.5$ is still a good approximation for the most common symmetric pulses (e.g., Gauss pulses), the exact value of the refocusing factor is erroneously not used by default in the MR sequences provided by Bruker. The exact calculations presented here ($\alpha = 0.63$ for the square pulses, $\alpha = 0.18$ for the first asymmetric 90° pulse P10, see chapter 5) were implemented in DW-SPECIAL.

1.8.4 An MR spectrum at ultra-high magnetic field

The elements in this section describe the typical workflow in Bruker Paravision.

The acquisition of a good spectrum relies on various parameters. First, the region of interest is positioned as close as possible to the gradients isocenter to help B_0 shimming (position compared to the isocenter typically $\leq$ 3 mm for all the directions in a preclinical MR scan). The two loops of the quadrature coil are then tuned and matched (reflected power between the spectrometer plug and the RF coil typically below 10% of the normalized amplitude at the central frequency), and the RF reference power is calibrated on a slab positioned at the same depth as the voxel (for a 300 g rat, with a surface coil, $P_{\mathrm{W,ref}} \approx 0.03$ W). This power will be used to compute the power required for all other non-adiabatic pulses of the acquisition (section 1.5.6). The receiver gain (typically optimized at the value 101 for spectroscopy sequences in vivo on Bruker scanners) and the optimal phase for the complex combination of the loops signal at reception (typically found between 90° and 110°, resulting from an imperfect quadrature

A From the solutions of the Bloch equations for a 90° square pulse of duration $\tau_p = 1\ ms$:

x: 200 Hz
y: -0.75 rad

x: -200 Hz
y: -2.35 rad

$$\alpha = \frac{|\Delta\psi|}{2\pi\Delta f \times \tau_p} = 0.63$$
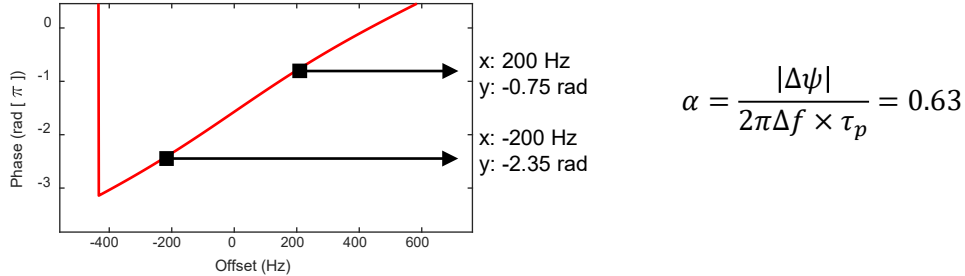
B With small flip angle approximation for a 90° hard pulse of duration $\tau_p = 1\ ms$:

$$\alpha = \frac{|\Delta\psi|}{2\pi\Delta f \times \tau_p} = \frac{2\pi\Delta f \times \dfrac{\tau_p}{2}}{2\pi\Delta f \times \tau_p} = 0.5$$

Figure 1.12: Comparison of the refocusing factors estimation based on **A**: the numerical integration of the Bloch equations (zoomed from **Figure 1.3**) and **B**: the Fourier transform approximation of the excitation profile by the time-dependent envelope of the pulse $B_{1,\text{env}}$.

position of the two loops, section 1.5.2) are calibrated. MR images (T2-turbo RARE, giving a high resolution image with multiple slices in one orientation, and a gradient-echo localizer multi-slice sequence, giving a low resolution image but with multiple slice orientations) are acquired to position the voxel. Following these calibrations, the choice of the MRS sequence should be tailored to the needs of the application. In our case, short echo time sequences such as the ones using STEAM or SPECIAL localizations were preferred to limit the loss by T_2 relaxation and J-evolution and thus to reliably quantify a large number of metabolites. The spectrum of **Figure 1.13** was acquired in the rat brain at 14.1T, with the diffusion-weighted semi-adiabatic SPECIAL sequence at low diffusion-weighting (TE = 18 ms, b-value = 0.05 ms/μm^2). 18 metabolites can be identified: alanine (Ala), ascorbate (Asc), aspartate (Asp), glycerophosphocholine (GPC), phosphocholine (PCho), creatine (Cr), phosphocreatine (PCr), γ-aminobutyric acid (GABA), glucose (Glc), glutamine (Gln), glutamate (Glu), glutathione (GSH), myo-inositol (mIns), lactate (Lac), N-acetylaspartate (NAA), N-acetylaspartylglutamate (NAAG), phosphoethanolamine (PE), and taurine (Tau). The role of these metabolites will be described in section 1.8.5. Large RF pulse bandwidths (≥ 10 kHz) were used and the RF carrier frequency was placed in the middle of the MRS spectrum at 3 ppm to limit the CSD. B_1 inhomogeneities (resulting in various flip angles across the sample) were limited by using adiabatic inversion and refocusing (see the details of the sequence in chapters 4 and 5). Higher magnetic field strengths result in higher SNR and increased chemical shift dispersion but also in larger linewidths due to shorter relaxation times. Good shimming (homogenization of the B_0 field) is therefore crucial at UHF [23]. Here, first and second order shimming was performed with the Bruker MAPSHIM method (shim values based on a measured map of

the B_0 field in the sample) followed by local iterative first order shimming in the MRS voxel, leading to a water linewidth of 17-19 Hz in a 175 μL voxel at the centre of the rat brain (used in chapter 5) and of 22-27 Hz in a 93 μL voxel in the cerebellum (used in chapter 4), at 14.1T. Outer volume suppression (OVS) and water suppression (WS) are applied prior to the MRS sequence in each repetition time (TR) to suppress signal from outside the voxel and saturate the water signal. Phase cycling (rotation of the inital phase of RF pulses and of the receiver in the rotating frame) and optimized (here empirically) spoilers/crushers schemes are used to spoil unwanted coherences.
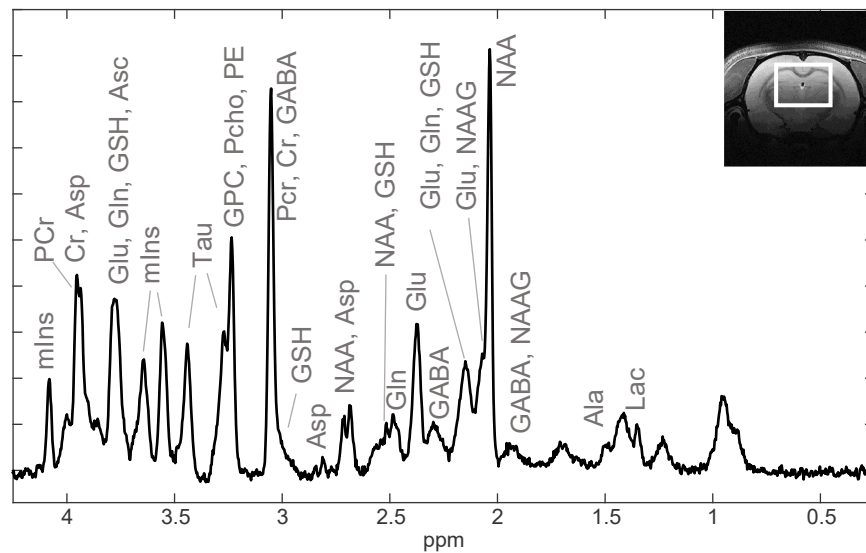
Figure 1.13: Representative ^{1}H MRS spectrum acquired at 14.1T with the diffusion-weighted SPECIAL sequence at low b-value (TE = 18 ms, b-value = 0.05 ms/μm^2) in the rat brain. Voxel positioned in the middle of brain, size: $7 \times 5 \times 5$ mm^3. Processing (see section 1.8.6): spectral registration between shots, outlier removal, overall 0-order phasing and 1 Hz line broadening.

1.8.5 Role and compartmentation of MR-observable metabolites

Table 1.1 summarizes the role, the concentration and the compartmentation of MR-observable metabolites (when this information is known), mainly based on the references from Caroline D. Rae [24] and Robin A. de Graaf [5].

Met.	Role	Localization	Concentration range (mmol/L)

Asc	• antioxidant (Asc-GSH cycle) • acts as metabolic switch between Glc and Lac substrate for neuronal activity [25]	• travels between neurons and astrocytes through glucose transporters • located within mitochondria, in neurons, glial cells, and extra-cellular space	0.5-3 (higher in rat than human brain)
tCho	• marker of membrane turnover (phospholipids synthesis and degradation) • precursor of ACh, neurotransmitter of cholinergic neurons • ↑ Cho in tumors, AD and MS, ↓ Cho in liver disease and stroke • not synthetized de novo, uptaken from the blood	• located within mitochondria, mostly in neurons, endothelial cells, and extra-cellular space [26]	0.2-2.5 (lower in rat than human brain)
tCr	• involved in energy metabolism and ATP synthesis and hydrolysis	• located within mitochondria, in neurons, glial cells, oligodendrocytes • higher concentration in GM than WM	7-15
GABA	• inhibitory neurotransmitter • synthetized from Glu • glutamine in the astrocytes in the major source for GABA synthesis • can synthesize SSA that will re-enter the TCA-cycle in the astrocytes (GABA shunt) • concentration modulated by external factors (hormones, drugs...)	• located in cell bodies and a small fraction in the synaptic cleft	0.5-2.5

Gln	• product of the detoxification of ammonia • precursor of glutamate in neurons • synthesis in the astrocytes by GS	• generally as an astrocyte-specific marker, although there is a fast dynamic exchange between Glu and Gln (faster than the diffusion time scale)	2-6
Glu	• major excitatory neurotransmitter • precursor of GABA	• different concentrations in GM and WM • present in all cell types • higher concentration in glutamatergic neurons, smaller in glia and Purkinje cells (GABAergic neurons in the cerebellum)	6-12.5
GSH	• antioxidant • synthesized from Glu and Cys • depletion results in mitochondrial dysfunction • ↓ GSH with stress and age	• mostly synthesized in the astrocytes • higher concentration in GM than WM • higher concentration in females than in males	0.5-3.5
Lac	• end product of glycolysis • main probe of the Warburg effect[Com. 2] • alternative energy supply to Glc (at max. 25%) • fast dynamic turnover	• located in neurons, astrocytes, extracellular space	0.2-3
mIns	• osmoregulator	• astrocytes have a higher ability to store mIns than neurons but cell-specificity is being challenged[Com. 1] • higher concentration in GM than WM	4-10

| tNAA | • marker of neuronal density and function
• NAA precursor of NAAG
• NAAG involved in excitatory neurotransmission
• ↓ NAA in cancer, stroke and MS | • concentration changes with brain development < 1 mM at birth to > 5 mM in adults
• 8-11 mM in GM and 6-9 mM in WM
• concentration changes with the brain region and the type of neurons (higher in elongated neurons like Purkinje cells in the cerebellum)
• small fraction in oligodendrocytes
• NAAG in microglia as well | 5-19.5 (lower in rat than human brain) |
| Tau | • osmoregulator | • present in all cell types at different levels
• ↓ Tau with age | 2-6 (higher in rat than human brain) |

Table 1.1: ^{1}H MRS metabolites role, localization and concentration in the brain, based on *A Guide to the Metabolic Pathways and Function of Metabolites Observed in Human Brain 1H Magnetic Resonance Spectra* by Caroline D. Rae [24] and *In vivo NMR Spectroscopy: Principles and Techniques* by Robin A. de Graaf [5]. Only the references not cited in these two sources are explicitly added in the table. ACh: acetylcholine, AD: Alzheimer's disease, Cys: cysteine, GM: grey matter, MS: multiple sclerosis, SSA: succinic semialdehyde, WM: white matter. Comment 1: older evidence showed it was a glial marker but it was challenged by more recent observations of mIns being also present in different types of neurons. Comment 2: shift from aerobic to anaerobic glycolysis in cancer.

1.8.6 Processing and quantification

Adequate processing of the data can enhance the metabolite quantification performance and accuracy [27]. Some of these steps are described below, which can be applied using FID-A [28].

ECC

The complex FID signal S_{ini} is corrected for eddy currents S_{ECC} using the non-water suppressed acquisition, whose phase evolution with time $\phi_{\mathrm{water}}(t)$ is only caused by eddy currents

distortions [29]:

$$S_{ECC}(t) = S_{\text{ini}}(t) \exp(-i\phi_{\text{water}}(t)) \tag{1.81}$$

Group delay and digital filter

On Bruker scanners, a digital filter is applied, delaying the first point with meaningful information. The first points of the FID can be removed (according to the value of the group delay) and zeros can be added at the end of the FID to maintain the total number of points constant.

Phase correction

Zero and first order phase correction can be applied on the spectrum:

$$S_{\text{ph0}}(t) = S_{\text{ini}}(t) \exp(i\phi_0) \tag{1.82}$$

The first order phase is frequency-dependent and is applied on the frequency domain signal. It is often created by an imbalanced delay in the sequence.

$$\tilde{S}_{\text{ph1}}(\omega) = \tilde{S}_{\text{ini}}(\omega) \exp(i\phi_1) = \tilde{S}_{\text{ini}}(\omega) \exp(i k \Omega_r) \tag{1.83}$$

where $\phi_1 = k\Omega_r$, with k the slope of the first-order phase. $\phi_1 = 0$ at the centre of the spectrum where $\Omega_r = 0$(receiver frequency).

Noise and zero-filling

The noise acquired in the FID resulting from the animal and from the electronics is assumed to be Gaussian distributed on the real and imaginary parts and on each coil. The frequency-domain noise σ_f (measured in a signal-free region of the real part of the spectrum) is related to the time-domain noise σ_t (measured in the queue of the FID) by [30]:

$$\sigma_f = \sqrt{N}\sigma_t \tag{1.84}$$

where N is the number of points in the FID. If the acquisition time is much longer than the time it takes for the FID to decay in the noise (dictated by T_2^* and J-evolution), it can be useful to replace the last part of the FID (region of noise only) with zeros. Doing so, the SNR in frequency domain will be increased (each noise point in the FID is spread around all frequency points by the FT operation), while maintaining the spectral resolution $\Delta f = \frac{1}{t_{\text{acq}}}$ (property of the discrete FT, convolution with a Dirac comb).

In addition, zero-filling, which consists of adding zeros after the end of the FID, is often applied

before Fourier Transform. Zero-filling can be done up to twice the initial number of points to increase the spectral resolution, then it becomes cosmetic [31]. In addition, the twice zero-filled FID satisfies the Kramers-Kronig relations [31] between the real and imaginary parts, which means that the Hilbert transform of the real part gives *exactly* the imaginary part. Because the real and imaginary parts have become interdependent, the imaginary part can be discarded after zero-filling. In practise, complex fitting or real fitting of the 0-filled FID both give an improvement of $\sqrt{2}$ over real fitting of the non zero-filled FID.

Apodization

Apodization is done by multiplying the FID by a smoothing function to reduce noise at the cost of line-broadening in the frequency domain. The most common functions are the Lorentzian and the Gaussian functions (or a combination):

$$S_{\text{apo}}(t) = S_{\text{ini}}(t) \exp(-c_{\text{Lor}} t) \exp(-c_{\text{Gau}} t^2) \tag{1.85}$$

where c_{Lor} and c_{Gau} are the apodization weighting coefficients.

Frequency shift

A shift in the frequency domain is applied in the time domain as:

$$S_{\text{shift}}(t) = S_{\text{ini}}(t) \exp(ikt) \tag{1.86}$$

where k is the frequency shift.

Corrections in-between spectra

The effect of phase and frequency drifts between shots, caused by gradient and B_0 instabilities, motion or flow, should be corrected prior to summation. They can be corrected simultaneously using spectral registration [32]. **Figure 1.14** shows the effect of summation before frequency drift correction, resulting in a decreased amplitude and artificial broadening of the summed spectrum.

Outlier spectra heavily corrupted by motion should be removed or rescaled. These steps are essential for diffusion-weighted MRS, where the high-b values spectra are often more corrupted than the low-b values ones.
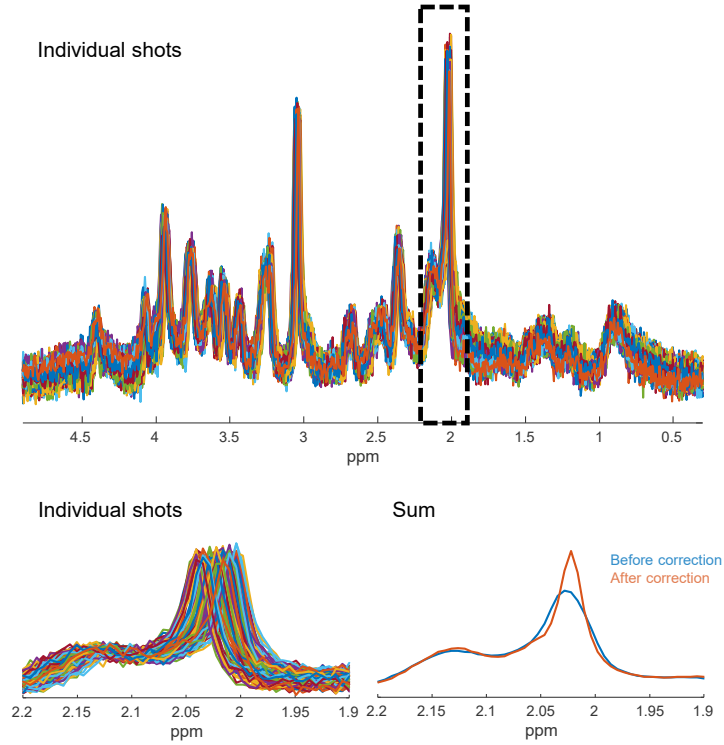
Figure 1.14: Effect of frequency drift on individual shots and the resulting decreased amplitude and artificial broadening of the summed spectra.

Metabolite fitting and quantification

Once the spectra are processed and summed, the resulting shot is fitted by linear combination model fitting and quantified to recover metabolite concentrations as shown in **Figure 1.15**. In this thesis, we used only LCModel to fit MRS data. The general model is given by:

$$\xi(t) = \sum_{n=1}^{N} A_n \exp(-i\omega_n t) \exp(-c_{\mathrm{Lor,n}} t - c_{\mathrm{Gau,n}}{}^2 t^2) \exp(i\phi_n) = \sum_{n=1}^{N} A_n \xi_n(t) \tag{1.87}$$

where A_n, ω_n, $c_{\mathrm{Lor,n}}$, $c_{\mathrm{Gau,n}}$, ϕ_n, are the amplitudes, frequency, Lorentzian weighting coefficient, Gaussian weighting coefficient and phase of metabolite n out of N in the basis set, and ξ_n the time-domain signal of the element n of the basis set. The cost function given by the squared error between the data and the model over all time points, $\chi^2 = \sum (y - \xi)^2$, will be minimized to find the coefficients A_n that are related to the concentrations of each metabolite. The concentrations are expressed either relative to water or in terms of ratio to another metabolite (often tCr). In the first case, the non-water suppressed reference scan is used, assuming a value for the water concentration in the rat brain [27], mostly made of grey matter (GM) [8] (LCModel parameter WCONC) and comparing the water and metabolites
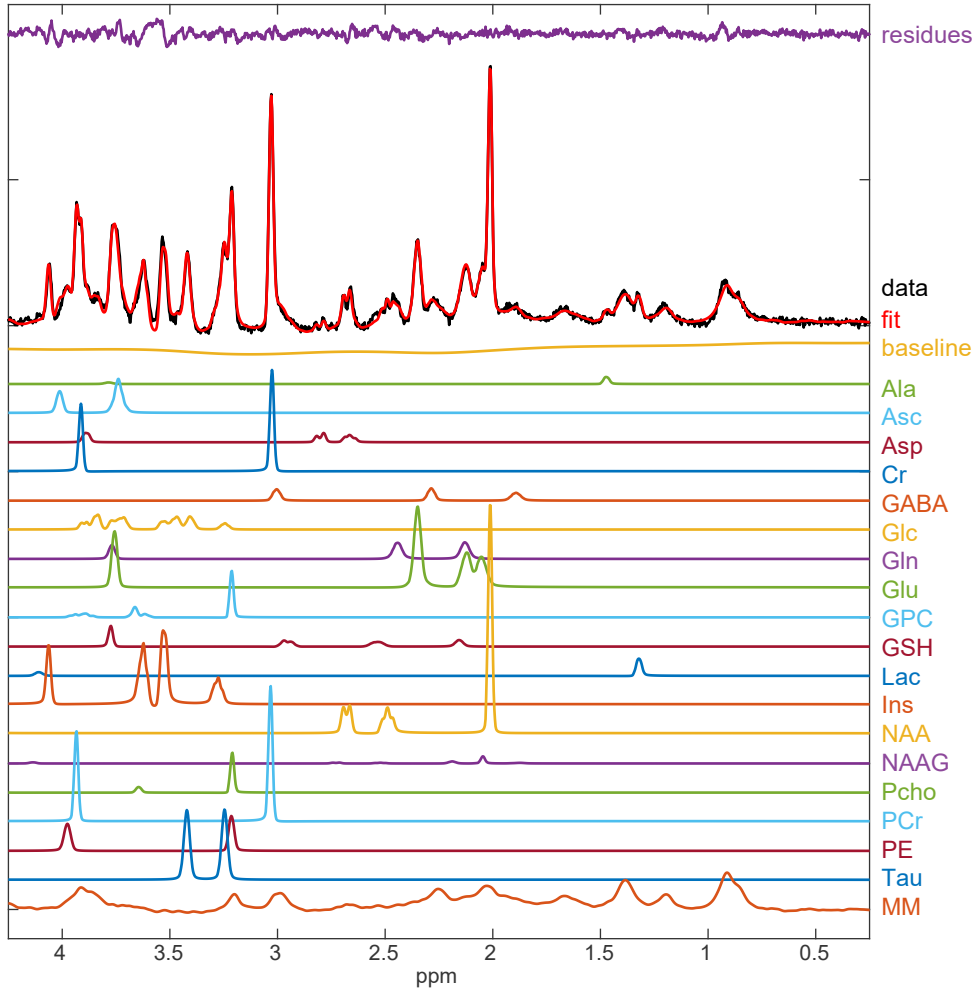
Figure 1.15: LCModel fit results for the spectrum of **Figure 1.13**.

signal areas normalized by their numbers of ^{1}H, their receiver gains and their relaxations ponderations (ATTH2O)). In that case the concentrations are expressed in mmol/kg wet weight, which should be multiplied by the tissue density to be expression in mM. Cramer-Rao lower bounds (CRLB) are used to estimate the lower bound of the standard deviation SD of the estimated concentrations c_l, assuming the model is correct [33]:

$$SD_{c_l} \geq CRLB_{c_l} = \sqrt{\left(F^{-1}\right)_{ll}} \tag{1.88}$$

where F is the Fisher matrix given by:

$$F = \Re(D^H D) \tag{1.89}$$

with H the hermitian conjugation and the elements of the matrix D given by:

$$D_{mn} = \frac{1}{\sigma_m} \frac{\partial \xi_m}{\partial c_n} \tag{1.90}$$

Moreover, it is recommanded that the mobile macromolecules (MM) spectrum is acquired separately with a dedicated sequence and processing (detail in the next chapters), for each animal group and brain region and included in the basis set [34, 35]. In LCModel, it is possible to give freedom to phase the input spectrum (zero order: DEGZER, SDDEGZ, first-order: DEGPPM, SDDEGP), to fix the ppm fitting range (PPMST, PPMEND), to cut the input spectrum (NUNFIL) and to adjust the prior knowledge on concentrations ratios (NRATIO). Some freedom should also given in the estimated baseline (DKNTMN) that accounts for eddy currents and distortions due to the water residual [35, 36]. Whatever remains after fitting the input data is attributed to the residuals.

1.9 From a spectrum to an image

In the same way that the frequency domain was the conjugate space of the time domain after Fourier transform, in MRI the 2D k-space is the conjugate space of the image-space after 2D FT.

$$\boldsymbol{k} = \frac{\gamma \boldsymbol{G} t}{2\pi} \tag{1.91}$$

To acquire an image in its simplest form (1D slice-selection, and 2D cartesian sampling of the k-space), a slice is selected first with the same slice-selection principle as in MRS. Then a phase-encoding gradient (for example G_y) is switched on before the acquisition for a time τ, leading to a phase $\phi_y = \gamma G_y y \tau$ that will encode a given y-position. Finally, a frequency-encoding gradient (for example G_x) is turned on during the acquisition, leading to a different frequency $\omega_x = \gamma G_x x t$ sampled at each position x. The k-space trajectory is represented in **Figure 1.16**. After sampling the entire k-space, the 2D FT provides the spin density $\rho(x, y)$ or a contrast that depends on the sequence parameters (TE, TR) and on the tissue constants (T_1, T_2, T_2^*).

$$\rho(x, y) = \int_{-\infty}^{+\infty} \int_{-\infty}^{+\infty} S(k_x, k_y) \exp(-2i\pi(k_x x + k_y y)) dk_x dk_y \tag{1.92}$$
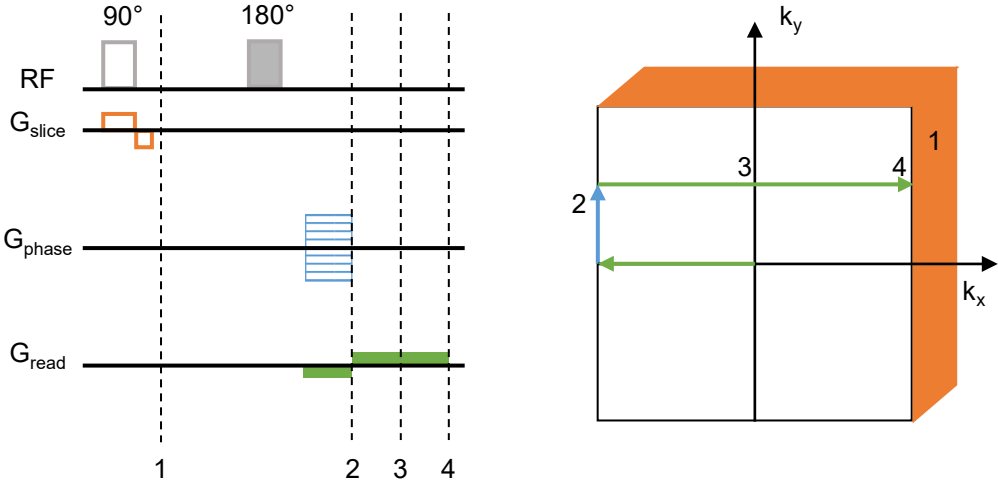
Figure 1.16: k-space trajectory in MRI. Orange: slice selection gradient. Blue: phase encoding gradient. Green: frequency encoding gradient. The acquisition start at point 2. The phase encoding and frequency encoding steps are repeated until the entire k-space in mapped (for cartesian sampling). In this sequence, the rewinding gradient G_{read} (of half the area of the gradient during the acquisition) before the beginning of the acquisition is used to position the time of the spin echo at the center of the k-space.

2 Diffusion weighting of the NMR signal

This chapter introduces the concept of diffusion measurements with MR and was written with the help of the following book: *Spin Dynamics* edited by Derek K. Jones [37]. This chapter and the following ones concerning diffusion are written with the following questions in mind, as stated by Pr. Ileana Jelescu in many of her educational talks about diffusion:

- which microstructure features are truly relevant for the tissue at stake?

- can I sensitize the diffusion MR signal to those features?

- can I reliably estimate all the model parameters from the data?

- how do the microstructure features inform about the disease investigated?

2.1 Concept

Diffusion experiments in magnetic resonance spectroscopy (MRS) and imaging (MRI) rely on the frequency modulation induced by a variation of magnetic field on the magnetization of nuclei of diffusing molecules. This variation can arise from natural inhomogeneities in the static magnetic field B_0, generally undesired, or from additional and controlled time-dependent magnetic field gradients (MFG), generally desired. If a diffusion gradient is applied in one direction, the accumulated phase of the net magnetization of any nucleus becomes position-dependent in that direction. If a gradient of opposite polarity is applied in the same direction, the net magnetization of an ensemble of static molecules will be refocused, and molecules having an identical translational motion (flow) in that direction will keep phase coherence. Molecules randomly diffusing in that direction will lose phase coherence and the net magnetization of the ensemble not entirely refocused, causing a loss of signal. When applied in vivo, the properties of this signal attenuation as a function of the sequence parameters

(diffusion time, gradient strength) allows one to extract information about molecular motions, which are connected to the tissue microstructure.

2.2 Characteristic diffusion length

A freely diffusing molecule in a liquid or a gas follows a Brownian motion and is described by its diffusion coefficient, D_0. In liquids, for a spherical molecule, D_0 is proportional to the temperature (T) and inversely proportional to the radius of the diffusing molecule (r) and to the viscosity of the medium (η). It is given by the Einstein-Stokes relation:

$$D_0 = \frac{k_B T}{6\pi\eta r} \tag{2.1}$$

The distance travelled during a diffusion process is sublinear with time. The root mean squared displacement associated with a random walk in N-dimensions, i.e. the characteristic diffusion length, is:

$$L(t) = \sqrt{\langle X^2 \rangle} = \sqrt{2ND_0 t} \tag{2.2}$$
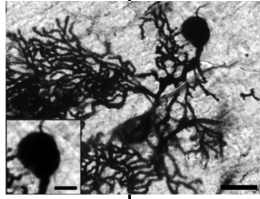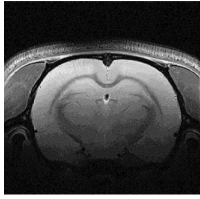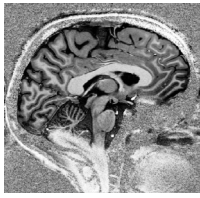
2.3 Sub-MRI resolution

The typical distance travelled by water molecules and probed by standard diffusion MRI acquisitions in humans and rodents is much smaller than the voxel resolution of MRI (**Figure 2.1**). As such, diffusion MRI allows one to probe phenomena below the MRI resolution limit. By serendipity, it can be noticed that the diffusion distance probed by standard diffusion MRI acquisitions is of the same order of magnitude as characteristic lengths and sizes of cells in the brain. This renders diffusion MRI powerful to probe processes and alterations at the cellular level in vivo.

2.4 Water versus metabolite diffusion

On the one hand, diffusion MR acquisition can be tuned to probe the water, generally in terms of images (**diffusion-weighted MRI (dMRI)**), made possible by the high sensitivity of the water measurement, and provides information on the tissue geometry. On the other hand, it can be tuned to probe the metabolites. **Diffusion-weighted MRS (dMRS)**, generally measured as a single-(big) voxel information, benefits from the cell-specificity of certain metabolites (e.g. NAA and Glu as neuronal metabolites and Gln, Ins as astrocytic metabolites, although this simplistic separation should be considered with care [24]) and allows to extract additional information on metabolites compartmentalization and tissue structure at the cellular or sub-cellular scale. However, it suffers from the low-sensitivity of metabolites with respect to water

	Typical cell sizes		Typical 1D MRI resolution	Diffusion MRI resolution (characteristic diffusion length)
	Soma radius	Length of processes		
Rat	1-15 µm	10-100 µm	80-100 µm	**9.5 µm** (with a realistic Δ = 15 ms)
Human	10-100 µm	100-1000 µm	400-600 µm	**17 µm** (with a realistic Δ = 50 ms)

Figure 2.1: Diffusion MRI resolution, as compared to typical MRI resolution and brain cell sizes in the rat and human brain. Δ is the diffusion time, chosen for this example as a typical value used for diffusion-weighted MR experiments on animal (Δ = 15 ms) and human scanners (Δ = 50 ms). The 3D characteristic diffusion length giving the length scale to which the diffusion signal is sensitive to (called here diffusion MRI resolution) is calculated as $L(t) = \sqrt{6 D_0 t}$ using $D_{0,\text{water}} = 1\ \mu m^2/\text{ms}$.

due to their low concentration (1-10 mM for metabolites versus 55 M for water), and are penalized by additional signal loss by J-evolution. Combining the sensivity of dMRI with the specificity of dMRS offers a versatile tool to study microstructure. Moreover, given that water diffuses faster than metabolites ($D_{0,\text{water}} \approx 1\ \mu m^2/\text{ms}$, $D_{0,\text{met}} \approx 0.1\ \mu m^2/\text{ms}$), dMRI and dMRS sequences parameters can be tailored to probe either the same or different ranges of characteristic length scales.

The synergetic application of dMRI and dMRS in the same study has rarely been performed so far. The water signal reported in dMRS studies is usually the one acquired in the entire spectroscopic voxel, which fails at informing on local variations.

One of the aims of this thesis was to explore the promising combination of dMRS and dMRI - where the water signal is acquired as an image. We will show that this combination provides unprecedented cell- and matter-specific microstructural information in rat model of hepatic encephalopathy.

2.5 History

2.5.1 First observation of the NMR signal influenced by diffusion due to B_0 inhomogeneities: *Hahn, Spin echoes, 1950*

Hahn's paper in 1950 [38] was the first to describe the effect of free diffusion on the echo amplitude, creating a loss of phase coherence and leading, together with T_2 relaxation, to a smaller echo amplitude. A serie of 90° - 180° spin echoes with different echo times was initially introduced by Hahn to measure T_2 relaxation. Hahn showed that echo amplitudes of non-viscous substrates like water were more affected by diffusion than T_2 relaxation due to the naturally occuring gradient over the sample arising from B_0 inhomogeneities. On more modern, well-shimmed magnets, this effect is not observed anymore.

2.5.2 First NMR sequence for measuring diffusion coefficients with time-dependent magnetic field gradients: *Stejskal et Tanner, Spin Diffusion Measurements: Spin Echoes in the Presence of a Time-Dependent Field Gradient, 1965*

In 1965, Stejskal et Tanner [39] proposed a new sequence based on Hahn's previous description of spin diffusion measurements, using time-dependent magnetic field gradients. This method has three main advantages compared to exploiting steady gradients. First, a smaller B_1 field can be used if the gradients are not applied during RF pulses. Second, the FID can be longer (i.e. wider echo, and consequently higher resolution) if the gradients are small during the echo. Third, a well defined and short diffusion time is of importance to measure hindered or restricted diffusion. From these observations, they proposed a SE sequence with time-dependent diffusion gradients (as shown in **Figure 2.3**). Their experiment paved the way for all the diffusion experiments that are conducted today.

2.5.3 First in vivo diffusion MRI measurement: *Le Bihan et al., MR imaging of intravoxel incoherent motions: application to diffusion and perfusion in neurologic disorders, 1986*

Twenty years later, Le Bihan et al. [40] performed the first in vivo diffusion MRI acquisition in the human brain. They also introduced the concepts of apparent diffusion coefficient (ADC) and b-value.

2.5.4 First in vivo diffusion MRS measurement: *Moonen et al., In Vivo NMR Diffusion Spectroscopy: 31P Application to Phosphorus Metabolites in Muscle, 1990*

In 1990, Moonen et al. [41] were the first to perform a diffusion MRS experiment in vivo. They showed the effect of restricted diffusion for PCr in a rat leg muscle, compared to water in vitro diffusion. They observed a plateau in the root mean square displacement curve as a function of square root of diffusion time, and extrapolated the size of fibers along which PCr was diffusing (**Figure 2.2**).
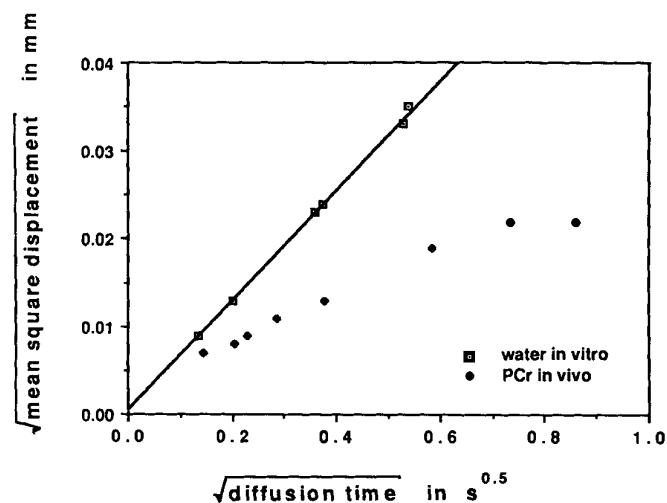
Figure 2.2: Reproduced from Moonen et al., [41]. Comparison of the root mean square displacement as a function of the square root of the diffusion time, for water measured in vitro (squared) and PCr measured in vivo in a rat leg muscle (circles), the latter exhibiting restriction effects.

With this paper, new challenges emerged for in vivo experiments: the diffusion gradient pairs should be well balanced and Eddy Current compensated to avoid phase or lineshape distortions, and motion should be minimized and accounted for. The first study of ^{1}H diffusion MRS in the human brain (looking at Cho, tCr, NAA) was by Posse et al. [42] in 1993.

2.5.5 First diffusion tensor measurement: *Basser et al., MR diffusion tensor spectroscopy and imaging, 1994*

In 1994, Basser et al. [43] published the first paper on diffusion tensor imaging (DTI), which is the generalisation of 1D diffusion experiments to three dimensions, thus accounting for diffusion in anisotropic media. The same authors also provided the tensor generalisation of the 1D diffusion equations [44].

2.6 Potential for studying microstructure in the healthy and diseased brain

In a clinical context, dMRI has emerged as a non-invasive imaging technique of unprecedented value and is used routinely for disease early detection and clinical follow-up.

Historically, **dMRI** was shown to be superior to T_1 and T_2-weighted MRI for the early detection and management of patients with stroke or tumors. Decreased ADC is observed quickly after the ischemia, before any change can be observed on T_2-weighted MRI [45] and is more accurate marker of re-vascularization (characterized by an increased ADC) after recovery [46]. In brain tumors, dMRI can distinguish types of masses that have the same appearance on T_1 and T_2-weighted MRI (bacterial abscesses have lower ADCs than necrotic tumors [47], CNS Lymphomas have lower ADCs than gliomas [48]) and differentiate radiation necrosis from tumor recurrence [49]. In prostate cancer, dMRI can differentiate cancerous versus healthy peripheral zones, the water ADC being higher in the latter [50]. dMRI can also provide key features of the brain under development, where more conventional MRI contrasts are poorer indicators. Decreased water mean diffusivity (MD) with the weeks of gestation is observed in the healthy brain, attributed to white matter complexification creating more crowding, and to a decrease in water content [51]. Fractional anisotropy (FA, which represents the degree of anisotropy, section 2.9.1) also increases with age due to the myelination process. An alteration of these mechanisms have been observed in the cases of acute strokes, meningitis, or traumatic brain injury in young children. The use of dMRI is now widespread for numerous other diseases and applications, including neuroinflammation or non-focal diseases like psychiatric disorders and neurodegenerative diseases.

dMRS provides, in addition, a valuable cell-specific information. Following the pioneering works of Moonen et al. [41] and Posse et al. [42], Wick et al. [52] measured the changes in diffusion properties upon ischemia in the rat brain with dMRS. They showed that, during ischemia, the increase in glial mIns ADC ($\approx +50\%$) was stronger than the one of neuronal NAA ($\approx +10\%$), tentatively probing cell-specific swelling. Pfeuffer et al. [53] later assessed Glc and Lac distribution between intra- and extracellular spaces in the rat brain in comparison to purely intracellular metabolites. Since then, many groups have shown that dMRS can probe cellular microstructure in the healthy brain [54, 55, 56, 57], and reflect properties of neurons [58] (with NAA), astrocytes [59] (with mIns) and microglia [60] (with mIns and tCho) and their alterations in disease populations with a unique specificity. In multiple sclerosis (MS) patients, decreased tNAA and tCr ADCs were observed in the thalamus, attributed to axonal damage and impaired energy supply [61]. In first-episode psychosis patients, a decreased tCho ADC was observed first, followed by an increased tNAA ADC in a two-year follow up, whereas no changes in water diffusion were measured with dMRI [62]. In stoke patients, the tCho ADC was

increased one month after ischemia before going back to control values after three months, while the tCr ADC stayed higher after three months, attributed to persistent astrogliosis [63]. In a mouse model of reactive astrocytes, Ligneul et al. [59] showed a difference in mIns diffusion properties, metabolite which is partially specific to astrocytes, whereas no difference in water diffusion was observed, confirming the potential and specificity of dMRS compared to dMRI. In the healthy brain, different Glu ADCs in white and grey matter, attributed to differential cellular location of Glu in each matter, have been reported by Valette et al. [64]. The diffusion profile at long diffusion time was the same for all metabolites both in monkeys [65] and humans [57], suggesting diffusion in elongated structures. More recently, the time-dependant kurtosis of metabolites have been reported in the mouse [66, 67] and human brain [68], offering new tools for exploring microstructure and exchange.

In this context, one of the aims of this thesis was to explore the potential of joint dMRI and dMRS acquisitions in the bile-duct ligated rat model of hepatic encephalopathy (HE) to elucidate the unanswered questions about brain microstructural alterations in HE.

2.7   Theory

2.7.1   Fick's law

The conditional propability (propagator) for a spin starting in position $\boldsymbol{r}$ and reaching position $\boldsymbol{r}'$ after travelling a time Δ, $P_s(\boldsymbol{r}'|\boldsymbol{r},\Delta)$, obeys Fick's law:

$$\frac{\partial P_s}{\partial t} = D\nabla^2 P_s \tag{2.3}$$

In the case of free diffusion, the initial condition $P_s(\boldsymbol{r}'|\boldsymbol{r},0) = \delta(\boldsymbol{r}'-\boldsymbol{r})$ gives the solution:

$$P_s(\boldsymbol{r}'|\boldsymbol{r},\Delta) = (4\pi D\Delta)^{-3/2}\exp\left(-\frac{(\boldsymbol{r}'-\boldsymbol{r})^2}{4D\Delta}\right) \tag{2.4}$$

Only the relative displacement $\boldsymbol{R} = \boldsymbol{r}'-\boldsymbol{r}$ appears in the expression of the propagator and it is Gaussian.

2.7.2   Echo attenuation for free diffusion

For free diffusion, the echo attenuation during a spin echo with MFG is given by the Bloch-Torrey equation. Solving this equation for M_{xy} is equivalent to solving the Fick's law on the propagator.

We suppose an experiment where molecules with a single resonance ω_0 diffuse isotropically.

A gradient G_x is applied along x and the echo attenuation is measured after a spin echo (SE) sequence with diffusion gradients (**Figure 2.3**).
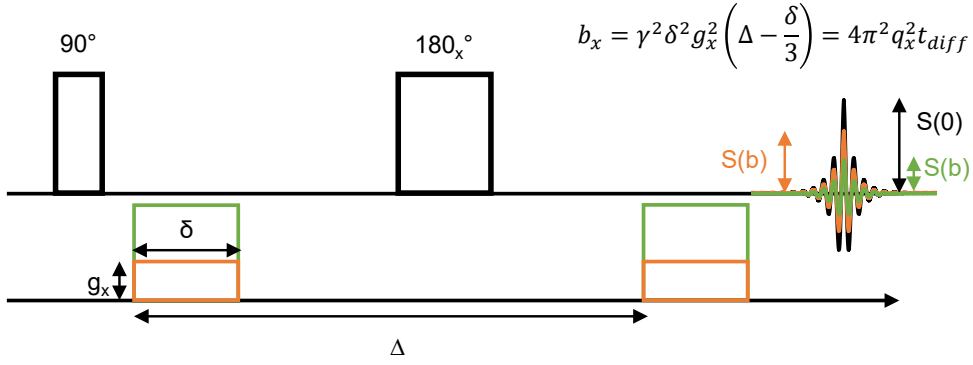
Figure 2.3: Spin echo sequence with time-dependent diffusion gradients, with weak (orange) and strong (green) diffusion gradients, arbitrarily applied on x here. The echo amplitude decreased with the increasing gradient strength. The expression of the b-value is given at the top, also expressed as a function of q. γ is the gyromagnetic ratio in rad/s/T, δ the duration of the diffusion gradient in sec, g_x the strength of the diffusion gradient in T/m, Δ the separation between the two diffusion gradients in sec, $q = \frac{\gamma \delta g_x}{2\pi}$ and t_{diff} is the effective diffusion time, which is for free diffusion accounting for diffusion during the gradient pulse: $\Delta - \frac{\delta}{3}$.

The complex magnetization in the xy plane, M_{xy}, can be expressed as follows, assuming that ω_0 and T_2 are position-independent:

$$M_{xy} = M_x + i M_y = \Psi(x, t) \exp\left(-i\omega_0 t - \frac{t}{T_2}\right) \tag{2.5}$$

where Ψ, the amplitude of the echo, evolves with an additional frequency term, $\gamma G_x x$, due to the gradient G_x. The effective resonant frequency is now: $|\omega| = \gamma B = \gamma(B_0 + G_x x) = \omega_0 + \gamma G_x x$. Ψ satisfies the Bloch equations without the relaxation term (already included in the second part of the expression of M_{xy}) but with an additional diffusion term $D\nabla^2\Psi$ (Bloch-Torrey equation, neglecting flow):

$$\frac{\partial \Psi}{\partial t} = -i\gamma z G_z \Psi + D\nabla^2\Psi \tag{2.6}$$

Assuming that the diffusion contribution in the expression of Ψ can be factorized $\Psi = A(t)B(z, t)$, the expression of B is found when nulling the diffusion term in equation (2.6). Equation (2.6) with diffusion can then be applied to Ψ to find the expression of A:

$$\ln\left(\frac{A(TE)}{A(0)}\right) = -D\gamma^2 \int_0^{TE} \left(\int_0^t G_z(t')dt'\right)^2 dt \tag{2.7}$$

and with the explicit 180° phase refocusing:

$$\ln\left(\frac{A(TE)}{A(0)}\right) = -D\gamma^2\left[\int_0^{TE}\left(\int_0^t G_z(t')dt'\right)^2 dt - 4f\int_{TE/2}^{TE}\left(\int_0^t G_z(t')dt'\right)dt + 2f^2 TE\right] \quad (2.8)$$

where TE is the echo time, $f = \int_0^{TE} G_z(t')dt'$, $A(TE)$ is the amplitude of the transverse magnetization at the echo time, $A(0)$ is the amplitude right after the 90° pulse. From this general equation, it becomes possible to calculate the echo attenuation depending on any diffusion gradient scheme.

For the sequence in **Figure 2.3**, with the hypotheses of no additional attenuation due B_0 inhomogeneities and infinitely short rise time of the diffusion gradients, the explicit solution of equation 2.8 is:

$$\ln\left(\frac{S(b)}{S(0)}\right) = -D \times \gamma^2\delta^2 g^2\left(\Delta - \frac{\delta}{3}\right) = -D \times b \quad (2.9)$$

where $S(b) = A(TE)$ is the amplitude of the signal at the echo time, proportional to the amplitude of the complex magnetization in the xy plane M_{xy}, for a diffusion-weighting measured by $b = \gamma^2\delta^2 g^2(\Delta - \frac{\delta}{3}) = 4\pi^2 q^2 t$, the so-called b-value. Here q is the phase warp and t is the effective diffusion time allowed for the molecules to mix while carrying that phase tag (more details given in section 2.7.5). D is the diffusion coefficient, δ the duration of the diffusion gradient, Δ the time interval between the two diffusion gradients and $S(0)$ is the signal amplitude when no diffusion gradient is applied. The term $\frac{\delta}{3}$ in the b-value is the correction term that accounts for diffusion during the finite gradient pulse duration.

When combining diffusion with localized spectroscopy, additional gradients for slice selection and crushing schemes, G_{imag}, are present in the sequence. These gradients, if placed within the echo time, generate additional dephasing and also participate in the echo attenuation. Their introduction adds two terms to the b-value expression in equation 2.9, and notably one that involves the product of diffusion and imaging gradients, $f(G_{\text{diff}}, G_{\text{imag}})$:

$$b = b_{\text{diff}} + b_{\text{imag}} + f(G_{\text{diff}}, G_{\text{imag}}) = \gamma^2\delta^2 g^2\left(\Delta - \frac{\delta}{3}\right) + b_{\text{imag}} + f(G_{\text{diff}}, G_{\text{imag}}) \quad (2.10)$$

If the imaging gradients are identical in all diffusion experiments, the term b_{imag} will create a constant offset in both echo amplitudes $S(b)$ (for all b) and $S(0)$, while diffusion attenuation will vary with b. This offset will be cancelled when taking $\ln\left(\frac{S(b)}{S(0)}\right)$ and will not bias the estimation of D. However, the last term in equation 2.10, $f(G_{\text{diff}}, G_{\text{imag}})$, known as a cross term, creates an offset which will depend on the diffusion gradients amplitudes. This term should either be removed (and it is very often possible by astutely designing the sequence, see below) or included in the expression of the b-value using equation 2.8 to accurately estimate D.

Taking into account this difficulty, one of the aims of this thesis was to propose a new diffusion-weighted MRS sequence where cross terms would be absent, maintaining an unequivocal expression of the b-value.

For restricted diffusion, it is not always possible to find a closed-form solution of the Bloch Torrey equation with any gradient waveform and thus approximations need to be made (see section 2.7.4).

2.7.3 Free, hindered, restricted, isotropic, anisotropic diffusion

Free, hindered, restricted, isotropic and anisotropic diffusion should be clearly distinguished as they represent different properties of the underlying geometries and lead to different formalisms and modelling of the signal attenuation.

The concept of free, hindered or restricted diffusion expresses the absence (**free**) or presence of obstacles (**hindered**) or barriers (**restricted**) in the diffusion path of molecules.

The concept of isotropic or anisotropic diffusion expresses the dependence of the diffusion properties with the direction in space. An **isotropic** diffusion process has the same properties in all directions, whereas an **anisotropic** diffusion process has different diffusion properties depending on the direction. This directional dependence could be at the **microscopic** level, i.e. at a scale much smaller than the one of the voxel, and may (**macroscopic anisotropy** - e.g. fibre tracks in WM, oriented at the voxel level) or may not survive voxel averaging (**macroscopic isotropy** - e.g. randomly oriented sticks model in orange in **Figure 2.4** [69]).

Isotropic free diffusion represents the motion of a molecule freely diffusing in all directions with a coefficient D_0. In practise, in vivo, we measure an information at the voxel level (not at the molecule level), and that cannot be characterized by a single diffusion constant D_0. The ADC is a phenomenological scalar coefficient that has been introduced to account for the within-voxel spatially-heterogeneous contributions to the total signal (microscopic anisotropy, distribution of sizes etc...). In the case where the diffusion gradient is applied only in one direction, the ADC describes the projection on the gradient axis of the molecular displacements reflecting the different micro-environments within the voxel. It is the coefficient we would measure in a given gradient direction from equation 2.9, i.e. assuming a mono-exponential decay.

In that case, equation 2.9 becomes:

$$\ln\left(\frac{S(b)}{S(0)}\right) = -\text{ADC} \times b \qquad (2.11)$$

When the diffusion is macroscopically isotropic, a powder average of the signal acquired with different gradient directions is performed before fitting equation 2.11.

When the diffusion is macroscopically anisotropic, diffusion gradients are then applied in different directions to probe the orientation dependence of the ADC. Equation 2.9 takes a tensor form:

$$\ln\left(\frac{S(\mathbf{b})}{S(\mathbf{0})}\right) = -\sum_{i=1}^{3}\sum_{j=1}^{3} b_{ij}D_{ij} + O(b^2) \tag{2.12}$$

where $\mathbf{D}$ and $\mathbf{b}$ are now 3x3 matrices representing anisotropic diffusion and 3D gradient application (the b-matrix), respectively. From this tensor expression (requiring at least 6 measurements in different directions to retrieve the 6 independent coefficients of $\mathbf{D}$), the diffusion tensor imaging (DTI) metrics are derived (first order cumulant expansion, see section 2.9.1).

In the case of free diffusion (either isotropic or anisotropic), the ADC is independent of the diffusion time at any time range.

Although free diffusion leads to a simplified formalism, this is in general not what the physical reality is in vivo. Hindrance and restriction effects from the brain micro-environment limit the molecular displacements and influence the dependence on the diffusion time of the ADC [70]. The hindrance effects, caused by immobile obstacles or mobile big molecules (like macromolecules) on the diffusion path, modify the ADC by a tortuosity factor $\left(\frac{D_0}{T^2}\right)$. In addition, molecules may experience restriction effects, due to confinement in cellular spaces. In that case, the ADC will tend to 0 at long diffusion times if there is no leakage through membranes. Whether for isotropic free, hindered or restricted diffusion, the attenuation as a function of the b-value (or q-value, see section 2.7.5) is mono-exponential at low q-regimes, displays kurtosis effects at intermediate q-regimes and diffraction patterns at high q-regimes when restricted (without anisotropy and size distribution) or hindered (see **Figure 2.4**). For hindered and restricted geometries, the slope of $\ln\left(\frac{S(b)}{S(0)}\right)$ will depend on the diffusion time.

The case of microscopic anisotropy but macroscopic isotropy measured with linear diffusion encoding is different from the above mentioned (orange in **Figure 2.4**, represented by the randomly-oriented stick model [69], mimicking the grey matter structure well and described in section 2.9.2). Here, the molecules diffuse freely along sticks with a diffusion coefficient D_{sticks}, the transverse diffusion is set to 0, the sticks are isotropically oriented in space. Importantly, the stick model is not a model of restricted geometry, and the ADC is expected to be constant with time. However, the attenuation of the signal as a function of the b-value is not mono-exponential anymore. This can be understood qualitatively as follows: the decay at low b-values is governed by the molecules diffusing along sticks that are aligned or almost aligned with the direction of the diffusion gradient, freely diffusing in that direction and causing a fast

decay. The decay at higher b-values is governed by the additional contribution of molecules diffusing along sticks that are almost perpendicular to the direction of the diffusion gradient, creating a slower attenuation.

2.7.4 Approximations for restricted diffusion

The short gradient pulse (SGP) approximation

The solution 2.7 of the Bloch Torrey equation is not valid for restricted geometries. However, in the case where the gradient pulse is short ($\delta \approx 0$), the frequency tagging during each pulse can be considered instantaneous (at least sufficiently short so that the spins do not have time to meet the barriers of the geometry), and the signal attenuation can be expressed as follows:

$$E_\Delta(\boldsymbol{g}) = \int \rho(\boldsymbol{r}) \int P_s(\boldsymbol{r}'|\boldsymbol{r},\Delta) \exp(i\gamma\delta\boldsymbol{g}\cdot(\boldsymbol{r}'-\boldsymbol{r}))d\boldsymbol{r}'d\boldsymbol{r} \qquad (2.13)$$

where $E_\Delta(\boldsymbol{g}) = \frac{S(\boldsymbol{g})}{S(0)}$, $\rho(\boldsymbol{r})$ is the probability of finding the spin at the starting position $\boldsymbol{r}$.

If the propagator $P_s(\boldsymbol{r}'|\boldsymbol{r},t)$ for a given geometry is known, the echo attenuation can be calculated with 2.13.

For example, the diffusion attenuation in a cylinder where the diffusion gradient is placed perpendicular to the cylinder axis is given by [72]:

$$E_{\perp\Delta}(g) = \frac{[2J_1(\gamma g\delta R)]^2}{(\gamma g\delta R)^2} + 8(\gamma g\delta R)^2$$
$$\sum_{n=0}^{\infty} \left\{ \frac{[J_n'(\gamma g\delta R)]^2}{1+\delta_{n0}} \times \sum_{m=1}^{\infty} \left[\frac{\alpha_{nm}^2}{\alpha_{nm}^2-n^2} \frac{1}{(\alpha_{nm}^2-(\gamma g\delta R)^2)^2} \exp\left(-\frac{\alpha_{nm}^2 D_0\Delta}{R^2}\right) \right] \right\} \qquad (2.14)$$

where J_1 is the Bessel function of the first kind, order one, R is the radius of the cylinder, J_n' is the derivative of the Bessel function of the first kind, order n, δ_{n0} is the Kronecker symbol, α_{mn} is the mth solution of the equation $J_n'(\alpha) = 0$.

The SGP approximation should however be considered with care. In order to be valid, it requires the duration of the diffusion gradient δ to be small compared to the diffusion time Δ (i.e $\delta \ll \Delta$) and that the characteristic distance travelled during the duration of the diffusion gradient is small compared to the restriction size a (i.e $\sqrt{6D_0\delta} \ll a$). Considering the experimentally-realistic acquisition and diffusion parameters for metabolites ($D_0 =$ 0.2 μm^2/ms and $\delta = 3$ ms), we have $\sqrt{6D_0\delta} = 1.89$ μm. This is, for example, in the same order as the characteristic diameter of an axon.
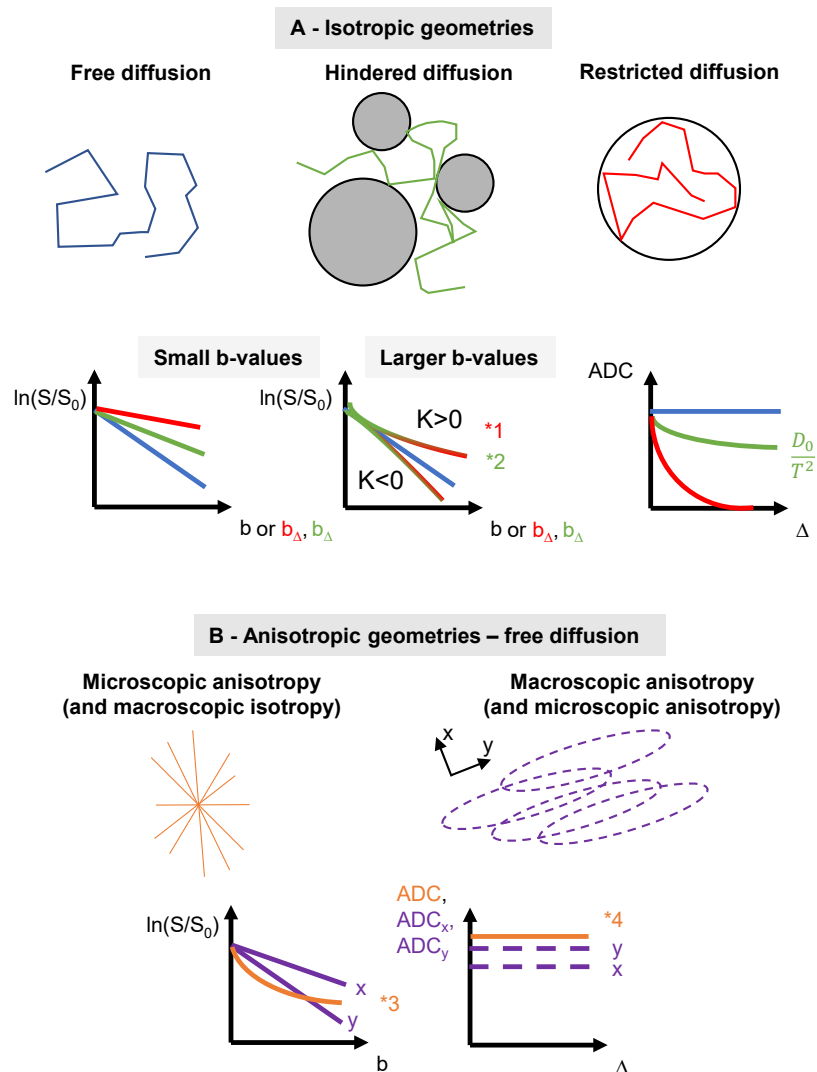
Figure 2.4: Diffusion signal attenuation as a function of the b-value and ADC evolution as a function of the diffusion time Δ, for different geometries. **A:** free, hindered, restricted diffusion. T is the tortuosity, b_Δ indicates that for hindered/restricted diffusion, the attenuation depends on the diffusion time (the q-value should be used instead). At small b-values, $\ln(S/S_0)$ is linear with b for free, hindered and restricted diffusion. For higher b-regimes, hindered/restricted diffusion behaviour deviates from the mono-exponential case (either with positive or negative kurtosis K). *1: Diffusion fraction patterns at very high q-regimes [4]. *2: Diffusion fraction patterns at high q-regimes might also exist in tortuous, non restricted geometries [71]. **B:** microscopic/macroscopic anisotropic free diffusion. Orange is the randomly-oriented sticks model [69]. *3: overall, the case of non-linear attenuation of $\ln(S/S_0)$ with b can be attributed to hindrance/restriction effects, microscopic anisotropy, heterogeneous systems (e.g., two compartments with slow and fast diffusivities). *4: ADC measured at small b-values.

The Gaussian phase approximation

The Gaussian phase approximation is an alternative the SGP approximation when gradient pulses are long. It assumes that the phase distributions can be assumed to be Gaussian even the diffusion is restricted [73].

In that case, the diffusion attenuation in a cylinder where the diffusion gradient is placed perpendicular to the cylinder axis is now given by [73, 74]:

$$E_{\perp\Delta}(g) = \exp\left(-2\gamma^2 g^2 \sum_{m=1}^{\infty} \frac{\begin{array}{c}2D_0\alpha_m^2\delta - 2 + 2\exp(-D_0\alpha_m^2\delta) + 2\exp(-D_0\alpha_m^2\Delta)\\ -\exp(-D_0\alpha_m^2(\Delta-\delta)) - \exp(-D_0\alpha_m^2(\Delta+\delta))\end{array}}{D_0^2\alpha_m^6(R^2\alpha_m^2-1)}\right) \tag{2.15}$$

where R is the radius of the cylinder, α_m is the mth solution of the equation $J_1'(R\alpha_m) = 0$, where J_1' is the derivative of the Bessel function of the first kind, order one.

Callaghan's formalism for a step-wise SGP approximation

Callaghan introduced a matrix formalism that decomposes the gradient waveform into small impulses of duration δt where the SGP is valid ($\delta t \ll \Delta$ and $\sqrt{6D_0\delta t} \ll R$) [75]. This allows to compute the echo attenuation in restricted geometries with any gradient waveform, where the propagator of the geometry will be computed for each δt. **Figure 2.5** shows the deviation of the echo attenuation in a cylinder with the diffusion gradient across its main axis (its main axis being along its longest dimension) as a function of the b-value for the two explicit equations with the SGP and Gaussian phase approximations (equations 2.14 and 2.15, respectively), as compared to the attenuation obtained with the matrix formalism of Callaghan, implemented in the MISST toolbox [76]. It confirms that with realistic acquisition parameters, the radius estimate is biased especially when the propagator is derived from the SGP approximation over the full gradient pulse duration (true R_{cyl} = 1.5 μm given in MISST, R_{cyl} = 1.2 μm is fitted with the SGP approximation and R_{cyl} = 1.53 μm is fitted with the Gaussian phase approximation). Although the difference in the estimation of R may not rise above the noise level, Callaghan's method is in general a safer approach to compute the echo attenuation in restricted geometries. These methods are however limited to cases where the expression of the propagator is known and renders the estimation more complex for heterogeneous microstructure substrates. In principle, the same attenuation can also be obtained using numerical simulations of random walkers in said geometry.

This observation made us cautious about the use of the cylinder model with SGP approximation. The MISST toolbox implementing the step-wise SGP approximation was preferred when fitting the cylinder model.
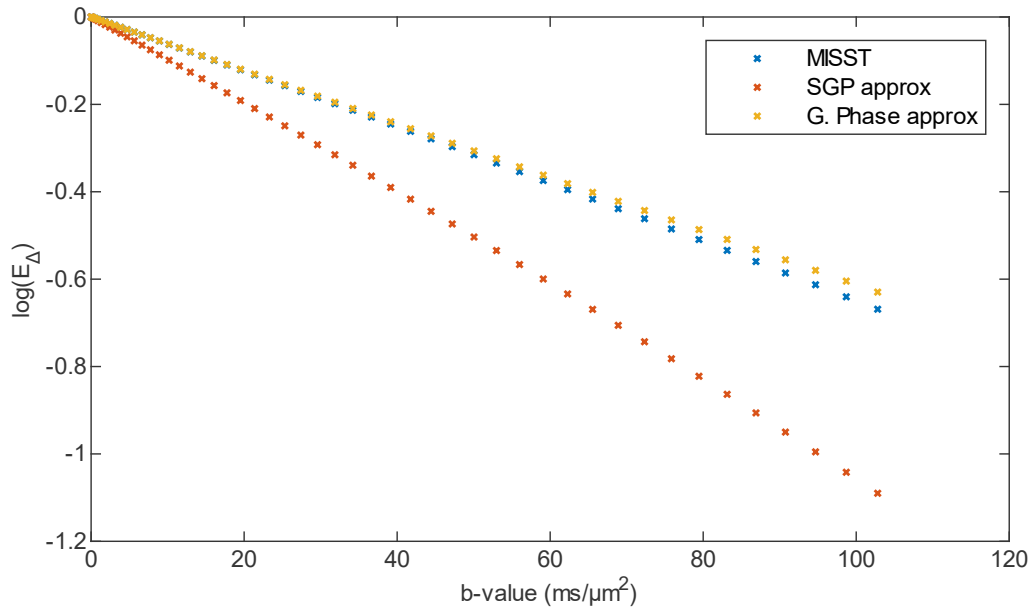
Figure 2.5: Echo attenuation simulation where the gradient is applied perpendicular to the axis of the cylinder. Simulations performed with the MISST toolbox using Callaghan's short gradient impulse formalism (blue), the analytical expressions with the short gradient pulse approximation (orange) and the Gaussian phase approximation (yellow). Simulations parameters: $\delta = 5$ ms, $\delta t = 0.01$ ms (step for gradient impulse), $\Delta = 60$ ms, $D_0 = 0.2\ \mu m^2/ms$, $R_{cyl} = 1.5\ \mu m$, $n_{max} = 20$ in equation 2.14, $m_{cyl} = 20$ in equations 2.14 and 2.15. The value of R_{cyl} for the SGP and Gaussian phase approximations were then changed to match the decay from the MISST toolbox and thus estimate the error of the two methods: we estimated $R_{cyl} = 1.2\ \mu m$ for the SGP approximation and $R_{cyl} = 1.53\ \mu m$ for the Gaussian phase approximation.

2.7.5 Diffusion regimes

The b-value masks the time-dependence of the diffusion coefficient and should theoretically be used only when the diffusion coefficients do not vary with time, i.e. when the diffusion is Gaussian (possibly anisotropic) in all compartments and not restricted [77]. The b-value is often expressed as a function of the parameter q, defined as $q = \frac{\gamma g \delta}{2\pi}$, to separate the effect of the diffusion gradients and of the diffusion time:

$$b = 4\pi^2 q^2 \times t_{\text{diff}} = \text{phase warp} \times \text{effective diffusion time} \tag{2.16}$$

Either varying q or t_{diff} ($= \Delta - \frac{\delta}{3}$ for free diffusion measured with a SE or a STE) can sensitize the diffusion signal to different structures.

Varying q, i.e. the diffusion gradients, will create a tighter phase warp and make it easier for spins to lose phase coherence at the ensemble level. High q-regimes at a given diffusion time

are necessary for estimating small geometries, on the order of the inverse of the pore size (see section 2.7.5).

Varying the diffusion time Δ will make the signal sensitive to different scales of a given environment, driven by the expression of the mean squared displacement in equation 2.2. The acquisition parameters should thus be tuned accordingly. For a metabolite with $D_{0,\mathrm{met}} = 0.1 \, \mathrm{ms/\mu m^2}$, at ultra short diffusion time (1 ms, typically obtained with oscillating gradients, 3D motion with $L(t) = 0.77 \, \mu m$), the loss of phase coherence represents the metabolites diffusion on very short distances having met very few obstacles, the information leads therefore to a good approximation of D_0. If L is smaller than the pore size, the signal is the Laplace transform of the histogram the local diffusion coefficients and the time-dependence of the diffusion coefficient depends on the surface-to-volume ratio S/V of the barriers.

At short diffusion time (1 to 10 ms approximatively, $L(t) = 0.77 - 2.44 \, \mu m$), the signal is sensitized to small range microstructures, the soma radius for example. At intermediate diffusion times (from 10 ms to 100 ms approximatively, $L(t) = 2.44 - 7.74 \, \mu m$), the signal is sensitized to middle range microstructures while features on smaller scales are already fully coarse-grained [77], e.g. the fiber radius for metabolites diffusing in long fibers.

At long and ultra long diffusion times (from 100 ms, $L(t) > 7.74 \, \mu m$), the signal is sensitized to long range microstructures, notably the length of processes.

An estimation of the characteristic restriction size often requires a model with a geometric parameter (like the cylinder, for which the radius is estimated, and unlike the stick, for which the radius is assumed to be 0.)

In the intermediate diffusion time regimes, D changes with Δ and converges towards its tortuous limit following a power law ($D(\Delta) = D_{\mathrm{tort}} + \mathrm{cst}\Delta^{-\theta}$, with $\theta > 0$). When the diffusion coefficients do not vary with Δ anymore, any system can be described as a sum of Gaussian (possibly anisotropic) compartments. The models are then insensitive to hindrance and restriction effects (D has converged to its tortuous limit or to 0, respectively, see **Figure 2.4**). D_{tort} because the diffusion coefficient decays to almost ≈ 0 at long diffusion times

q-space imaging

In MRI, the Fourier transform links the position $\boldsymbol{r}$ to the $\boldsymbol{k}$-space:

$$S(\boldsymbol{k}) = \int \rho(\boldsymbol{r}) \exp(2i\pi \boldsymbol{k} \cdot \boldsymbol{r}) d\boldsymbol{r} \tag{2.17}$$

where $k_i = \frac{\gamma G_i t_i}{2\pi}$. The resolution in the spatial domain $\delta \boldsymbol{r}$ is limited by the maximum value of $\boldsymbol{k}$.

An analogy can be made between $\boldsymbol{k}$-space and $\boldsymbol{q}$-space. Using the voxel-averaged propagator, $\overline{P_s(\boldsymbol{R}, \Delta)}$ which is a sum over all the starting positions:

$$\overline{P_s(\boldsymbol{R}, \Delta)} = \int \rho(\boldsymbol{r}) P_s(\boldsymbol{R} + \boldsymbol{r} | \boldsymbol{r}, \Delta) d\boldsymbol{r} \tag{2.18}$$

where $\boldsymbol{R} = \boldsymbol{r}' - \boldsymbol{r}$. Equation 2.13 giving the echo attenuation under the SGP approximation can be rewritten:

$$E_\Delta(\boldsymbol{g}) = \int \overline{P_s(\boldsymbol{R}, \Delta)} \exp(i\gamma\delta\boldsymbol{g} \cdot \boldsymbol{R}) d\boldsymbol{R} \tag{2.19}$$

and using $\boldsymbol{q} = \frac{\gamma\boldsymbol{g}\delta}{2\pi}$:

$$E_\Delta(\boldsymbol{q}) = \int \overline{P_s(\boldsymbol{R}, \Delta)} \exp(2i\pi\boldsymbol{q} \cdot \boldsymbol{R}) d\boldsymbol{R} \tag{2.20}$$

Similarly to the Fourier transform relation between the frequency $\boldsymbol{k}$-space and the image $\boldsymbol{r}$-space, there is a Fourier transform relation between the diffusion $\boldsymbol{q}$-space and the relative displacement $\boldsymbol{R}$-space.

This is an interesting concept because the distribution of distances travelled can be studied without assuming a specific geometry (i.e. without the need to know the expression of the propagator).

At high q-regimes, diffraction patterns appear, i.e. signal drops in the plot of the echo amplitude $E_\Delta(\boldsymbol{q})$ as a function of $\boldsymbol{q}$, expressing a point where the phases almost completely cancel out [4]. It was shown that, in the case of perfectly aligned and homogenous substrates (e.g. aligned cylinder with the same radius), the first signal drop is linked to the pore geometry [78]:

$$d = \frac{1.22}{q_{1,\text{min}}} \tag{2.21}$$

The diffraction pattern in **Figure 2.6** represent the signal attenuation across a cylinder of radius 2 µm. The first signal drop occurs at $q_{1,\text{min}} \approx 3065$ cm^{-1}, which estimates the cylinder diameter as d = 3.98 µm according to equation 2.21 (not exactly 4 µm likely due to a poor resolution around the minimum).

Recently, it was shown that diffraction patterns may also occur in non-restricted but disordered (tortuous) systems with locally varying diffusivity [71].

The resolution limit

The resolution in the $\boldsymbol{R}$-domain $\delta\boldsymbol{R}$ is limited by the maximum value of $\boldsymbol{q}$, i.e. the maximum gradient amplitude. This gives a lower resolution limit for axon diameter. For restricted diffusion, the resolution is additionally impacted by the short gradient pulse approximation.
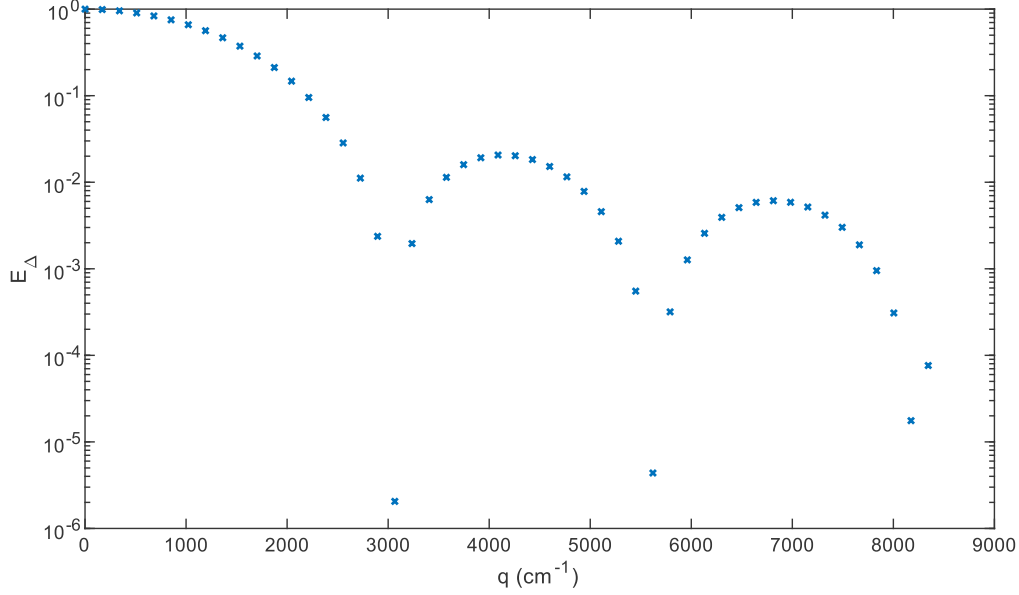
Figure 2.6: Diffraction patterns in restricted geometries at high q-values using MISST. Simulation for one cylinder with the diffusion gradient across its main axis and the parameters: $\delta = 0.5$ ms, $\delta t = 0.1$ ms (step for gradient impulse), $\Delta = 600$ ms, $D_0 = 0.2\ \mu m^2/ms$, $R_{cyl} = 2\ \mu m$. The first signal drop occurs at $q_{1,min} \approx 3065\ cm^{-1}$, which estimates the cylinder diameter d as $3.98\ \mu m$, not exactly $4\ \mu m$ likely due to a poor resolution around the minimum.

For example, for a collection of parallel cylinders under the Gaussian phase approximation and single diffusion encoding, the resolution is given by [79]:

$$d_{min} = \left(\frac{768}{7} \frac{\bar{\sigma} D_0}{\gamma^2 \delta g_{max}^2} \right) \qquad (2.22)$$

For $\bar{\sigma} = 5\%$, $D_0 = 0.2\ \mu m^2/ms$, $g_{max} = 628$ mT/m ($b_{max} = 15$ ms/μm^2), $\Delta = 60$ ms and $\delta = 3$ ms:

$$d_{min} = 1.9\ \mu m \qquad (2.23)$$

Moreover, the resolution in **R**-space is also limited by how fast the signal decays below the noise floor, similarly to the resolution in frequency domain being limited by T_2 relaxation in MRS.

Following these observations, this resolution limit made us cautious about the possibility to extract realistic axon diameters from dMRS acquisitions.

2.8 Acquisition sequences for dMRS

During the first diffusion (tagging) gradient, a different frequency is attributed to the particles depending on their position. For those diffusing, the frequency attributed during the second (untagging) gradient will *not* be the same as their initial frequency, and they will contribute to a loss of phase coherence at the ensemble level. This concept is depicted in **Figure 2.7**.

This section will present an overview of the main sequences used for dMRS acquisitions, and describe how these diffusion gradient pairs can be optimally combined with standard MRS sequences. The choice of the sequence should be tailored to the system under investigation. We recently summarized dMRS implementation guidelines in a consensus paper in which I am a co-author [80].

Three types of sequences are currently used for localized dMRS in vivo [70]: STEAM-, PRESS-, and LASER-based sequences. These sequences are shown in **Figure 2.8** (reproduced from the review *Insights into brain microstructure from in vivo DW-MRS*, Palombo et al. [70]).

DW-STEAM

A few years after Stejskal [39] introduced the SE sequence, Tanner [81] formalised the use of stimulated echo (STE) sequences for diffusion experiments. He showed that there was no difference in the attenuation term linked to time-dependent MFG between STE and SE sequences (i.e. the two sequences have the same b-value for same gradient configuration), yet with a loss of half the magnetization in STE. Only the term depending on steady magnetic field variations differed, making the STE sequence less sensitive to B_0 inhomogeneities (attenuation term for SE linked to B_0: $\frac{2}{3}\tau^3$, τ time between the 90° and 180° and for STE: $\tau_1^2(\tau_2 - \frac{1}{3}\tau_1)$, τ_1, time between the first 90° and the second, τ_2, time between the first 90° and the third, with $\tau_2 > \tau_1$ i.e. $\frac{2}{3}\tau^3 > \tau_1^2(\tau_2 - \frac{1}{3}\tau_1)$ in all cases).

Moreover, in DW-STEAM, diffusion gradients are inserted between the two first 90° pulses and after the third pulse (**Figure 2.8.A**). The sequence benefits from the possibility to reach long diffusion times and high b-values while the magnetization is stored along z, thus unaffected by T_2 relaxation and J-evolution (long T_1 relaxation in vivo, around 1.5 s in the rat brain at 14T [82]). It is the most widespread sequence in human experiments due to the absence of 180° pulses and the limited SAR deposition. However, it suffers from the presence of cross terms between diffusion and slice-selection gradients.
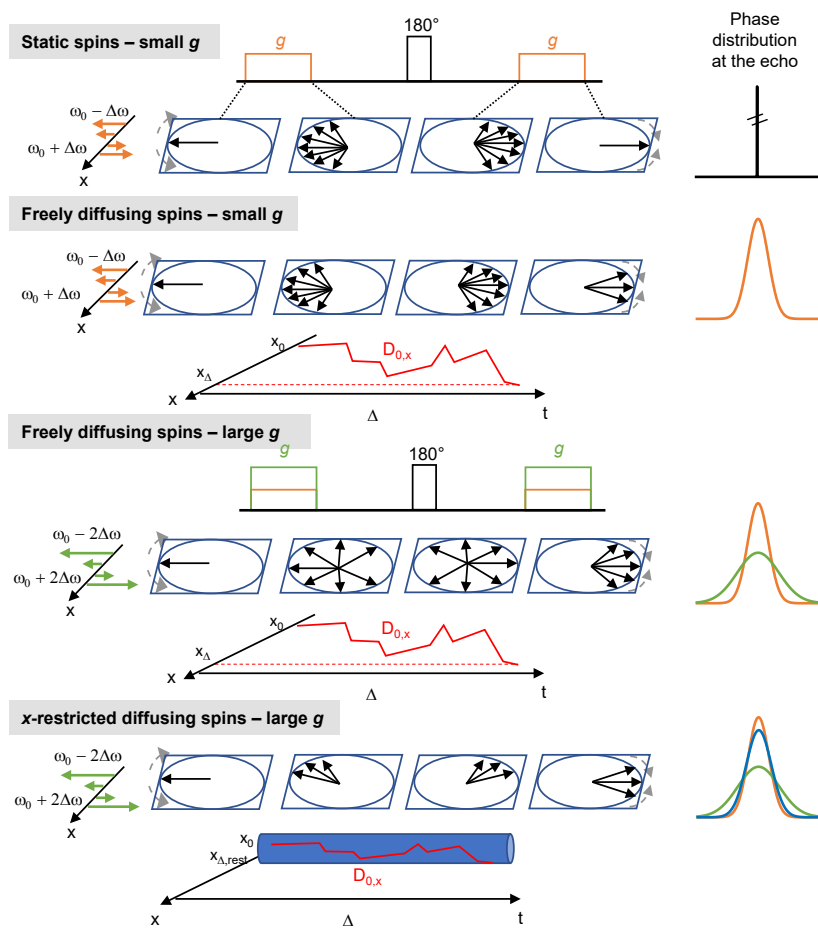
Figure 2.7: Effect of a SE with MFG on the phase distribution at the time of the echo. In the first case, when all spins are static, the first MFG will attribute a frequency ($\omega_0 \pm \Delta\omega$) that depend on their x-position, perfectly refocused by the second gradient and the phase distribution is a delta function. In the case of freely diffusing spins ($D_{0,x}$, starting at a position x_0 and finishing at x_Δ after the diffusion time Δ) with a small gradient (g, orange), the frequency attributed by the second gradient to the diffusion spins is different from the first one, resulting in a small loss of phase coherence at the ensemble level. The resulting phase distribution (orange) is less peaked. In the case of freely diffusing spins with a strong gradient (g, green), the spread of frequencies attributed by the tagging gradient is wider ($\omega_0 \pm 2\Delta\omega$), making it easier for spins to be attributed a mismatched untagging frequency. The loss of phase coherence is stronger and the phase distribution (green) even less peaked. In the last case of restricted restriction, the spread of frequencies attributed to the spins in the cylinder by the first gradient is limited (and not necessarily centred), and the loss of phase coherence is smaller than in the free diffusion case.

DW-PRESS

In DW-PRESS, diffusion gradients are inserted around the two 180° pulses (**Figure 2.8.C**), often in a bipolar fashion to minimize the Eddy Currents distortions. The sequence benefits
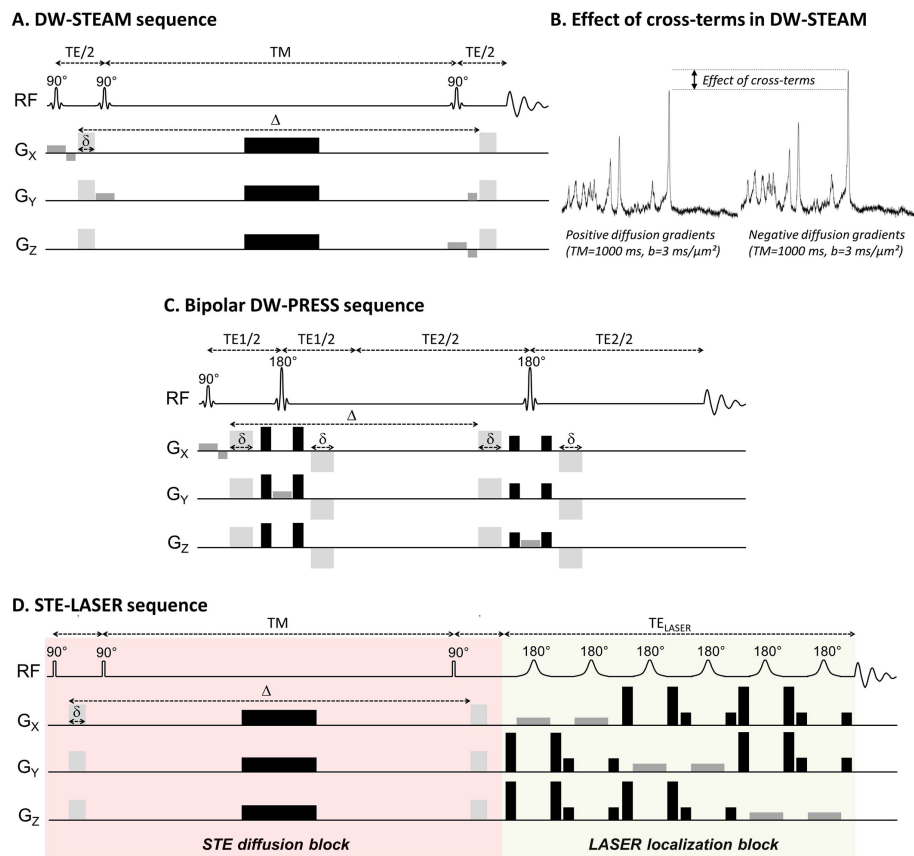
Figure 2.8: In vivo localized spectroscopy diffusion sequences, from Palombo et al. [70]. Gradients: light grey - diffusion gradients, dark grey - slice selection gradients, black - spoiler/crusher gradients. **A**: DW-STEAM with the effects of cross-terms in the b-value on representative diffusion spectra (**B**). **C**: DW-PRESS. **D**: STE-LASER, showing the separation between the diffusion (pink) and the localization blocks (green).

from the full magnetization compared to DW-STEAM but the diffusion time occurs while the magnetization is in the transverse plane, preventing its use for long diffusion times.

STE-LASER

More recently, a new sequence has been proposed by Ligneul et al. [83] and successfully applied [59] by the same group to measure metabolites diffusion in a mouse model of reactive astrocytes at 11.7 T. This block-type sequence, with a LASER sequence for localization, was early described by Shemesh et al. [84] for relaxation-enhanced measurements at ultra high field. The STE-LASER sequence used for diffusion consists of two blocks: the first one, a diffusion block, is based on a non-localized stimulated echo sequence with additional bipolar diffusion gradients, and the second one, a localization block, is based on a full adiabatic LASER sequence (Figure 2.8.D). It benefits from the combined advantages of DW-STEAM over DW-PRESS and of a good 3D localization with the LASER sequence. The full LASER module however limits its clinical translation due to SAR limitations. In addition, with its block design, it benefits from the absence of cross terms. Indeed, in the STE-diffusion block, the only gradients applied are the diffusion gradients (and the spoiler in the mixing time), which are refocused within the echo time of the STE sequence and before the application of localisation gradients in the LASER block. This nulls cross terms in the echo attenuation. In vivo, the macromolecules (MM) spectrum is acquired before each experiment with the metabolites inversion recovery (IR) nulling technique [85], sometimes combined with diffusion to remove all metabolite contribution from the spectrum [86]. Ligneul et al. [83] showed that their sequence yields to similar SNR compared to DW-STEAM.

The STE-LASER sequence was programmed, implemented and used for most of the diffusion acquisitions presented in this thesis, until we proposed an alternative sequence where the minimum echo time achievable was reduced to improve the detection of J-coupled metabolites.

At the acquisition and post-processing level, dMRS presents many challenges for which guidelines have been provided in a recent consensus effort [80]. The overall low SNR of the dMRS acquisitions, especially at high b-values, extends acquisition times and sometimes prevents accurate quantification.

One of the aims of this thesis was to investigate the effects of a denoising technique based on the principal component analysis (PCA) method for dMRS data, to circumvent the inherently low SNR. The goal was to see whether such technique applied on a dataset with fewer repetitions per b-value, i.e. lower SNR, could perform as well as longer high SNR acquisitions in terms of quantification.

2.9 Signal representation vs biophysical modelling

In vivo, the deviation of the water or metabolites diffusion signal attenuation from the one expected for free diffusion can be modelled and inform on the underlying microstructure, and be the specific to grey/white matter or to the cell type. The information extracted from the modelling of dMRS experiments in the brain has been thoroughly described by Palombo et al. [70, 87, 55, 88].

Important distinctions have to be made when estimating geometrical parameters from the diffusion attenuation. Signal representation has to be distinguished from biophysical modelling: the former being mathematical formulas, the latter being a model mimicking in vivo reality through realistic geometries. Signal representations are sensitive but not specific. Biophysical models are specific but require in addition validation from independent methods such as histology. Modelling can be done with an analytical approach (from the MR acquisition, fitted with a model to retrieve the microstructure information) or with a numerical approach (from synthetic cells, where particles will diffuse in the cell structure and be tagged with a given sequence, predicting the expected diffusion decay for each cell, and finding the best match to experimental decay). Forward approaches generally need strong hypotheses on the model for convergence, while reverse approaches face the issue of the degeneracy of solutions.

Moreover, knowing, from the underlying microstructure, *what survives voxel averaging*, is of key importance. The concept of effective medium theory has been developed by Novikov et al. [89, 77]. The measured signal results from a first averaging from the single-particle quantum mechanical behaviour to the local phenomenological constants (such as the diffusion coefficient, and the relaxation times T_1 and T_2), and from a second averaging of phenomenological constants over space to the information at the voxel level.

2.9.1 Signal representation: DTI and DKI

The cumulant expansion is the most widespread signal representation. Equations 2.11 and 2.12 can be expanded to the second order in b to express the kurtosis:

$$\ln\left(\frac{S(b)}{S(0)}\right) = -\mathrm{ADC} \times b + \frac{1}{6}\left(\mathrm{ADC} \times b\right)^2 K_{\mathrm{app}} + O(b^3) \tag{2.24}$$

and in the tensor form:

$$\ln\left(\frac{S(\mathbf{b})}{S(\mathbf{0})}\right) = -\sum_{i=1}^{3}\sum_{j=1}^{3} b_{ij} D_{ij} + \frac{1}{6}\left(b\overline{D}\right)^2 \sum_{i,j,k,l=1}^{3} g_{ijkl} K_{ijkl} + O(b^3) \tag{2.25}$$

where $\overline{D}$ is the MD, **D** the rank-2 diffusion tensor and **K** the rank-4 kurtosis tensor and **g** the direction of the diffusion gradient. The kurtosis expresses the deviation from Gaussian behaviour at higher q-regimes. From equation 2.25, one can derive rotational invariants of the diffusion tensor **D** and of the kurtosis tensor **K**, independent of the position of the object with respect to the laboratory frame. Because the diffusion tensor is symmetrical, six experiments are sufficient to express the 3x3 diffusion tensor. Because of its symmetry, the matrix can be diagonalized on an orthogonal basis (spectral theorem). This new basis corresponds to the tissue three principal diffusion directions, with eigenvectors $\boldsymbol{\epsilon_1}$, $\boldsymbol{\epsilon_2}$, $\boldsymbol{\epsilon_3}$ and eigenvalues λ_1, λ_2, λ_3 with $\lambda_1 >, \lambda_2 > \lambda_3$.

From these values, we derive:

$$
\begin{aligned}
MD &= \frac{\text{Tr}(\boldsymbol{D})}{3} = \frac{\lambda_1 + \lambda_2 + \lambda_3}{3} \\
AD &= \lambda_1 \\
RD &= \frac{\lambda_2 + \lambda_3}{2} \\
FA &= \sqrt{\frac{3\left[(\lambda_1 - MD)^2 + (\lambda_2 - MD)^2 + (\lambda_3 - MD)^2\right]}{2\left(\lambda_1^2 + \lambda_2^2 + \lambda_3^2\right)}} \\
MK &= \frac{1}{4\pi} \int_{\mathbb{S}^2} K(\boldsymbol{n}) d\mathbb{S}_{\boldsymbol{n}}^2 \\
AK &= K(\boldsymbol{\epsilon}_1) \\
RK &= \frac{1}{2\pi} \int_0^{2\pi} K(\boldsymbol{\epsilon}_2 \cos(\phi) + \boldsymbol{\epsilon}_3 \sin(\phi)) d\phi
\end{aligned}
\tag{2.26}
$$

where MD is the mean diffusivity, AD the axial diffusivity, RD the radial diffusivity, FA the fractional anisotropy, MK the mean kurtosis, AK the axial kurtosis and RK the radial kurtosis. FA, corresponding to the normalized standard deviation of the three diagonal coefficients in the new basis, is used to assess anisotropy of the water diffusion process. It is exploited in clinical applications such as tractography in the brain, which follows the orientation of white matter tracks. Similar water MD values are found in WM and GM, but generally higher AD, FA and lower RD are found in white matter compared to grey matter due to the presence of myelinated axons and the strong directionality of white matter tracks. In the case of anisotropic diffusion, the ADC and the MD are different (the ADC would be different in each direction, accounting for the voxel-averaged behaviour).

Alterations in the brain structure and function are reflected in the water **D** and **K** tensors metrics. Microgliosis and astrogliosis during inflammation are associated with decreased D and increased K metrics [90]. Cytotoxic edema is also associated with decreased D and increased K metrics [91], whereas vasogenic edema is associated with increased D with constant K metrics [92]. Axonal beading and swelling is associated with a strong decrease in AD with a strong

increase in AK [93, 94] and demyelination a strong increase in RD and strong decrease in RK [95].

However, it is sometimes difficult to extract the unique underlying phenomenon responsible for the change in these metrics. For example, a decreased diffusivity could result from a greater contribution of the slowly-diffusing intracellular space [96], increased tortuosity of the extracellular space [97], neurite beading [93], increased cytoplasmic viscosity [98] or increased fraction of membrane-bound water [99]. Similarly, increased radial diffusivity could be associated to demylination, axonal loss or vasogenic edema. Biophysical modelling of realistic cellular architectures holds the promise of alleviating these degeneracies.

2.9.2 Biophysical modelling

Comprehensive reviews about biophysical models are done here [77, 100, 80]. The biophysical models used in this thesis are presented in **Figure 2.9**.

The sticks model is given by:

$$\frac{S}{S_0} = \int_0^1 \exp(-bD_{\mathrm{intra}}x^2)dx = \sqrt{\frac{\pi}{4bD_{\mathrm{intra}}}}\,\mathrm{erf}(\sqrt{bD_{\mathrm{intra}}}) \tag{2.27}$$

where D_{intra} is $D_{\mathrm{neurite,MRS}}$ in **Figure 2.9**. The Taylor expansion of $\mathrm{erf}(z)$ in $z \to 0$ is $\frac{2}{\sqrt{\pi}}\left(z - \frac{z^3}{3}\right) + o(z^3)$, which shows the link between the ADC measured at small b-values and D_{intra}:

$$\frac{S}{S_0} \underset{b\to 0}{=} \sqrt{\frac{\pi}{4bD}} \times \frac{2}{\sqrt{\pi}}\left(\sqrt{bD} - \frac{\sqrt{bD}^3}{3}\right) + o(b^{\frac{3}{2}}) \approx 1 - b\frac{D}{3} \tag{2.28}$$

and thus:

$$ADC \underset{b\to 0}{=} \frac{D_{\mathrm{intra}}}{3} \tag{2.29}$$

This model accounts for the macroscopic isotropy of the GM, schematically represented by an ensemble of fibres (dendrites, axons, astrocytic processes) with no directional preference, contrary to the well-aligned WM tracks. Interestingly, a bi-exponential fit with well chosen diffusivities can give the *exact* same decay as the stick model. Consequently, a bi-exponential fit should not be automatically attributed to the presence of two distinct compartments with different diffusivities, as it could also originate from one anisotropic compartment.

The ensemble of fibres is also used in the SANDI model (soma and neurite density imaging, [101]) applied on the dMRI signal in GM, with an additional soma contribution of fixed diffusivity and an isotropic extracellular space. The increased number of fitted parameters is justified by the higher sensitivity of the water signal compared to the metabolites signal.

dMRS	dMRI	
Voxel made of grey and white matter	Gray matter	White matter
Δ = 40 - 63 ms	Δ = 12 ms	
Randomly oriented sticks model b_{max} = 15 ms/µm²	SANDI model b_{max} = 8 ms/µm²	WM standard model b_{max} = 3 ms/µm²
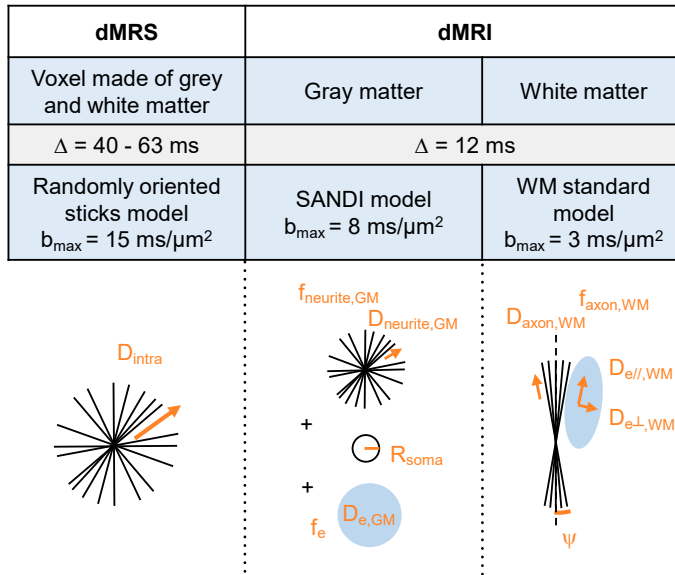
Figure 2.9: Overview of the biophysical models used in this thesis for dMRS and dMRI. The randomly-oriented sticks model [69] was used for dMRS, the SANDI model for dMRI in grey matter [101] assuming $D_{soma,GM}$ = 3 µm²/ms and the standard model (SM) for dMRI in white matter, either with the WMTI implementation [102] assuming a Watson distribution of the ODF [103] and $D_a > D_{e,//}$ [100], or using the rotational invariants [104]. The parameters estimated from each model are shown in orange: D_{intra}, metabolite intra-stick diffusivity in µm²/ms, $f_{neurite,GM}$, neurite fraction in GM, $D_{neurite,GM}$, water intra-stick diffusivity in GM in µm²/ms, R_{soma}, soma radius in GM in µm, $D_{e,GM}$, extracellular isotropic water diffusivity in GM in µm²/ms, f_e, extracellular-space fraction, $D_{axon,WM}$, water intra-stick diffusivity in WM in µm²/ms, $f_{axon,WM}$, axon fraction in WM, $D_{e//,WM}$, extracellular water diffusivity parallel to the fibre bundle in WM in µm²/ms, $D_{e\perp,WM}$, extracellular water diffusivity perpendicular to the fibre bundle in WM in µm²/ms, Ψ, orientation dispersion of the fibre bundle in degrees.

Moreover, contrary to metabolites being mostly intracellular (except for Lac and Glc), a non-negligible fraction of water is present in the extracellular space which justifies the additional compartment in the dMRI models.

The standard model of WM consists of sticks with a preferential orientation given by the orientation dispersion function (ODF) (Ψ in **Figure 2.9**) and an anisotropic extracellular space. The soma contribution is neglected in WM because it is essentially made of axons. Overall, the standard model offers more specific information than the diffusion and kurtosis metrics. $f_{axon,WM}$, which represents the axonal density, holds the promise of differentiating neuroinflammation (increased $f_{axon,WM}$ due to increased cellular crowding) from neurodegeneration (cell death, decreased axonal density). A change in $D_{axon,WM}$ could reflect axonal injury, and of $D_{e\perp,WM}$ in myelination. Transient effects can also be observed: in a cuprizone mice model of MS, $D_{e\perp,WM}$ was decreased after 3 weeks of intoxication, associated with glial crowding,

then increased after 12 weeks associated with demyelination [95]. Histology validation are nonetheless required and the previous study confirmed their results with electron microscopy.

Sticks versus cylinders

There has been growing evidence that the metabolites diffusion measured with dMRS is well represented by the randomly-oriented cylinder model, given by [74, 72]:

$$E_\Delta(g) = \frac{\int_0^\pi E_{\perp\Delta}(g\sin(\theta)) \exp\left(-D_0\gamma^2\delta^2[g\cos(\theta)]^2\left(\Delta - \frac{\delta}{3}\right)\right)\sin(\theta)\,d\theta}{\int_0^\pi \sin(\theta)\,d\theta} \tag{2.30}$$

Najac et al. [65, 57] showed that, at very long diffusion times, the ADC of most metabolites in the monkey and human brain is stable but does not go to 0. This suggests that metabolites are not confined in subcellular regions but rather experience long range structures. This was also confirmed in the human brain when comparing metabolites and water diffusion in GM and WM at a fixed diffusion time [105]. The authors measured a similar subdiffusive behaviour for tCho, tCr and tNAA in WM, although these molecules are located in different cell types. They concluded that the diffusion process measured in their study was occuring in elongated fibers, a feature shared by most cell types. This observation was further confirmed by the dependence of the echo attenuation in double diffusion encoding experiments, exhibiting strong microscopic anisotropy [106, 107]. Moreover, no correlation was found between relaxation and diffusion properties with TE ranging from 50 to 110 ms at 11.7T, suggesting that the metabolites are located in one compartment [108].

However, it has also been acknowledged that the estimation of the cylinder radius can be compromised by the b-range and the noise level (in addition to being sensitive to the resolution limit (section 2.7.5) and to the bias of the approximated propagators (section 2.7.4)) [80]. **Figure 2.10** shows the estimated values for the diffusion coefficient D and the cylinder radius R_{cyl} based on Monte Carlo simulations with different maximum b-values and noise levels σ. The echo attenuation was generated from equation 2.30 with the expression of $E_{\perp\Delta}$ under the SGP approximation given by equation 2.14. The following input values were used: $D = 0.4$ ms/μm^2 and the cylinder radius $R_{cyl} = 4$ μm (shown in red in **Figure 2.10**). The decay was then corrupted by noise (σ) and fitted again with the same model up to different maximum b-values (b_{max}) for 100 Monte Carlo iterations. The blue dots show 100 results for the coordinate (R_{cyl},D). The two parameters are correlated even with a large b-range and a realistic noise level. A similar behaviour was reported in ref. [107] for double-diffusion encoding (DDE) acquisitions where the cylinder model was fitted with the MISST toolbox.

From this observation (together with the observation of the bias introduced by the approxi-

mated propagators and the resolution limit), although its lacks geometrical parameters like the radius, we decided to use the randomly-oriented sticks model for the dMRS data presented in this thesis.
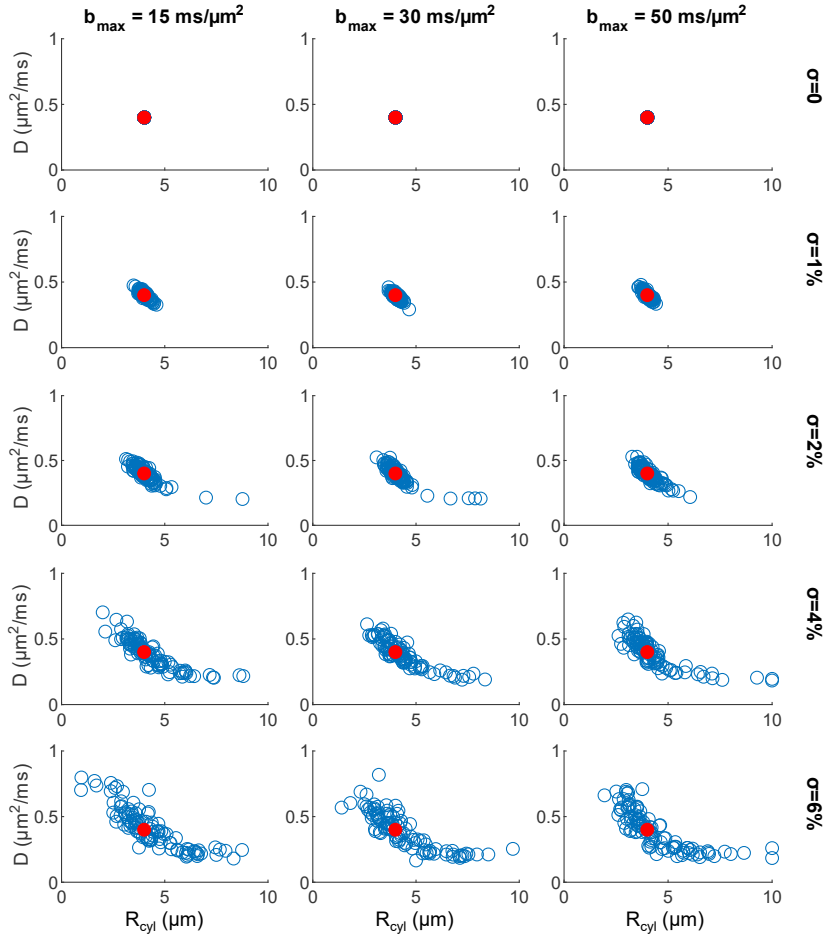
Figure 2.10: Correlation between the estimated parameters D and R_{cyl} of the randomly-oriented cylinders model depending on the maximum b-value (b_{max}) and the noise level σ. The echo attenuation was generated from equation 2.30 with the expression of $E_{\perp\Delta}$ under the SGP approximation in equation 2.14. The following input values were used: $D = 0.4\,\mu\mathrm{m}^2/\mathrm{ms}$ and the cylinder radius $R_{\mathrm{cyl}} = 4\,\mu\mathrm{m}$ (shown in red in **Figure 2.10**). The decay was then corrupted by Gaussian noise (σ) and fitted again with the same model up to different maximum b-values (b_{max}) for 100 Monte Carlo iterations. The blue dots show the 100 results for the coordinate (R_{cyl}, D).

2.10 Current trends and perspectives

2.10.1 Oscillating gradients

Oscillating gradients have also been introduced in diffusion sequences to achieve ultra short diffusion times. They are sinus or cosinus modulated gradients, their associated diffusion time depends on their shape and is inversely proportional to the gradient frequency [109]. The 1D signal attenuation is given in the frequency domain by [110]:

$$\ln\left(\frac{S(b)}{S(0)}\right) = -\frac{1}{\pi}\int_0^\infty D(\omega)|F(\omega)|^2 d\omega \qquad (2.31)$$

where $D(\omega)$ is the diffusion spectrum (Fourier transform of the velocity autocorrelation function [111]) and $F(\omega)$, the Fourier transform of $\gamma\int_0^t G_z(t')dt'$.

One of the challenges is the difficulty to reach high b-values and sufficient diffusion attenuation, especially for metabolites which have smaller diffusion coefficients than water [112]. Initially, diffusion sequences with oscillating gradients were proved efficient to reach short diffusion times but suffered from the aftermath of a longer TE (150 ms) which consequently led to a decrease in SNR [113]. Later, the same group optimized their oscillating gradients shapes (stretched cosine shape to maximize the b value reached in one oscillation period), reaching ultra short diffusion times (1 ms) while maintaining a relatively short TE (60 ms) [112]. The main advantage of oscillating gradients is that no *a priori* cellular model is required if sufficiently high gradient frequencies can be reached, hence providing a direct measurement of D from a linear fit of $D(\omega)$ as a function of the oscillating gradients angular speed ω [70] [114].

2.10.2 Exchange and disorder

The origin of the time dependence of the diffusion and kurtosis metrics is currently debated in the dMRI field (as seen in the ISMRM 2022 session: "Diffusion MRI in Gray Matter: Exchange and Restriction"). Exchange between intra- and extra-cellular compartments and intracellular restriction/disorder could both explain the observed behaviours. In principle, exchange only will lead to kurtosis time-dependence but no diffusion time-dependence, whereas structural disorder will lead to both diffusion and kurtosis time dependence.

It is argued that dMRI models in GM should account for exchange between the intracellular compartments and the extracellular space when $\Delta > 20$ ms [115, 116, 117], illustrated by the fact that the neurite fraction in the standard model decreases with the diffusion time in GM if exchange is not accounted for and that time-dependent kurtosis was observed in that range [116]. In WM, exchange is usually neglected because of the myelin sheath. In dMRS, the

diffusion times are sufficiently short (considering slower metabolites than water diffusivity) so that exchange can be neglected.

For structural disorder, the axonal models as a collection of perfectly straight, infinite sticks or cylinders of constant diameter have been revisited to account for spines [55] and axonal beading [94] and better describe the time-dependence of the diffusion and kurtosis metrics.

Free gradient waveforms that are numerically optimized to render the acquisition sensitive to restriction or exchange have recently been introduced [118].

During this PhD, we investigated the possibility to include exchange in the SANDI model of GM for dMRI, solely based on the dMRS and dMRI acquisitions we had already performed: a dMRI acquisition at short diffusion time and a water signal from the dMRS acquisition at long diffusion time. We evaluated whether two diffusion times were sufficient to accurately measure exchange. This project was done with the help of two master students that I supervised independently.

2.10.3   Double or multiple-diffusion encoding

In vivo relaxation enhanced double diffusion encoding (DDE) experiments were pioneered by Shemesh et al. [119] at ultra high field. In this type of acquisition, two or more pairs of diffusion gradients used, and the angles between each pair vary. Conceptually, in the example of two pairs, the product of diffusion attenuations originating from the first **q** and from the second **q**-vector is performed before voxel averaging. Because diffusion in different directions is correlated in anisotropic pores, the DDE signal retains a unique signature of microscopic anisotropy, inaccessible by single-diffusion encoding. Microscopic anisotropy can be extracted from the difference in signal attenuation when the diffusion vectors are parallel or perpendicular. If macroscopic anisotropy exists in the sample (in addition to microscopic anisotropy), the difference should be taken on the powder-averaged signal. Moreover, this type of sequence uses small diffusion-weighting which reduces the acquisition time and circumvents SNR drop at high b-values. Vincent et al. [107] showed that the amplitude modulation $\frac{S(\Psi)}{S(0)}$ as a function of Ψ was stronger for neuronal metabolites than glial ones, explained by a soma contribution for glial cells (isotropic medium with many possible diffusion directions) or a larger number of ramifications in glial cells compared to neurons.

3 Hepatic encephalopathy

Hepatic encephalopathy (HE) is the severe neurological condition that arises as a consequence of (acute and/or chronic) liver disease or portosystemic shunting [120].

3.1 Prevalence

The causes of chronic liver disease (CLD) leading to HE include non-alcoholic fatty liver disease (which accounts for $\approx$ 60% of the cases), viral infections (mostly hepatitis A, B and C), alcohol abuse, obesity, diabetes or autoimmune diseases [121]. In 2017, 1.5 billion people suffered from chronic liver disease worldwide, out of which 10.6 million people developed a decompensated form of cirrhosis [122]. HE is a decompensating event of cirrhosis that occurs in 30 to 40% of the patients [123]. Portosystemic shunting (PSS) without liver disease can develop at birth (congenital PSS, very rare, affecting $\approx$ 30 000 to 50 000 births [124, 125]) or be acquired, often as a result of portal hypertension (spontaneous PSS, affecting $\approx$ 6% to 30% of patients with portal hypertension [126]). 25% to 50% of patients with PSS will develop HE [127].

HE is classified in terms of severity and of etiology.

3.2 Covert and overt HE

Covert HE is characterized by mild cognitive symptoms (impairment in executive decision-making, working memory and coordination, attention deficits [128]) that require a psychometric test to be identified. Overt HE is characterized by severe cognitive and motor impairment (personality changes, confusion, disorientation, lethargy, ataxia) that can evolve into coma and death [129]. Overt HE can occur in episodes, for which covert HE is a precipitating factor [130]. For overt HE patients, the survival rate in a one year follow-up without liver transplantation,

being the only curative treatment to date, is below 40% [131].

3.3   Type A, Type B, and Type C HE

The disease is also classified depending on the associated liver disease or PSS [120]:

- type A HE if HE is a consequence of an acute liver failure (ALF)

- type B HE if HE is the consequence of a portosystemic shunt

- type C HE if HE is the consequence of liver cirrhosis

On the one hand, the symptoms develop fast in type A HE, characterized by high ammonia blood levels, elevated intracranial pressure and edema with astrocyte swelling [132, 133]. On the other hand, in type C HE, the symptoms develop more gradually and compensation mechanisms come into play [134].

The focus of this thesis is type C HE, for which a rat model has been validated by the International Society for Hepatic Encephalopathy and Nitrogen Metabolism (ISHEN) [135]. The bile duct ligated (BDL) rat model is a model of type C covert HE, extensively used and studied in our group [136, 137, 138, 139, 140], where the rat's bile duct is ligated and resected (**Figure 3.1**). The animals develop liver failure, resulting in HE symptoms such as motor [141] and cognitive [142] impairments, and survive for up as 6 to 8 weeks after BDL surgery. Increased blood ammonia and bilirubin are systemic markers of the disease progression and are followed with longitudinal blood samplings [135]. In the brain, an increased glutamine with a compensatory decreased in the brain osmolytes such as myo-inositol, taurine and choline, accurately measured by ^{1}H MRS, is one of the hallmarks of the disease [143, 136].

3.4   The role of ammonia

Excessive ammonia production and accumulation (NH_3 in its gaseous form, NH_4^+ in its ionic form, the latter being dominant ($\approx$ 98%) at physiological pH [144]) is believed to be one of the major factors in the pathogenesis of HE. Ammonia is a dangerous toxin for the brain because its ionic form NH_4^+ resembles potassium ions (K^+) and can enter the cells through potassium pumps, in addition to aquaporins (water channels) and ammonium transporters [145].

In non-pathological conditions, ammonia is produced in the gut [146] and eliminated by two main processes:

- Extraction into urea by the urea cycle in the liver, later processed and evacuated by the
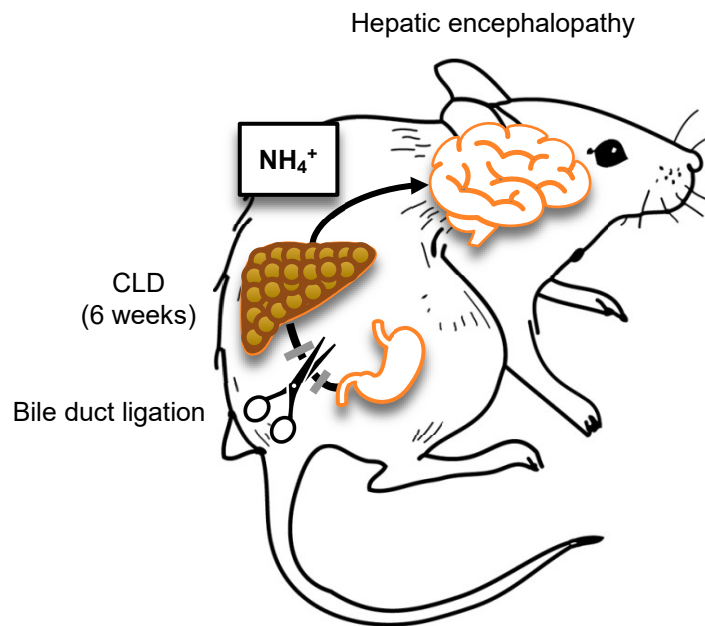
Figure 3.1: Bile duct ligated (BDL) rat model of type C covert HE, used throughout this thesis. A ligation of the bile duct in performed, leading to chronic liver disease with hepatic encephalopathy symptoms after 6 to 8 weeks.

kidneys.

- Conversion into glutamine (Gln) by the glutamine synthetase (GS) enzyme located in muscles and in astrocytes in the brain [147, 148]. The presence of GS in the muscles renders sarcopenia a risk factor for HE in patients with cirrhosis [149]. In the brain, the production of glutamine is the only possible metabolic fate of ammonia due to the absence of an urea cycle (although this theory has been recently challenged [150]).

In the case of cirrhosis, the urea cycle in the liver is down-regulated. Ammonia accumulates in the bloodstream and leads to systemic inflammation with an accumulation of pro-inflammatory cytokines, bilirubin, lactate, bile acids and reactive oxygen species (ROS) in the blood [151, 139]. These factors compromise the integrity and function of the blood brain barrier (BBB) [152]. Consequently, ammonia in excess enters the brain and is detoxified via its conversion into Gln in the astrocytes. Glutamine excessive production is also believed to be neurotoxic [153], and possibly responsible for the mitochondrial dysfunctions observed in HE [154]. In type A HE, the glutamine increase is fast, leading to cytotoxic brain edema with Alzheimer type 2 astrocytosis [155]. In type C HE, the glutamine increase is slower and partially compensated by a release of the metabolites playing an osmotic role (myo-inositol, taurine and choline), as shown for the first time in patients in 1990 [143] and confirmed later on by many studies in humans and animal models, including in our group [136]. The presence

of edema in type C HE is still controversial [156, 132]. The gradual change in metabolite content (increased brain Gln and decreased brain osmolytes), sign of osmotic stress, can be interpreted as low-grade edema eventually leading lead to cellular microstructure alterations despite osmoregulation mechanisms. A decrease in glutamate, produced from glutamine in the neurons, is observed in both type A and type C HE, and is attributed to alterations of glutamate metabolism and/or transport [157]. Other consequences of ammonia toxicity on the brain have been reported: pH and mitochondrial membrane potential changes [158], impaired neurotransmission (both excitatory and inhibitory) [159], impaired α-ketoglutarate dehydrogenase enzyme activity [160], and profound alterations of brain astrocytes and neurons morphology [132]. In the hippocampus of BDL rats, our group observed a change in the shape of astrocytes and neurons: astrocytes were more numerous, but shorter and with fewer ramifications [136] and CA1 neurons had a increased soma size with decreased dendritic (basal and apical) spines density compared to control rats (unpublished data), as shown in **Figure 3.2**. However, histology staining requires sample fixation which can alter the tissue structure and these observations have so far not been confirmed in vivo.

In this context, the first central aim of this thesis was to implement and optimize in vivo diffusion-weighted MRS to probe these cell-specific microstructural changes non-invasively in the BDL rat model of type C HE.

3.5 Energy metabolism and other debated mechanisms

Other mechanisms that play an important role in HE pathophysiology are current topics of investigation [161]: energy metabolism, inflammation, oxidative stress, the three which will be detailed in this section, but also manganese deposition [162], and alterations of the intestinal microbiota [163], to list a few.

An overview of our current understanding of HE pathophysiology in presented in **Figure 3.3**.

- inflammation and oxidative stress: systemic inflammation is observed in a vast majority of patients with ALF [133] and CLD [164]. It is believed that microglial activation in the brain is mediated either through blood inflammatory markers (TNF-α and interleukines) binding to the BBB receptors and triggering a cascade of secondary messengers or through ammonia. Neuroinflammation will impair cognition and neurotranmission and cause neuronal death [165]. As a result, the most widespread treatments of HE so far (Lactulose, Rifaximin, L-ornithine-L-aspartate (LOLA), Ornithine phenylacetate) have aimed at decreasing plasma ammonia and/or systemic inflammation. The role of oxidative stress (OS) in the pathophysiology of HE is increasingly acknowledged [166, 167] and is also investigated in our group in BDL rats [168, 139]. CLD leads to

Figure 3.2: Histology of the hippocampus in BDL (week 8 post surgery) and SHAM rats. A) Astrocytes stained with anti-GFAP (red) and DAPI-nuclei (blue)-morphological characterization of the number and length of processes. B) Representative micrographs of Golgi-Cox staining and neuronal morphology analysis of pyramidal CA1 neurons. Data are presented as mean ± SD and statistical significance (Two way Anova with post-hoc Tukey HSD): *$p<0.05$, **$p<0.01$, ***$p<0.001$, ****$p<0.0001$. *Courtesy of Dr. Katarzyna Pierzchala.*

an imbalance in reactive oxygen species (ROS): an increased production linked to the excess of ammonia [169] and/or of glutamine [170], combined with a diminution of the antioxidants who normally act as scavengers of the ROS to restore the redox balance. In particular, albumin, a powerful anti-oxidant secreted by the liver, is decreased in CLD patients [171]. Decrease ascorbate (Asc), a brain anti-oxydant, has been observed in the hippocampus of BDL rats with ^{1}H MRS [136]. In the same animal model, our group recently showed the interplay between inflammation and oxidative stress [139], a cross-talk which was previously linked to neuronal damage and neurodegeneration [172]. In HE, recent evidence suggests that the inflammatory response mediated by brain and systemic cytokines and ammonia will trigger a self-amplifying loop between between astrocyte osmotic stress and cerebral OS and nitrosative stress (NS) [173].

A recent study in female versus male BDL rats (the possible sex-specific response to HE being so far poorly studied) evidenced different responses to overt HE episodes depending on the sex of the animal, tentatively attributed to a difference response
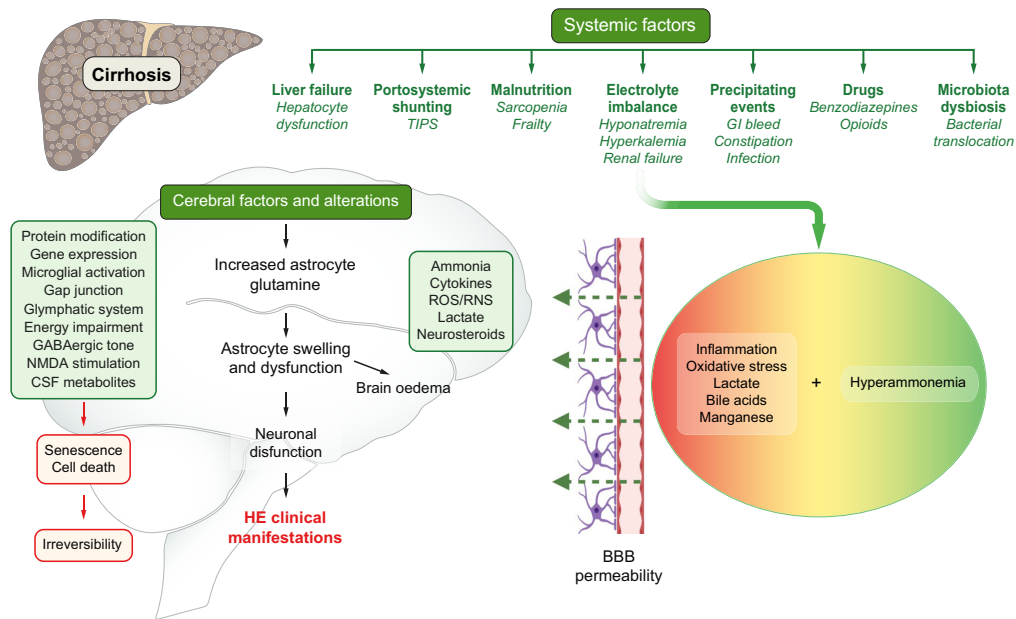
Figure 3.3: Reproduced from Rose et al., "Hepatic encephalopathy: Novel insights into classification, pathophysiology and therapy", *Journal of Hepatology*, 2020 [121]. Pathogenesis and pathophysiology of hepatic encephalopathy. CSF, cerebrospinal fluid; NMDA, N-methyl-D-aspartate; TIPS, transjugular intrahepatic portosystemic shunt.

to oxidative stress [174]. Female BDL rats were naturally protected against overt HE episodes thanks to their higher albumin levels and lower levels of ROS markers compared to male BDL rats. Moreover, female rats did not develop muscle mass loss, brain edema and short term memory impairment compared to female sham-operated rats, where as male BDL rats did compared to male sham-operated rats. Overall these findings shed a new light on the possible sex differences in the vulnerability to HE and its possible link with OS.

• alterations of energy metabolism: references [175] and [176] summarize the findings related to energy metabolism in HE, tightly linked to oxygen metabolism and cerebral blood flow. Autoradiography studies in portacaval-shunted rats report contradictory results in the same animal model: Cruz *et al.* [177] report an increased glucose cerebral metabolic rate (CMR_{glc}), reflecting the very first two steps of glycolysis and glucose uptake, while Jessy *et al.* [178] and Hawkins *et al.* [153] a decreased CMR_{glc}. Human studies focused mostly on patients with minimal HE, where Lockwood *et al.* report a decreased CMR_{glc} measured with ^{18}F fluorodeoxyglucose (^{18}F-FDG) in the cingulate gyrus [179] and in cortical areas, but an increased CMR_{glc} in the cerebellum, thalamus and caudate [180]. A study in cirrhotic patients without over HE also showed brain regional differences but in partial contradiction with Lockwood *et al.*: increased glucose

uptake (as measured from the quantified PET image, not from the compartmental modelling yielding to CMR_{glc}) in the hippocampus and hypometabolism in the parietal, occipital and limbic lobes [181]. In parallel to the observed decreased CMR_{glc} in the cingulate gyrus of HE patients [179], a reduced cerebral blood flow (CBF) was also observed in the same brain region in cirrhotic patients with overt HE [182]. Finally, a clinical case study of a patient with decompensated liver cirrhosis also showed a hypometabolism of glucose in the cerebellum and cerebral cortices [183].

It is argued that a decreased CMR_{glc} is dragged by a decreased demand of glucose from the cells. This could be the consequence of decreased downstream glycolysis requirements (decrease in aerobic or anaerobic glycolysis) and/or of the use of alternative substrates than glucose for energy production. A recent study on cirrhotic patients during an acute HE episode argued that the decreased oxygen metabolism observed in these patients is a consequence of a decreased metabolic demand of the HE brain rather than directly associated with the liver disease, as oxygen metabolism was restored after the acute HE episode [184]. In the BDL rat model, decreased brain oxygenation, together with decreased lactate and glucose concentrations were observed, yet restored after reducing systemic ammonia concentration [185]. Together these results triggered a debate on the origin of decreased oxygen metabolism, be it a consequence of impaired oxygen homeostatis or decreased energetic demand from the brain [186, 187].

The energy metabolites involved in the downstream glycolysis steps have also been investigated in HE, including by our group. In adult BDL rats, we observed no changes in reliably-quantified brain metabolites involved in energy metabolism (lactate, γ adenosine triphosphate (γ-ATP)) using in vivo ^{1}H or ^{31}P MRS [136, 188, 189], except in a recent ^{1}H MRS study where lactate and glucose were found decreased in BDL versus sham-operated rats [185]. The discrepancy may reside in the difficulty to quantify glucose and lactate with standard single voxel ^{1}H MRS sequences (low concentrated and overlapping metabolites). Using carbon 13 (^{13}C) MRS after ^{13}C-labelled glucose (Glc) injection, a steady-state increased Lac pool has been detected in BDL rats with uniformly labelled Glc [190],potentially suggesting a preference for anaerobic glycolysis. No changes in brain mitochondrial fluxes have been measured in the same animal model following [1,6–$^{13}C_2$] Glc injections [191], but studies in cirrhotic patients with HE showed decreased levels of ATP [192, 193].

Given the strong interest and yet unclear answer, the second central aim of this thesis was to investigate in vivo the question of energy metabolism in the BDL rat model. We hypothesized *a posteriori* that the use of a semi-quantitative metric to quantify PET results prevents a fair comparison between animal groups in which systemic metabolism greatly differs. Alternatively, we aimed at providing a fully-quantitative and minimally-invasive method for measuring the CMR_{glc} in small animals using an

image-derived input function and Sokoloff's autoradiography approach [194].

3.6   Outcome

The outcome of HE has long been estimated based on the survival rate after liver transplantation. Nowadays, because of the good success rate of the surgery [195], the outcome has shifted towards evaluating the quality of life of patients after liver transplantation. This shift shed light on the fact that 15% to 45% of the patients still suffer from neurological symptoms after liver transplant, and it is now being hypothesized that the outcome correlates negatively with the number of episodes of overt HE before the transplantation [196]. Additionally, children with HE show irreversible motor and cognitive damages even after liver transplantation [197, 198]. A study in BDL rats in our group confirmed the stronger metabolic changes in the young-operated versus adult-operated BDL rats [137] and showed that the neurometabolic changes in young BDL rats depend on the age at liver disease onset [138]. Taken together, these findings point towards an enhanced vulnerability to CLD leading to HE of the brain under development.

In the light of these observations, the central study of this thesis involving single-voxel MRS and diffusion-weighted MRS/MRI was performed on young BDL rats, where the effect of HE on the developing brain could be studied.

3.7   The role of magnetic resonance spectroscopy (MRS) and positron emission tomography (PET) imaging in the study of HE

The complementary information offered by MRS and PET is schematically represented in **Figure 3.4**.

As can be seen from the introduction chapter and from the study in chapter 4, MRS provides a powerful and versatile tool to study brain metabolism non-invasively. It allows one to probe steady-state pools of metabolites involved in a variety of brain functions, such as osmoregulation (mIns, tCr), neurotransmission (Gln, Glu, GABA), energy metabolism (Lac [Glc is difficult to measure]) or oxidative stress (Asc, GSH). Importantly, at high magnetic fields, Gln and Glu are well resolved on the frequency scale and can thus be quantified separately (not only as the sum Gln+Glu=Glx), enabling us to study their differential role in the development in HE [136, 189]. In vivo longitudinal ^{1}H MRS has been acknowledged as a predictive tool of the early stages of HE in clinical settings [199, 200].

Our group studied longitudinally the metabolic changes occurring in the rat brain after the BDL surgery, both in adult (surgery performed 6 weeks after birth) [136] and young (surgery

performed 21 days after birth) BDL rats [137, 138]. A strong increase in Gln, a decrease in the main osmolytes (Ins, Tau, Cho and tCr), overall stronger in young than adults rats have been observed. Ascorbate, which is an anti-oxidant and is also involved in energy metabolism, also decreased in young and adult BDL rats versus control rats. In adult BDL rats, the Gln increase was also stronger in the cerebellum than in the hippocampus and in the striatum [201]. Taken together, these results suggest a differential effect with the brain region and with the brain development stage.

If, in addition, the MRS signal is weighted by diffusion, cell-specific microstructural information can be derived. This is also of particular interest in the study of HE because most studies so far have focused on brain edema and astrocyte swelling, which might only be a limited view of cellular alterations occurring in HE.

^{18}F-FDG PET holds the promise of proving a complementary dynamic information on local brain glucose uptake and thus uniquely inform on energy metabolism in HE. Details about the information provided by this imaging modality and methodological implementations will be presented in chapter 7. Because the FDG uptaken from the blood is converted on FDG-6-phosphate but not further metabolized into glycolysis [194], the FDG PET signal at labelling steady-state reflects the very first two steps of glycolysis. Provided that the FDG input function is accessible, this metabolic information can be extracted in a quantative manner.

To the best of our knowledge, FDG PET had never been employed in BDL rats before the work presented in this thesis, and it holds the promise of shedding new light on energy metabolism alterations in HE.
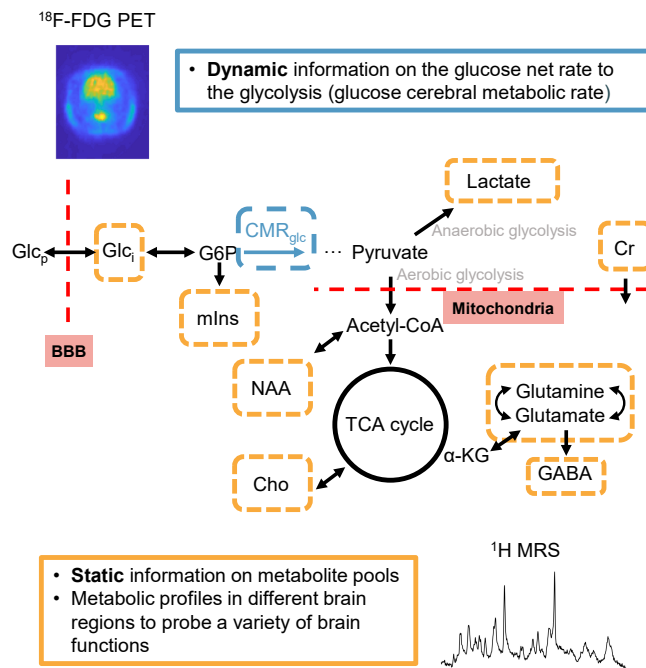
Figure 3.4: Complementary value of PET and ^{1}H MRS in the study of HE. Whereas PET probes the specific information of glucose dynamic rate to glycolysis, MRS provides a broader information on pools of metabolites involved in a variety of the brain functions and active at different stages of the glycolysis, and whose concentrations might vary between different cells or cellular compartments. α-KG: α-ketoglutaric acid, BBB: blood brain barrier, Cho: choline, Cr: creatine, GABA: γ-aminobutyric acid, Glc$_i$: intracellular glucose, Glc$_p$: plasma glucose , G6P: glucose 6-phosphate, mIns: myo-inositol, NAA: N-acetylaspartate.

Study of microstructure with diffusion-weighted MR

Part II

4 Diffusion-weighted MR in HE

Abstract

Type C hepatic encephalopathy (HE) is a severe brain condition arising from chronic liver disease. While adults often recover from HE after liver transplantation, children suffer from irreversible cognitive damage. As such, exploring both the adult and the developing brain longitudinally at the preclinical level is necessary for improving our understanding of the pathophysiology of HE. To date, it remains unclear how the increased osmotic pressure triggered by Gln accumulation in type C HE alters the morphology of brain cells, and dMRI and dMRS could offer a new perspective on this question.

In the present study, a rat model of type C HE (the bile duct-ligated (BDL) rat model) where the disease induction is performed either on adult rats (> 6 weeks after birth) or on pups (21 days after birth, p21) was used. The animals were scanned in the cerebellum, a region of particular interest in HE as it was shown to be more vulnerable to the increase in Gln than the hippocampus and the striatum. Single-voxel MRS acquisitions were performed with the STEAM sequence (TE = 3 ms, TM = 10 ms), the dMRS acquisitions with the STE-LASER sequence (Δ = 60 ms, δ = 3 ms, b_{max} = 15 ms/μm^2) and the dMRI acquisitions with a multi-shell spin echo EPI sequence (Δ = 12 ms, δ = 4 ms, b_{max} = 8 ms/μm^2, # directions: 12-60). The randomly oriented sticks model was used for dMRS, and SANDI and standard model for dMRI grey matter and white matter, respectively. Combining diffusion MRS and diffusion MRI with matter-specific biophysical modelling, we measured increased metabolites' diffusivities, especially of osmolytes (mIns, Tau) and glial markers (Gln), as well as an increased intra-neurite/axon water diffusivity in white and grey matter in the cerebellum of HE animals compared to control rats. These results suggest an alteration of cell density and/or of neurite network complexity, confirming the changes observed with post-mortem immuno-histochemistry. This study highlights that dMRS and dMRI are valuable and sensitive tools to study brain microstructure in HE, with the additional cell-specificity offered by dMRS, and holds the promise of reorienting the debate from the restrictive hypothesis of astrocytes swelling to the wider hypothesis of complex multi-cellular microstructure alterations in type C HE.

Publications

This work is partially adapted the following two ISMRM abstracts, for which a journal publication is in preparation:

[202]: **J. Mosso**, J. Valette, K. Pierzchala, D. Simicic, I. O. Jelescu, and C. Cudalbu, "Diffusion-weighted magnetic resonance spectroscopy in the cerebellum of a rat model of hepatic encephalopathy at 14.1T," in *Proc. Intl. Soc. Mag. Reson. Med. 29*, 2021. - **oral presentation - Magma Cum Laude award**.

[203]: **J. Mosso**, M. Rey, D. Simicic, K. Pierzchala, I.O. Jelescu, and C. Cudalbu, "Diffusion MRI and MRS probe cerebellar microstructure alterations in the rat developing brain during hepatic encephalopathy," in *Proc. Intl. Soc. Mag. Reson. Med. 30*, 2022. - **oral presentation**.

This work led to an authorship contribution in the following two reviews:

[132]: K. Pierzchala, A. Hadjihambi, **J. Mosso**, R. Jalan, C. Rose, C. Cudalbu. "Lessons on brain edema in HE: from cellular to animal models and clinical studies," *Metabolic Brain Disease* (2023) https://doi.org/10.1007/s11011-023-01269-5.

[80]: C. Ligneul, C. Najac, A. Döring, C. Beaulieu, F. Branzoli, W. T. Clarke, C. Cudalbu, G. Genovese, S. Jbabdi, I. Jelescu, D. Karampinos, R. Kreis, H. Lundell, M. Marjanska, H. E. Möller, **J. Mosso**, E. Mougel, S. Posse, S. Ruschke, K. Simsek, F. Szczepankiewicz, A. Tal, C. Tax, G. Oeltzschner, M. Palombo, I. Ronen, and J. Valette, "Diffusion-weighted MR spectroscopy: consensus, recommendations and resources from acquisition to modelling," accepted in *Magnetic Resonance in Medecine* (2024) https://doi.org/10.1002/mrm.29877.

The sub-project on exchange led to a conference abstract:

[204]: **J. Mosso**, M. Chan, M. Rey, I. O. Jelescu, C. Cudalbu, "Exploiting dual diffusion MRS and MRI acquisitions in the rat cerebellum at 14.1 T: a measurement of intra-extracellular water exchange," MRS Workshop 2022.

Contributions

I contributed to the optimization of MRS protocols on the new Bruker console (formerly Varian) and to the conversion of the STE-LASER sequence (given to us by Julien Valette in Paravision 6) to Paravision 360 with Dunja Simicic and Cristina Cudalbu. I then performed independently the optimization of the dMRS/dMRI protocols, data acquisition, data analysis and modelling. The histology was performed by Katarzyna Pierzchala and Dario Sessa. BDL surgeries were performed by Stefanita Mitrea and Dario Sessa. I designed the study on exchange, implemented with two master students, Mickael Rey and Michael Chan, whom I supervised independently.

The **first part** of this chapter will present the preliminary study performed in adult BDL rats and its limitations. From these limitations, conclusions were drawn on how to improve the acquisition, leading to the development of the second study and to the **following chapter**. The **second part** of this chapter will present the optimized study in young BDL rats, combined with dMRI and histology. The study on water exchange will be briefly presented in a **third part**.

4.1   Introduction

The pathophysiology of type C HE as well as the potential of diffusion-weighted MR to study microstructural alterations in the HE brain have been presented in the introduction chapters. Briefly, HE is characterized by a strong increase in brain glutamine following toxic accumulation of ammonia in the blood and in the brain. The excessive concentration of ammonia and glutamine triggers a cascade of metabolic, structural and functional damages of the brain which are not fully understood yet.

Mounting evidence suggests that children are more vulnerable to irreversible neurological damages associated with CLD than adults, even after liver transplantation [197, 198]. This finding echoes observations in a rat model of type C HE, where the neurometabolic changes (increased Gln, decreased osmolytes) in the hippocampus were stronger in the developing brain than in the adult brain [137, 136], and dependent on the age at liver disease onset, something our group studied in details [138].

In that context, it remains unclear how brain cells react to the Gln load, especially in type C HE, where the metabolic changes are gradual and partially compensated by a release of osmotic metabolites. Past studies in type C HE have focused on brain edema (increased water content) and its origin (intra or extracellular), but the presence of an uncompensated net water increase in type C HE has later been challenged [156, 132], also due to the difficulties of its measurement in vivo. It has also been postulated that HE is the clinical manifestation of astrocytes swelling and/or "Alzheimer type II astrocytosis" due to increased osmotic pressure triggered by Gln accumulation, driving water into the cells. Although the pathological role of astrocytes in animal models and humans with severe hyperammonemia and liver failure has been confirmed, it has also become clear that additional cell types in the brain are also involved in the pathogenesis of HE. For example, changes in cerebellar neurons (Purkinje cells) shape have been reported by our group in the BDL rat model of type C HE using post-mortem immuno-histochemistry stainings [136, 139], but in vivo confirmations of these findings are still required. Diffusion-weighted MRS and MRI could offer a powerful tool to study these alterations non-invasively in the context of HE.

In parallel, in animal studies using the BDL rat model of type C HE, the cerebellum has shown stronger metabolic changes (Gln increase and osmotic response measured by ^{1}H MRS) compared to hippocampus and striatum [201], underlining its crucial role in the disease development. The cerebellum is a brain region involved in motion, coordination, working and procedural memory [205]. In cirrhotic patients, the cerebellum exhibits reduced blood flow and gray matter volume [206], increased vulnerability to neuroinflammation even at early stages of the liver disease [207], and increased ammonia uptake [208]. Yet, it remains challenging for MRS investigation due to the presence of fat and macroscopic motion caused

by the respiration. From an imaging standpoint, its complex and unique structure, divided in three layers (molecular, Purkinje cell and granular layers, all containing specific types of neurons and glial cells) with a core of white matter, enforces the need for comprehensive acquisition and modelling schemes.

The **aim** of the present work was to perform a first in vivo longitudinal study of microstructural alterations in the cerebellum of the adult and developing brain during type C HE. Using dMRS and dMRI with matter- and cell-specific biophysical modelling, we investigated water and metabolites diffusion properties in the BDL rat model of type C HE at ultra-high field (14.1T), and linked these properties to astrocytic and neuronal microstructural changes observed ex vivo by histology. Joint information from in vivo dMRS and dMRI presented here will shed new light on the complex, multi-cellular microstructure alterations occurring in HE, beyond the simplistic view of edema and astrocyte swelling.

4.2   *Preliminary study*: **Diffusion-weighted MR in adult BDL rats**

We first performed a preliminary dMRS study in the cerebellum of adult BDL rats at 14.1T. This allowed us to implement and validate the STE-LASER sequence, and it constituted overall the first study with dMRS in a rat model of HE. We used the observations from this preliminary study to improve the methodology for the second study on young BDL rats.

4.2.1   Methods

The methods for this chapter will be presented in more details in section 4.4.1. This section will highlight the elements that were improved for the second study on young BDL rats (denoted as [**problem n**]).

The STE-LASER sequence (given to us by Dr Julien Valette) was first converted from Paravision 6 (Bruker's software) to Paravision 360 on our 14.1T scanner and calibrated as described in sections 1.8.4 and 1.5.6 of the introduction chapter. It was then validated in a multi-metabolite phantom containing alanine, asparate, Cr, GABA, Gln, Glu, GSH, Lac, mIns, NAA, PCho, PCr and Tau with concentration ratios mimicking in vivo ones. The following acquisitions parameters were used: TE = 33.7 ms, TR = 4000 ms, duration of diffusion gradients δ = 3 ms, diffusion time Δ = 43.4 ms, b-values: 0.05, 0.1, 0.3, 0.5, 1, 1.5, 2, 2.5, 3, 3.5 and 4 ms/μm^2, with a number of shot NS = 16 for b $\leq$ 1 ms/μm^2 and NS = 32 for b > 1 ms/μm^2. The spectra were quantified with LCModel as described in details in section 4.4.1.

All in vivo experiments were approved by The Committee on Animal Experimentation for the Canton de Vaud, Switzerland (VD3022.1). For this preliminary study, the BDL rat model

for CLD-induced HE [135] was used (N=5 BDL, N=6 sham-operated rats, undergoing the anaesthesia and a placebo surgery where the bile duct ligation is not performed) on male adult ($\approx$ 200 g at surgery [**problem 1**]) Wistar rats (Charles River Laboratories, France). The animals were scanned at week 6 post-surgery on a 14.1T scanner with a quadrature transmit/receive surface coil located over the cerebellum (voxel size: 30-78 μL [**problem 2**]).

The STE-LASER sequence [83] was used for the dMRS acquisitions, with the following timings: TE_{STE} = 8.7 ms (echo time of the stimulated echo block, in pink in **Figure 2.8**), TE_{LASER} = 25 ms (echo time of the LASER block, in green in **Figure 2.8**), TR = 2000 ms [**problem 3**], duration of diffusion gradients δ = 3 ms, diffusion time Δ = 63.4 ms (characteristic 1D diffusion length of $\approx$ 4.2 μm, for $D_{0,met}$ = 0.15 μm^2/ms). The maximum spoiler strength around the 180° in the LASER module was set to 20% of 1 T/m, i.e. to 200 mT/m and no OVS were used [**problem 4**]. The b-values, where the diffusion gradient was applied in the direction (1,1,1), with their respective number of shots, were: 0.05 (320 shots), 0.1 (320), 0.5 (320), 1 (320), 3 (320), 5 (320), 15 ms/μm^2 (608). Spectra were corrected for eddy currents with a non-water suppressed reference scan was acquired for ECC and an initial B_0 drift compensation was performed on the scanner with a navigator. For preprocessing, blocks of 8 consecutive shots were created [**problem 5**].

Corrections for phase distortions (value such that the metabolite area under curve on the real part of the spectrum is maximized, for each block sequentially) and B_0 drifts (aligning the NAA peak maximum amplitude on the real part of the spectrum, for each block sequentially) were performed [**problem 6**].

Metabolites were quantified with LCModel (see details procedure in section 4.4.1) and a macromolecule spectrum, acquired previously with a short TE sequence (SPECIAL, TE = 2.8 ms) in one healthy animal, was used [**problem 7**]. Quality control at each b-value based on relative CRLBs ($< 40\%$) was applied [**problem 8**]. The metabolite signal decay from the individual animals were normalized to one and group-averaged [**problem 9**].

A mono-exponential decay was fitted to the normalized decays up to b = 5 ms/μm^2. The spectra at b = 15 ms/μm^2 were discarded due to low SNR. The SD on the ADC estimates was assessed by generating and fitting 100 times the group-averaged signal decay with different noise generations, where the noise was chosen as the standard deviation of the difference between the group-averaged signal decay and the best fit [**problem 10**]. The ADC estimates between the groups were compared with a Student t-test.

4.2.2 Results

The STE-LASER sequence was first validated in a phantom (**Figure 4.1**). The sequence yielded good quantification of the in vitro diffusion decays: $\ln(S/S_0)$ was linear with the b-value, as expected for free diffusion. Moreover, we checked that the metabolites' free diffusion
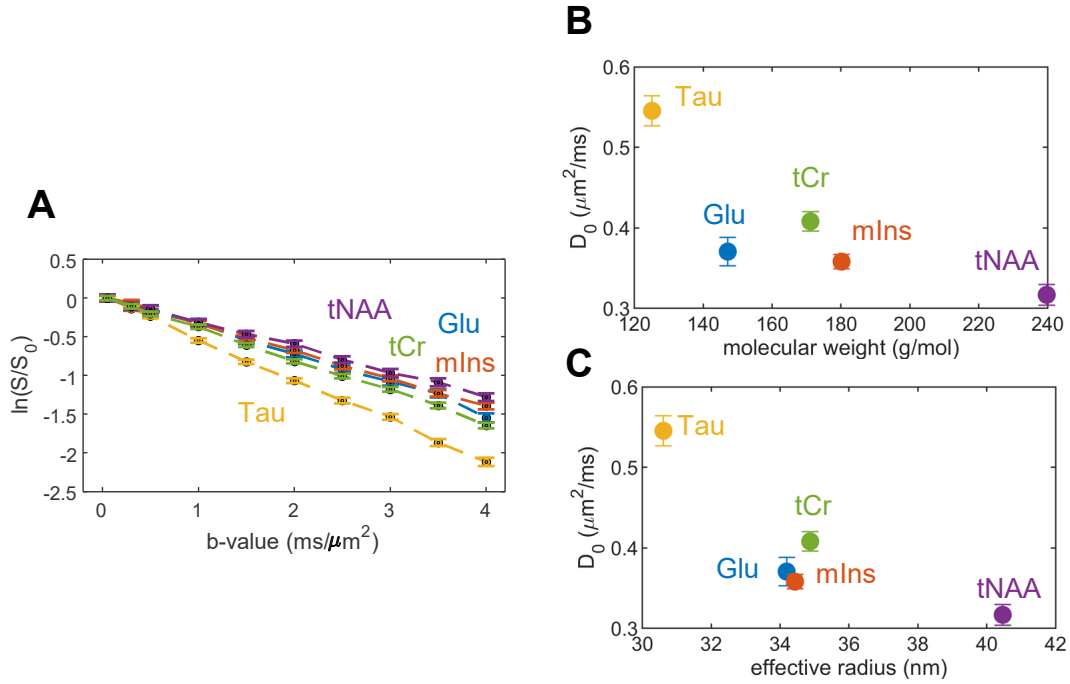
Figure 4.1: Diffusion decays (**A**) and coefficients of well-quantified metabolites measured in a multi-metabolite phantom at $\approx 15°C$ after LCModel quantification, as a function of the molecular weight (**B**) or of the effective radius r (**C**) of the corresponding metabolite. The natural logarithm of S/S_0 shows a linear trend with b-value (Gaussian diffusion). The diffusion coefficients approximately scale inversely with the effective radius (**C**) but not so well with the molecular weight (**B**), which is predicted by the Einstein-Stokes relation: $D_0 = \frac{k_B T}{6\pi\eta r}$. Here the effective radius was approximated for a sphere as $r = \left(\frac{3M}{4\pi\rho N_A}\right)^{1/3}$, where M is the molar mass, ρ the density and N_A the Avogadro constant.

coefficients D_0 obeyed the Einstein-Stokes relation: $D_0 = \frac{k_B T}{6\pi\eta r}$ (also given in equation 2.1). This was indeed the case as can be seen in **Figure 4.1C**: the diffusion coefficients scale inversely with the effective radius of the metabolite. Interesting, the diffusion coefficients do not scale as linearly with the molecular weight (**Figure 4.1B**), because it overlooks the volume occupied by the molecule, also affecting its motion.

An example of in vivo spectra is shown in **Figure 4.2A**. The spectral quality dropped from b = 5 ms/μm^2 onwards, and few animals could be used for b = 15 ms/μm^2 (missing values for Tau for example on **Figure 4.2B**), resulting in a poor quality of the individual animal signal decays. Despite this poor quality, the in vivo apparent diffusion coefficients (ADC) fitted on the averaged signal decay up to b = 5 ms/μm^2 (**Figure 4.2**) are in good agreement with literature [59]. The ADC were higher in BDL rats compared to sham rats for all metabolites (significant for Glu, Tau and tNAA).
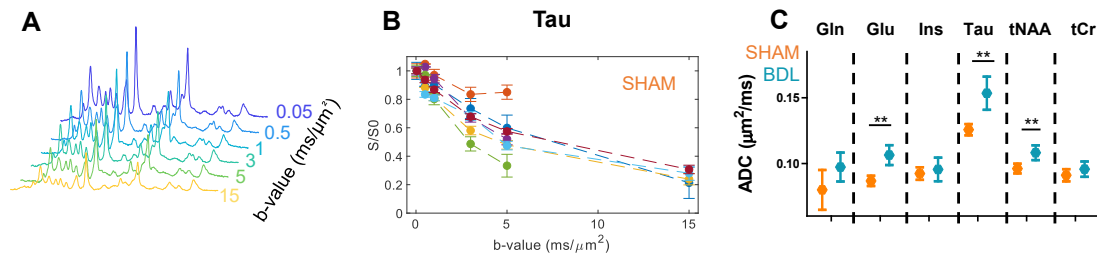
Figure 4.2: Representative diffusion set in one animal (5 Hz LB for display) (**A**), overlap of the Tau diffusion decays for all the SHAM rats (**B**) and estimated ADC from a mono-exponential fit up to b = 5 ms/μm² for six metabolites (**C**). Cr+PCr=tCr, NAA+NAAG=tNAA. On panel **B**, the concentrations at certain b-values are not displayed because they were below the quality threshold (40% relative CRLB). The error bars are the absolute CRLB. On panel **C**, the error bars are the standard deviation from Monte Carlo simulations (noise: standard deviation in the difference between mean and best fit). Student t-test for the mean ADC between groups: * p<0.05, ** p<0.01, *** p<0.001.

4.3 Take-home messages from the preliminary study

From these first experiments, several problems were identified and further improved for the next study in section 4.4:

- **problem 1**: the first difficulty we faced was associated with the weight of the animal. Adult rats are heavier than young rats at all timepoints (i.e. before surgery and also 6 weeks post BDL surgery). Heavier rats have more fat around the neck resulting in more difficulties for the coil to be positioned close to the cerebellum. In addition, extra fat leads to more loading of the coil and higher power required for the pulses. In that case, it was important to make sure that the power of the adiabatic pulses was well calibrated. Magnetic susceptibility boundaries specific to the cerebellum and the proximity with a fat region prone to motion due to respiration led to a worse shim in heavy rats. Although not mentioned here, some preliminary dMRI acquisitions were performed on adult rats, also with some difficulties. We hypothesized that the worse shim and possible motion close to the neck led to distortions in the EPI readout, that were solved once working on smaller animals.

- **problem 2**: the second problem was the size of the voxel that was initially too small (and which was increased in the middle of the study). Specifically important for dMRS acquisitions, the single shot SNR should be high enough so that phase and frequency drift corrections can be performed between single shots. In the next study, the voxel size was increased to 93 μL.

- **problem 3**: a short TR (2 s) with an increased number of shots was used since this

combination provided a higher SNR for a given acquisition time (see **Figure 4.3**, for tCr with a T_1 of 1.3 s at 14.1T [82], the TR that maximizes the total SNR was found to be around 1.6 s). For dMRS acquisitions, it is not necessary to ensure that the magnetization has fully recovered to its equilibrium value at each TR (i.e, it is not necessary to be quantitative with TR $\approx$ 5 T_1 [5]). The scaling caused by an incomplete T_1 recovery will be applied identically to all the spectra at all the b-values. However, again specific to dMRS, it is fundamental to have enough SNR on a single shot to perform the phase and B_0 drift corrections. This is in practise achieved by a higher TR (3 s used in the next study), even if it reduces the overall SNR for a given acquisition time. An insufficient single shot SNR will lead to incoherent summation, with an even stronger effect at high b-values, and bias the diffusion coefficients estimation.

- **problem 4**: no OVS were used in the STE-LASER sequence, as they can in general be omitted with the LASER localization due to a good volume selection of the six adiabatic pulses [20, 8] . We noticed however strong spurious echoes in the water region and around 1 ppm (**Figure 4.4B**). The appearance of single shots needs to be investigated since the corruption was not immediately clear on the summed spectrum which appears of fairly good quality (**Figure 4.4A**). As such, OVS were added in the next study and the maximum spoiler strength increased to 600 mT/m. Of note, a too strong spoiling will cause an additional diffusion-weighting around each 180° pulse (for a spoiler of 600 mT/m during 1 ms around each 180° pulse lasting for 2 ms, an additional b = 0.04 ms/μm^2 per pulse is created). It will cause a constant offset for all b-values and will not bias the estimation of the diffusivities but will lead to a lower SNR: the spoilers strength increase should thus be limited to the minimum value that removes spurious echoes.

- **problem 5**: because of the low SNR on single shot at TR = 2 s, blocks of eight consecutive shots were created first, and corrections were applied between the blocks (**Figure 4.4C** and **D**). This was a consequence of **problems 2** and **3** that led to partially incoherent (within each block) averaging.

- **problem 6**: the phase and frequency drift correction procedures were suboptimal. Indeed, for the phase correction, maximizing the area under curve can lead to errors at low SNR. For the frequency correction, aligning the spectra based on the amplitude of one peak can make this peak artificially narrow. In the next study, the pre-processing was done following the consensus on preprocessing for MRS data [27] using spectral registration [32] in FID-A [28] where the phase and frequency are corrected simultaneously.

- **problem 7**: the initial macromolecules spectrum included in the basis-set was acquired previously, with a different sequence, at a different TE and in a different brain region. Because the macromolecule resonances have short and different T_2 [35, 34], a sequence with a TE = 2.8 ms or 33 ms for the STE-LASER makes a difference in the MM pattern and

can bias the overlapping metabolite concentration estimates. Further details about the MM acquisition and validation of residual metabolite removal can be found in chapter 5, section 5.2.4. In the next study, the MM spectrum was acquired with the STE-LASER in the cerebellum in one healthy animal.

- **problem 8**: the exclusion criterion of removing individual concentrations when their relative CRLB is below 40% is debatable. First, this might create an artificial shift towards higher concentrations in the average at high b-values (the low concentrations being removed), as reported for MRS [209], and thus bias the diffusion coefficient estimates. Second, if instead of removing individual concentrations, the metabolites reaching a CRLB of 40% for at least one of the b-values are removed as a whole, this also led to a problem. The selection of reported metabolites will then be biased towards the high concentrated and the slow diffusing ones, the low concentrated or fast diffusing metabolites being more likely to reach this criterion at high b-values. In the next study, the quality filtering was applied on the first b-value only.

- **problem 9**: because of all the difficulties mentioned above, the individual animal diffusion decays were not of sufficient quality as to allow for the diffusion coefficient to be fitted on each decay separately (see **Figure 4.2B**). Instead, they were averaged and one diffusion coefficient was fitted on the averaged decay. Although this lead to coherent ADC values (**Figure 4.2C**, similar to [59]), it hampered the estimation of the error on the ADC, which does not represent the group dispersion. When enabled by a good data quality, the fit should be performed on individual animal decays. In the next study, individual animal fitting was made possible with the improvements listed above. The estimation of diffusion metrics on individual decays were found to be in good agreement with the mean fit.

- **problem 10**: the error on the diffusion coefficient was estimated based on a Monte Carlo study, where the noise was set to the difference between the mean decay and the best fit. This informs on the agreement between the model and the data rather than on the group dispersion, the latter being meaningful, especially in the BDL group. Therefore, in the next study, the noise of the Monte Carlo study was set to the SD of the group concentrations at each b-values.

In addition to the above-listed technical problems, the diffusion decay of glutamine was poorly estimated compared to the ones of the other reported metabolites. This was unfortunate because of its great importance in the study of HE. We hypothesized that, because Gln has strong J-coupling constants (up to 15 Hz), the long echo time of STE-LASER impaired its quantification due to J-evolution (and T_2 relaxation). From the basis-set simulations in NMRScope-B, we compared the shape of Gln obtained with the STE-LASER (TE = 8.7 + 25 ms,
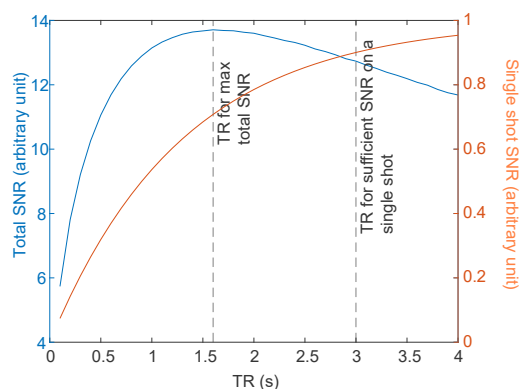
Figure 4.3: Total SNR (left axis) and single shot SNR (right axis) as a function of the repetition time TR, for a fixed acquisition time of 10 min, considering only the effect of T_1. The total SNR is proportional to $(1 - \exp(-TR/T_1)) \times \sqrt{NS}$ = single shot SNR $\times \sqrt{NS}$ where $NS = \frac{\text{acquisition time}}{TR}$ [5]. T_1 = 1.3 s was used (value for tCr at 3.03 ppm in [82]), with a varying TR. The TR that maximizes the overall SNR is found around 1.6 s, and the one used to in the next study to ensure sufficient SNR on single shots is 3 s (black lines).
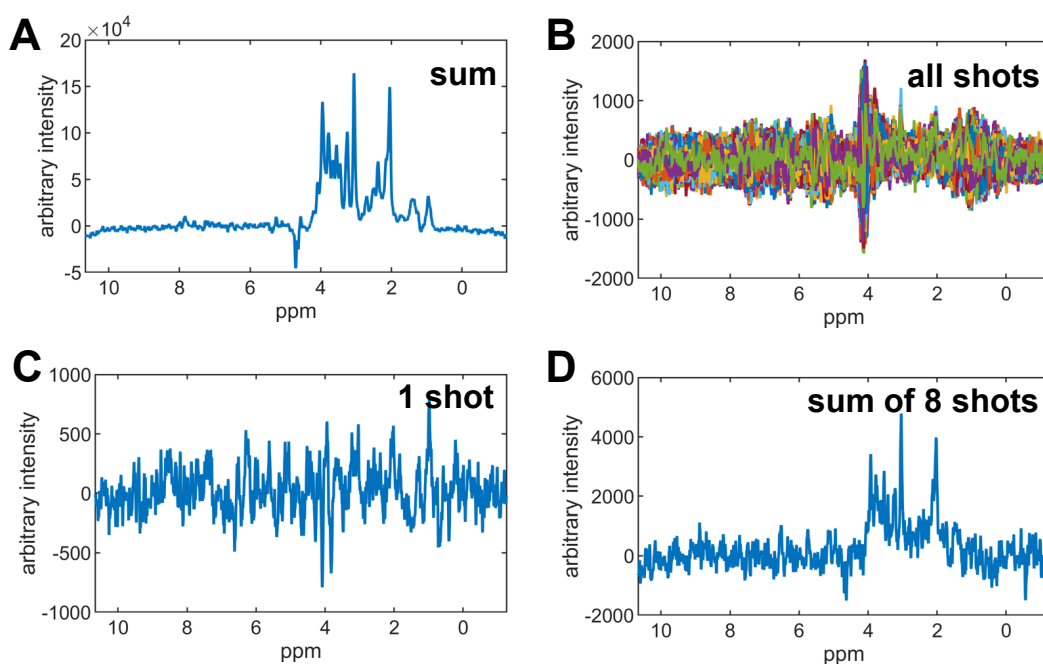
Figure 4.4: Representative spectrum acquired at a low b-value (0.05 ms/μm^2), as the sum of the non-corrected 320 shots (**A**), as the overlap of the non-corrected 320 shots (**B**). A single shot is display in **C** and the sum of eight consecutive non-corrected shots in **D**. Strong spurious echoes can be observed in panel **B** close to the water region at ≈ 4 ppm and around 1 ppm. The single shot SNR (panel **C**) was insufficient and blocks of 8 shots (panel **D**) had be to constructed first to apply frequency and phase corrections.

8.7 ms being the echo time of the STE diffusion block and 25 ms the one of the LASER block) and with a STEAM sequence with the same echo time as the STE part in STE-LASER (TE = 8.7 ms, **Figure 4.5**). The basis set was generated with exact timings and pulse shapes but no relaxation (more details given in 4.4.1 and a representation of the metabolites of the basis set fitted with LCModel is shown in **Figure 1.15** of the introduction chapter). The addition of the LASER localization creates significant additional loss by J-evolution, despite the reduced apparent J-evolution and T_2 relaxation known for trains of adiabatic pulses [15, 16]. **From this observation, we proposed a new diffusion-weighted MRS sequence, based on the SPECIAL instead of the LASER localisation to reduce the TE, with the initial aim of improving the diffusion decay of Gln. The DW-SPECIAL sequence will be presented in the next chapter.**
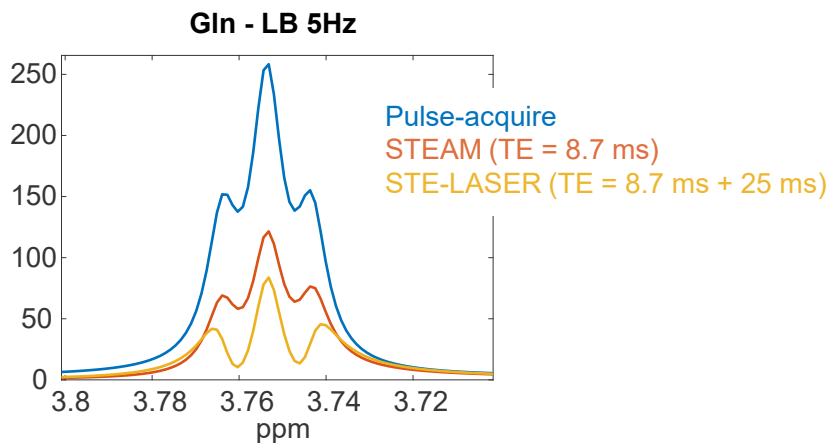
Figure 4.5: NMRScope-B simulation of Gln, zoomed on its resonance at 3.75 ppm, with a pulse-acquire sequence (blue), a STEAM sequence with the same echo time as the STE part of the STE-LASER sequence ((TE = 8.7 ms, orange), and with the full STE-LASER sequence ((TE = 8.7 + 25 ms, yellow). Exact pulse shapes and delays were used, but no relaxation. Half-signal loss is observed in STEAM compared to the pulse-acquire sequence as expected (orange versus blue). The additional loss due to J-evolution during the LASER part is manifest (yellow versus orange).

4.4 Diffusion-weighted MR in young BDL rats

4.4.1 Methods

Animals

All experiments were approved by The Committee on Animal Experimentation for the Canton de Vaud, Switzerland (VD2761.1). The BDL rat model for CLD-induced HE [135] was used on young male Wistar rats (surgery performed 21 days after birth at $\approx$ 50 g; Charles River

Laboratories, France). The rat brain development stage at p21 corresponds, for the human brain development, to a 8-month old infant approximately (details and sources found in ref. [137]). Plasma bilirubin, aspartate aminotransferase (AST/GOT), alanine aminotransferase (ALT/GPT) (Reflotron Plus analyzer, Roche, Switzerland), blood ammonia (PocketChem BA, Arkray, Japan) and blood glucose (Contour XT, Bayer, Germany) were measured from the sublingual vein longitudinally at weeks 4 and 6 in BDL and sham rats (undergoing anaesthesia and a placebo surgery where the bile duct ligation is not performed) to follow the disease progression. BDL rats were compared to sham rats at the same age to account for the effect of normal brain development. In this study, blood samplings, dMRS, dMRI, and histology were performed on the same animals.
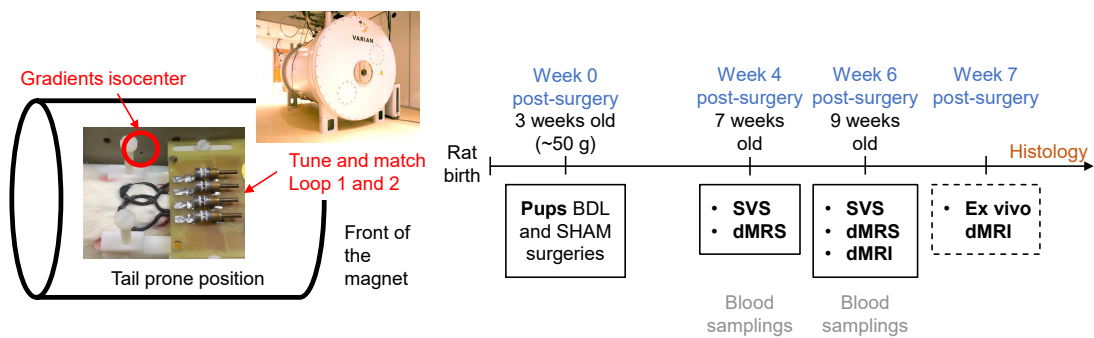
Figure 4.6: Study design. The position of the animal and of the coil in the holder is shown on the left. The surgeries are performed at p21 (3-week old rats), which corresponds to a 8-month old infant [137]. The same animals were used for blood samplings, dMRS, in vivo/ex vivo dMRI and histology. SVS: single-voxel MRS. Ex vivo dMRI results will be presented in the perspectives only (section 4.7), as they require further investigation.

Single-voxel MRS and dMRS acquisitions

Each MRS complex free induction decay (FID) is referred to as a *shot* [30] in the current section. BDL and sham-operated groups were scanned 4 and 6 weeks post-surgery (study design presented in **Figure 4.6**) on a 14.1T scanner (Varian/Magnex Scientific magnet, Bruker console (Avance Neo, Paravision 360 v1.1)) with a gradient system of 1 T/m and a rise time of 270 µs. A homemade transmit/receive quadrature surface coil (loop diameter ≈ 2 cm, **Figure 4.6**) was positioned above the cerebellum (voxel size: 93 µL). Isoflurane anaesthesia (≈ 1.5%, in a 50%/50% air/O_2 mix, 0.9 L/min) was used. Strict monitoring of the respiration rate (65 resp/min) and of body temperature at 37.7°C (SA Instruments, New York, NY, USA) were ensured. The reference power was adjusted on a 2 mm slab close to the skull (typical value 0.03 W for a square 90° pulse of 1 ms adjusted with a Gauss pulse). For a given acquisition, if the reference power exceeded this value by more than 25%, the power of the adiabatic pulses was also adjusted. A localizer multi-slice (FLASH sequence) and a T2-turbo RARE sequence

were acquired first to position the voxel and the shimming region (Localizer multi-slice - 25×25 mm^2 FOV, 98×98 µm^2 in-plane resolution, 10 slices/direction, 0.8 mm slice thickness (1 mm gap), TE/TR: 2.92/18 ms, 1 average and T$_2$-turbo RARE sequence - 16×16 mm^2 FOV, 63×63 µm^2 in-plane resolution, 10 axial slices, 0.8 mm slice thickness (0.2 mm gap), RARE factor 6, TE/TR: 27/3000 ms, 2 averages). Bruker MAPSHIM method was used for first and second order shimming, followed by local iterative first order shimming in the MRS voxel (22-27 Hz water linewidth). The STEAM sequence was used for single-voxel MRS (TE/TM/TR = 3/10/4000 ms, 192 shots, week 4: N=4 sham, N=11 BDL, week 6: N=9 sham, N=6 BDL). The STE-LASER sequence [83] was used for dMRS acquisitions (sham week 4 and 6 combined N=10, week 4: N=10 BDL, week 6: N=6 BDL). For dMRS, the following timings were used: TE$_{STE}$ = 8.7 ms (echo time of the stimulated echo block, in pink in **Figure 2.8**), TE$_{LASER}$ = 25 ms (echo time of the LASER block, in green in **Figure 2.8**), TR = 3500 ms, duration of diffusion gradients δ = 3 ms, diffusion time Δ = 63.4 ms (characteristic 1D diffusion length of $\approx$ 4.2 µm, for D$_{0,met}$ = 0.15 µm^2/ms). The b-values, with the diffusion gradient applied in the direction (1,1,1), with their respective number of shots, were: 0.1 (320 shots), 0.5 (320), 1 (320), 3 (320), 5 (320), 10 (512), 15 ms/µm^2 (640). 4096 complex points and 7142 Hz of spectral width were used. The RF carrier frequency for excitation was centred at 3 ppm for the water-suppressed shots. The VAPOR water suppression module [210] (pulse bandwidth: 350 Hz, last delay: 22.8 ms, flip angles: 84°/150°) was optimized and interleaved with outer volume suppression (OVS) pulses (slab thickness: 12 mm, gap to voxel: 0.3 mm, sech pulse (1 ms), gradients (x/y/z: 150/250/350 mT/m, duration 3 ms)). A reference non-water suppressed spectrum was acquired for ECC (with increasing number of shots per b-value: 16/16/64/64/64/128/128) and an initial B$_0$ drift compensation was performed on the scanner with a navigator scan. Each b-value was acquired in full as single shots and in a random order between b-values. *Of note, for future studies, the orientation of the diffusion gradient should be varied and a powder averaged performed to cancel out the effects, expected to be small, of microscopic anisotropy.*

MRS Processing

Prior to quantification with LCModel, Eddy Currents were corrected with the water reference scan and phase and B$_0$ drifts using spectral registration in FID-A [32, 27, 28]. A metabolites basis set was simulated using the exact RF pulse shapes and sequence delays and previously published J-coupling constants and chemical shifts [211, 212, 5] with NMRScope-B [213] from jMRUI [214, 215]. The following metabolites were simulated: alanine (Ala), ascorbate (Asc), aspartate (Asp), β-hydroxybutyrate (bHB), glycerophosphocholine (GPC), phosphocholine (PCho), creatine (Cr), phosphocreatine (PCr), γ-Aminobutyric acid (GABA), glucose (Glc), glutamine (Gln), glutamate (Glu), glutathione (GSH),myo-inositol (mIns), lactate (Lac), N-acetylasparate (NAA), N-acetylaspartylglutamate (NAAG), phosphoethanolamine (PE), scyllo-Inositol (Scyllo), and taurine (Tau). The macromolecules spectrum was acquired in one

healthy animal in the same region with a double-inversion recovery module (inversion times TI_1=2200 ms and TI_2 = 800 ms) in the STE-LASER sequence and additional diffusion weighting (b = 5 ms/μm^2). Residual metabolites were removed from the macromolecule spectrum following the procedure described by our group in ref. [35] using AMARES [216] from jMRUI (procedure detailed in the next chapter, section 5.2.4). For MRS, metabolites are reported as a ratio to the fitted water signal (concentration set to 44.4 mol) and when their relative CRLB for all rats were below 15%. For dMRS, metabolites are reported when their relative CRLB were below 10% at b = 0.1 ms/μm^2.

dMRI acquisitions and processing

In vivo dMRI experiments were conducted at week 6 post-surgery (N=5 sham, N=5 BDL) on a subset of animals from the group used for SVS and dMRS. A spin echo EPI sequence with the following parameters was used: 0.2×0.2×0.5 mm^3 resolution (15 slices), TE = 29 ms, TR = 3500 ms, δ = 4 ms, Δ = 12 ms (characteristic 1D diffusion length of $\approx$ 4.9 μm, for $D_{0,wat}$ = 1 μm^2/ms), 250 kHz bandwidth, 2 segments, 4 averages, 4 FOV saturation bands, direction of frequency encoding: anterior-posterior (the largest dimension) and partial FT of 1.2 in the phase encoding direction. The following b-values and directions were used: 1 (12), 1.8 (16), 2.5 (30), 5 (60), 8 (60) ms/μm^2 with 2 non-diffusion weighted images per shell and an acquisition of 4 non-diffusion weighted images with reverse phase encoding to correct for eddy currents and EPI distortions in post-processing.

MP-PCA denoising, Gibbs ringing artefacts, Rician noise bias, and Eddy currents/motion artefact corrections were performed following the DESIGNER pipeline [217].

Modelling

Metabolite signals were normalized to the first b-value. For each metabolite, the apparent diffusion coefficient ADC and kurtosis K_{app} $\left(\frac{S}{S_0} = \exp\left(-b\text{ADC} + \frac{(b\text{ADC})^2 K_{app}}{6} \right) \right)$ and the intra-stick diffusivity D_{intra} from the randomly oriented sticks model [69] were fitted up to b = 10 ms/μm^2 and b = 15 ms/μm^2, respectively. The fit was performed either on the group-averaged signal decay or on the individual animal metabolite diffusion decay with a non-linear least squares method. To estimate the error on the parameters estimated from the group-averaged signal decay, we performed a Monte Carlo estimation where the group-averaged signal decay was corrupted by *noise* (taken from a normal distribution) and fitted again *nMC* times. For each b-value, the *noise* used for the Monte Carlo study was set to the standard deviation of the normalized signal decay across animals at this b-value. For the smallest b-value, the standard deviation was 0 because of the normalization and we used instead the mean CRLB across animals at this b-value.

For dMRI, the kurtosis tensor was fitted up to $b = 2.5$ ms/μm^2. The SANDI model [101] for gray matter (GM) (hypothesis: $D_{soma} = 3\ \mu m^2$/ms) was fitted up to $b = 8$ ms/μm^2 on each voxel of the powder-averaged data using AMICO [218] (estimated parameters: fraction of neurites $f_{neurite,GM}$, fraction of extracellular space (ES) f_e, intra neurite diffusivity $D_{neurite,GM}$, extracellular diffusivity $D_{e,GM}$ and soma radius R_{soma}). The standard model for white matter was fitted up to $b = 2.5$ ms/μm^2 on each voxel of the directional data with the rotationally invariant implementation [104, 219] (estimated parameters: fraction of axons $f_{axon,WM}$, intra axon diffusivity $D_{axon,WM}$, extracellular diffusivity parallel and perpendicular to the fibre bundle $D_{e//,GM}$ and $D_{e\perp,GM}$ and orientation dispersion Ψ). In addition, the WMTI-Watson ([102, 103], with the hypothesis $D_{neurite,WM} > D_{e//,WM}$ [100]) was also used and the results with both models were compared. A graphical representation of the models and of the parameters estimated in each case is given in **Figure 2.9**, section 2.9.2 of the introduction chapter. GM and WM masks were created with ANTS (using the map of $f_{neurite,GM}$ from SANDI, atropos function, k-means 2 clusters), and the fitted parameters averaged over each masked regions.

Statistics

Data are presented as mean $\pm$ SD and the individual values are displayed when relevant. Blood values were compared with a 2-way ANOVA (disease and time factors) with Bonferroni multiple comparison post-hoc test, for each biomarker individually. Metabolite concentrations were compared with a 2-way ANOVA (disease and time factors) with Bonferroni multiple comparison post-hoc test, for each metabolite individually. dMRS diffusion coefficients fitted on the individual animal signal decays were compared with a 1-way ANOVA (group factor - SHAM, BDL week 4, BDL week 6) with Bonferroni multiple comparison post-hoc test, for each metabolite individually. dMRS diffusion coefficients fitted on the group-averaged signal decay were compared with a 1-way ANOVA (group factor - SHAM, BDL week 4, BDL week 6, SD: Monte Carlo SD, N: number of animals per group) with Bonferroni multiple comparison post-hoc test, for each metabolite individually. dMRI diffusion coefficients were compared with an unpaired Student t-test for each parameter, corrected for N=2 multiple comparisons (WM; GM). The p-values were: * $p<0.05$, ** $p<0.01$, *** $p<0.001$, ****$p<0.0001$.

Immunohistochemistry and neurofilaments

Animals (sham and BDL) were sacrificed for histological evaluation after the last in vivo scan at week 6. Deeply anesthetized (4% isoflurane for 5 min) animals were injected with analgesic (Temgesic (ESSEX), 0.1 mg/kg) before transcardial perfusion with PBS. Brains were fixed in 4% formaldehyde PBS solution overnight at 4°C, cryopreserved in 30% sucrose PBS solution at 4 °C for 48 hours, and then embedded in Tissue-Tek O.C.T. compound for histology. Immunohisto-chemistry (IHC) and Golgi-Cox stainings were performed for cerebellar astrocytes and neurons

cytoarchitecture. IHC consisted of 16 μm brain sagittal-sections, where GFAP (glia-specific intermediate-filament protein, MAB360 Merck Millipore) and DAPI (nucleus) stainings were used (seven slides/rat). Morphometric measurements were performed using Sholl-analysis ($\approx$ 1000 processes/group/region) as done in ref. [136]. Golgi-Cox staining, consisting of metallic impregnation of neurons, here Purkinje cells, was also performed (110 μm-sagittal-sections, 25 slides/hemisphere).

For the quantitative determination of neurofilament light chain (NfL) levels, an integral part of the axonal structure, blood samples (1 mL) were taken from the sublingual vein into anti-coagulated tubes (EDTA) at week 4 (N=6 sham, N=6 BDL) and week 6 (N=3 sham, N=4 BDL) post surgery. The NfL assay ELISA was performed as described by the manufacturer (CUSABIO: CSB-EL015688RA, analytical sensitivity: 7.8 pg/mL-500 pg/mL). The absorbance was measured at 450 nm (Hidex Sense Beta, Hidex Oy).

4.4.2 Results

Biochemical measurements confirmed the induced liver disease
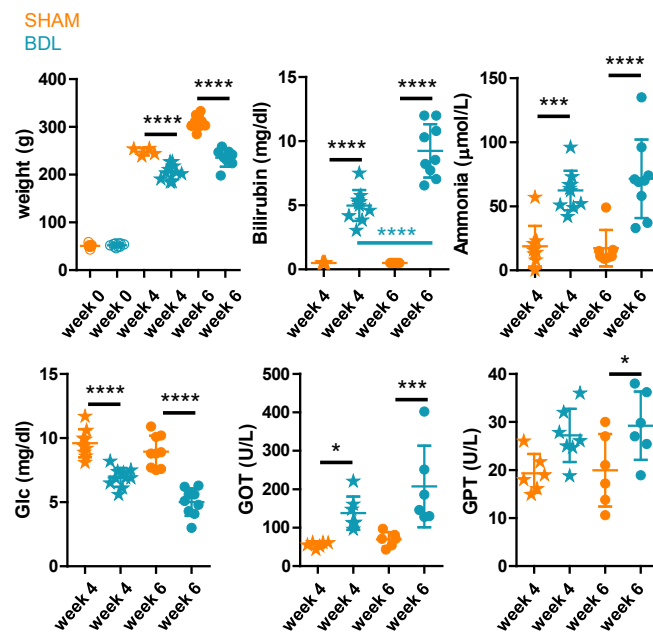
Figure 4.7: Biochemical measurements in the blood and plasma in the BDL and sham groups, showing strong changes in systemic biomarkers: increased bilirubin, ammonia, and liver enzymes (GOT, GPT), decreased glucose and body weight. The same color code will be used throughout this section: orange - SHAM, blue - BDL, stars - week 4, circles - week 6. Circles: individual animals, bars: mean and SD. U: enzymatic unit.

To assess the evolution of the disease, systemic biomarkers of liver dyfunction were measured

longitudinally. Plasma bilirubin, blood ammonia, and liver enzymes (GOT and GPT) increased from week 4 onwards in the BDL compared to the sham group (**Figure 4.7**). At week 6, bilirubin was below the detection limit (<0.5 mg/dL) in the sham group and 9.2±2.1 mg/dL in the BDL group, blood ammonia increased by +313% (****,17.3±14.2 μmol/L in the sham group and 71.4±30.6 μmol/L in the BDL group), GOT by +198% (***,69.6±19.0 U/L in the sham group and 207.2±106.1 U/L in the BDL group), and GPT by +47% (*,19.9±7.5 U/L in the sham group and 29.2±7.1 U/L in the BDL group). The expected weight increase with age was reduced in BDL rats from week 4 onwards (week 6: sham: 309±14 g and BDL: 235±18 g). Blood glucose also decreased from week 4 onwards, reaching concentrations below 5 mg/dL at week 6 for some BDL animals (week 6: sham: 8.9±1.2 mg/dL, BDL: 5.0±1.1 mg/dL).

Altered brain metabolism shown by ^{1}H MRS

Metabolism in BDL rats was assessed with single-voxel ^{1}H MRS in the cerebellum. The metabolites reliably quantified in this study are reported in **Figure 4.8**. The ultra-high field led to a good spectral separation of glutamine and glutamate, allowing to disentangle their behaviour. A strong increase of Gln concentration (+130% at week 4,*, +204% at week 6,****) in the BDL group and a decrease in the summed concentrations of the main osmolytes (mIns, Tau, tCho and tCr, -15% at week 4,****, -31% at week 6,****) were observed from week 4 onwards. Among the osmolytes, mIns and Tau decreased earlier in the disease development than tCho (mIns: -32% at week 4,****, -44% at week 6,**** and no significant difference for tCho at week 4, -57% at week 6,****). Glu, GABA and GSH decreased at week 6 in the BDL group compared to the sham group (Glu: -11.7%,*, GABA: -21%,***, GSH: -18%,**). Tau significantly decreased in the sham group between week 4 and week 6 (-8%,*). No significant differences between groups at any week were observed for Asc, tCr, Lac and tNAA.

Altered microstructure probed by dMRS and dMRI

To assess potential microstructure alterations in BDL rats, dMRS was acquired longitudinally in the same voxel as ^{1}H MRS (**Figure 4.9**). The sham rats at week 4 and 6 were combined for the dMRS analysis because no significant differences were observed in the diffusion estimates between these two groups for any metabolite (2-way ANOVA with metabolite and week factors, p-values for the week factor: 0.35 (D_{intra}), 0.53 (ADC), 0.65 (K_{app}), no significant interaction between the factors).
An increased ADC for Glu (+16%,**) and mIns (+19%,*) and an increased D_{intra} for Gln (+16%,*), Glu (+15%,***), mIns (+26%,****), Tau (+22%,***) and tCr (+9%,*) were observed at week 6 post-surgery compared to the sham-group when the parameters were estimated on the group-averaged signal decay (**Figure 4.9D**). The same trend was observed when the parameters were estimated on the individual animal decays (**Figure 4.9C**), yet with fewer significant differences:
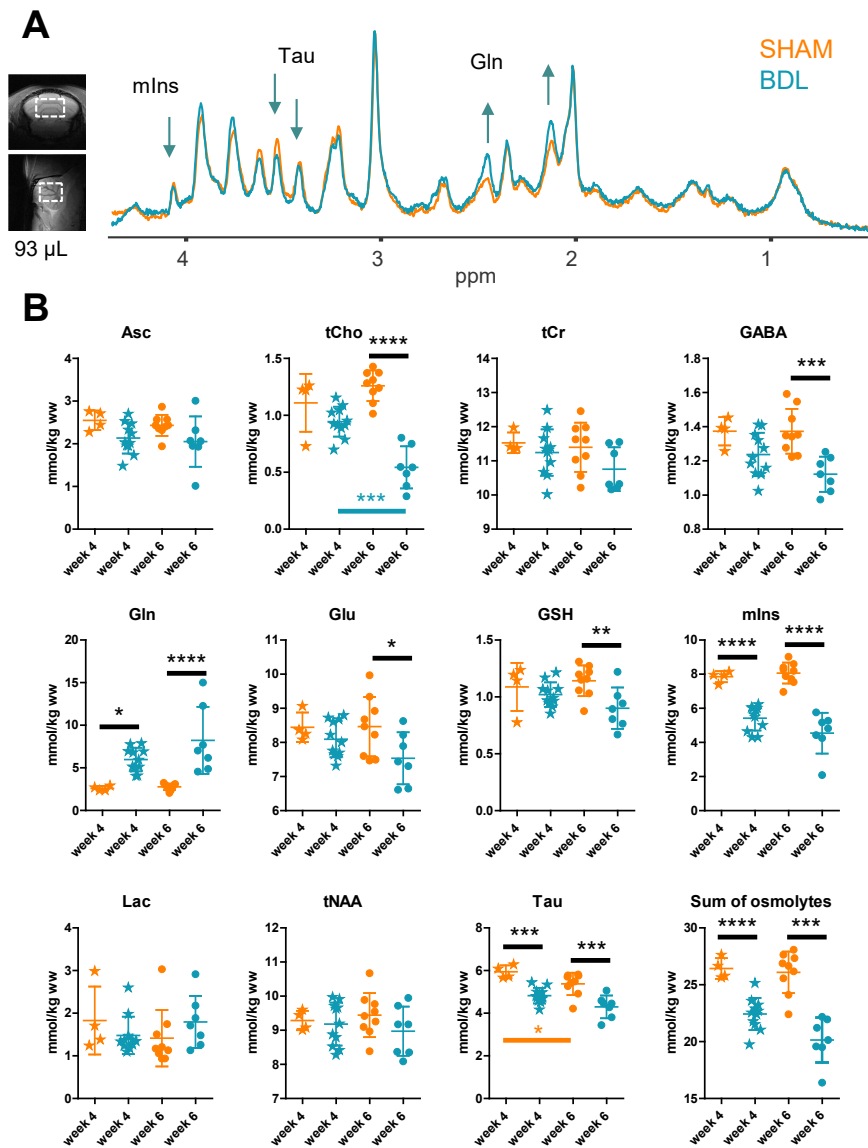
Figure 4.8: Representative voxel position and spectra (**A**) and metabolite concentrations from single voxel ^{1}H MRS in the cerebellum in the BDL and sham groups. Concentrations in mmol/kg of wet weight (ww), reference to the water signal whose concentration was set to 44.4 mol. Sum osmolytes is: tCr+tCho+mIns+Tau.

only the significant increased D_{intra} for Glu (+17%,*), mIns (+27%,*), and Tau (+24%,*) survived. tNAA ADC decreased at week 4 when fitted on the group-averaged signal decay (-12%,***). The apparent kurtosis K_{app} decreased for most metabolites, significant for Gln (-39%,*), mIns (-44%,**) and tNAA (-23%,**)on the group-averaged fit at week 4 and for Tau (-19%,*) and tNAA (-11%,**) on the individual animal decay at week 6.
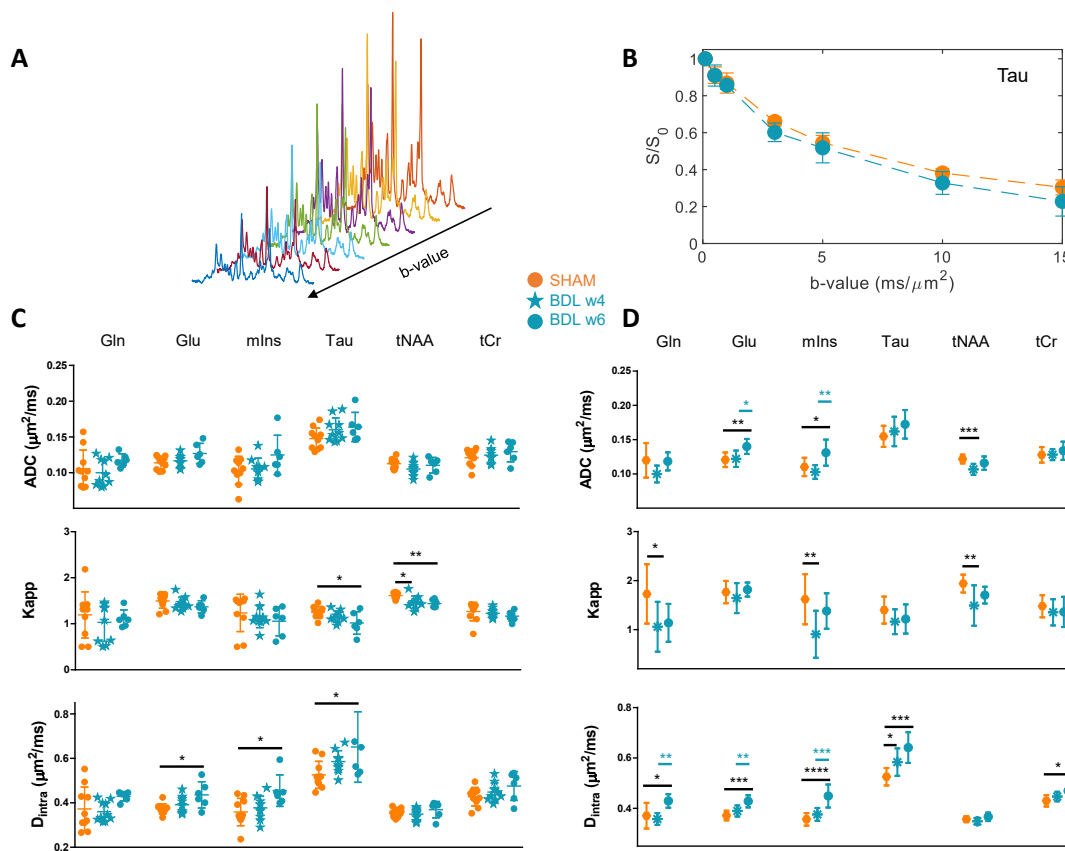
Figure 4.9: dMRS results at weeks 4 and 6 in the cerebellum of BDL and sham rats. Representative dMRS spectra in the cerebellum (**A**) and group-averaged diffusion decay for Tau in sham and BDL rats at week 6 (**B**). Estimated ADC, K_{app} and D_{intra}, either on individual animal signal decays (**C**) or on the group-averaged signal decay (**D**). The apparent diffusion and kurtosis were fitted up to b = 10 ms/μm^2 and the randomly-oriented sticks model up to b = 15 ms/μm^2. Error bars in **B**: standard deviation of the normalized signal decay across animals at each b-value. Error bars in **D**: standard deviation estimated from Monte Carlo simulations (noise: of the normalized signal decay across animals at each b-value and the mean CRLB for the first b-value).

To evaluate the complementary information brought by metabolites and water diffusion, dMRI was acquired in the cerebellum at week 6 post-surgery in BDL and sham rats (**Figure 4.10**). Short and artefact-free dMRI acquisitions in a brain region prone to motion artefacts due to the animal's respiration were achieved due to strong gradients (1 T/m) and a tailored acquisition scheme. The diffusion tensor estimation yielded significant increase in water axial, mean and radial diffusivities in both GM (+23%,*;+20%,*;+17%,*) and WM (+21%,*;+17%,*;+13%) (except for radial diffusivity, being significant only in GM). No trend of decreased water kurtosis was measured. Increased $D_{neurite,GM}$ (+8%,**) and $D_{axon,WM}$ (+12%,*) were observed in BDL rats in GM and WM, respectively. The SANDI model in GM also showed a significant decrease in
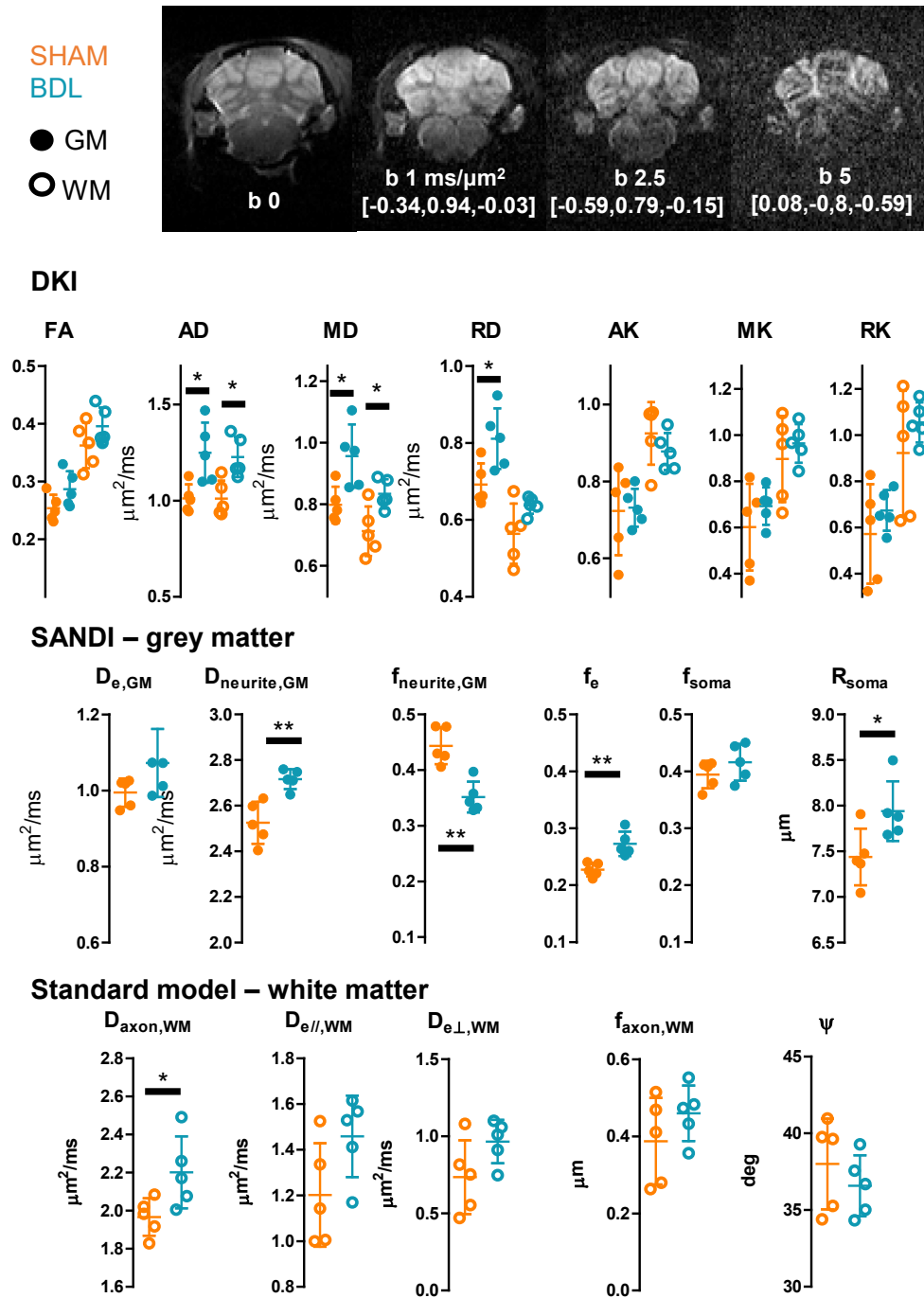
Figure 4.10: dMRI results at week 6 in the cerebellum of BDL and sham rats. Representative diffusion-weighted images in one animal (top) and fitted parameters from the cumulant expansion (diffusion and kurtosis tensors), SANDI in GM and the standard model in WM. Of note, the soma fraction was not fitted with SANDI but derived from $f_{soma} + f_e + f_{neurite,GM} = 1$. Full circles: grey matter, open circles: white matter.

$f_{neurite,GM}$ (-21%,**), compensate by an increase in extracellular space fraction f_e (+20%,**), and an increase in soma size R_{soma} (+7%,*). No difference was observed in any of the other parameters in WM.

Altered microstructure probed by histology
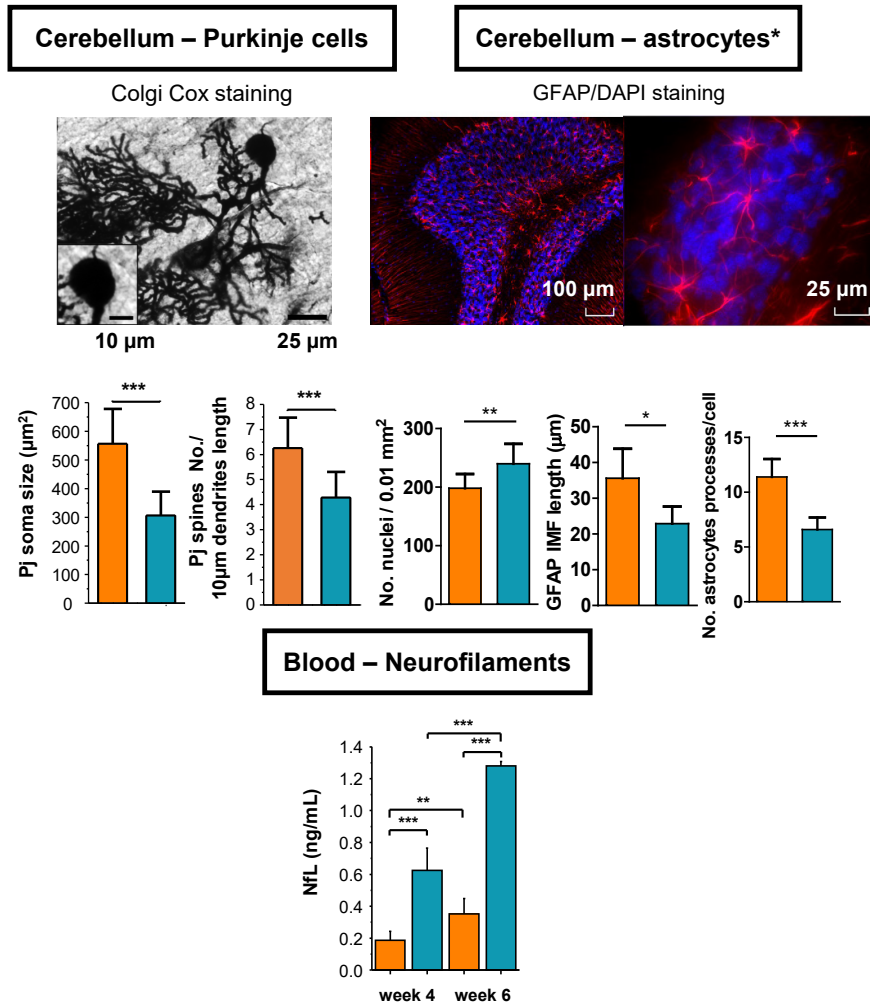
Figure 4.11: IHC staining in the cerebellum of sham and BDL rats. Top right: anti-GFAP(red)/DAPI(blue) staining of the cerebellar folium (left) and of the granular layer (right) and their quantifications. Top Left: Colgi-Cox staining of Purkinje cells, and their quantifications. *: the histology of the astrocytes was performed on adult BDL rats, the histology on young BDL rats is being processed at the moment. Bottom: quantitative determination of neurofilament light chain levels. *Courtesy of Dr Katharzyna Pierzchala.*

A significant increase in GFAP+ cells and nuclei number was observed for cerebellar protoplasmic astrocytes (+21%,**), together with a significant decrease of the number of processes (-42%,***) and of the mean length of intermediate filaments (-35%,*) in the granular layer

(**Figure 4.11**). Golgi-Cox staining of Purkinje cells showed a significant decrease of the neuronal soma surface (-22%,***) and dendritic spines density (-24%, apical,***). The p21 BDL rats exhibited significantly higher levels of NfL as compared to the sham group already at 4 weeks post BDL surgery ($\approx$ 3 fold increase), which continued to increase until week ($\approx$ 3.7 fold increase).

4.4.3 Discussion

The present work describes the first longitudinal and joint in vivo implementation of MRS, dMRS and dMRI in the cerebellum of young rats with chronic liver disease induced HE. In this context, MRS probed an increase in Gln, and a decrease in the osmolytes, in Glu, GABA and GSH in the cerebellum of BDL compared to sham rats. These metabolic changes, starting already at week 4 post surgery, highlighted the presence of an osmotic and oxidative stress together with possibly impaired neurotransmition. The additional use of dMRI and dMRS in the same animals enabled the characterization of microstructural changes in a complex region made of interleaved WM and GM through the implementation of tissue- and method-specific biophysical modelling. Collectively, the dMRS/dMRI results suggest a loss of neurite network complexity and/or density in the cerebellum of BDL rats, confirmed by histological measures.

These findings provide new insights into metabolic and microstructural alterations linked to increased brain Gln and its consequences in type C HE, for which dMRS emerged as a highly valuable methodology. These results also confirm that the hypothesis of intracellular edema with astrocyte swelling is maybe too restrictive to describe the complexity and multicellular nature of these alterations in type C HE.

Metabolism

The strong increase in **Gln** already at week 4 post-surgery in BDL rats is a direct consequence of blood ammonia excessively entering the brain, and being converted into Gln by the glutamine synthetase in the astrocytes [147, 148]. Among the metabolites playing an osmotic role (mIns, Tau, tCr, tCho) and regulating cellular volume following Gln increase, **mIns** was the first to decrease in young BDL rats, as also observed in the hippocampus of young BDL rats [138]. In contrast, the decrease of mIns occured later (from week 6 onwards) in the hippocampus of adult BDL rats [136], suggesting an age-dependent vulnerability. mIns is involved in second messenger signalling in the central nervous system (CNS) [24], is known to enhance motor activity [220], and its receptors are present in higher concentration in Purkinje cells [221]. mIns depletion observed in the present study due to its osmotic role in the cerebellum could therefore be linked to the motor deficits elsewhere observed in young BDL rats [138, 136].

Decreased **Glu** at week 6 can be caused by its overuse in the detoxification process of ammonia in the brain, Glu being the precursor of Gln through the glutamine synthetase enzyme in the astrocytes, or to altered glutamatergic neurotransmission. Decreased **GABA** was also reported in the cerebellum of adult rats [140], but not in the hippocampus, neither in adults [136] nor in young BDL rats [138].

Oxidative stress has been suggested as a key mechanism in the pathophysiology of HE [168]. **GSH**, a strong brain antioxidant, decreased at week 6 post-surgery in BDL rats in the present study and could reflect the limited capacity of the brain to fight against reactive oxygen species, as we have shown in adult BDL rats [139].

Finally, metabolic changes in the healthy developing brain are expected after p21. Tkac et al. [222] showed that Gln and Tau decrease and mIns increases in the hippocampus, striatum and cortex between 21 and 28 days postnatal. This is reflected by the significant decrease in Tau observed here in cerebellum of the sham rats between week 4 (49 day postnatal, p49) and week 6 (63 days postnatal, p63) post-surgery.

Microstructure - diffusion MR and histology

An summary of the significant results is presented in tables 4.1 and 4.2.

Table 4.1: Summary of significant differences observed for intracellular space parameters in the cerebellum of BDL rats (versus sham rats) with diffusion MR and histology. The colors link the observations with the hypothetical explanations.

Intracellular space			
dMRS	**dMRI bio. model.**	**Histology**	**Hypotheses**
• ↑ diff. and ↓ kurtosis of osmolites (Gln, mIns, Tau) • ↑ diff. and ↓ kurtosis of glial markers (Gln, mIns) • ↑ diff. of Glu, a neuronal marker • Possible ↓ NAA ADC and kurtosis	• ↑ sticks diff. in WM and GM • ↓ sticks fraction in GM • ↑ soma radius in GM	• Astrocytes: more numerous, shorter and less ramified • Neurofilaments in the blood: increased • PJ cells: reduced spines density, smaller soma	• Less restricted/ramified cellular architecture of neurons and astrocytes • fiber loss • Less hindered neuronal intracellular space • Glial cells more affected than neurons? • GM more affected than WM?

In the **BDL group**, increased diffusivities of brain Gln and of the main brain **osmolytes** (mIns, Tau, tCr) were observed compared to sham rats, in agreement with the presence of an osmotic

Table 4.2: Summary of significant differences observed for extracellular space (ES) and non-space specific parameters in the cerebellum of BDL rats (versus sham rats) with diffusion MR and histology. The colors link the observations with the hypothetical explanations.

Extracellular space				Non specific
dMRS	**dMRI bio. model.**	**Histology**	**Hypotheses**	**dMRI sig. rep.**
• Not accessible	• ↑ extracellular space fraction in GM	• *Future steps: aquaporin histology, electron microscopy, measurement of exchange*	• Fibres replaced by extracellular space? • Omsolytes experiencing freer diffusion in the ES: increased permeability with the ES, osmotic stress?	• ↑ AD, MD, RD in GM • ↑ AD, MD in WM

stress. Upon leaking into the extracellular space to restore osmotic balance due to Gln increase, the osmolytes might exhibit a freer diffusion due to their temporary presence in the extracellular space before being cleared out (the clearance is supported by a steady-state net decrease of osmolytes observed with MRS).

Increased diffusivities of Gln and mIns, assumed to be **glial markers** [223, 224, 225], in BDL rats may reflect astrocyte alterations following the strong glutamine increase, supported by GFAP histological findings (in adult rats for now, the same histology in young BDL rats is being processed). A significant increase in GFAP+ protoplasmic astrocytes, the main type of cerebellar astrocytes [226], and nuclei number were observed in BDL rats, suggesting astrocytic activation. Although the length of processes is likely not probed with diffusion in this study due to the short and unique diffusion time, the decreased length of intermediate filaments measured by histology in BDL rats points towards a less restricted and less ramified cellular architecture, explaining increased diffusivities for astrocytic metabolites in BDL rats. The number of processes per astrocyte was also decreased in BDL rat but simulations from ref. [88] showed that the number of processes departing from the soma has almost no influence on the measured ADC at any diffusion time.

Glu and NAA, both expected to be preferentially **located in neurons** [223, 224, 225], exhibited opposite trends. Increased Glu diffusivity and a constant or decreased NAA diffusivity were observed in the BDL group compared to the sham group. Histology probed a reduced soma size of Purkinje cells in the BDL group, which was not highlighted by the diffusion results (significant increased R_{soma} fitted in GM with SANDI). Whether the increased R_{soma} measured with SANDI is a consequence of the decreased $f_{neurite}$, two parameters likely partially corre-

lated, or if it represents other neurons than Purkinje cells [226], the latter being present in low concentrations in cerebellum, should be further investigated.

NfL is a component of axonal cytoskeleton. Elevated NfL levels in bodily fluids (CSF and blood), resulting from brain neurofilaments being cleared out, have been linked to brain damage and atrophy [227, 228, 229] and correlated significantly with cognitive function impairment [230, 231]. An increased number of NfL was observed in the blood of BDL versus sham rats, pointing towards a loss of internal neuronal structure, and thus towards a freer intracellular diffusion of neuronal metabolites, here observed for Glu.

Moreover, Purkinje cells in BDL rats showed decreased dendritic spines density. It has been suggested, based on numerical simulations [55] and on experimental data from brain slices [232, 233], that decreased dendritic spine density would increase the ADC of neuronal metabolites, which is consistent with the increased Glu diffusivity observed here. Finally, Glu is the main precursor of Gln synthesis in the astrocytes, and its increased diffusivity might also be explained by the reduced complexity of astrocytic structures. Whether a competing mechanism occur for NAA, opposing the trend towards freer diffusion due to the loss of internal neuronal structure as observed for Glu, should be further investigated and constitutes a future step in this study.

Metabolite **kurtosis** coefficients were overall decreased in the BDL group, suggesting that the intracellular space might be less hindered or restricted. It supports the hypothesis of a loss of internal structure, reflected in the loss of neurofilaments, the decreased neuronal spines density, and the decreased length of astrocytes processes and number of ramifications.

Overall, the diffusion coefficients fitted on the averaged diffusion signal decay exhibited more significant differences between the groups than the ones fitted on the individual animals signal decays, the latter being a more conservative approach. Yet, both approaches highlighted similar trends.

In the **sham group**, the ADCs were in good agreement with the values found in the mouse brain in ref. [59]. Tau ADC and D_{intra} were higher than the ones of other metabolites, attributed to its small molecular weight and effective molecular radius (125.15 g/mol and r = 30.6 nm, **Figure 4.1**).

The trend of increase diffusivities in BDL rats for most metabolites was also observed in another dMRS study at 9.4T in the same animal model and where the voxel was placed at the centre of brain [234].

dMRI provides complementary information compared to dMRS, with the opportunity to also explore the extracellular space and to benefit from a higher sensitivity. Diffusion tensor estimates showed increased water AD, MD and RD in both GM and WM (except for RD significant only in GM) in the BDL group. Because of the low FA of GM, AD, MD and RD were more

similar than the same metrics in WM. No change in water kurtosis was observed in any matter, whereas kurtosis significantly decreased for some metabolites in the BDL group (Tau at week 6, tNAA at weeks 4 and 6 for the individual fits and Gln at week 4, mIns at week 4, tNAA at week 4 on the group-averaged fit). Increased water diffusivity with constant kurtosis is generally associated with vasogenic edema [92], but this hypothesis alone does not hold in the present study. Indeed, the complementary information on increased intracellular metabolite ADC and decreased kurtosis observed here pointed rather, or in addition, towards a freer intracellular space. The intracellular space information provided by dMRS could have been overlooked considering only DTI and DKI metrics in this study, thus highlighting the importance of performing combined dMRI and dMRS studies.

In GM and WM, increased $D_{neurite,GM}$ and $D_{axon,WM}$, respectively, are observed in BDL rats, echoing metabolites increased diffusivity in dMRS, whereas extracellular space water diffusivities are unchanged both in GM and WM, suggesting again a freer intracellular space. In addition, in GM, $f_{neurite,GM}$ is decreased and the extracellular space fraction f_e increased, possibly pointing towards cellular loss in GM. Interestingly, the same trend of decreased $f_{neurite}$ and increased f_e has been observed in MS patients and was associated to cellular loss and axonal damage in WM [235].

Overall, the combination of in vivo diffusion-weighted MRS and MRI suggest a preferential alteration of GM (over WM) and of astrocytes (over neurons), as shown by the decreased $f_{neurite}$ and increased $D_{neurite,GM}$ in SANDI, and by osmolytes and astrocytic metabolites increased diffusivities, respectively. The conclusion on preferential alteration of GM, however, relies on the assumption that the standard model parameters in WM and the SANDI model parameters in GM are equally well estimated in our case. The results obtained by dMRS and dMRI were further validated by histology (shorter astrocytes with few ramifications, decreased neuronal spines density and loss of neurofilaments in BDL rats). Histology stainings performed in this study provide a global and zoomed-out picture of how HE affects the brain. Indeed, no information is provided on the diameter of the axonal processes for example, which would require other techniques like electron microscopy, and GFAP staining prevents the observation of isolated astrocytes. Diffusion-weighted MR results were thus interpreted at the same global scale, with this limitation in mind.

Model fitting validations

Some technical validations relative to model fitting were conducted.

First, different implementations of the standard model in WM were compared (**Figure 4.12**). Good agreement was found between the two implementations of WMTI-Watson, the machine learning version being faster than the non-linear least squares (NLLS) version [236]. No
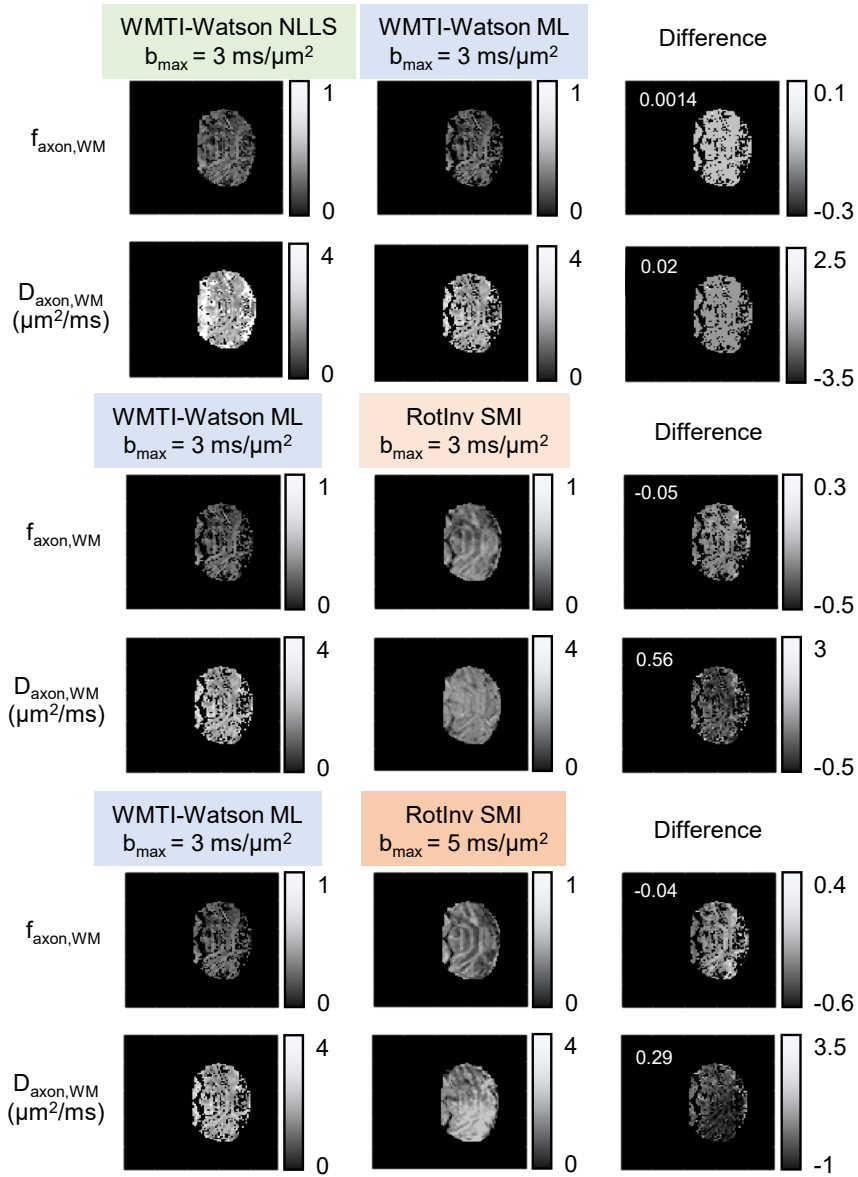
Figure 4.12: Comparison of standard model implementations for dMRI in WM: WMTI-Watson with non linear least squares fitting (green), WMTI-Watson fitted with encoder-decoder recurrent neural networks implemented in ref. [236] (blue) and the rotational invariants method with the SMI toolbox [219] (orange). $f_{axon,WM}$ and $D_{axon,WM}$ maps of one slice for one rat are displayed in each case with the difference map in the last column and the mean difference displayed in white.

structure in the difference map were observed (right column), yet additional black spots (non attributed values) are found with the ML implementation due to the exclusion of values reaching the fit boundaries. Whereas RotInv up to $b_{max} = 5$ ms/μm^2 led to hyperintense regions, RotInv up to $b_{max} = 3$ ms/μm^2 led to similar maps to the WMTI-Watson ones, with

fewer edge values and without assuming an ODF. This implementation was kept in the present study.
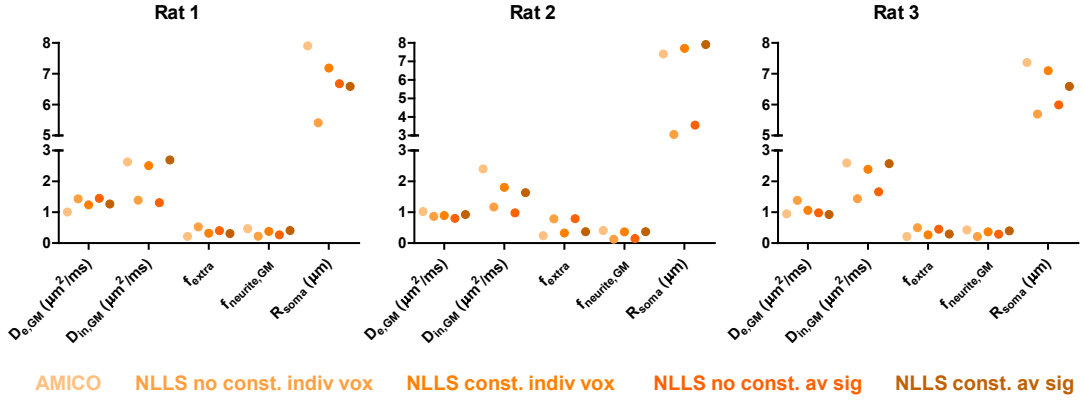
Figure 4.13: Comparison of SANDI implementations for dMRI in GM: using AMICO [218], NLLS on the individual voxels or on the signal averages over the GM mask, with and without constraints. The following hypotheses and constraints were used. **AMICO**: fixed soma diffusivity (3 $\mu m^2/ms$), and lower (lb) and upper bounds (up) for R_{soma} in μm, $D_{neurite,GM}$ and $D_{e,GM}$ in $\mu m^2/ms$: lb = [1,0.25,0.25], ub = [12,3,3], and the regularization parameters λ_1 = 1E-4 and λ_2 = 5E-3. **NLLS**: for R_{soma} in μm, $D_{neurite,GM}$ and $D_{e,GM}$ in $\mu m^2/ms$, f_i, and f_e, with light constraints (called "no constraints" in the figure): lb = [0,0,0,0,0], ub = [10,3,3,1,1], and with constraints: lb = [0,1.5,0,0,0], ub = [10,3,1.5,1,0.4]. $f_{neurite,GM} = (1 - f_e)f_i$ and $f_{soma,GM} = (1 - f_e)(1 - f_i)$.

Second, different implementations of SANDI were compared, where the fit was performed either with AMICO [218] or with NLLS regression of the analytical expression on the powder-averaged dMRI signal from individual voxels or from the signal averaged over GM (**Figure 4.13**). NLLS with constraints on the individual voxels was in good agreement with AMICO. The latter, faster and more stable because of the regularization, was used in this work.

Finally, we verified that the orientation dispersion of the WM tracks in the MRS voxel did not bias the estimated diffusion coefficient fitted with the randomly-oriented sticks model, as the rat cerebellum contains an important fraction of WM compared to other brain regions where GM is predominant. To do so, we followed the procedure described in supplementary materials of ref. [87]. First, the MRS voxel was masked to extract the fraction of WM (f_{WM} = 0.64, **Figure 4.14A**). Then, for each voxel in the WM mask, the angle Φ_i between the first eigenvector of the diffusion tensor in that voxel and the direction of the dMRS gradient (1,1,1) was estimated (**Figure 4.14B**). Finally, the signal was reconstructed based on equations 4.1 and 4.2, assuming randomly-oriented sticks in GM and partially-oriented sticks in WM:

$$S_{tot} = f_{WM} \times \text{oriented sticks} + (1 - f_{WM}) \times \text{randomly oriented sticks} \tag{4.1}$$
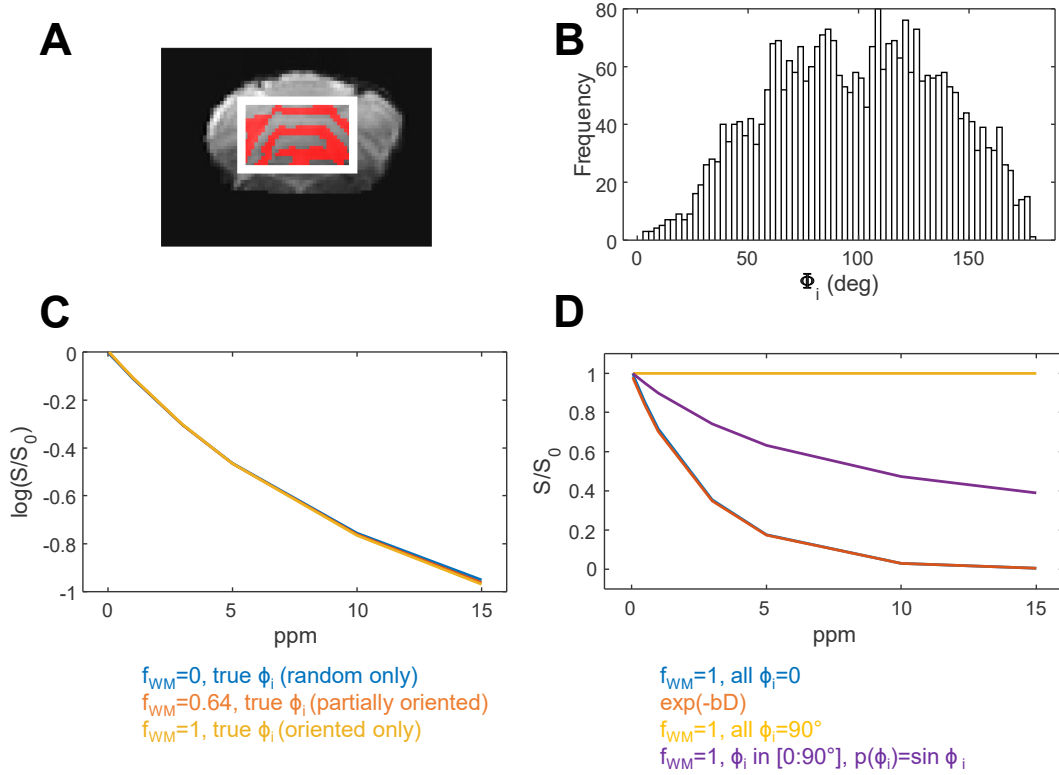
Figure 4.14: Influence of the orientation dispersion of the WM fibers in the MRS voxel on the estimated diffusion coefficient from the randomly-oriented sticks model in one rat. **A**: MRS voxel and WM mask, **B**: histogram of the angles Φ_i between the first eigenvector and the direction of the gradient of the dMRS acquisition (1,1,1) in the WM voxels. **C**: reconstructed signal under different fractions of WM. **D**: additional verifications of the formula with different angles distributions.

$$S_{\text{tot}} = f_{\text{WM}} \frac{\sum_{i=1}^{i=N} p(\Phi_i) \exp\left(-bD\cos(\Phi_i)^2\right)}{\sum_{i=1}^{i=N} p(\Phi_i)} + \left(1 - f_{\text{WM}}\right) \times \sqrt{\frac{\pi}{4bD}} \, \text{erf}\left(\sqrt{bD}\right) \qquad (4.2)$$

Figure 4.14C shows that no difference was found in the signal attenuation whether the true distribution of the WM fibre bundle in the WM is accounted for (orange) or not (blue). This confirms that the randomly oriented sticks model can be applied in the cerebellum. Moreover, even if the composition of the voxel were 100% WM (yellow), the signal would also be very similar because the distribution of angles found on **Figure 4.14B** is very close to a sin distribution. Additional verifications were performed in **Figure 4.14D**. The case $f_{\text{WM}} = 1$ and all $\Phi_i = 0$ (i.e. the sticks perfectly aligned with the dMRS gradient in each voxel) (blue) corresponds to free diffusion (orange). The case $f_{\text{WM}} = 1$ and $p(\Phi_i) = \sin(\Phi_i)$ is the randomly-oriented sticks (purple) and the case $f_{\text{WM}} = 1$ and all $\Phi_i = 90°$ (i.e. the sticks perfectly perpendicular to the dMRS gradient in each voxel) (yellow) correspond to no diffusion at all.

4.5 *Side project:* exploiting dual diffusion MRS and MRI acquisitions to measure intra-extracellular water exchange in the cerebellar GM

This side project was presented at the MRS workshop in Lausanne, August 2022.

Background: Recent dMRI studies have highlighted the need to account for inter-compartment water exchange at diffusion times longer than 20 ms, when fitting diffusion models of GM [116, 117]. This often requires multi-diffusion time protocols, which can substantially increase the acquisition time. In the context of hepatic encephalopathy, where poor ammonia detoxification by the liver results in an excessive synthesis of glutamine in the astrocytes and in an osmotic pressure which may alter water exchange, we have shown in the present study paralleled results of diffusion MRS and diffusion MRI in the cerebellum of an HE rat model, using non-exchanging models only.

Aims: We propose here a dual modelling of these preclinical dMRS and dMRI data at 14.1T in the cerebellum during type C HE in order to estimate cerebellar GM intra-extracellular water exchange time (t_{ex}). Our aim was to test whether a reliable estimate of t_{ex} could be obtained *without* additional dMRI data at multiple diffusion times (Δ), and solely based on the water signal from the dMRS voxel at long diffusion time and the dMRI acquisitions at short diffusion time. This methodology was tested on a small sample-size of young sham (N=3) and BDL rats operated at p21 (N=2).

Methods: Detailed dMRS and dMRI acquisition parameters have been described in section 4.4.1: dMRS was performed using the STE-LASER sequence [83] with Δ = 63 ms, and dMRI using a multi-slice 2D spin-echo EPI sequence with Δ = 12 ms. The procedure for t_{ex} estimation is described in **Figure 4.15**. The dMRS signal from the entire voxel was reconstructed based on equations 4.3 and 4.4, where the elements in red in the SANDI model were modified to account for exchange with the Karger model [237].

$$S_{\text{WMTI}}(b,\mathbf{g}) = \int \left(f_{\text{axon}} A_{\text{axon}}(b, D_{\text{axon,WM}}, \mathbf{g.n}) + (1 - f_{\text{axon}}) A_{\text{e}}(b, D_{\text{e//,WM}}, D_{\text{e}\perp,\text{WM}}, \mathbf{g.n}) \right) \mathscr{P}(\mathbf{n}) d\mathbf{n}$$
$$(4.3)$$

$$S_{\text{SANDI}}(b, t_{\text{ex}}) = f_{\text{e}} A_{\text{e}}(b, D_{\text{e,GM}}) + (1 - f_{\text{e}}) \left(f A_{\text{neurite}}(b, D_{\text{neurite,GM}}) + (1 - f) A_{\text{soma}}(b, R_{\text{soma}}) \right)$$
$$(4.4)$$

with f_{axon} the fraction of sticks in the standard model, A_{axon} the signal attenuation caused by the diffusion at D_{axon} in the sticks, $\boldsymbol{g}$ the dMRS gradient direction and $\boldsymbol{n}$ describing the WM fibre bundle orientation, A_{e} the signal attenuation caused by diffusion at $D_{\text{e,//,WM}}$ and $D_{\text{e},\perp,\text{WM}}$ in WMTI or $D_{\text{e,GM}}$ in SANDI in the ES, f_e the fraction of ES in SANDI, f the fraction of neurite in SANDI, A_{neurite} the signal attenuation caused by the diffusion at $D_{\text{neurite,GM}}$ in the sticks in

SANDI, A_{soma} the signal attenuation caused by the diffusion in the soma of radius R_{soma}, *b* the b-value, and t_{ex} the exchange time (**Figure 4.15**).

We assumed that the exchange could be neglected: **1)** in WM due to the myelin sheath; **2)** in GM at $\Delta = 12$ ms; and **3)** between the soma and the extracellular space in GM (SANDI [101]) at $\Delta = 63$ ms.

Results and Discussion: Predicted diffusion decays depending on the value of t_{ex} confirmed that different t_{ex} in a realistic range can be distinguished accurately with the proposed reconstruction (**Figure 4.16**). The fitted t_{ex} values were: mean t_{ex} SHAM: 40.1 ± 24.4 ms, mean t_{ex} BDL: 50.3 ± 7.8 ms. They are in good agreement with literature [116], although somewhat longer, potentially due to the longer diffusion time in dMRS than the ones used in NEXI [116]. The comparison suggests a slower rate of water exchange (higher residency time t_{ex}) in BDL rats although not statistically significant. An increased sample-size may help further investigate possible differences in t_{ex} between the groups.

Overall, dual modelling of dMRS and dMRI enabled an estimation of: geometric features of GM and WM estimated from biophysical models at short diffusion time, diffusion coefficients of compartment-specific metabolites, and, using the dMRS water signal jointly with dMRI, an estimation of membrane permeability in GM, without the need for prohibitively long acquisition times.

4.6 Conclusion

We showed the feasibility of performing joint MRS, dMRS and dMRI in the cerebellum of young and adult CLD-induced HE rats, something which could greatly enhance our understanding of the biological mechanisms occurring in the BDL rat model of type C HE. In addition to the fundamental information on metabolism provided by ^{1}H MRS, diffusion-weighted MR informed here on cerebellar microstructure alterations in vivo: increased metabolites and intracellular water diffusivities reflected a loss of internal cellular structure and morphological architecture complexity. Exploiting the complementary information of water and metabolite shed new light on these microstructure alterations, seemingly more specific to GM, to the intracellular space and to astrocytes in HE, a finding which is unprecedented. Finally, the non-invasive nature of MR allows one to probe these changes longitudinally, a key aspect in the study of the developing brain.

4.7 Perspectives

As perspectives to this study, we envision to:
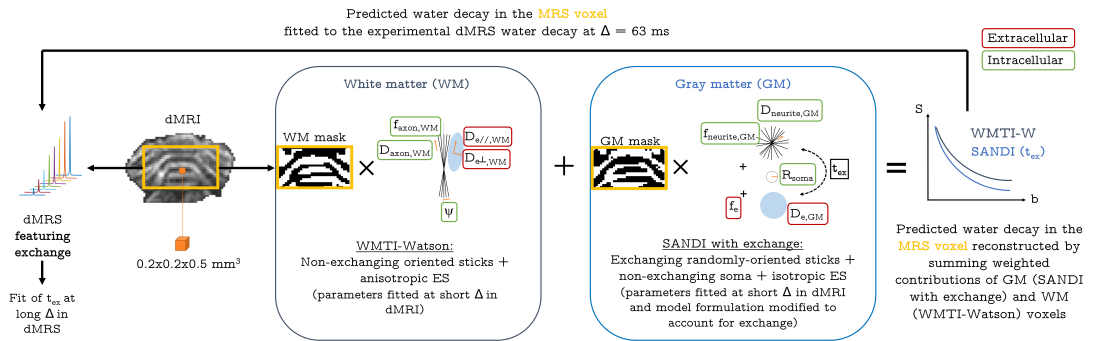
Figure 4.15: Pipeline for the exchange time estimation from dMRS and dMRI water acquisitions. First, the WMTI-Watson [102] parameters were fitted at short diffusion time (Δ = 12 ms) on each voxel of the WM mask. Second, the SANDI model [101] parameters were fitted at short diffusion time (Δ = 12 ms) on each voxel of the GM mask and the SANDI model formulation in GM was then modified to account for exchange between the sticks and the extracellular space [237]. Third, the predicted water decay in the MRS voxel $S_{tot}(b, t_{ex})$ was reconstructed by summing weighted contributions of GM (SANDI with exchange) and WM (WMTI-Watson) voxels, and fitted to the experimental dMRS water decay at long diffusion time (Δ = 63 ms) to estimate t_{ex}. Other model parameters (relative fractions, compartment diffusivities, orientation dispersion...) were assumed unchanged between Δ = 12 ms and Δ = 63 ms.

- investigate the potential of ex vivo dMRI in this study. Preliminary experiments on N=3 sham and N=3 BDL brains from this study were performed after heart perfusion, with similar experimental conditions as the in vivo dMRI acquisitions but at higher resolution. Preliminary images and reconstructions of the diffusion tensor (color-coded FA) are shown in **Figure 4.17**. In a future step, diffusion and kurtosis tensors parameters need to be derived and their potential to provide complementary information to in vivo results investigated.

- implement double-diffusion encoding to enhance the sensitivity of our measurement to microscopic anisotropy and restriction without the need to reach high q or high Δ regimes (both challenging in the cerebellum due to macroscopic motion) [238].

- further exploit the dMRI and dMRS signal informations in a joint model. This idea was implemented in the project on water exchange in GM (see ***Side Project***), where dMRS and dMRI information were used jointly to enhance the complexity of the dMRI model for **water** (e.g., introduce exchange in the SANDI model by benefiting from a prior information of the water signal in dMRS). We aim to continue this project by increasing the sample size and implementing a MRSI version to derive a spatial distribution of exchange times. The next idea is to implement a joint dMRS-dMRI model to enhance the complexity of the **metabolite** fit (e.g., going from sticks to cylinders by benefiting
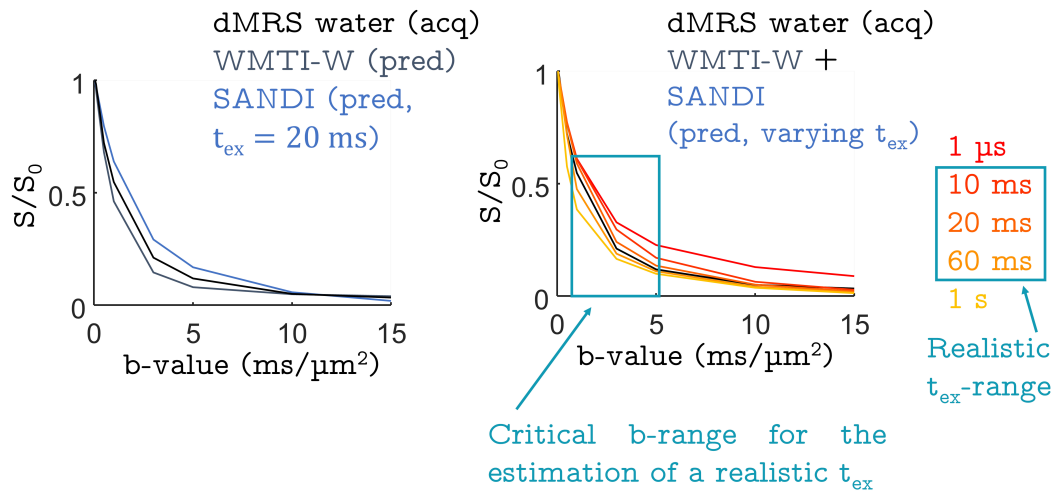
Figure 4.16: Validation of t_{ex} estimation. **Left panel**: diffusion decays generated from the entire MRS voxel with **1)** the WMTI-Watson contributions summed over the WM voxels, **2)** the SANDI contributions summed over the GM voxels with $t_{ex} = 20$ ms, and **3)** the experimental MRS diffusion decay. **Right panel**: influence of t_{ex} on the reconstructed signal in the MRS voxel (red to yellow colors). Both panels confirm that realistic exchange times are described by diffusion decays that can be distinguished given a realistic noise level. They also highlight that b-values below 5 ms/µm^2 are critical to differentiate two exchange times.
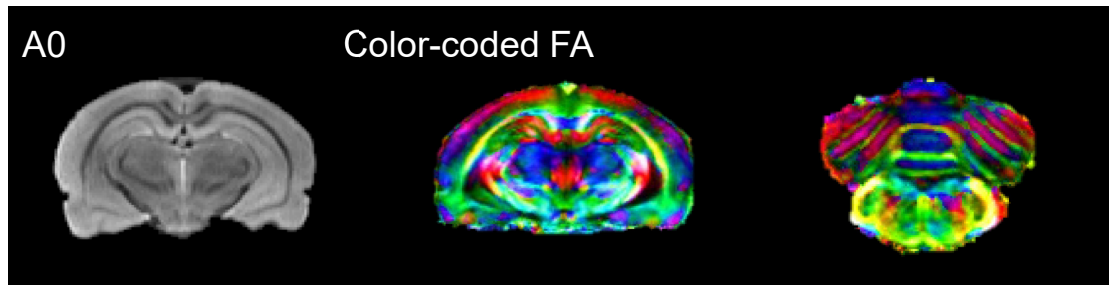
Figure 4.17: Ex vivo dMRI representative quality for one rat brain, with one A0 (no diffusion-weighting, left) and color-coded FA maps (additive overlap of the 3 eigenvectors scaled by FA, used for display only) from two slices, one in the centre of the brain (centre) and one in the cerebellum (right).

from prior knowledge brought by the dMRI information, adding a soma where R_{soma} and f_{soma} could be derived from the dMRI SANDI fit, or linking water and metabolites diffusion coefficients depending on the molecular radius, etc...). Another idea that we would like to investigate is the possibility to estimate Gln compartmentation based on phantom diffusion estimates as done in ref. [239] for lactate. The authors estimated lactate fractions in different cell types and compartments, fitting purely astrocytic (mIns) and neuronal metabolites (NAA) and linking the diffusion coefficients in vivo with the ones measured for free diffusion in a phantom.

- implement diffusion-weighted MRSI to benefit from the spatial information of the diffusion properties. This task will be however very challenging and requires new hardware like cryocoils which will be available on the 9.4T scanner at CIBM in the coming months.

- study the potential sex-differences with respect to metabolism in HE, comparing ^{1}H MRS results in male and female BDL rats. This is motivated by the observation that sex-differences exist in children with biliary atresia [240] and that male and female BDL rats exhibit different responses to episodes of overt HE [174].

5 DW-SPECIAL: improved detection of J-coupled metabolites

Chapter 5. DW-SPECIAL: improved detection of J-coupled metabolites

Abstract

The detection and subsequent estimation of the diffusion properties of strongly J-coupled metabolites with diffusion-weighted magnetic resonance spectroscopy is challenging due to the additional signal loss caused by J-evolution compared to non or weakly J-coupled metabolites. A new sequence for single-voxel diffusion-weighted, named DW-SPECIAL, is proposed. It combines the semi-adiabatic SPECIAL sequence with a stimulated echo (STE) diffusion block. Acquisitions with DW-SPECIAL and STE-LASER, the current gold-standard for rodent DWS experiments at high fields, were performed at 14.1T on phantoms and in vivo on the rat brain. The apparent diffusion coefficient and intra-stick diffusivity (Callaghan's model) were fitted and compared between the sequences for glutamate, glutamine (Gln), myo-inositol, taurine, total N-acetylaspartate, total choline, total creatine and the macromolecules. The shorter echo time achieved with DW-SPECIAL (18 ms against 33 ms with STE-LASER) substantially limited the metabolites' signal loss caused by J-evolution. In addition, DW-SPECIAL preserved the main advantages of STE-LASER: absence of cross-terms, diffusion time during a STE and limited sensitivity to B1 inhomogeneities. In vivo, compared to STE-LASER, DW-SPECIAL yielded the same spectral quality and reduced the Cramer Rao Lower Bounds (CRLB) for J-coupled metabolites, irrespective of the b-value. DW-SPECIAL also reduced the standard deviation of the metabolites' diffusion estimates based on individual animal fitting without loss of accuracy compared to the fit on the averaged decay. We conclude that due to its reduced echo time, DW-SPECIAL can serve as an alternative to STE-LASER when strongly J-coupled metabolites like Gln are investigated, thereby extending the range of accessible metabolites in the context of DWS acquisitions.

Publications

Contributions

I highlighted the limitations of the STE-LASER sequence to quantify accurately J-coupled metabolites and worked out an alternative solution (the SPECIAL sequence for localisation) with Rolf Gruetter. I then programmed independently the sequence from scratch on our 14.1T scanner (both the SPECIAL - currently unavaible on Bruker scanners, and the DW-SPECIAL versions), initiated and conducted the strategies to validate the sequence on phantoms and

in vivo, acquired, and analyzed the data. I wrote the first draft of the manuscript, which was reviewed by all the co-authors.

The chapter will present the creation, implementation and validation of a new dMRS sequence, following the observations of the limitations of STE-LASER described in the previous chapter. In particular, its long echo time led to difficulties in the quantification of J-coupled metabolites, especially of Gln (see **Figure 4.5** in the previous chapter), of great importance in the study of HE. We thus aimed at designing a sequence that could preserve the advantageous properties of STE-LASER while enabling a shorter minimum echo time. Based on a theoretical calculation of the b-value (**Appendix**), DW-SPECIAL was designed to maintain the absence of cross-terms, a major advantage of STE-LASER.

5.1   Introduction

In vivo diffusion-weighted magnetic resonance spectroscopy (dMRS) and imaging (dMRI) have emerged as powerful techniques to probe tissue morphology at the micrometer scale via the non-invasive assessment of a variety of diffusion metrics [241, 242, 70, 243]. By inserting diffusion-sensitizing gradients into traditional single-voxel ^{1}H magnetic resonance spectroscopy (MRS) sequences, the diffusion properties of metabolites measured by ^{1}H MRS can be retrieved. Investigating the deviation of these diffusion properties from the ones expected for free diffusion allows one to infer the environment that a given metabolite is experiencing. Contrary to water measured with dMRI, brain metabolites detectable by MRS are mostly intracellular and some of them are believed to be cell-specific: myo-inositol (mIns) and glutamine (Gln) are predominantly located in the astrocytes and N-acetylaspartate (NAA) and glutamate (Glu) in the neurons [223, 224, 225]. Given this prior knowledge, dMRS has the potential to provide unique cell-specific microstructural information, synergetic to the non-specific, yet more sensitive information obtained from dMRI probing water molecules located in all cell types and exchanging between compartments. Since the pioneering work in animals and humans [41, 42], dMRS has explored and revealed microscopic signatures of brain cells [54, 55, 56, 57]. Neurons [58], astrocytes [59] and microglia [60] and their alterations in disease populations have been investigated with dMRS, also in cases where dMRI failed to probe any change due to its non-cell specific nature [59].

However, unlike dMRI, dMRS suffers from low sensitivity due the low concentration of metabolites compared to water. It is thus important to improve dMRS experiments at the acquisition and processing levels.

Traditionally, dMRS has been performed using diffusion-weighted (DW-) PRESS or STEAM sequences. Both sequences have their respective advantages and disadvantages: DW-PRESS

benefits from full-signal intensity but is impacted by signal losses from the transverse magnetization during the diffusion time due T_2 relaxation and J-evolution, and by the limitations of the non-adiabatic 180° pulses at high fields (chemical shift displacement (CSD) artefacts, sensitivity to B_1 inhomogeneities with surface coils, high power deposition). DW-STEAM benefits from the slow T_1 relaxation of the longitudinal magnetization originating the signal during the diffusion time and from better radio-frequency (RF) pulse selection properties by using only 90° pulses, but has the drawback of the resulting halved signal intensity. Additionally, both DW-STEAM and DW-PRESS are affected by cross-terms, namely contributions to the b-value proportional to $\mathbf{g_{diff} \cdot g_{other}}$ (where $\mathbf{g_{other}}$ stands for imaging/spoiler/crusher gradients), which need to be accounted for to accurately estimate the diffusion properties.

More recently, the DW-semiLASER [244] and the STE-LASER [83] sequences have been introduced, both being based on the LASER [19, 10] localization, whose adiabatic volume selection is generally recommended at high magnetic fields despite its high specific absorption rate (SAR)[20, 8]. STE-LASER became the gold-standard in rodent dMRS studies: its block-design separates the stimulated echo diffusion module from the LASER localization and thus prevents the appearance of cross-terms, while preserving the other advantages of DW-STEAM. However, the use of STE-LASER leads to longer echo times, thus hindering the detection limits of J-coupled metabolites. Currently, mostly singlets (NAA, total choline (tCho), total creatine (tCr)) and few J-coupled metabolites (taurine (Tau), mIns) are reported in dMRS studies. Gln for example is seldom investigated, owing to challenges in its quantification, even more so when the MRS signal is strongly weighted by diffusion: its overlap with Glu at fields < 9.4T, a low concentration and strong J-coupling. Yet, Gln is a desired target for dMRS studies as it plays an important role in various pathologies and is an astrocyte-specific marker due to the exclusive location of glutamine synthetase (GS) in the astrocytes [148]. A striking example is hepatic encephalopathy (HE), where brain Gln is increased by more than 100% as a result of excessive ammonia reaching the brain [136, 245, 140, 188]. In that context, dMRS probed an increase in metabolite diffusivities, including in Gln, in the cerebellum of a rat model of the disease, consistent with the loss of neuronal and astrocytic internal structure observed by histology [202, 203]. Yet, a reliable estimation of Gln diffusion properties in the control group, where its concentration is not as high as in HE, still remains challenging.

The SPECIAL sequence [21] and its semi-adiabatic counterpart [246] have been introduced in animal and human ^{1}H MRS studies to reach shorter echo times and thus reduce signal loss by J-evolution and T_2 relaxation and are among the sequences recommended by the MRS consensus manuscripts recently published [20, 8]. As compared to LASER, SPECIAL reintroduces partial sensitivity to B_1 inhomogeneities along the direction of the non-adiabatic slice selective RF pulse, requires outer volume suppression (OVS) and can be sensitive to motion due to its 1D ISIS scheme. However, the possibility to reach very short echo times

while reducing the SAR promoted SPECIAL as an attractive alternative to LASER in single-voxel MR spectroscopy, providing the most accurate quantitative information from a ^{1}H MR spectrum by minimizing the J-evolution in coupled spin systems and reducing T$_2$ losses [20, 8].

Following this trend, we propose a new diffusion-weighted MR spectroscopy sequence, the DW-SPECIAL sequence, based on the semi-adiabatic SPECIAL sequence combined with a stimulated echo (STE) diffusion block, with the aim of preserving the advantages of the gold-standard STE-LASER sequence in rodent dMRS studies, while reaching a shorter echo time.

5.2 Methods

5.2.1 Sequence design

The DW-SPECIAL combines a STE diffusion block with a semi-adiabatic SPECIAL [21, 246] localization (sequence diagram in **Figure 5.1**). The first slice-selective 90° pulse is an asymmetric P10 pulse[210] (0.5 ms, 13.5 kHz bandwidth, 3.3 kHz γB$_{1,max}$, numerically optimized, 5 lobes, 18% refocusing factor), whose gradient refocusing lobe is applied before the first diffusion gradient to avoid cross-terms between these two gradients in the b-value (see **Appendix**). Two additional non-slice-selective 90° hard pulses (0.1 ms, 12.8 kHz bandwidth) are used to form the STE block. The adiabatic 180° pulses are hyperbolic-secant HS1-R20 pulses[10] (2 ms, 10 kHz bandwidth, 4.8 kHz γB$_{1,max}$ for adiabatic inversion and rephasing). The slice-selective adiabatic inversion is inserted in the mixing time of the STE block and is applied in the direction with strongest B$_1$ inhomogeneity (here the y direction, perpendicular to the transmit/receive (T/R) quadrature surface coil). It is alternatively switched on and off to perform the 1D ISIS scheme (a two-step phase cycling is required to obtain a spectrum). An additional water suppression Hermite pulse (15.4 ms, 350 Hz bandwidth, 89 Hz γB$_{1,max}$) is inserted in the mixing time to saturate the water signal relaxing during the diffusion time. Bipolar diffusion gradients that minimize the effects of eddy currents are used around the two non-slice-selective 90° pulses. Spoiler and crusher gradient amplitudes were adjusted empirically to minimize spurious echoes and outer voxel contributions while limiting the additional unwanted diffusion-weighting created by crushers around the 180° pulses. The following phase cycling, following Bruker's nomenclature (phases in units of 90° in brace brackets, phase increment for the second cycle given by the exponent n ($+n \times 90°$)), was used:

$$ph_{\text{bp}} = 0$$
$$ph_{\text{HS,on/off}} = \{0000000022222222\}^1$$
$$ph_{\text{P10}} = \{0000222200002222\}^1 \qquad (5.1)$$
$$ph_{\text{HS}} = \{0011223300112233\}^1$$
$$ph_{\text{receive}} = \{0202202002022020\}^3$$
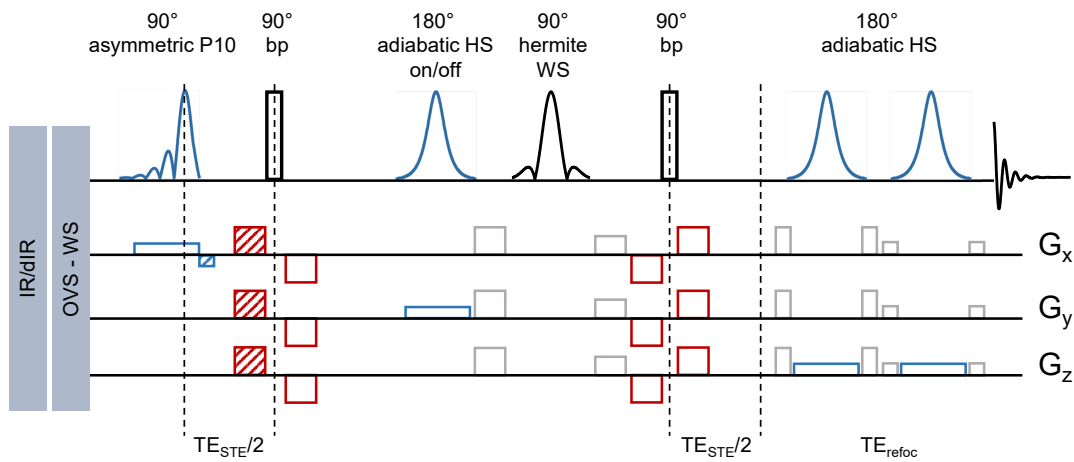
Figure 5.1: DW-SPECIAL sequence. 1$^{\text{st}}$ row: RF pulses, the ones from the semi-adiabatic SPECIAL sequence are highlighted in blue. 2$^{\text{th}}$ to 4$^{\text{th}}$ row: gradients - Blue: slice-selection gradients, red: bipolar diffusion gradients, grey: spoiler/crusher gradients (arbitrary values displayed). WS, OVS and (d-)IR modules are inserted before the first excitation pulse. The slice-refocusing gradient of the first slice-selective 90° pulse (blue) and the first diffusion gradients (red) are striped to indicate that they should not be applied simultaneously to avoid cross-terms in the b-value calculation. The details of the RF pulses are provided in the *Sequence design* subsection of the **Methods** section.

5.2.2   In vivo acquisitions

All experiments were approved by The Committee on Animal Experimentation for the Canton de Vaud, Switzerland (VD3022.1). Three adult male Wistar rats were scanned twice with a two-week interval to acquire five diffusion sets (rat 1, rat 2 and rat 3 at week 0, rat 1 and rat 2 at week 2) and one macromolecules profile (rat 3 at week 2), with DW-SPECIAL and STE-LASER. During the dMRS experiments, isoflurane anaesthesia ($\approx$1.5%, in a 50%/50% air/O$_2$ mix, 0.9 L/min) was used, the respiration rate and the body temperature were monitored (SA Instruments, New York, NY, USA), the latter being maintained at 37.7°C by circulating warm water.

Diffusion-weighted ^{1}H MRS experiments were performed on a 14.1T Bruker scanner (Avance Neo, Paravision 360 v1.1), with maximum gradient amplitude of 1 T/m (rise time: 270 μs), and a home-made T/R quadrature surface radio-frequency (RF) coil (two loops of 20 mm diameter). Anatomical MR images were acquired first to position the MRS voxel and define the shimming region using a localizer multi-slice gradient echo sequence (FOV: 25×25 mm^2, 98×98 μm^2 in-plane resolution, 15 slices/direction, slice thickness: 0.8 mm, slice gap: 1 mm, TE/TR: 2.92/18 ms, 1 average) and a T$_2$-turbo RARE sequence (FOV: 20×20 mm^2, 78×78 μm^2 in-plane resolution, 15 axial slices, slice thickness: 1 mm, slice gap: 0.2 mm, rare factor 6, TE/TR: 27/3000 ms, 2 averages). The position of the MRS voxel ($7 \times 5 \times 5$ mm^3) is displayed in **Figure 5.3**. First and second order shimming was performed with the Bruker MAPSHIM method (shim values based on a measured map of the B$_0$ field in the object) followed by local iterative first order shimming in the MRS voxel, leading to a water linewidth of 17-19 Hz. For the DW-SPECIAL acquisition, the shortest achievable TE was used (TE = 18.4 ms with TE$_{STE}$ = 8.9 ms, TE$_{refoc}$ = 9.5 ms, as labelled in **Figure 5.1**), and a mixing time of 40 ms, yielding a diffusion time (Δ) of 42.6 ms (characteristic 1D diffusion length of $\approx$ 3.5 μm). The minimum TE$_{refoc}$ was in fact 8.4 ms but was slightly increased to 9.5 ms to prevent baseline distortions. The STE-LASER sequence[83] was used for comparison with its respective minimum achievable TE of 33.7 ms (TE$_{STE}$ = 8.7 ms, TE$_{refoc}$ = 25 ms) and a mixing time of 40 ms, yielding a diffusion time (Δ) of 43.4 ms.

For both sequences, the diffusion gradients duration (δ) was set to 3 ms. The following b-values in the direction (1,1,1) were used: 0.05, 1, 3, 5, 10 and 30 ms/μm^2 for STE-LASER and 0.05, 0.94, 2.8, 4.7, 9.4 and 28.2 ms/μm^2 for DW-SPECIAL. The last b-value was acquired in one animal only as a proof of feasibility. The mismatched b-values between DW-SPECIAL and STE-LASER was not intended: for clarity, only the round values from STE-LASER will be referred to in the following text, but the true b-values were used for fitting and display. The following other acquisition parameters were used identically for the two sequences: TR = 3000 ms, 4096 complex points, 7142 Hz of spectral width, carrier frequency for excitation of water-suppressed signals at 3 ppm. The number of metabolites shots for dMRS acquisitions was NS = 160 for b-values up to 5 ms/μm^2 and was increased to 320 for b = 10 ms/μm^2 and 30 ms/μm^2 to compensate for the signal to noise ratio (SNR) drop caused by the high b-values and potentially additional motion-corrupted shots removed during post-processing. The VAPOR water suppression module[210] (pulse bandwidth: 350 Hz, last delay: 22.8 ms, flip angles 1 and 2: 84°/150°) was optimized and interleaved with outer volume suppression (OVS) pulses in both DW-SPECIAL and STE-LASER (6 OVS slabs, slab thickness: 12 mm, gap to voxel: 0.3 mm, sech pulse (1 ms), OVS crusher gradients (*x/y/z*: 150/250/350 mT/m, 3 ms)). A reference non-water suppressed spectrum was acquired for eddy currents correction (ECC) and between-scan B$_0$ drift compensation was performed with a navigator scan. Each b-value was acquired in full as single shots and in a random order between sequences and b-values.

The total duration of the scan per animal was approximately 2h30 (MRI and adjustments: 30 min, diffusion set per sequence: 60 min).

The term shot will be used throughout the manuscript to refer to each MRS complex free induction decay (FID) acquired and stored individually (e.g. two shots are needed to complete the 1D ISIS scheme)[30].

5.2.3 Phantom acquisitions

Phantom experiments were performed to validate the J-evolution observed in the simulated basis-set. Three phantoms were prepared (a) 8 mM Gln, b) 8 mM γ-aminobutyric acid (GABA), c) 8 mM mIns + 8 mM Cr, with 0.5 mM DSS in PBS) and scanned with the same sequence parameters at b = 0.05 ms/μm^2). A diffusion acquisition on a fourth phantom containing all the metabolites observed in vivo (see the *Processing* subsection of the **Methods** section) with realistic concentrations was also performed. The diffusion attenuation of mIns, Tau, Glu and tCr signals in solution were measured with DW-SPECIAL and STE-LASER to validate experimentally the absence of cross-terms in DW-SPECIAL. The same sequence parameters as for the in vivo acquisitions were used, except for the b-values, which were the following: 0.05, 0.1, 0.3, 0.5, 1, 1.5, 2, 2.5, 3, 3.5 and 4 ms/μm^2.

5.2.4 Processing

The same processing was applied for the two sequences. Individual shots were corrected for EC with the water signal. Phase and frequency drifts were performed simultaneously with spectral registration [32] in FID-A [28] (time domain, spectral region restricted to the NAA peak at 2.01 ppm, aligned to the median of the shots, 12 Hz line broadening for processing only), followed by motion-corrupted shots removal (z_i: square difference between the real part of spectrum i and the real part of the median spectrum, averaged over spectral points. Rejection criterion: $(z_i - \bar{z})/SD(z) > 1.5$, where $\bar{z}$ and $SD(z)$ are the mean and SD of z_i across shots). For DW-SPECIAL, the above-mentioned processing was applied separately on odd and even shots and if one shot was corrupted and removed, its corresponding on/off shot from the 1D ISIS scheme was also removed (**Figure 5.7**).

A metabolite basis-set was simulated for each sequence with NMRScope-B [213] (jMRUI [214, 215] - http://www.jmrui.eu), using the exact RF pulse shapes and delays. It included: alanine (Ala), ascorbate (Asc), aspartate (Asp), β-hydroxybutyrate (bHB), glycerophosphocholine (GPC), phosphocholine (PCho), creatine (Cr), phosphocreatine (PCr), GABA, glucose (Glc), Gln, Glu, glutathione (GSH), mIns, lactate (Lac), NAA, N-acetylaspartylglutamate (NAAG), phosphoethanolamine (PE), scyllo-inositol (Scyllo), and Tau using previously published J-coupling

constants and chemical shifts[211, 212, 5]. Metabolite signal amplitudes were quantified with LCModel and the diffusion coefficients were fitted only for the metabolites with Cramer Rao Lower Bounds (CRLB) below 5% at b = 0.05 ms/μm^2 (Glu, mIns, Tau, tNAA, tCr, tCho, and the mobile macromolecules (MM)) and Gln (CRLB = 6.4±0.5%). The macromolecules displayed in **Figure 5.3** were acquired in the same voxel in one animal using double inversion-recovery (dIR) and diffusion-weighting [86] (TE = 18.5 ms, TR = 4000 ms, TI = 2200/850 ms for DW-SPECIAL and TI = 2200/800 ms for STE-LASER, 7 blocks of 64 shots, b = 10 ms/μm^2), and metabolites residuals were removed using AMARES [216] from jMRUI, as described previously [35]. The metabolites residual patterns were further confirmed with the acquisition of MM spectra at multiple inversion times and with/without diffusion gradients (**Figure 5.2**).
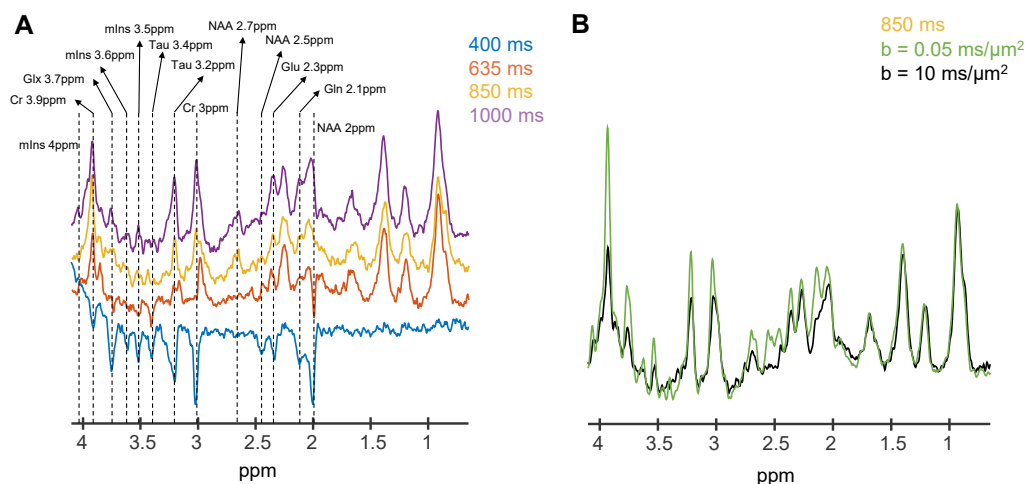
Figure 5.2: Validation of metabolite residuals removal on the macromolecule spectrum using multiple double inversion recovery experiments (**A**) and with high/low diffusion-weighting (**B**). In **A**, the first TI delay was fixed to 2200 ms and the second TI delay was varied (colors) to identify the metabolites residuals, also following [34, 35]. In **B**, the second TI delay was fixed to 850 ms (the one featuring the least metabolite residuals, the one chosen here) and the macromolecular spectrum was acquired with high/low diffusion-weighting to confirm the pattern of metabolites removal found in **A**. For visual inspection, the amplitude of the MM at 0.9 ppm was matched for the two conditions.

A detailed table of the acquisition and processing parameters following the ISMRM experts' consensus recommendations on minimum reporting standards in in vivo MRS (MRSinMRS) [247] is presented in **Appendix 3**.

5.2.5 Fitting

A Gaussian diffusion model up to b = 3 ms/μm^2:

$$\frac{S}{S_0} = \exp\left(-b \times ADC\right) \tag{5.2}$$

and the randomly-oriented sticks model [69] up to b = 10 ms/μm^2:

$$\frac{S}{S_0} = \sqrt{\frac{\pi}{4bD_{\text{intra}}}} \, \text{erf}\left(\sqrt{bD_{\text{intra}}}\right) \tag{5.3}$$

were fitted to each metabolite signal diffusion decay as a function of b-value. The fits were performed individually for each animal and on the averaged metabolite signal diffusion decay normalized to its value at b = 0.05 ms/μm^2, the latter being referred to as mean fit. A non-linear least squares algorithm was used (*Matlab* fit function, Trust-Region method), weighted with the inverse of absolute CRLB for the individual fit case, and with the standard deviation (SD) of each normalized signal amplitude across animals for the mean fit case.

5.2.6 Statistics

The apparent diffusion coefficient (ADC) and the intra-stick diffusion coefficient (D_{intra}) are reported as mean and SD across animals, and with their corresponding value fitted from the mean decay. We approximated that the two rats scanned twice with a two-week interval and used for the diffusion sets could be considered as independent samples for statistics. A two-way repeated measures ANOVA was performed on the ADC and D_{intra} values fitted on the metabolite signal diffusion decays of individual animals, comparing the sequence effect for all metabolites, with animal-matched values and Bonferroni multiple comparisons post-hoc test. For a given metabolite, an *F*-test was performed to compare the SD across animals of the normalized signal decays at b = 3 ms/μm^2 and b = 10 ms/μm^2 and the SD across animals of the estimated ADC and D_{intra}, between the two sequences. For each metabolite ADC or D_{intra}, the mean fit estimates were also compared to a Gaussian distribution created from the mean and SD of the corresponding individual fits to assess the null hypothesis (mean estimate of individual fit = estimate of the mean fit) for a *p*-value of 0.05.

5.3 Results

To compare the spectral quality of DW-SPECIAL and STE-LASER, a diffusion set up to b = 10 ms/μm^2 was acquired with both sequences. Good and comparable quality between the

two sequences was observed at all b-values (**Figure 5.3C**).
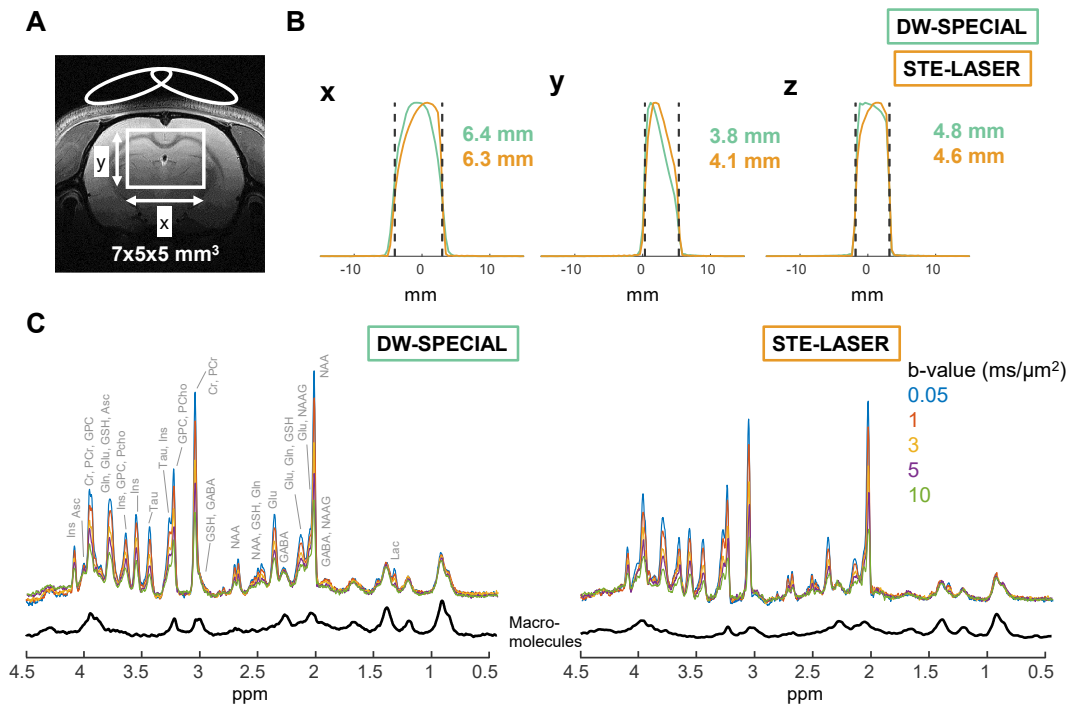
Figure 5.3: A: Representative voxel location in one animal with *x, y* directions labelled: *y*, perpendicular to the plane of the surface coil, is the most inhomogeneous direction in B_1 amplitude. **B**: 1D projections of voxel profiles on *x, y, z* normalized to 1 (obtained by switching on the corresponding gradient during the acquisition of the water signal) for DW-SPECIAL (green) and STE-LASER (orange), measured in the multi-metabolite phantom with a nominal voxel size of $7 \times 5 \times 5$ mm^3. The VOI dimensions were approximated by numerical step-wise integration of the normalized voxel profiles y_i over the distance step ($\sum y_i \times \delta_{mm}$ where $\delta_{mm} = FOV_{mm}/$#points). The dashed black lines represent the nominal voxel position in each direction (nominal position ± nominal size/2). **C**: Representative in vivo ^{1}H MR spectra of DW-SPECIAL and STE-LASER pulse sequences for five b-values are displayed. Pre-processing with ECC, phase/frequency drift correction, outlier removal and a 2 Hz line broadening were applied. Macromolecules are also displayed (black). Spectra amplitudes are normalized by the receiver gain, the voxel size and the number of shots (same with both sequences): the remaining difference between DW-SPECIAL and STE-LASER diffusion sets amplitudes results from the additional loss by T_2 relaxation and J-evolution in STE-LASER. Voxel profiles were very similar on *x* and *z*. On *y*, the more B_1-inhomogeneous direction, STE-LASER selected more signal distant from the coil (towards *y* positive). The diffusion sets and macromolecules with both sequences were of good quality.

Figure 5.4 also shows that strong diffusion-weighting was feasible (b = 30 ms/µm^2) with DW-SPECIAL. Although not shown here, the same quality at b = 30 ms/µm^2 was also achieved with STE-LASER [83].
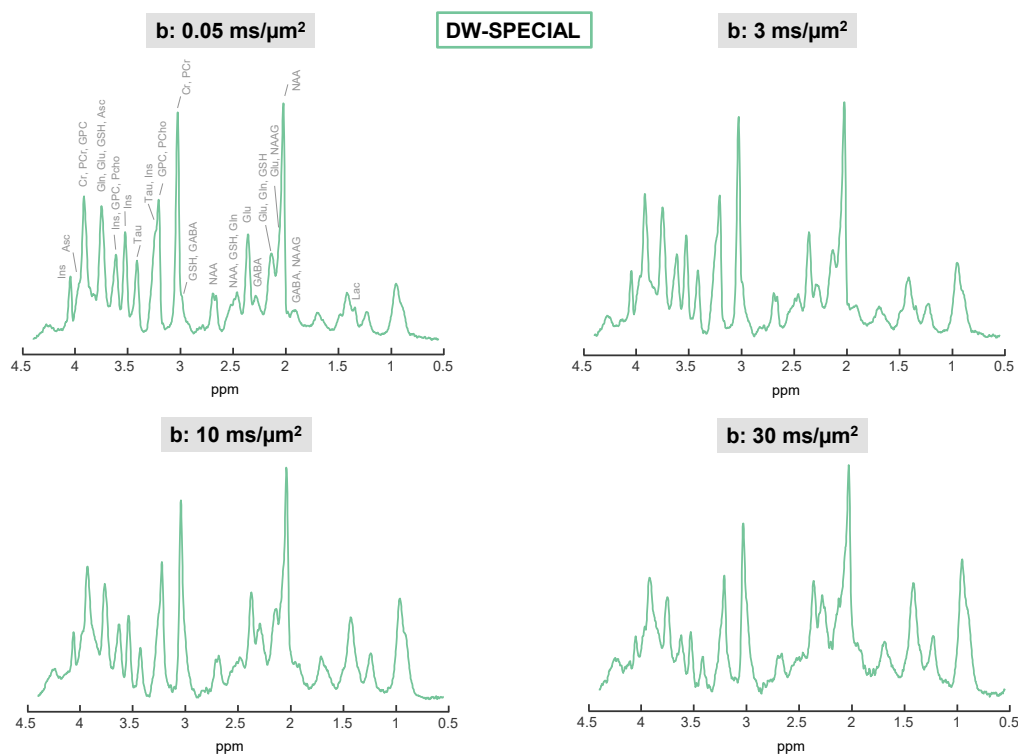
Figure 5.4: Representative DW-SPECIAL diffusion spectra after processing (ECC, phase and frequency alignment and motion-corrupted shots removal), for four b-values, plotted with 5 Hz line broadening. Metabolites with relative CRLB below 10% at b = 0.05 ms/μm^2 are labelled on the first panel. The spectrum at b = 30 ms/μm^2 acquired in one animal is shown here as a proof of feasibility. The diffusion spectra are of good quality and the increasing contribution of the macromolecules with respect to the metabolites can be observed with increasing b-values as a result of their slower diffusivity.

The MM contribution was higher in DW-SPECIAL due to the shorter TE (**Figure 5.3C**).

To compare the volume selection between the two sequences, the pulse profiles on the three directions were measured in one phantom experiment (**Figure 5.3B**). Similar x and z profiles and dimensions were obtained with DW-SPECIAL and STE-LASER (x: 6.4 mm for DW-SPECIAL and 6.3 mm for STE-LASER for a nominal size of 7 mm, z: 4.8 mm for DW-SPECIAL and 4.6 mm for STE-LASER for a nominal size of 5 mm). The slice-selection profile on y shows a higher contribution of signals distant from the coil (towards y positive) with STE-LASER than with DW-SPECIAL (4.1 mm and 3.8 mm, respectively), while remaining within the 5 mm nominal selection for both sequences.

To validate the J-evolution observed in the basis set simulations (**Figure 5.5A**), in vitro experiments were performed in phantoms at b = 0.05 ms/μm^2 with both sequences (**Figure**

5.5B).
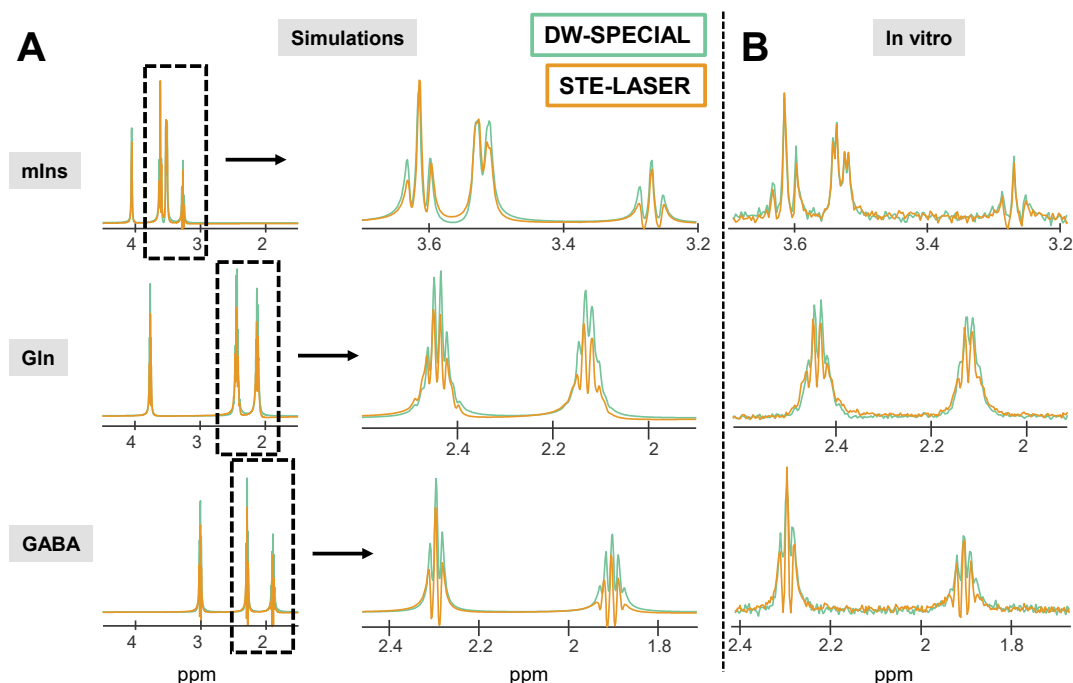
Figure 5.5: Basis set simulations (**A**) of some selected metabolites (mIns, Gln and GABA) (left column), with a zoom on a multiplet region (central column) and the equivalent spectral region measured in vitro in phantoms (**B**) for DW-SPECIAL (green) and STE-LASER (orange). Zero-filling and a 5 Hz line broadening were applied for the simulations and a 0, 0.6 and 1.6 Hz for mIns, Gln and GABA, respectively, for the in vitro experiments. The simulations were created with the exact delays and pulse shapes for both sequences and accounted for J-evolution but not T_2 relaxation. Simulations of Cr for both sequences featured no difference (not displayed here). The multiplet patters measured in vitro matched the simulated ones and confirmed the reduced J-evolution in DW-SPECIAL versus STE-LASER due its shorter total TE.

The matching J-evolution patterns between the simulations and the in vitro experiments indicated that, for strongly coupled metabolites like Gln, mIns or GABA, the shorter TE achieved in DW-SPECIAL yielded less signal loss due to J-evolution and T_2 relaxation.

To confirm experimentally the absence of cross-terms in DW-SPECIAL, the diffusion attenuation of mIns, Tau, Glu and tCr (given as examples) was measured in vitro with both sequences and compared (**Figure 5.6**), as STE-LASER is known to have no cross-terms in the b-value. An identical diffusion decay was found for these metabolites, attesting the absence of cross-terms in DW-SPECIAL as well. This was also shown theoretically in **Appendix 1**.

To further investigate the spectral quality of single shots obtained in vivo with DW-SPECIAL, the pre-processing results with FID-A were analysed and compared to the ones of STE-LASER.
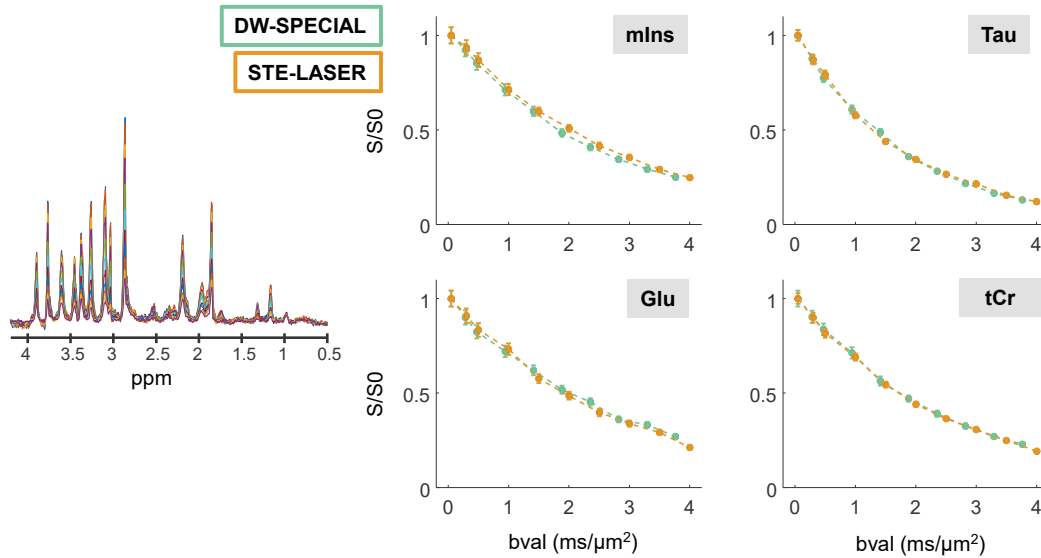
Figure 5.6: Phantom experiment confirming the absence of cross-terms in DW-SPECIAL. A phantom mimicking realistic in vivo metabolite concentrations (left panel, 4 Hz line broadening for visualisation) was scanned with DW-SPECIAL and STE-LASER, the latter featuring no cross-terms in the b-value as previously shown in [83]. The example diffusion attenuations over b-value (after normalization to the first b-value) for mIns, Tau, Glu, and tCr after LCModel quantification show no difference between the two sequences, confirming the absence of cross terms in DW-SPECIAL as well. The small offset observed for mIns could have been caused by a quantification error in the first point for either one of the sequences.

The frequency correction factors (**Figure 5.7C**) were small, stable across b-values and similar between the two sequences (mean over all b-values: $freq_{corr}$ = 1.2 ± 0.7 Hz for DW-SPECIAL and $freq_{corr}$ = 2.1 ± 1.7 Hz for STE-LASER). The absolute phase correction factors (**Figure 5.7D**) were increasing with b-value and also comparable between sequences (at b = 0.05 ms/μm^2: ph_{corr} = 2.8 ± 0.3° for DW-SPECIAL and ph_{corr} = 3.3 ± 0.6° for STE-LASER, at b = 10 ms/μm^2: ph_{corr} = 16.1 ± 3.0° for DW-SPECIAL and ph_{corr} = 24.3 ± 8.5° for STE-LASER). The fraction of shots removed at each b-value was higher in DW-SPECIAL versus STE-LASER when performing outlier removal on individual shots (**Figure 5.7B**, top) (at b = 0.05 ms/μm^2: %Sremoved = 18.0 ± 4.6 for DW-SPECIAL and %Sremoved = 7 ± 0.5 for STE-LASER, at b = 10 ms/μm^2: %Sremoved = 12.8 ± 4.5 for DW-SPECIAL and %Sremoved = 6.3 ± 2.8 for STE-LASER) due to the conservative condition of removing the on/off 1D ISIS pair when at least one of the shots is corrupted. When performing outlier removal on shots already combined into pairs, the fraction of outliers removed at each b-value for DW-SPECIAL was similar to the one for STE-LASER (**Figure 5.7B**, bottom and **Figure 5.7E** for tabular values).

To evaluate the fit quality of the metabolite signal diffusion decays of individual animals,
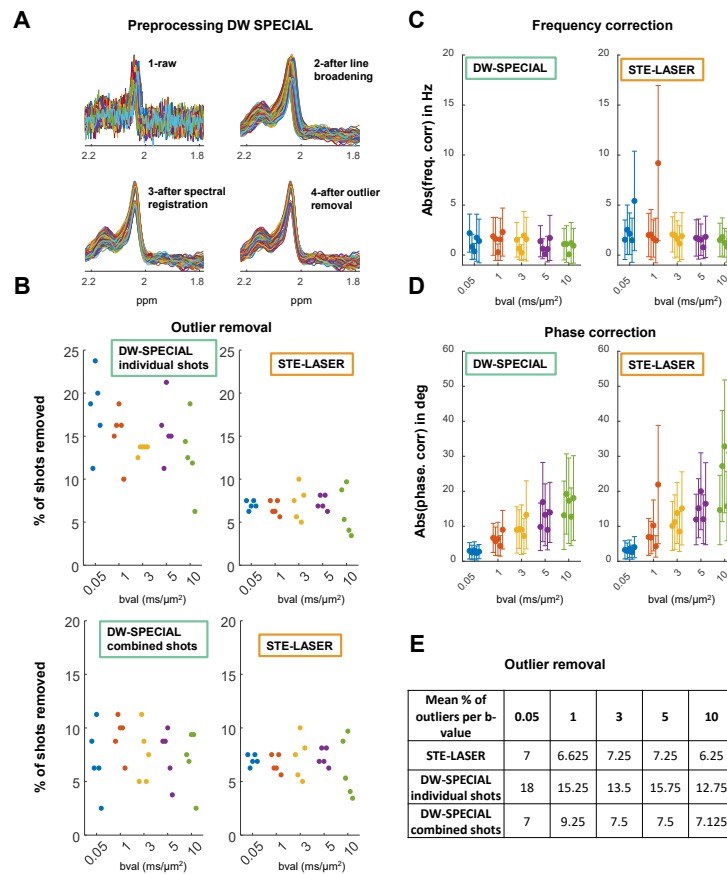
Figure 5.7: Processing results for the two sequences. **A**: visualisation of the processing results for one spectrum at b = 0.05 ms/μm^2 acquired with DW-SPECIAL. The on and off shots were processed separately but combined here for the display. **B**: Fraction (in %) of motion-corrupted shots removed for each sequence, 1 dot per animal and b-value, one color per b-value, performed either before shot combination into each pair (top, "individual shots") or after shot combination into each pair (bottom, "combined shots") in DW-SPECIAL. **C**: Frequency correction factors (absolute value) found by spectral registration in FID-A, mean and SD across shots, 1 error-bar per animal and b-value, one color per b-value. **D**: Phase correction factors (absolute value) found by spectral registration in FID-A, mean and SD across shots, 1 error-bar per animal and b-value, one color per b-value. The frequency and phase factors are displayed in absolute value but all the distributions are centered on 0. **E**: Tabular mean values for panel **B**. Due to the conservative condition of removing the on/off 1D ISIS pair when at least one of the shots is corrupted, the number of shots removed at each b-value is higher in DW-SPECIAL versus STE-LASER. Yet, when performing outlier removal on combined shots, the two sequences performed similarly (panel **B**, bottom). Similar phase and frequency correction factors are obtained with both sequences, with more outlier values for STE-LASER, confirming the good data quality of DW-SPECIAL.

LCModel relative CRLB were compared between the sequences.
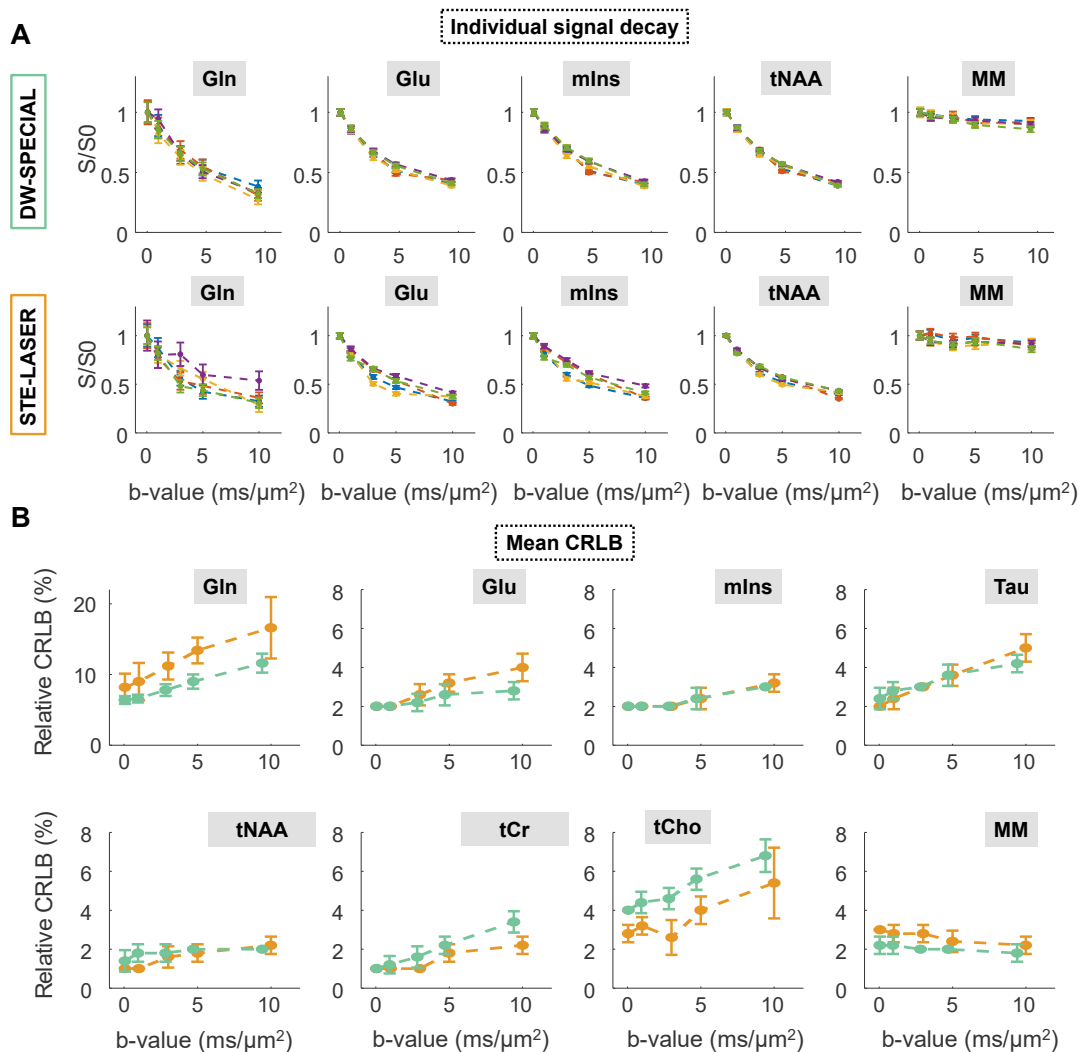
Figure 5.8: A: Metabolite signal diffusion decays of Gln, Glu, mIns, tNAA and MM as a function of b-value for all animals (different colors) and both sequences, normalized to their value at b = 0.05 ms/μm². Error bars: absolute CRLB from LCModel quantification. **B**: Relative CRLB (%) averaged over animals, as a function of b-value, for both sequences (DW-SPECIAL: green, STE-LASER: orange) and all quantified metabolites. Error bars: SD across animals at each b-value. For the relative CRLB, all metabolites are plotted with the same *y*-range except Gln. Of note, LCModel relative CRLB output being rounded to the nearest integer %, the SD for the CRLB are artificially high. DW-SPECIAL reduced the group variability of metabolite signal diffusion decays and improved or equalled LCModel fit quality (reduced relative CRLB) with respect to STE-LASER, for all metabolites except for tCho and tCr. For these two metabolites, the relative CRLB still remained low at all b-values for the two sequences (below 8% for tCho and below 4% for tCr).

The fit quality improved for DW-SPECIAL compared to STE-LASER, as judged from reduced CRLB for most metabolites, with the exception of GSH, tCr and tCho. Most noticeably, Gln CRLB were reduced irrespective of the b-value (**Figure 5.8B**, Gln: $CRLB_{b3,STE-LASER}$ = 11.2±1.9%, $CRLB_{b3,DW-SPECIAL}$ = 7.8±0.8%, $CRLB_{b10,STE-LASER}$ = 16.6±4.3%, $CRLB_{b10,DW-SPECIAL}$ = 11.6±1.3%). Metabolite signal amplitudes and CRLB tables for all reported metabolites can be found in **Appendix**.

To evaluate the group variability within the diffusion data, the metabolite signal diffusion decays were further averaged across animals for each metabolite and each sequence, after normalization to b = 0.05 ms/μm^2. Compared to STE-LASER, DW-SPECIAL reduced the group variability of diffusion decays (**Figure 5.8A** for the individual decays, **Figure 5.9** for the mean and SD and **Appendix** for the SD tabular values) for J-coupled metabolites like Gln and mIns (Gln: $SD_{b3,DW-SPECIAL}$ = 0.02 smaller than $SD_{b3,STE-LASER}$ = 0.13, (*p*-value = 0.0053,**), $SD_{b10,DW-SPECIAL}$ = 0.04 smaller than $SD_{b10,STE-LASER}$ = 0.10 (*p*-value = 0.089)), while maintaining the small variability obtained with STE-LASER for weakly coupled metabolites (tNAA) and MM.
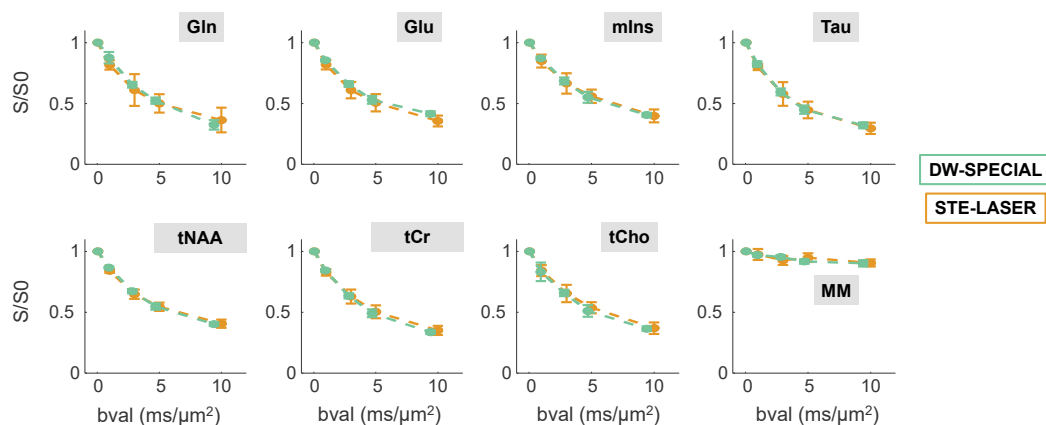
Figure 5.9: Normalized metabolite signal diffusion decays averaged over animals, as a function of b-value, for both sequences (DW-SPECIAL: green, STE-LASER: orange) and all quantified metabolites. Error bar: SD of S/S0 values across animals at each b-value. It contains the same information as **Figure 5.8A**, displayed here as mean and SD across animals.

Finally, to assess the reliability of the diffusion estimates derived from DW-SPECIAL, the ADC and D_{intra} fitted on the metabolite signal diffusion decays of individual animals and on the mean decay were compared between the sequences. DW-SPECIAL reduced the SD of estimated ADC and D_{intra} between animals (expected to be part of a homogenous control cohort) (**Figure 5.10A** and **B**, Gln: $SD_{ADC,DW-SPECIAL}$ = 0.013 μm^2/ms smaller than $SD_{ADC,STE-LASER}$ = 0.073 μm^2/ms (*p*-value = 0.0054,**), $SD_{Dintra,DW-SPECIAL}$ = 0.076 μm^2/ms

smaller than $SD_{Dintra,STE-LASER} = 0.25\ \mu m^2/ms$ (p-value = 0.036,*)). No significant difference (ADC: p-value = 0.4, D_{intra}: p-value = 0.9) was found between the two sequences for the mean ADC or D_{intra} of the individual metabolite fits. For DW-SPECIAL, the mean fit for all metabolites was also not significantly different from the mean of ADC or D_{intra} based on individual animal fitting when assuming a Gaussian distribution around the mean and SD across animals ($p > 0.05$, **Figure 5.10C** and **D**).
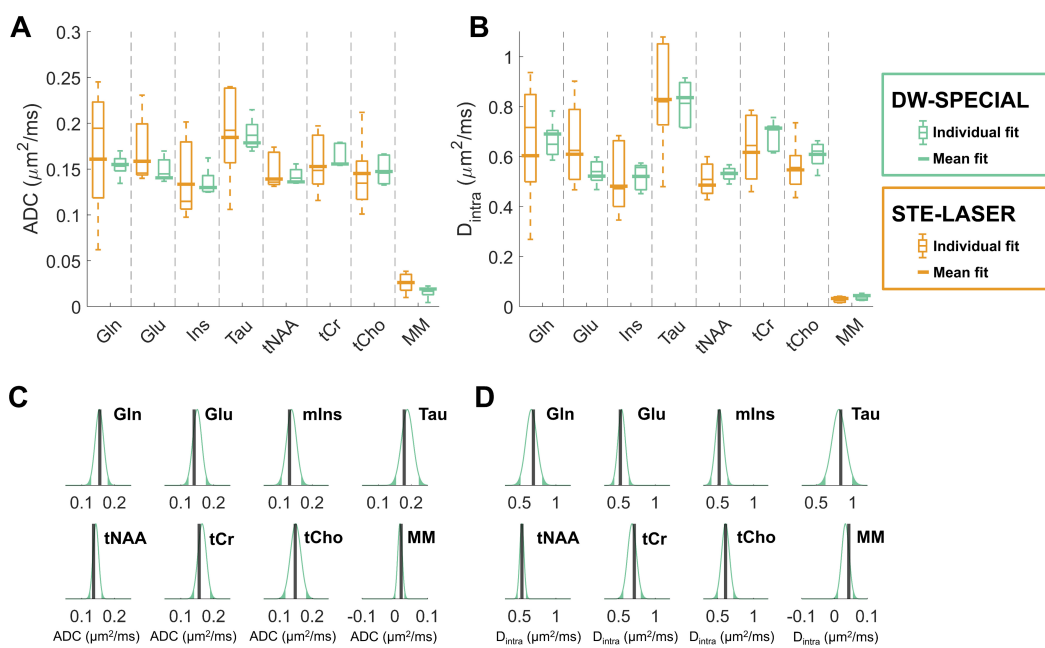
Figure 5.10: ADC (**A**) and D_{intra} (**B**) fitted for all animals with both sequences. Box plots: individual fit for each animal (line: median, top and bottom edges: 25th and 75th percentiles, whiskers: extreme values, dots: outliers). Wide bar: fitted ADC and D_{intra} on the averaged diffusion decay decay over all animals ("mean fit"). D_{intra} from the mean fit was in very good agreement between the two sequences and the SD across animals were reduced with DW-SPECIAL for all metabolites, most notably for the J-coupled ones for which the improvement is major. No statistically significant difference was found for the individually fitted ADC or D_{intra} for any of the metabolites between the two sequences (p-value = 0.4 for ADC, p-value = 0.9 for D_{intra}, two-way repeated measures ANOVA). **C** and **D**: from the mean and SD of individual fits with DW-SPECIAL, Gaussian distributions of ADC (panel **C**) and D_{intra} (panel **D**) were generated for each metabolite and compared to the mean fit (wide black bar) ($p<0.025$ regions on each side of the Gaussian distribution are dark green). The mean fit fell into the Gaussian distribution of the individually fitted ADC and D_{intra} ($p>0.05$) for all metabolites, which confirmed the agreement between the estimates from the mean fit and from the individual fits for DW-SPECIAL.

5.4   Discussion

This paper reports the first implementation and validation of a new diffusion-weighted MRS sequence, the DW-SPECIAL sequence. Our goal was to preserve the advantages of STE-LASER18 used for rodent dMRS acquisitions (absence of cross-terms, slower T_1 than T_2 relaxation during the diffusion time, good voxel localization with limited CSD artefacts and limited sensitivity to B_1 inhomogeneities) while reaching a shorter echo time. By doing so, we improved the detection and estimation of diffusion metrics of J-coupled metabolites and widened the range of investigated metabolites in rodent high field dMRS studies (e.g. to Gln, a metabolite of interest in numerous pathologies).

5.4.1   Preserved advantages of the STE-LASER sequence

Our initial goal was to create a new sequence that will benefit from the advantages of STE-LASER over other conventional dMRS sequences such as diffusion-weighted STEAM, diffusion-weighted PRESS or diffusion-weighted semi-LASER, with a shorter TE. Firstly, DW-SPECIAL allows one to reach long diffusion times, the diffusion gradients being inserted in a stimulated echo block where the magnetization relaxes with T_1 instead of T_2 (like STE-LASER and DW-STEAM but unlike DW-PRESS and DW-LASER). Secondly, asymmetric 90° and adiabatic 180° pulses led to a sharp volume selection and a limited CSD (like DW-LASER and DW-STEAM but unlike DW-PRESS). The slice-selection profile of the asymmetric P10 pulse [210] along the x dimension matched well the one generated by the two adiabatic 180° pulses used in STE-LASER (**Figure 5.3B**).

Its large bandwidth at lower power compared to a symmetric 90° pulse limited CSD artefacts at ultra-high field [248] and its slice-selective nature limited the presence of spurious echoes originating from outside the volume of interest (VOI), whereas STE-LASER excites the whole volume before performing 3D localization [20]. The y profiles for both sequences are convoluted with the coil sensitivity drop at reception on the axis perpendicular to the surface coil, but the smaller contribution of signals distant from the coil with DW-SPECIAL did not substantially reduce the selected y dimension. The y profile in DW-SPECIAL was also similar to the profile shown in the SPECIAL sequence original paper [21]. The inner VOI signal in the y-direction accounted for approximately 75% of the total signal on y (measured with and without slice inversion), thus limiting the subtraction artefacts of the ISIS scheme (**Figure 5.11**).

The z profile is expected to be similar for DW-SPECIAL and STE-LASER as this dimension is selected by a pair of adiabatic pulses in each case: the remaining difference could originate from the shift of the x and y profiles' maximum between the two sequences, leading to a

	Inner VOI	Outer VOI
S_0 without slice inversion (signal from the entire column in the y-direction)	+	+
S_1 with slice inversion (and 180° phase shift of the receiver phase in the phase cycling)	+	−
$S_0 + S_1$	2 x inner VOI	0

$$f_{intra} = \frac{S_0 + S_1}{2\, S_0} = 77\%$$
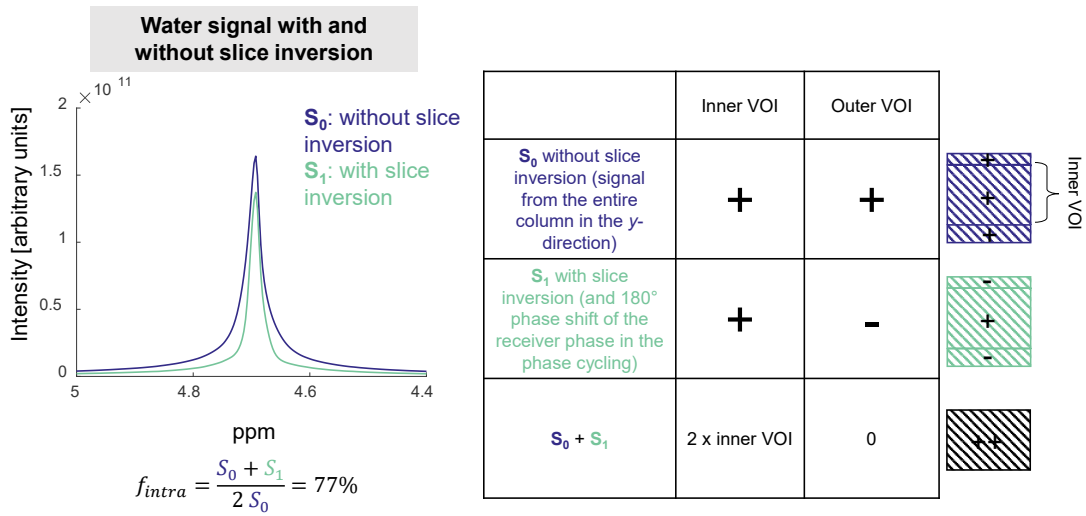
Figure 5.11: Estimation of outer versus inner VOI signal contributions on the y-direction in DW-SPECIAL. Non-localized estimation based on the water signal in a phantom (absolute value of the spectrum) measured on an odd (blue, S_0) and on an even shot (green, S_1). The single-shot intra VOI signal is given by $0.5 \times (S_0 + S_1)$ and the single-shot extra VOI signal is given by $0.5 \times (S_0 - S_1)$. Note that the receiver phase shift is included in the even shots such that the intra VOI signal is given by the sum of 2 consecutive shots (instead of the difference). f_{intra} is 77%: the main contribution of the signal on y comes from inside the VOI, which limits the subtraction artefacts in the ISIS scheme. In vivo, the signal will in addition be weighted by the spatial variations of water and metabolite concentrations.

contribution of signals experiencing different effective B_1 fields. To validate the voxel selection with DW-SPECIAL, the 3D profiles were measured for a smaller voxel in the same phantom (3x3x3 mm^3) positioned in a B_1-homogeneous region. In that case, almost identical profiles were observed between DW-SPECIAL and STE-LASER for the three directions (**Figure 5.12**), further confirming the accurate volume selection with DW-SPECIAL.

Finally, an attractive aspect of the STE-LASER sequence is its block-design, where the diffusion weighting is fully separated from the localization performed with the LASER sequence, leading to the absence of cross-terms between diffusion and imaging gradients contributing to the b-value (unlike DW-STEAM, DW-PRESS and DW-LASER). Although this block-design was not preserved in our newly proposed sequence, the absence of cross-terms was however ensured as follows: a) the localization gradient applied during the on/off 180° ISIS pulse in the mixing time does not take part in the b-value calculation (like all other gradients in the mixing time[81]), and b) the slice-refocusing gradient of the first slice-selective 90° P10 pulse and the first diffusion gradient (striped in **Figure 5.1**) were not applied simultaneously to prevent cross-terms originating from the first part of the STE. The absence of cross-terms was supported experimentally with the within error in vitro diffusion attenuations of mIns, Tau,
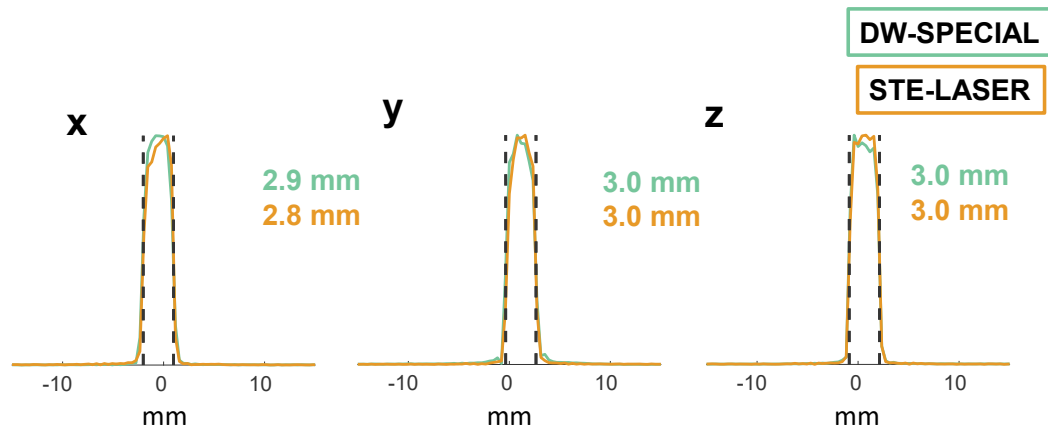
Figure 5.12: 1D projections of the *x, y, z* selection profiles for a small voxel (3x3x3 mm^3) in a B$_1$-homogeneous region measured with DW-SPECIAL (green) and STE-LASER (orange) in the multi-metabolite phantom. The profiles are obtained by switching on the corresponding gradient during the acquisition. The integral values of the profile shapes are displayed. The dashed black lines represent the nominal voxel position in each direction. Negligible difference is observed in the voxel selection between the two sequences when the factor of B$_1$ inhomogeneity is removed, confirming the good selection performed with DW-SPECIAL.

Glu and tCr with DW-SPECIAL and STE-LASER and with a detailed calculation of the b-value (see **Appendix - 1** and **Figure 5.6**). To minimize the increase in minimum TE caused by the separation of these two gradients, we used an asymmetric 90° pulse with an 18% refocusing factor, thus limiting the slice-selective gradient duration and contribution to the echo time. The echo time of the STE diffusion period was similar between the two sequences and mostly governed by the duration of the diffusion gradients. The shorter total echo time achieved with DW-SPECIAL arose from the use of one pair of adiabatic pulses after the STE block, instead of three with STE-LASER.

The pre-processing yielded similar results between the two sequences (**Figure 5.7**), as measured by the amplitude of the frequency and phase correction factors, confirming similar data quality. The frequency-drift correction was small and consistent across b-values ascribed to the recording of a navigator scan at the end of each TR used to dynamically adjust the B$_0$ frequency between each acquisition. The phase fluctuations, however, increased with b-value due to gradient imperfections, motion and flow. Although the number of shots removed did not impair the spectral quality of DW-SPECIAL, a less conservative condition for outlier removal could be considered: indeed, instead of removing an ISIS on/off pair as soon as at least one of the shots is corrupted, one could either equalize, after outlier identification on each of the two subsets, the number of odd and even shots over the total number of shots, irrespective of the pairs forming each ISIS module, or perform outlier removal on already-combined pairs

of shots in DW-SPECIAL (**Figure 5.7B**, bottom).

5.4.2   Improved detection of J-coupled metabolites

In addition to the forementioned properties, the DW-SPECIAL sequence allows one to nearly halve the minimum echo time as compared to STE-LASER (18 ms versus 33 ms). As predicted by simulations, this led to an improved detection of J-coupled metabolites, such as Gln, mIns or GABA experimentally (in phantoms (**Figure 5.5**) and in vivo (**Figure 5.8** and **Figure 5.10**)).

To ensure a reliable comparison of the diffusion properties obtained at different echo times (here with two different sequences), there should be no correlation between the metabolites' relaxation and diffusion properties. This aspect has been investigated in vivo in the mouse brain at 11.7T [108] and showed negligible correlation between the metabolites' relaxation and diffusion properties for a range of echo times between 50 to 110 ms. We expect that this observation can be extended to the range of echo times used in the present work (18 to 33 ms), at least for intracellular metabolites, thus ensuring a reliable comparison of the two sequences.

Although the LASER sequence benefits from a reduced apparent J-evolution and T_2 relaxation compared to other single-voxel spectroscopy sequences at the same TE due to the succession of adiabatic 180° pulses [15, 16] and its current implementation could be further optimized [249], the SPECIAL localization is advantageous when short echo times are desired [20, 8]. At lower fields, the echo time could be even further reduced by converting the pair of adiabatic pulses into a single large bandwidth asymmetric 180° pulse (i.e. converting the semi-adiabatic SPECIAL an asymmetric SPECIAL, as initially proposed [21]). The improvement brought by shortening the echo time was particularly clear for Gln, as shown by a smaller variability of metabolite signal diffusion decays across animals (left-most panels of **Figure 5.8A**) and a better LCModel fit quality (CRLB, top left panel of **Figure 5.8B**) with DW-SPECIAL. An improved Gln quantification with shorter TE could be directly beneficial as Gln concentration is low in healthy cohorts. In hepatic encephalopathy for example, brain Gln can be elevated by more than 100% in rodents [136] and is thus well quantified in the disease group, but remains low in the control group, where DW-SPECIAL could help better quantifying its diffusion properties. Importantly, although well quantified with both sequences, the within-group dispersion of Glu diffusion decays was reduced with DW-SPECIAL, possibly due to a better quantification of Gln and thus a better separation of Glx (Gln + Glu) into Gln and Glu. GABA is also strongly J-coupled and is generally not reported in diffusion studies due to its low concentration and difficult spectral resolution. Data quality obtained with DW-SPECIAL may facilitate the quantification of the diffusion decays of such low-concentrated metabolites as shown on **Figure 5.13** and/or the access to higher b-values.

For the metabolites traditionally reported in rodent dMRS studies (NAA, tCr, tCho, Glu, mIns,

144
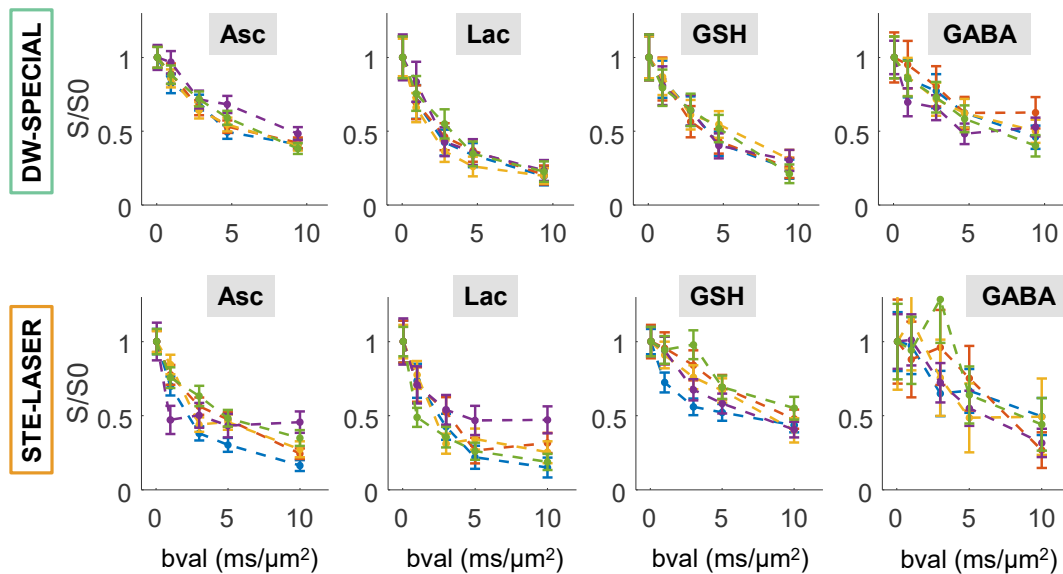
Figure 5.13: Signal diffusion decays of Asc, Lac, GSH and GABA as a function of b-value for all animals (different colors) and both sequences, normalized to their value at b = 0.05 ms/μm². Error bars: absolute CRLB from LCModel quantification. Although these metabolites are generally not reported in DWS studies owing to their low concentration and poor quantification, the shorter TE achieved in DW-SPECIAL leads to a smaller within-group dispersion of their diffusion decays and suggests that these metabolites could possibly be investigated in future studies (through a fit of the mean diffusion decay).

Tau), the ADC values were in good agreement with the ones measured in the mouse brain at 11.7T [59], slightly higher in the present study due to the shorter diffusion time.

Another important feature of DW-SPECIAL is that it may render possible the fit of ADC and D_{intra} based on the metabolite signal diffusion decays of individual animals. Due to the low SNR of dMRS experiments, the authors in the dMRS community have traditionally fitted the diffusion coefficients on the normalized signal decay averaged over animals or subjects, or on cohort-averaged spectra. These two approaches render the estimation of the uncertainty difficult. Even when error propagation or Monte Carlo simulations are used, the computed error on the diffusion coefficients may not accurately represent the dispersion within one group. The agreement between the mean fit and the fit on individual animals for DW-SPECIAL (**Figure 5.10C** and **D**) suggests that, with the spectral quality obtained herein, individual animal fitting may become feasible without a substantial penalty in accuracy. Although the choice of the diffusion model is outside the scope of the present manuscript, it should be noted that the randomly oriented sticks model may not apply well to the macromolecules diffusion decay, which can be described by a mono-exponential decay up to high b-values [250].

5.4.3 Translation to human scanners and limitations

The 1D ISIS module in DW-SPECIAL makes it sensitive to motion artefacts. Whereas this is not a problem in general for rodent experiments where the animal head is fixed by stereotaxic bars, additional care should be taken in human experiments [20]. The introduction of a 90° slice-selective pulse in place of a pair of adiabatic pulses in the same direction in STE-LASER reintroduces some sensitivity to B_1 inhomogeneities. This selection should be performed on the direction with less B_1 inhomogeneities, here the x-direction.

OVS is generally recommended for semi-LASER (at least in the direction of the non-adiabatic slice selection) [249, 251, 252] and SPECIAL (at least in the ISIS and in the non-adiabatic slice selection directions) [8, 21]. In practice here, an OVS module in the three directions was used for both sequences. In the case of STE-LASER, this was done to prevent the creation of spurious echoes originating from outer volume signals relaxing during the mixing time and excited by the non-localized 90° excitation pulse in the stimulated echo diffusion block. However, OVS creates additional RF power deposition and contributes to increasing the SAR. To evaluate the contribution of the OVS module to the average RF power of each sequence, we evaluated the energy deposited in the RF coils during a cycle of 160 shots for STE-LASER and DW-SPECIAL, with and without the OVS module (**Table 5.1**). A 24% lower average RF power was measured for DW-SPECIAL with OVS versus STE-LASER without OVS and a 42% lower average RF power for DW-SPECIAL with OVS versus STE-LASER with OVS (DW-SPECIAL without OVS: 7.6 mW, DW-SPECIAL with OVS: 13.1 mW, STE-LASER without OVS: 17.3 mW, STE-LASER with OVS: 22.8 mW, for a reference power of 27 mW for a 1 ms, 90° hard pulse), confirming that the train of adiabatic pulses is the main cause of elevated SAR in STE-LASER, especially at high fields [20]. In DW-SPECIAL, two pairs of 180° adiabatic pulses were replaced by an on/off adiabatic 180° pulse and an asymmetric 90° pulse, which considerably reduced the SAR and rendered its implementation on human scanners feasible.

Table 5.1: Average power in mW measured in a phantom as the total energy deposited in the RF coils during 160 TR, for the typical RF loading of an in vivo experiment (Reference power for a 90° square pulse (1 ms): 27 mW). This measurement was done with the RF duty cycle tool in PV360 v3.3 for both sequences with and without OVS. The RF power deposition is lower for DW-SPECIAL with OVS than for STE-LASER without OVS, thus demonstrating the benefits of DW-SPECIAL over STE-LASER for SAR considerations.

Power in mW	DW-SPECIAL	STE-LASER
with OVS and VAPOR	13.1	22.8
without OVS but with VAPOR	7.6	17.3

5.5 Conclusion

We conclude that the reduced echo time achieved in DW-SPECIAL improves the detection of short T_2 and J-coupled metabolites compared to STE-LASER, the current gold-standard in rodent dMRS studies at high fields, while preserving the absence of cross-terms in the b-value. Taken together, these advantages make DW-SPECIAL a good candidate to extend the range of investigated metabolites, e.g. to Gln, which is rarely reported in dMRS studies. We further conclude that the reduced number of RF pulses makes DW-SPECIAL an attractive alternative for human dMRS studies, especially at high fields.

5.6 Perspectives

As perspectives to this study, we envision to:

- measure the metabolites ADC and kurtosis at different diffusion times with DW-SPECIAL in BDL and sham rats to information on exchange/restriction as done in ref. [67].

- measure the TE-dependence of diffusion estimates at 14.1T and with shorter TE than in literature [108], now accessible with DW-SPECIAL.

- combine DW-SPECIAL with metabolite cycling, the latter enabling the simultaneous acquisition of water and metabolites. The high-intensity water signal will help with the corrections performed in dMRS: frequency and phase drift corrections and outlier removal [253].

- implement DW-SPECIAL on a human scanner.

- validate modelling hypotheses by performing dMRS experiments (with DW-SPECIAL) in controlled systems like 3D organotypic brain cell cultures [254].

5.7 Appendix

5.7.1 Appendix 1: absence of cross-terms in the b-value in DW-SPECIAL

The b-value is defined as:

$$b = \gamma^2 \int_0^{TE_{seq}} \mathbf{F}(t)^2 dt \tag{5.4}$$

where:

$$\mathbf{F}(t) = \int_0^t \mathbf{g}(t')dt' \tag{5.5}$$

and $\mathbf{F}(t)^2 = <\mathbf{F}(t).\mathbf{F}(t)>$ is the scalar product, $\mathbf{g}$ a vector of gradient amplitudes - including diffusion, slice-selection and spoiler/crusher gradients, and TE_{seq} is the echo time of the sequence.

The cross-terms in the expression of the b-value are terms which are proportional to the scalar product of the diffusion gradients and any other gradients: $\mathbf{g_{diff}}.\mathbf{g_{other}}$. If present, these terms result in an additional contribution to the b-value that does not scale with the sole diffusion gradients amplitude anymore.

In practice, for DW-SPECIAL, the upper bound of the integral can be set to TE_{seq}, the time when the stimulated echo is formed: if no cross-terms appeared in the STE period, none will appear in the second part of the sequence where no diffusion gradients are applied.

We will assume no gradient contribution due to B_0 inhomogeneities. According to *Tanner, Chem. Phys., 1970*, equation 5.4 can be rewritten as:

$$\frac{b}{\gamma^2} =$$

$$\int_0^{\tau_1} \mathbf{F}(t)^2 dt \tag{5.6}$$

$$+ (\tau_2 - \tau_1)(\mathbf{F}(TE_{STE}) - \mathbf{F}(\tau_2))^2 \tag{5.7}$$

$$+ \int_{\tau_2}^{TE_{STE}} (\mathbf{F}(TE_{STE}) - \mathbf{F}(t))^2 dt \tag{5.8}$$

where τ_1 is the time of application of the first 90° block pulse, τ_2 is the time of application of the second 90° block pulse, the time 0 is set the asymmetric center of the first slice-selective 90°, and $TE_{STE} = \tau_1 + \tau_2$. The expressions of (5.7) and (5.8) match the original calculation by *Tanner* because only a diffusion gradient is present in time period between τ_2 and TE_{STE}. We thus have for (5.7):

$$(\tau_2 - \tau_1)(\mathbf{F}(TE_{STE}) - \mathbf{F}(\tau_2))^2 = \mathbf{g_{diff}}^2 \delta^2 (\tau_2 - \tau_1) \tag{5.9}$$

and for (5.8):

$$\int_{\tau_2}^{\text{TE}_{\text{STE}}} (\mathbf{F}(\text{TE}_{\text{STE}}) - \mathbf{F}(t))^2 \, dt = \mathbf{g}_{\text{diff}}^2 \delta^2 (t_2 - \tau_2) + \mathbf{g}_{\text{diff}}^2 \frac{\delta^3}{3} \tag{5.10}$$

where $\mathbf{g}_{\text{diff}}$ is the vector of the diffusion gradient amplitudes, δ is the duration of the diffusion gradients and t_2 is the time of application of the diffusion gradient in time period between τ_2 and TE_{STE}.

The expression of (5.6) differs from the original derivation due to the slice-refocusing gradient $\mathbf{g_s}$. When the latter is applied before the first diffusion gradient (**Figure 5.14A**), the expression of (5.6) is:

$$\int_0^{\tau_1} \mathbf{F}(t)^2 \, dt = \int_0^{t_0} \mathbf{F}(t)^2 \, dt + \int_{t_0}^{2t_0} \mathbf{F}(t)^2 \, dt + \int_{2t_0}^{t_1} \mathbf{F}(t)^2 \, dt + \int_{t_1}^{t_1+\delta} \mathbf{F}(t)^2 \, dt + \int_{t_1+\delta}^{\tau_1} \mathbf{F}(t)^2 \, dt$$

$$= \mathbf{g_s}^2 \frac{t_0^3}{3} + \mathbf{g_s}^2 \frac{t_0^3}{3} + 0 + \mathbf{g}_{\text{diff}}^2 \frac{\delta^3}{3} + \mathbf{g}_{\text{diff}}^2 \delta^2 (\tau_1 - t_1 - \delta) \tag{5.11}$$

where t_0 is the time of application of the slice-refocusing gradient, and t_1 is the time of application of the first diffusion gradient.

The expression (5.11) has no cross terms and is the one used in the present manuscript. If we define the diffusion time Δ as the time between the first and the second diffusion gradients (i.e $t_1 + t_2$) and if we sum the expressions (5.9), (5.10) and (5.11), we retrieve the known expression of the b-value proportional to $\mathbf{g}_{\text{diff}}^2$:

$$\frac{b}{\gamma^2} = \mathbf{g_s}^2 \frac{2t_0^3}{3} + \mathbf{g}_{\text{diff}}^2 \delta^2 (\Delta - \frac{\delta}{3}) \tag{5.12}$$

However, in the case of **Figure 5.14B** where the slice-refocusing gradient and the first diffusion gradient are applied simultaneously (shown in green), (5.6) becomes:

$$\int_0^{\tau_1} \mathbf{F}(t)^2 \, dt = \int_0^{t_0} \mathbf{F}(t)^2 \, dt + \int_{t_0}^{t_1} \mathbf{F}(t)^2 \, dt + \int_{t_1}^{t_1+\delta} \mathbf{F}(t)^2 \, dt + \int_{t_1+\delta}^{\tau_1} \mathbf{F}(t)^2 \, dt$$

$$= \mathbf{g_s}^2 \frac{t_0^3}{3} + \mathbf{g_s}^2 t_0^2 (t_1 - t_0) + \mathbf{g}_{\text{diff}}^2 \frac{\delta^3}{3} + \mathbf{g_s}^2 t_0^2 \frac{\delta}{3} + \mathbf{g}_{\text{diff}} \cdot \mathbf{g_s} \, t_0 \frac{\delta^2}{3} + \mathbf{g}_{\text{diff}}^2 \delta^2 (\tau_1 - t_1 - \delta) \tag{5.13}$$

Cross-terms $\mathbf{g}_{\text{diff}} \cdot \mathbf{g_s}$ appear and are proportional to $t_0 \frac{\delta^2}{3}$.
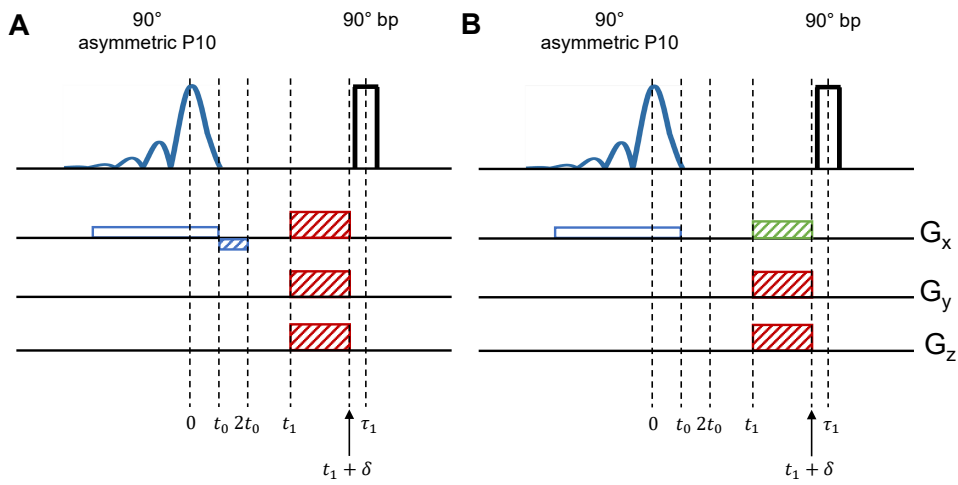
Figure 5.14: Possible positions for the slice-refocusing gradient of the first slice-selective 90°. **A**: slice-refocusing gradient applied before the diffusion gradient, which is the option chosen for DW-SPECIAL and yields to no-cross term. **B**: slice-refocusing gradient and the first diffusion gradient applied simultaneously, allowing to reduce the minimum TE but yielding to cross-terms.

5.7.2   Appendix 2: concentration tables

Table 5.2: Signal amplitudes and relative Cramer Rao Lower Bounds from LCModel fit of DW-SPECIAL spectra averaged over animals at all b-values and for every reported metabolite. Metabolite signals are not referenced to water and their amplitudes are in arbitrary unit: only their relative amplitudes at b = 0.05 ms/µm^2 is of biological relevance. The MM basis-set spectrum was scaled such that its concentration at b = 0.05 ms/µm^2 is in the range 1-4 mM (Cudalbu et al., *https://doi.org/10.1002/nbm.4393*).

DW-SPECIAL – LCModel signal amplitudes (arbitrary units)				
Metabolite	**b = 0.05 ms/µm^2**	**b = 1 ms/µm^2**	**b = 3 ms/µm^2**	**b = 5 ms/µm^2**	**b = 10 ms/µm^2**
Gln	4.8	4.2	3.1	2.5	1.5
Glu	16.4	14	10.8	8.7	6.8
mIns	12.8	11.1	8.8	7	5.2
Tau	9.9	8.1	5.9	4.4	3.2
NAA+NAAG	14.1	12.2	9.5	7.7	5.7
Cr+PCr	14.2	12	9	7	4.8
GPC+PCho	1.7	1.4	1.1	0.9	0.6
MM	2.3	2.3	2.2	2.1	2.1
Asc	7	6.2	4.8	4	2.9
Lac	1.6	1.2	0.7	0.5	0.3
GSH	1.4	1.2	0.9	0.7	0.4
GABA	2.4	2	1.8	1.4	1.2
DW-SPECIAL – LCModel relative CRLB				
Metabolite	**b = 0.05 ms/µm^2**	**b = 1 ms/µm^2**	**b = 3 ms/µm^2**	**b = 5 ms/µm^2**	**b = 10 ms/µm^2**
Gln	0.064	0.066	0.078	0.09	0.116
Glu	0.02	0.02	0.022	0.026	0.028
mIns	0.02	0.02	0.02	0.024	0.03
Tau	0.024	0.028	0.03	0.036	0.042
NAA+NAAG	0.014	0.018	0.018	0.02	0.02
Cr+PCr	0.01	0.012	0.016	0.022	0.034
GPC+PCho	0.04	0.044	0.046	0.056	0.068
MM	0.022	0.022	0.02	0.02	0.018
Asc	0.052	0.054	0.06	0.066	0.072
Lac	0.1	0.124	0.176	0.216	0.284
GSH	0.106	0.114	0.13	0.156	0.234
GABA	0.1	0.11	0.11	0.122	0.124

Table 5.3: Signal amplitudes and relative Cramer Rao Lower Bounds from LCModel fit of STE-LASER spectra averaged over animals at all b-values and for every reported metabolite. Metabolite signals are not referenced to water and their amplitudes are in arbitrary unit: only their relative amplitudes at b = 0.05 ms/μm^2 is of biological relevance. The MM basis-set spectrum was scaled such that its concentration at b = 0.05 ms/μm2 is in the range 1-4 mM (Cudalbu et al., *https://doi.org/10.1002/nbm.4393*).

STE-LASER – LCModel signal amplitudes (arbitrary units)					
Metabolite	**b = 0.05 ms/μm^2**	**b = 1 ms/μm^2**	**b = 3 ms/μm^2**	**b = 5 ms/μm^2**	**b = 10 ms/μm^2**
Gln	4	3.3	2.4	2	1.4
Glu	14.8	12.1	9	7.5	5.3
mIns	10.8	9.1	7.2	6	4.3
Tau	8	6.4	4.6	3.6	2.4
NAA+NAAG	13.5	11.3	8.7	7.4	5.5
Cr+PCr	12	9.9	7.6	6.1	4.2
GPC+Pcho	2.2	1.9	1.5	1.2	0.8
MM	3	2.9	2.8	2.8	2.7
Asc	4.6	3.3	2.3	2	1.3
Lac	1.9	1.3	0.8	0.6	0.5
GSH	1.9	1.6	1.4	1.2	0.8
GABA	2	2	1.7	1.3	0.8
STE-LASER – LCModel relative CRLB					
Metabolite	**b = 0.05 ms/μm^2**	**b = 1 ms/μm^2**	**b = 3 ms/μm^2**	**b = 5 ms/μm^2**	**b = 10 ms/μm^2**
Gln	0.082	0.09	0.112	0.134	0.166
Glu	0.02	0.02	0.026	0.032	0.04
mIns	0.02	0.02	0.02	0.024	0.032
Tau	0.02	0.024	0.03	0.036	0.05
NAA+NAAG	0.01	0.01	0.016	0.018	0.022
Cr+PCr	0.01	0.01	0.01	0.018	0.022
GPC+PCho	0.028	0.032	0.026	0.04	0.054
MM	0.03	0.028	0.028	0.024	0.022
Asc	0.062	0.09	0.106	0.118	0.164
Lac	0.092	0.118	0.174	0.246	0.268
GSH	0.07	0.072	0.08	0.092	0.124
GABA	0.176	0.162	0.176	0.242	0.342

Table 5.4: SD of normalized signal diffusion decays over animals at all b-values and for every reported metabolite, for DW-SPECIAL and STE-LASER.

DW-SPECIAL – SD of normalized signal decays over animals (arbitrary units)				
Metabolite	**b = 0.05 ms/μm^2**	**b = 1 ms/μm^2**	**b = 3 ms/μm^2**	**b = 5 ms/μm^2**	**b = 10 ms/μm^2**
Gln	0	0.05	0.02	0.03	0.04
Glu	0	0.01	0.02	0.03	0.02
mIns	0	0.01	0.03	0.04	0.02
Tau	0	0.02	0.03	0.03	0.02
NAA+NAAG	0	0.01	0.02	0.03	0.02
Cr+PCr	0	0.01	0.02	0.03	0.02
GPC+PCho	0	0.08	0.03	0.05	0.02
MM	0	0.01	0.02	0.02	0.03
Asc	0	0.05	0.03	0.07	0.04
Lac	0	0.07	0.07	0.04	0.02
GSH	0	0.03	0.03	0.06	0.04
GABA	0	0.09	0.06	0.06	0.08

STE-LASER – SD of normalized signal decays over animals (arbitrary units)				
Metabolite	**b = 0.05 ms/μm^2**	**b = 1 ms/μm^2**	**b = 3 ms/μm^2**	**b = 5 ms/μm^2**	**b = 10 ms/μm^2**
Gln	0	0.04	0.13	0.08	0.1
Glu	0	0.04	0.07	0.07	0.04
mIns	0	0.05	0.08	0.05	0.05
Tau	0	0.03	0.1	0.07	0.05
NAA+NAAG	0	0.02	0.04	0.03	0.03
Cr+PCr	0	0.03	0.06	0.05	0.04
GPC+Pcho	0	0.04	0.07	0.05	0.05
MM	0	0.04	0.04	0.04	0.03
Asc	0	0.14	0.1	0.07	0.11
Lac	0	0.11	0.1	0.1	0.13
GSH	0	0.1	0.16	0.08	0.06
GABA	0	0.1	0.26	0.1	0.1

5.7.3 Appendix 3: MRS in MRS table

Table 5.5: MRSinMRS checklist from Lin et al. « Minimum Reporting Standards for in Vivo Magnetic Resonance Spectroscopy (MRSinMRS): Experts' Consensus Recommendations ».

1. Hardware	
a. Field strength [T]	14.1T
b. Manufacturer	Bruker
c. Model (software version if available)	Avance Neo, Paravision 360 v1.1
d. RF coils: nuclei (transmit/receive), number of channels, type, body part	Homemade quadrature 2 loops surface coil (2 cm diameter for each loop)
e. Additional hardware	Gradient strength: 1 T/m, rise time: 270 µs

2. Acquisition	
a. Pulse sequence	DW-SPECIAL and STE-LASER
b. Volume of Interest (VOI) locations	Full brain (voxel location on Fig 2. A)
c. Nominal VOI size [cm^3, mm^3]	$7 \times 5 \times 5$ mm^3
Repetition Time (TR) d. Echo Time (TE) Mixing time (TM)	DW-SPECIAL: TE: 18.4 ms TM: 40 ms TR: 3000 ms STE-LASER: TE: 33 ms TM: 40 ms TR: 3000 ms
e. Total number of Excitations or acquisitions per spectrum	160 shots per b-value for b<10 ms/μm^2 320 shots for b = 10 ms/μm^2 5 b-values from 0.05 to 10 ms/μm^2
f. Additional sequence parameters (spectral width in Hz, number of spectral points, frequency offsets)	7142 Hz 4096 points Duration of diffusion gradients: 3ms
g. Water Suppression Method	VAPOR
h. Shimming Method, reference peak, and thresholds for "acceptance of shim" chosen	MAPSHIM and local iterative shimming in the MRS voxel, target LW: 17-19Hz
i. Triggering or motion correction method	None

3. Data analysis methods and outputs	
a. Analysis software	LCModel v6.3
b. Processing steps deviating from quoted reference or product	EC, phase and frequency drifts correction (spectral registration in FID-A), motion-corrupted shots removal
c. Output measure (e.g. absolute concentration, institutional units, ratio)	Signal amplitudes in arbitrary units
d. Quantification references and assumptions, fitting model assumptions	The basis set includes an in vivo acquired MM spectrum NUNFIL 2048 NRATIO 0 NSIMUL 0 Fit region: 0.2-4.3 ppm

4. Data Quality	
a. Reported variables (SNR, Linewidth (with reference peaks))	SNR: not reported LW: not evaluated Mean and SD across individual animal diffusion decays, CRLB and estimated diffusion parameters. Agreement between these diffusion parameters and the ones derived from the fit of the mean decay.
b. Data exclusion criteria	Shots whose MSE with the median of the shots in frequency domain deviating from more than 1.5 SD from the mean MSE are discarded
c. Quality measures of postprocessing Model fitting (e.g. CRLB, goodness of fit, SD of residual)	SD across animals and LCModel CRLB
d. Sample Spectrum	Figure 2 and 3

6 Denoising for diffusion-weighted MRS

Abstract

Diffusion-weighted magnetic resonance spectroscopy (dMRS) suffers from a lower signal to noise ratio (SNR) compared to conventional MRS owing to the addition of diffusion attenuation. This technique can therefore strongly benefit from noise reduction strategies. In the present work, Marchenko-Pastur principal component analysis (MP-PCA) denoising is tested on Monte Carlo simulations and on in vivo dMRS data acquired at 9.4T in rat brain and at 3T in human brain. We provide a descriptive study of the effects observed following different MP-PCA denoising strategies (denoising the entire matrix versus using a sliding window), in terms of apparent SNR, rank selection, noise correlation within and across b-values and quantification of metabolite concentrations and fitted diffusion coefficients. MP-PCA denoising yielded an increased apparent SNR, a more accurate B_0 drift correction between shots, and similar estimates of metabolite concentrations and diffusivities compared to the raw data. No spectral residuals on individual shots were observed but correlations in the noise level across shells were introduced, an effect which was mitigated using a sliding window, but which should be carefully considered.

Publications

This chapter has been published as:

[255]: **J. Mosso**, D. Simicic, K. Şimşek, R. Kreis, C. Cudalbu, and I. O. Jelescu, "MP-PCA Denoising for Diffusion MRS Data: Promises and Pitfalls," *NeuroImage*, 263: 119634, November 2022.

Contributions

I suggested and implemented the simulations framework, elaborated the denoising strategies and analyzed the data independently. The in vivo rodent data were acquired at 9.4T by Cristina Cudalbu and her group before I started my PhD. The in vivo human data were added at the revision stage of the manuscript and were acquired by Kadir Simsek and Roland Kreis. I wrote the first draft of the manuscript that was editing by all co-authors.

The chapter will present a post-processing denoising method. In parallel to **Chapter 5** targeting an improvement of dMRS data presented in **Chapter 4** at the acquisition level with DW-SPECIAL, this chapter aims for an improvement of dMRS data at the post-processing level. The Marchenko Pastur principal component analysis (MP-PCA) was applied for the first time to dMRS data and its potential to *denoise* spectra was investigated. MP-PCA was already successfully implemented on diffusion MRI data [256, 257] and emerged as an attractive solution to enhance the low SNR of dMRS data. Most importantly, we provide a description of

the non-trivial effects affecting the data properties and the resulting diffusion estimates after MP-PCA, elements which we believe were lacking in the previous literature on the method. A MRS simulation framework (available on https://github.com/jessie-mosso/DWMRS-MPPCA) that could serve other applications was made broadly accessible with the recommendation that the effects of MP-PCA should be thoroughly investigated for each input data before broad application of the method.

6.1   Introduction

Magnetic resonance spectroscopy (MRS) is a powerful technique that provides unique information about brain metabolite concentrations in vivo. Combined with diffusion weighting (DW), information on metabolites' diffusivities which are expected to reflect properties of the tissue microstructure can be extracted [53, 242, 258, 70, 59, 65, 58, 60]. These properties include cell geometry, characteristic sizes of compartments, cytosol viscosity and molecular crowding. Unlike water, metabolites are naturally compartmentalized and probe the intracellular space almost exclusively. Some metabolites are even considered to be largely specific to glial cells, such as glutamine (Gln) or myo-inositol (Ins), some to neurons, such as N-acetyl aspartate (NAA) or glutamate (Glu) [70, 59, 223, 224, 225], while others are found in all cell types, such as creatine in all its forms [259] (total creatine: tCr). This intrinsic compartment specificity makes dMRS an extremely powerful tool to probe brain microstructure, in combination or in contrast to water diffusion MRI.

However, MRS is an inherently low signal-to-noise (SNR) technique due to the much lower concentration of metabolites relative to water, resulting in the need for substantial spectral averaging. For dMRS, even more extended averaging is needed to compensate for diffusion attenuation, and acquisition times become prohibitively long to parse multiple diffusion weightings (b-values), directions or diffusion times. dMRS data is typically acquired in single-voxel fashion. When fine spatial localization is required to study small structures, low SNR cannot be compensated by large voxel volumes. In this case, post-processing methods aiming to minimize the noise variance and its impact on the quantification of MRS signals are needed.

Several denoising schemes have been proposed, but remarkably none of them has been fully adopted by the MRS community [260, 261, 262, 263, 264, 265, 266, 267, 268, 269, 270, 271, 272]. Some of these denoising techniques, typically based on singular value decomposition (SVD) or another sparse representation such as Fourier space or wavelets [270, 271], have been implemented for spectroscopic imaging data (MRSI) [263, 264, 265, 266, 267, 268], and mainly in clinical applications. These methods rely on linear predictability, partial separability of spatial-temporal modes, or both, of such data [264, 265, 266, 267]. In addition, constraints on the spatial distribution of the signal with specific regularization, such as total generalized

variation (TGV), has shown to further enhance the SNR in MRSI reconstruction [267]. TGV regularization aims to denoise by enforcing smooth spatial variations, however with known limitations in terms of detecting focal pathology [269].

The main challenge of sparse representations such as SVD resides in the determination of the appropriate thresholds that separate the noise from the signal. In MRS, this arbitrary threshold can lead to possible elimination of spectral features that are on the same order of magnitude as noise components. Other approaches based on smoothing using splines, sliding windows or Gaussian windows lead to a deterioration of spectral/temporal resolution as well as artefactual auto-correlation [271] Finally, deep learning approaches have been very recently suggested [273, 274], but likely require more investigation to become robust.

One solution to choosing a threshold in a sparse domain has been proposed recently, with the initial aim to denoise diffusion MRI data [256]. It is based on the Marchenko-Pastur principal component analysis (MP-PCA) technique, which exploits the fact that noise eigenvalues follow the asymptotic universal Marchenko-Pastur distribution, a result of the random matrix theory for noisy covariance matrices. This method thus provides a data-driven (more specifically, noise-driven) approach to distinguish noise from the signal components in SVD, since the cut-off is obtained by iteratively fitting the MP distribution to the tail of eigenvalues, and has shown its superiority to TGV for instance [256]. In practice, MP-PCA is suitable for the denoising of data with a high level of redundancy and a constant noise level across them. In the case of a diffusion MRI dataset for example, this could correspond to images acquired with different diffusion-weightings and directions. Since its initial development for diffusion MRI, its applications have been extended to functional MRI [275, 276], T_2 relaxometry [277], preclinical ^{1}H MRSI [268] and ^{31}P MRSI [278]. More recently, the NORDIC [279] method has been introduced and addresses issues that are largely related to clinical diffusion MRI data, namely the use of multi-channel coils for image acquisition acceleration, whose recombination results in a spatially varying and non-Gaussian noise distribution (cf. g-factor maps), and the fact that most data are retrieved and processed in magnitude space, further skewing the noise distribution. In the field of MRS, these two issues are in general not problematic since the multiple coil data featuring Gaussian noise are linearly combined maintaining the Gaussian characteristics, and since complex-valued data is used. In the broader context of matrix denoising, soft thresholding and optimal shrinkage of singular values [280, 281, 282] have shown to outperform hard thresholding like MP, especially in the case of low SNR input matrices.

The aim of the present study was to implement and test the potential of MP-PCA for denoising ^{1}H dMRS. The performance of MP-PCA was tested using Monte Carlo simulations and in vivo experiments in rat brain at 9.4T and in human brain at 3T.

6.2 Methods

The following terminology will be used throughout the manuscript. The SNR referred to as *time-domain SNR* in simulations is defined as the magnitude (absolute value) of the first complex point of the FID over one standard deviation (SD) of noise, taken on the real part of the FID tail (time points 1500 to 2048) [30]. The SNR referred to as *spectral SNR* or *SNR* corresponds to the SNR of the NAA singlet at 2.01 ppm, defined as the NAA peak height taken on magnitude spectra to avoid phasing and linewidth issues, over one standard deviation of noise taken in a noise-only region of the real part of the spectra (from 8.2 to 10.9 ppm for simulations and rodent data, and 13.0 to 20.1 for human data).

The term *apparent SNR* will be used to refer to the SNR after denoising. The term *shot* will be used to refer to every complex FID in each shell, i.e. of a row of matrix Z, according to a recent consensus on terminology in MRS [30]. The terms *shell* will be used to designate a set of 100 (simulations), 128 (in vivo – rodent), and 32 (in vivo – human) shots for a given b-value. The term *estimated spectral fit uncertainty (ESFU)* [283] will be used to refer to the estimated lower error bounds for the concentration estimates determined by LCModel, for which the term *Cramer Rao Lower Bounds (CRLB)* may not apply after denoising.

6.2.1 Theory

Let Z be an initial noisy matrix in the temporal domain, $Z \in \mathscr{M}_{n \times m}(\mathbb{C})$, where n is the number of shots, and m is the number of time points in the FID signal:

$$Z = \widetilde{Z} + \varepsilon$$

where $\widetilde{Z} \in \mathscr{M}_{n \times m}(\mathbb{C})$ is the signal information and $\varepsilon \in \mathscr{M}_{n \times m}(\mathbb{C})$ the Gaussian, uncorrelated noise. For this section, we will assume that $2n < m$ and $2n \gg 1$ (asymptotic condition of the MP law). The real and imaginary parts of Z are concatenated on the first dimension (n), and the resulting matrix $Y \in \mathscr{M}_{2n \times m}(\mathbb{R})$ is centered, such that:

$$X = Y - \mathbf{1}_{2n}^{T} \overline{Y}$$

where $X \in \mathscr{M}_{2n \times m}(\mathbb{R})$, $\overline{Y} \in \mathscr{M}_{1 \times m}(\mathbb{R})$ is the column-wise mean of Y and $\mathbf{1}_{2n}^{T}$ is a column vector of $2n$ ones. Matrix X is then decomposed using the singular value decomposition:

$$X = USV^{T}$$

where $U \in \mathcal{M}_{2n \times 2n}(\mathbb{R})$, $S \in \mathcal{M}_{2n \times m}(\mathbb{R})$ and $V \in \mathcal{M}_{m \times m}(\mathbb{R})$. Columns of U are singular vectors of the first dimension (shots), columns of V are singular vectors of the second dimension (time points) and S contains the singular values of X, arranged in descending order, which are also the square root of the eigenvalues of $X^T X$. Since $X = Y - \mathbf{1}_{2n}^T \overline{Y}$, $\frac{1}{2n} X^T X$ is the covariance matrix of Y. The Marchenko-Pastur distribution is then fitted to the smallest non-zeros eigenvalues λ of $\frac{1}{2n} X^T X$:

$$p\left(\lambda \middle| \sigma, \frac{(2n - P)}{m}\right) = \begin{cases} \frac{\sqrt{(\lambda_+ - \lambda)(\lambda - \lambda_-)}}{2\pi\lambda\sigma^2 \frac{(2n-P)}{m}} & \text{if } \lambda_- \leq \lambda \leq \lambda_+ \\ 0 & \text{otherwise} \end{cases}$$

where σ is the noise level estimated from the input matrix X, P is the number of signal-carrying eigenvalues, λ_- the smallest noise-related eigenvalue and λ_+ the largest. P corresponds to the number of values λ such that $\lambda \geq \lambda_+$, with $\lambda_+ = \sigma^2 \left(1 + \sqrt{\frac{2n-P}{m}}\right)^2$. The matrix Y can then be approximated by:

$$\widehat{Y} = U S_P V^T + \mathbf{1}_{2n}^T \overline{Y}$$

where S has been truncated at rank P.

6.2.2 Monte Carlo simulations

Synthetic ^{1}H MR spectra were created (Matlab, MathWorks, Natick, MA, USA) to mimic experimental conditions in the rat brain (see Section 2.3 below). 19 metabolites, listed with their corresponding concentrations in **Table 6.1** were simulated using NMRSCOPE-B from jMRUI [213], with published J-coupling and chemical shifts constants [211, 212] and the SPE-CIAL sequence (9.4T, echo time (TE) = 2.8 ms). The lineshapes of the individual signals were constructed using a sum of 0.2 Hz Lorentzian and 1.8 Hz Gaussian apodizations, and a full macromolecule spectrum acquired in vivo (MM, 1.3mM) was included [35].

The free induction decays (FID) were generated with 2048 points. Diffusion weighting was simulated using Callaghan's model of diffusion in randomly oriented sticks [69], with ten b-values: 0.4, 1.5, 3.4, 6, 7.6, 13.4, 15.7, 20.8, 25.2, 33.3 ms/μm^2. Intra-stick free diffusion coefficients ranging from 0.265 to 0.67 μm^2/ms (**Table 6.1**) were attributed to the 19 metabolites and 0.005 μm^2/ms to the MM. Metabolite free diffusivities were set to be five times the apparent diffusion coefficient (ADC) of the ensemble of randomly-oriented cellular processes in the rodent brain from literature [59]. These values were retrospectively found to be in the same range as the intra-stick free diffusion coefficients estimated in vivo in the present work. A resid-

Table 6.1: Simulated metabolites with their respective concentrations and diffusion coefficients used in the MC simulations.

Metabolite	Conc (mM)	D_{intra} (μm^2/ms)	Metabolite	Conc (mM)	D_{intra} (μm^2/ms)
Alanine (Ala)	0.8	0.2695	Lactate (Lac)	0.8	0.65
Ascorbate (Asc)	1.5	0.3115	N-acetylaspartate (NAA)	9	0.4
Aspartate (Asp)	2	0.67	scyllo-Inositol (Scyllo)	0.1	0.3805
Creatine (Cr)	4	0.5	Taurine (Tau)	4.5	0.55
Phosphocreatine (PCr)	4.5	0.5	Glucose (Glc)	1.7	0.57
gamma-Aminobutyric acid (GABA)	1.6	0.378	N-acetylaspartyl-glutamate (NAAG)	0.3	0.4
Glutamine (Gln)	3	0.384	Phosphatidyl-ethanolamine (PE)	0.5	0.318
Glutamate (Glu)	10	0.5	Glycerophos-phocholine (GPC)	0.8	0.45
Glutathione (GSH)	1.5	0.2655	Phosphocholine (PCho)	0.2	0.45
myo-inositol (mIns)	6.5	0.45			

ual water signal was added to each spectrum (16 Hz Lorentzian line width, mono-exponential decay with apparent diffusivity 0.2 μm^2/ms, random phase). An additional 5 Hz Lorentzian line broadening was finally applied to all spectra. To simulate the full dataset for MP-PCA denoising (matrix Z), Gaussian noise was added to the real and imaginary parts of the FID, with a single shot time-domain SNR of 13. One hundred noisy FIDs were generated for each b-value (constituting a "shell") and B_0 drifts (random -15/+15 Hz drift) and phase distortions (random 0/30° phase) were added on individual shots, mimicking high SNR experimental in vivo rodent dMRS data. The initial matrix Z thus consisted of 1000 rows (10 b-values, 100 shots per b-value) and 2048 columns (FID time points).

Finally, the matrix Z was generated 100 times with different noise realizations, water residual signal, B_0 drifts and phase distortions, and the effect of denoising on simulations was assessed in terms of variations across the MC iterations.

6.2.3 In vivo rodent experiments

All experiments were approved by The Committee on Animal Experimentation for the Canton de Vaud, Switzerland. ^{1}H dMRS acquisitions were performed on a horizontal actively shielded

9.4 Tesla system (Magnex Scientific, Oxford, UK) interfaced to a Varian Direct Drive console (Palo Alto, CA, USA) and equipped with 400 mT/m gradients using a home-built 14 mm diameter surface ^{1}H-quadrature transceiver.

Four adult male Wistar rats were scanned under isoflurane anesthesia ($\approx$ 1.5%). During the dMRS experiments, animals were placed in an in-house-built cradle, and their head was fixed in a stereotaxic system (bite bar and a pair of ear bars). The respiration rate and body temperature were monitored using a small-animal monitor system (SA Instruments, New York, NY, USA). Body temperature was measured with a rectal thermosensor and maintained at 37.7 ± 0.2 °C by warm water circulation.

First- and second-order shims were adjusted using FASTMAP [284], achieving water linewidths of 18-21 Hz in the volume of interest (VOI). dMRS data were acquired using a diffusion-weighted STEAM sequence [4, 17, 86] (TE/mixing time (TM)/repetition time (TR) = 15/112/4000 ms) in a VOI of 162 to 245 μL depending on the animal. The water signal was suppressed by using the VAPOR module interleaved with outer volume suppression blocks [210]. Diffusion gradients were applied simultaneously along three orthogonal directions (δ = 6 ms, Δ = 120 ms). A total of eleven b-values with 128 shots were acquired: 0.4, 1.5, 3.4, 6.0, 7.6, 9.3, 13.4, 15.7, 20.8, 25.2 and 33.3 ms/μm^2.

6.2.4   In vivo human experiments

Human ^{1}H dMRS acquisitions were performed on a 3 Tesla Magnetom Skyra Connectom-A system (Siemens Healthineers Erlangen, Germany), equipped with 300 mT/m gradients and using a 32-channel head coil.

Four healthy volunteers (3 males/1 female) out of the twelve in the cohort of ref [250], featuring the highest water SNR at b = 1.4 ms/μm^2 and the least drop for the 0.9 ppm MM signal, were selected to test the denoising procedure. All experiments had been approved by the competent ethical review board. A voxel (23±2 cm^3) was positioned in the occipito-parietal cortex and dMRS acquisitions were performed with an ECG-triggered diffusion-weighted STEAM sequence (TE/TM/TR$_{min}$=30/65/1800 ms). Eleven b-values were acquired (0.37, 1.4, 2.7, 5.4, 8.2, 10.9, 15.5, 18.4, 21.6, 23.3 and 25.1 ms/μm^2) using metabolite cycling, where some of the b-values had multiple sets of thirty-two shots. Thirty-two metabolite and thirty-two water spectra (4000 Hz spectral width, 4096 complex points) were constructed from 64 shots per b-value by difference and summation, respectively.

6.2.5 MP-PCA denoising

For simulations and rodent data, the raw data individual spectra in matrix Z were first eddy-current- and phase-corrected (maximization of the area of the metabolite region for each spectrum). For human data, frequency drifts between shots were corrected prior to denoising as part of the M-MoCom script in refs [250, 253]. The water spectral region was cut out to remove artefactual residuals (20.9 to 9.05 ppm-region concatenated to the 4.16 to -11.5 ppm-region.) After denoising and before summation, motion correction was applied in two steps (W-MoCom, M-MoCom) as described in ref [250], except that the W-MoCom factors were derived for the metabolite spectra (2-shots) instead of for the individual shots. The correction factors were derived on the raw data and applied to both the raw and denoised data. These two steps, which rescale each spectrum differently, and thus change the noise level, have to be performed after MP-PCA. For all input data, the resulting complex-valued FID were split into real and imaginary parts and organized into a matrix Y where the second dimension contained the time domain sampling and the first dimension a concatenation of all shots/b-values/real and imaginary parts. This was done in order to balance the number of rows with the number of columns and to increase the smallest dimension of X. The matrix Y was centered column-wise and assigned to matrix X. A summary of the denoising strategies and of the study design is presented in **Figure 6.1**.

MP-PCA denoising performances were first tested on shots with no diffusion weighting ("single-shell") and different noise generations on the MC simulations, and compared to summation of the individual shots. A matrix X of size 200 × 2048 was made of 100 single shots of the same shell (here: b = 0), for multiple noise levels (SNR 13 – **Figure 6.2** and SNR 1, 2 and 5 – **Figure 6.3**), as well as without or with phase/frequency drifts in the original spectrum (**Figure 6.2** and **Figure 6.3**, respectively).

For denoising heterogeneous matrices X composed of all b-values ("multi-shells"), two strategies were compared, both on MC simulations and on in vivo data:

1) **Multi-shell full matrix denoising - strategy 1**: MP-PCA denoising was performed on the full matrix. For MC simulations, the matrix X to denoise was of size 2000 × 2048: 10 shells with 100 shots (i.e. noise realisations), and recreated 100 times. For in vivo rodent data, the matrix X to denoise was of size 2816 × 2048: 11 shells with 128 shots. For in vivo human data, the matrix X to denoise was of size 832 to 960 × 3481: 13 to 15 shells with 32 shots.

2) **Multi-shell sliding window (sw) denoising - strategy 2**: MP-PCA denoising was performed on a subset of the full matrix, using a sliding window of sub-blocks of three shells among all shells, and the denoised spectra output is selected when the shell is the
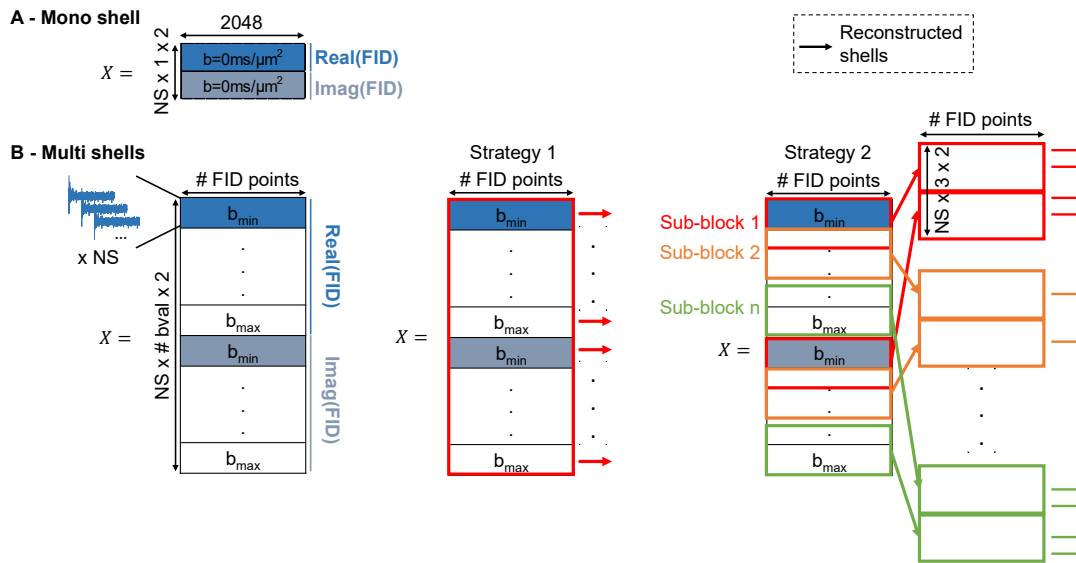
Figure 6.1: Study design and denoising strategies. **A:** Matrix organization for denoising a single-shell. This approach led to a similar result as summation of the shots on MC simulations (see **Figure 6.2**). **B:** Matrix organization for multi-shell full matrix (strategy 1) and sliding window denoising (strategy 2), the latter showing a reduced noise heterogeneity across shells. Strategy 3 (identical to strategy 2 with half the number of shots) is not displayed, showing similar results as strategy 3, yet with an increased number of outliers in the diffusion decay estimates. NS: number of shots, # bval: number of b-values.

middle of the 3-shell sub-block (similarly to the dMRI procedure [256]). The first and last shells were selected together with the second shell and one before last from the first and last sub-blocks, respectively (**Figure 6.1**).

The same denoising procedure as strategy 2 but using only half of available shots (**strategy 3)** was tested on simulations and on in vivo rodent data, with 50 and 64 shots per b-value, respectively. This strategy aimed at assessing whether a reduction in scan time for the same data quality could be achieved, comparing datasets with fewer and denoised shots to the original complete sets.

6.2.6 Quantification and modelling

Raw and denoised simulations and rodent spectra were further corrected for B_0 drifts (alignment of the tCr peak at 3.03 ppm or NAA at 2.01 ppm in each spectrum to its position in the first spectrum after 8 Hz apodization) and summed (for each b-value).

Metabolite concentrations were quantified using LCModel. The metabolite basis set was composed of the noiseless simulated signals for the MC study, and of spectra simulated using

the acquisition parameters for the in vivo acquisitions, all basis sets containing an in vivo-acquired macromolecule signal. In addition, for the in vivo rodent data, separately simulated MM and lipid components from LCModel were included to compensate for possible lipid contamination due to the large size of the voxel and its position close to the scalp [285, 34]. The LCModel parameter controlling the baseline stiffness, DKNTMN, was set to 0.25.

The randomly oriented stick model was fitted to the decay of each metabolite concentration as a function of b-value using a non-linear least squares algorithm in Matlab (*fit* function, *Trust-Region* method). The concentration decays as a function of b-value were fitted for each of the 100 MC iterations for simulations, and for each rat or volunteer individually for the in vivo data. The median estimated diffusion coefficients D_{intra} with SD (across the 100 MC iterations or across the animals/volunteers) were extracted. Percentage bias is reported for the concentrations and D_{intra} ((Value$_{method}$-Value$_{noiseless}$)/Value$_{noiseless}$).

Statistical tests were performed in RStudio (RStudio, PBC, Boston, MA). For simulations, D_{intra} estimates based on raw and denoised data (from each denoising strategy) were compared to the D_{intra} estimate from the noiseless data using a repeated-measures one-way ANOVA, and p-values were corrected for multiple comparisons with Dunnett's post-hoc test. For in vivo data, D_{intra} estimates based on raw and denoised data (from each denoising strategy) were compared using a repeated-measures one-way ANOVA, and pairwise p-values were corrected for multiple comparisons with Tukey's post-hoc test. The following statistical significance values were used: * $p<0.05$, ** $p<0.01$, *** $p<0.001$, **** $p<0.0001$.

Data availability statement: the MP-PCA Matlab code had been made publicly available by the authors of ref. [256], on the following repository: https://github.com/NYU-DiffusionMRI/mppca_denoise. The Matlab code used to generate the simulation data is available on the following repository: https://github.com/jessie-mosso/DWMRS-MPPCA. Rodent experimental data used in the present manuscript are available upon reasonable request to the Corresponding Author.

6.3 Results

The performance of the denoising strategies was assessed in terms of apparent SNR, spectral residuals (denoised summed spectra minus raw summed spectra for a given shell), rank selection, noise correlation within and across shells, as well as precision and accuracy of metabolite quantification for each b-value and of resulting diffusivity estimation.

6.3.1 Monte Carlo simulations

This section aims to study the effect of MP-PCA denoising on simulated dMRS data while having access to the ground truth.
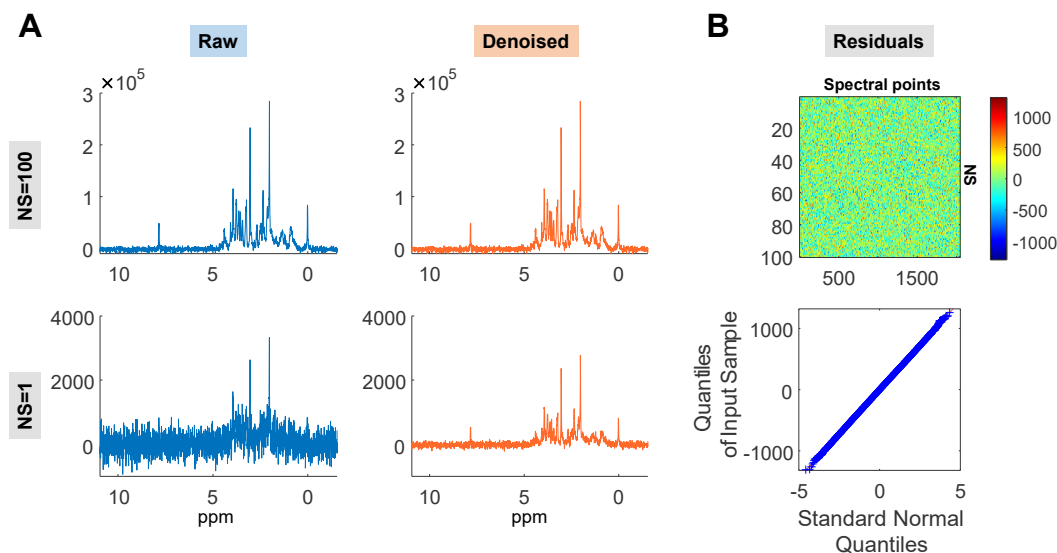
Figure 6.2: MP-PCA denoising performance on NS = 100 shots of the same shell (with different noise realizations and no phase/frequency drifts). **A**: Raw (blue) and denoised (orange) spectra, of the summed 100 shots (top) and of a single shot (bottom): $SNR_{raw,100}$ = 101.9, $SNR_{raw,1}$ = 11.0, $appSNR_{dn,100}$ = 101.8, $appSNR_{dn,1}$ = 51.2. **B** top: Residuals (Denoised minus raw matrix) for the real part of the spectra. **B** bottom: Quantile-quantile (Q-Q) plot of the spectral residuals. Denoising a single-shell performs similarly to the summation of single shots (rank P = 1 selected by the MP fit) and yields a Gaussian distribution of residuals.

Single-shell: MP-PCA denoising versus summation

Figure 6.2 shows the performance of MP-PCA denoising on a single-shell matrix, i.e. NS = 100 shots of a spectrum with no diffusion weighting. Since summation (accumulation of spectra with different noise realisations but the same signal content) is a very efficient denoising strategy, it will be compared to MP-PCA. For a single-shell, denoising performs similarly to averaging on the summed spectra (NS = 100, **Figure 6.2A**, top) and a rank P = 1 is selected by the MP fit. Single shots are also strongly denoised (NS = 1, **Figure 6.2A**, bottom) but this representation should be handled with care since single shots are reconstructed from the entire denoised matrix and thus are not an equivalent representation of single shot raw data. The spectral residuals (100 shots × 2048 real spectral points) follow a Gaussian distribution and no structure in the metabolites' region was observed (**Figure 6.2B**). When phase and
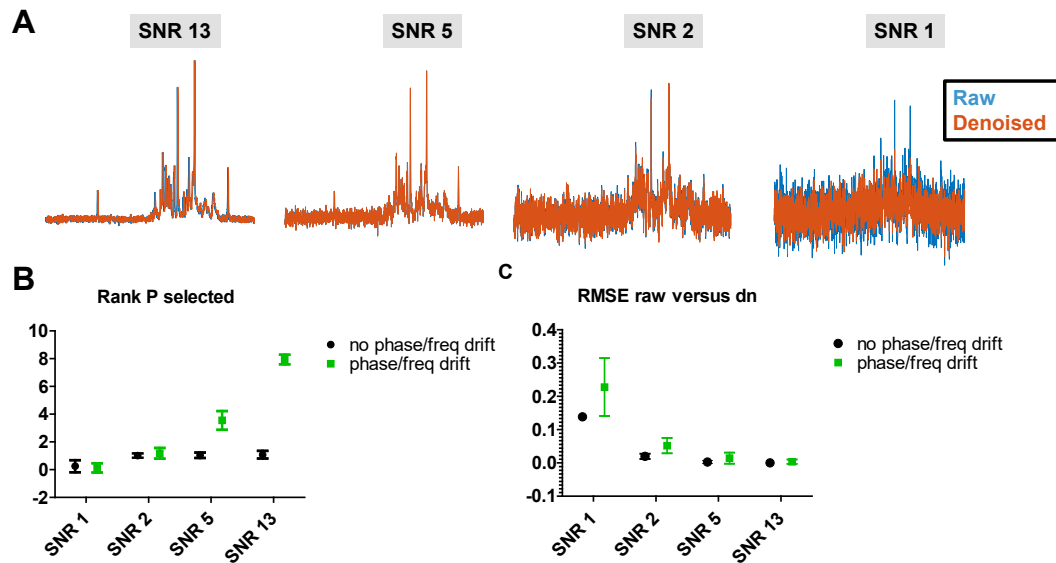
Figure 6.3: Dependence of denoising performance on the original signal to noise ratio (SNR) of the spectra, and on potential phase and frequency drifts, for a series of 100 individual, non-diffusion-weighted spectra. **A**: Overlap of the raw and denoised spectra (sum over 100 shots) for multiple SNR values, in the absence of phase or frequency drifts. For SNR 1, the spectral information is hardly recovered. From SNR 2 to 13, no or little difference between raw and denoised spectra is observed, even in the presence of phase and frequency drifts, which confirms MP-PCA denoising is similar to averaging in the case of repeated measurements at sufficiently high SNR. **B**: Number of signal-carrying principal components P retained by the MP fit, as a function of SNR and of the presence/absence of phase and frequency drifts. P is expected to be 1 in the general case of repeated measurements only altered by noise between different iterations. In our work, for the single-shell, the concatenation of real and imaginary parts yields a rank 2 before centering, and a rank 1 after centering. In practice, it is on average equal to 1 for SNR 2 to 13 in the absence of drift and phase distortions. When adding drift and phase distortions, P increased with the SNR. The frequency drift plays a larger role than phase in this observation, since it adds structured information in both dimensions of the matrix, which is preserved and rendered as signal-carrying components at high SNR. For SNR 1, P is close to zero and hardly no signal information is retained. **C**: Root mean squared error (RMSE) between the real part of the summed raw versus denoised spectra, where the amplitude of NAA is normalized to one. The RMSE increases with decreased SNR and addition of phase and frequency drifts, as previously observed [266]. For panels **B** and **C**, the mean and standard deviations across 100 Monte Carlo iterations are displayed.

frequency drifts are applied across shots on the simulated spectrum, and at sufficiently high SNR, a rank P > 1 is retained by the MP fit (**Figure 6.3B**).
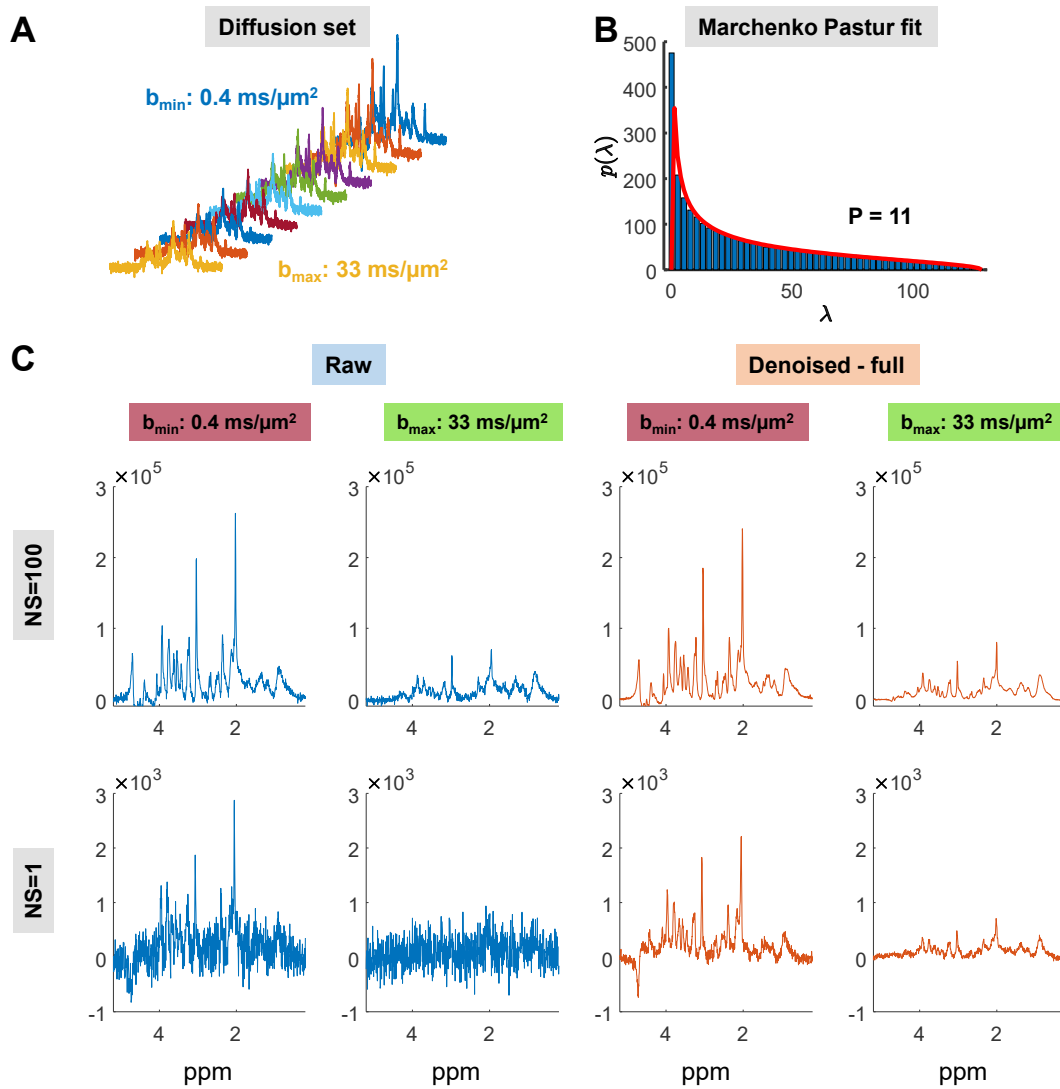
Figure 6.4: MP-PCA denoising performances on the full diffusion-weighted matrix X made up of 10 shells, with 100 shots (NS) each ($10 \times 100 \times 2 \times 2048$ FID points – '$\times 2$' is for the concatenation of real and imaginary parts of the FID) – strategy 1. **A**: Simulated diffusion-weighted spectra at each b-value. **B**: Example MP fit on matrix X for strategy 1 for one MC iteration. **C**: Example raw and denoised spectra, at low and high b-value, of the sum of the 100 shots (top) and of a single shot (bottom). $SNR_{raw,100,bmin} = 90.4$, $SNR_{raw,1,bmin} = 11.9$, $SNR_{raw,100,bmax} = 24.0$, $SNR_{raw,1,bmax} = 4.3$, $appSNR_{dn,100,bmin} = 229.3$, $appSNR_{dn,1,bmin} = 41.8$, $appSNR_{dn,100,bmax} = 155.4$, $appSNR_{dn,1,bmax} = 27.7$. Denoising improves apparent spectral SNR.

Multi-shell - strategy 1: MP-PCA denoising on the entire diffusion-weighted matrix

Figure 6.4A shows simulated diffusion-weighted spectra at 10 b-values. 11 principal components were retained by the MP fit (**Figure 6.4B** and **Figure 6.5C** for their representation). The
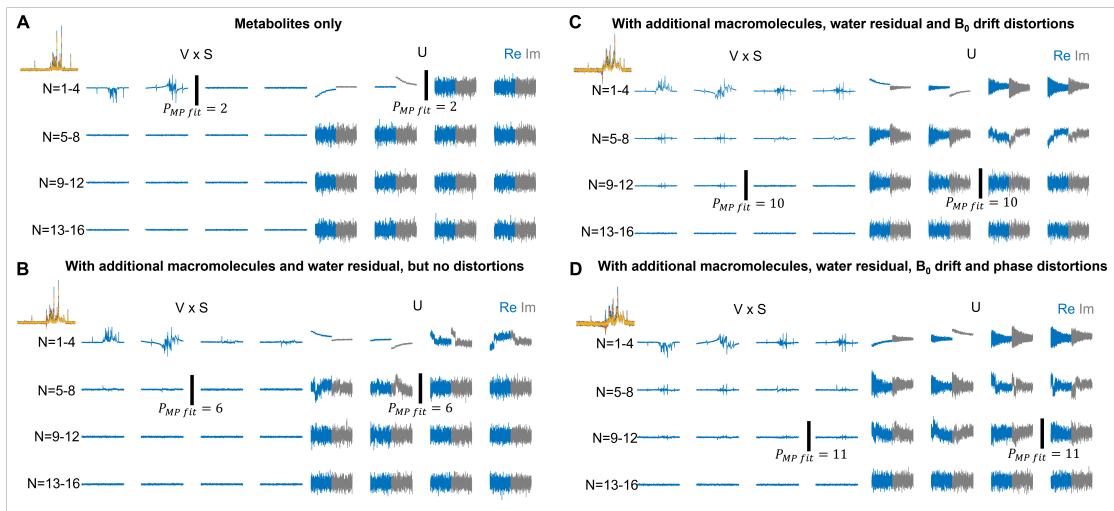
Figure 6.5: Representation of principal components for a simulated matrix made up of 10 shells of 100 shots each, where the real and imaginary parts have been concatenated and where MP-PCA has been applied on frequency-domain for an easier visualisation of the PC. The input matrix has been simulated with varying levels of complexity: metabolites only (**A**), panel **A** + macromolecules and residual water (**B**), panel **B** + B_0 drift distortions (**C**), panel **C** + phase distortions (**D**). Panel **C**, where macromolecules and water residual have been included and B_0 drift is uncorrected prior to denoising, is the case described in the main manuscript: a rank P = 10 is selected by the MP-fit and the spectral and B0 drifts components are well separated from the noise.

raw and denoised spectra for the two extreme b-values are shown in **Figure 6.4C**, for a single shot (bottom) and for the sum of the 100 shots (top). Denoising yields an improved spectral apparent SNR, on individual shots and on their sum.

The central panel of **Figure 6.6A** shows that the noise level is non-uniform across shells after denoising with strategy 1, the shell containing the higher b-value experiencing a stronger denoising effect, as evidenced by the ratio of spectral noise variances at b_{min} and b_{max}. Although the noise level is shell-dependent, its distribution in a noise-only spectral region within one shell remained Gaussian after denoising.

Multi-shell - strategy 2 versus strategy 1

An alternative strategy of denoising using a sliding window of 3 shells, denoted as a "sub-block", is proposed (strategy 2), and aims at reducing the non-uniform noise level across shells introduced by strategy 1. This resulted in minimal SNR heterogeneity within each sub-block on which the denoising was applied and is similar to what is used in dMRI [257] where the columns of matrix X are composed of a sliding spatial kernel of voxels. However, here we strive to reduce heterogeneity in the diffusion dimension (row-wise).
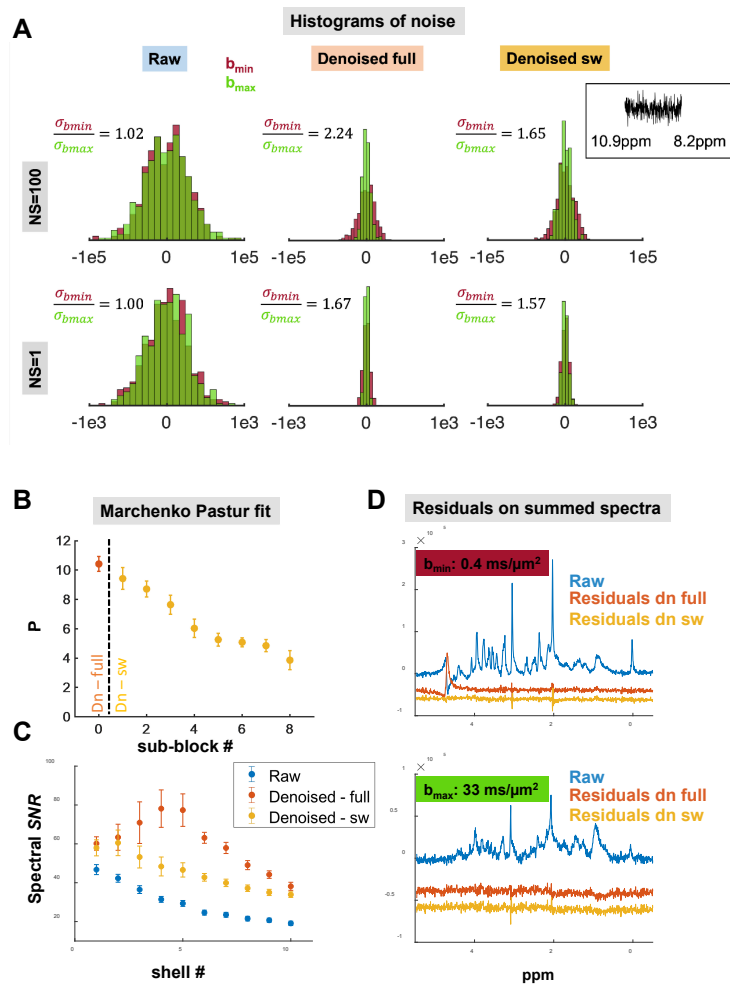
Figure 6.6: Comparison of MP-PCA denoising performance on the full matrix (strategy 1) or using a sliding window of 3 shells over the diffusion-weighted matrices (strategy 2). **A**: Histograms of spectral noise between 8.2 and 10.9 ppm (a region with no signals), for a single shot (bottom) and for the sum of the 100 shots (top), before and after denoising using strategies 1 and 2, for the lowest (red) and highest (green) b-values. The mean ratio across MC iterations of the noise level at b_{min} over the one at b_{max} is displayed in each case. Standard deviations across MC associated to the mean ratios displayed: for NS = 100, 0.04 (raw), 0.24 (dn full), 0.15 (dn sw), and for NS = 1, 0.05 (raw), 0.33 (dn full), 0.40 (dn sw). **B**: Number of principal components retained as signals (i.e. the rank P) by the MP fit, in strategy 1 (orange) and for each sub-block in strategy 2 (yellow), as mean and SD across MC iterations. **C**: Spectral (apparent) SNR on the summed spectra for each shell of raw and denoised data (strategy 1 & 2), as mean and SD across MC iterations. **D**: Spectral residuals on the summed spectra for the two denoising strategies at low (top) and high (bottom) b-values, shifted downwards for display. Both denoising strategies gave heterogeneous noise levels and increases in apparent SNR with no structure in spectral residuals. Strategy 2 mitigates some effects of strategy 1, namely the non-uniform SNR gain and variance across shells.

Although strategy 2 shows smaller noise reductions versus raw compared to strategy 1 (at b_{min}, 2.3 apparent SNR increase for strategy 2 versus 2.7 for strategy 1, at b_{max}, 3.6 apparent SNR increase for strategy 2 versus 6.8 for strategy 1, **Figure 6.6C**), it reduced the non-uniform noise levels across shells (**Figure 6.6A**). On the summed spectra: $\frac{\sigma_{bmin}}{\sigma_{bmax}} = 2.24$ for strategy 1 and $\frac{\sigma_{bmin}}{\sigma_{bmax}} = 1.65$ for strategy 2, whereas this ratio before denoising was close to 1 since single shots were created with the same noise level in each shell. The excessive noise reduction at high b-values (and potential wiping of signal) is also manifest, yet reduced with strategy 2. Noise levels on single shots display the same overall pattern as on the sum (**Figure 6.6A**, bottom). These observations suggest that some correlation is introduced in the noise, also shown in **Figure 6.7**.

The decreasing number of signal-carrying components retained by the MP fit as a function of sub-block number (**Figure 6.6B**) highlights that, at low SNR (i.e. the noisiest sub-matrix, containing the highest b-values), less meaningful information can be separated from the noise (also shown in **Figure 6.3**). In strategy 2, the apparent spectral SNR (**Figure 6.6C**) increases by a factor of 2.3 at b_{min} and 3.7 at b_{max} and follows a similar trend as in the raw data. However, it reaches a maximum for central b-values in strategy 1, possibly resulting from a "decay" of the apparent noise levels, as detailed in **Figure 6.8**. The term SNR after denoising should be used carefully in the light of the noise correlations described below (**Figure 6.7**).

The summed residuals across shots (**Figure 6.6D**) show hardly any structure in the metabolites' region. The weak residuals around the NAA and Cr peaks may be caused by differences between the phase and frequency drift correction factors estimated from the raw or denoised data, or a change in linewidth after denoising, leading to spectral misalignment before summation [286].

We further analysed the correlations of the NAA peak amplitude and of the noise between single shots and the sum of NS = 100 introduced by MP-PCA (**Figure 6.7**). The NAA peak amplitude at b_{min} (top left) scales with the number of shots (NS = 100), as expected, both for raw and denoised data. At lower SNR (b_{max}, bottom left), the NAA peak amplitude on the raw data does not exactly scale with NS because of possible artefacts in the summation, such as improper frequency/phase drifts correction, leading to partially incoherent summation. For the denoised data, the coherent summation property seems to be restored (amplitude ratio close to 100), which can be due to an improved frequency/phase drifts correction after denoising (**Figure 6.9**) and/or to the creation of more self-similar spectra after rank truncation. The noise level in the raw data displays a ratio that scales with $\sqrt{NS}$, as expected, both for b_{max} and b_{min}. For the denoised data, some correlation in the noise across shots is introduced by both denoising strategies, leading to a noise ratio scaling with a factor greater than $\sqrt{NS}$.
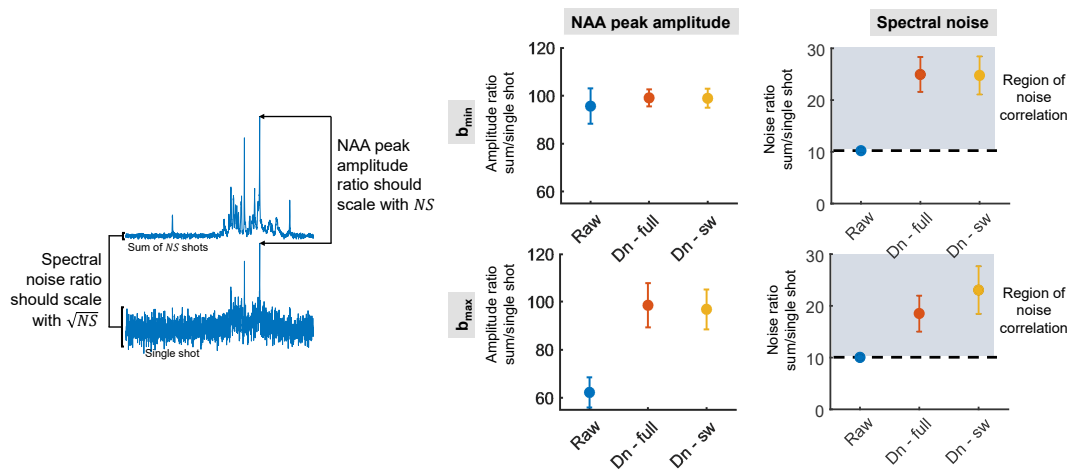
Figure 6.7: Increased correlation in NAA peak amplitude and noise level after denoising, for low and high diffusion weighting, between one shot and the sum of NS shots within a shell. Mean and SD across MC are displayed. The region of noise correlation is shaded in grey.

Estimation of metabolite concentrations as a function of b-value

In our post-processing pipeline, denoising was performed before B_0 drift correction. This allowed for a more accurate realignment of spectra within each b-value, most noticeably at b_{max} (**Figure 6.9**): the correction factors derived from the denoised data were closer to ground truth (RMSE: 2.7 Hz) compared to the ones derived from the raw data (RMSE: 6.0 Hz), although the latter yielded a higher amplitude of the summed signal. Metabolite concentrations at b_{min} and b_{max} for all denoising strategies, together with relative ESFU, are presented in **Appendix**. They highlighted an overall stronger bias introduced by the denoising strategies with respect to the one of the raw data for low-concentrated metabolites, but a weaker one for high-concentrated metabolites, even with strategy 3. Fit precision (ESFU) is strongly improved after denoising for all metabolites. When comparing strategies 1 and 2 on concentration decay curves, their impact was metabolite-dependent (**Figure 6.10A-B**). In the case of Lac, strategy 1 introduced a systematic bias (overestimated concentration) with respect to the noiseless fit, an effect largely mitigated using strategy 2. For Gln, however, both strategies (1 and 2) improved the decay curve accuracy, while no benefit was brought by any of the strategies for NAA.

In terms of D_{intra} estimation (**Figure 6.10C-D**), strategy 2 led to an improvement in accuracy for some metabolites compared to the raw data and strategy 1 (Ala, tCho, Ins, Tau), a deterioration for some low concentrated metabolites (GABA, GSH, Lac) and similar accuracy for the remaining ones. The number of outliers was slightly reduced by all the denoising strategies.

Unfortunately, strategy 3, using half the data (i.e. NS = 50) to assess if the total duration of
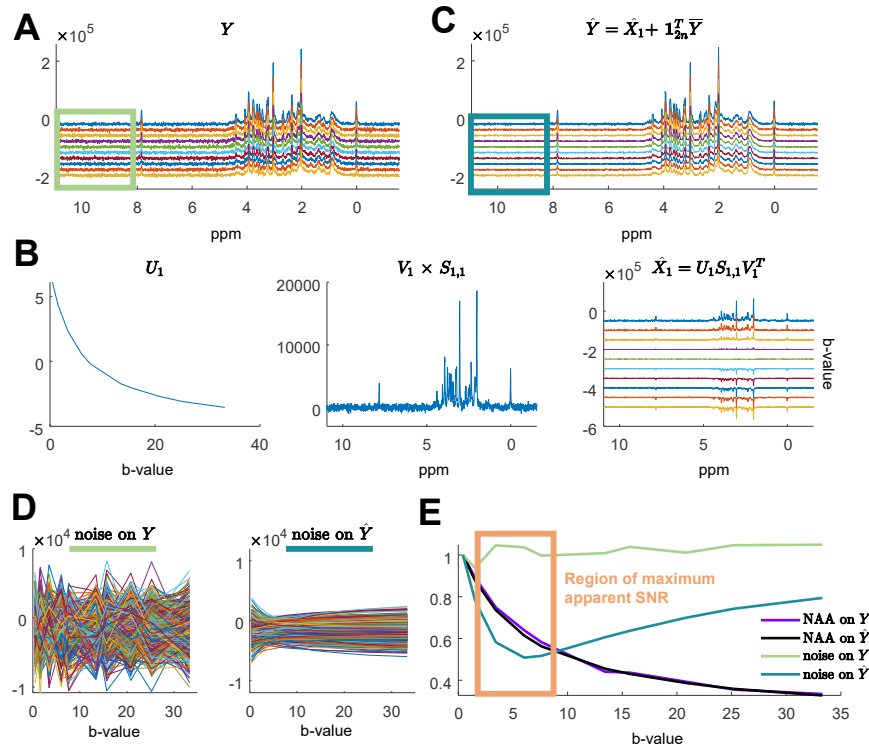
Figure 6.8: Graphical representation of the effect of MP-PCA on one simulated diffusion dataset denoised with strategy 1. For an easier visualisation of the effects, and for this figure only, MP-PCA has been applied on the real part of spectral matrix (instead of the FID time points, with concatenated real and imaginary parts), and no phase/frequency distortions were introduced in the initial matrix, nor a residual water signal. The matrix is however centered as described above. **A**: Initial matrix Y (1000×2048) where each shell has been summed. **B**: Decomposition of $X = Y - \overline{Y}$ in terms of singular vectors of the shot dimension U, and of the spectral dimension V. A rank P = 1 was selected by the MP fit, such that $\widehat{X} = \widehat{X_1} = U_1 S_{1,1} V_1^T$. **C**: Denoised matrix $\widehat{Y}$ (1000×2048) where each shell has been summed and the initial mean $\overline{Y}$ reintroduced. D: Noise profile across b-values for each spectral point in the noise-only region between 8.2 and 10.9 ppm, shown in panels **A** and **C**, before (left) and after (right) denoising. **E**: Standard deviation of noise values from panel **D**, at each b-value, for raw (light green) and denoised (dark green), together with the decay of the maximum real value of the NAA peak at 2.01 ppm. Panel **E** shows that, in that case, points from a noise-only region, which are reconstructed from a decaying component U_1, will also decay. Consequently, the noise level (standard deviation over the points from a noise-only region) after denoising reaches a minimum value at an intermediate b-value (around b $\approx$ 6 ms/μm^2) and grows again at higher b-values due to the initial positive/negative distribution of the noise points. On the other hand, the NAA signal decays similarly before and after denoising, and explains why the apparent SNR reaches a maximum for one of the intermediate b-values, for simulations (**Figure 6.6C**) and in vivo data (**Figure 6.11B**).
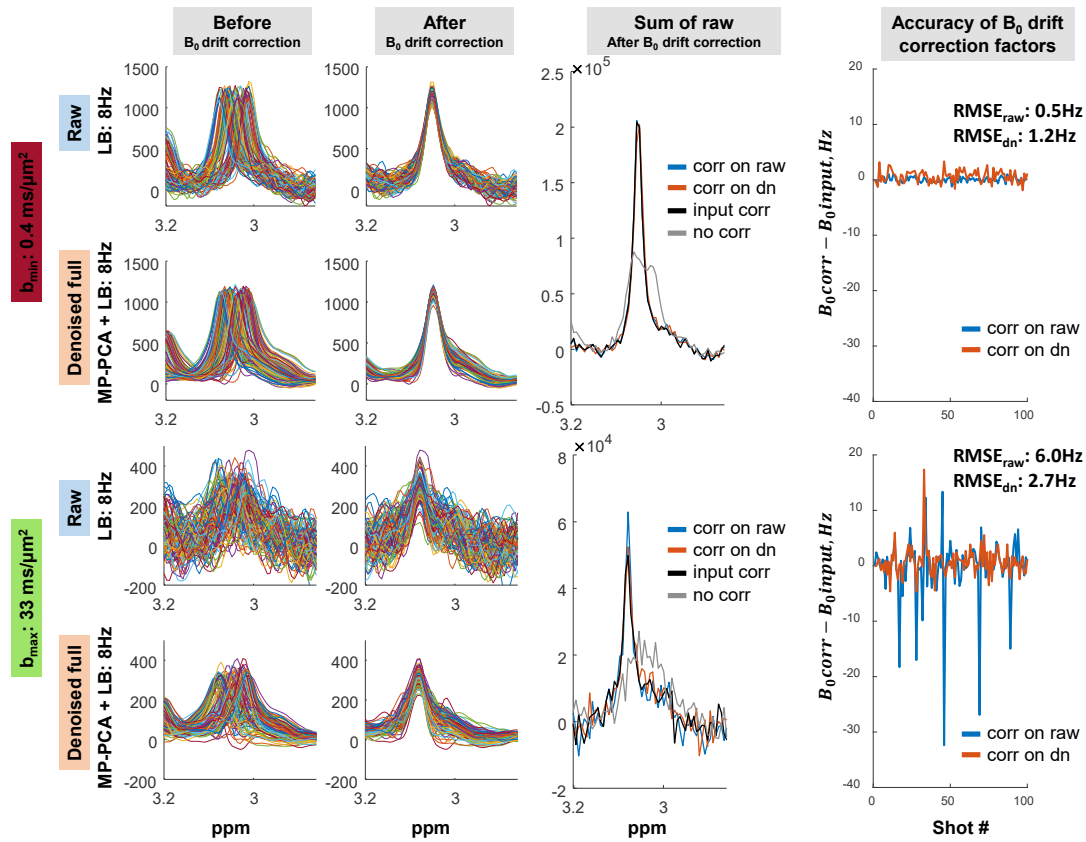
Figure 6.9: Spectral realignment (B_0 drift correction) after denoising. The B_0 drift correction was performed by aligning the frequency-domain position of the tCr peak to its position on the first spectrum, using a Lorentzian apodization of 8 Hz, on raw and denoised data, for 1 MC iteration (left panels, before/after, for b_{min} and b_{max}). The central panel shows the summed raw spectra with corrections derived either from the raw or the MP-PCA data, as compared to the summed raw spectra where the negative input B_0 drifts have been applied. Denoising yields no benefit of on B_0 drift correction in the case of sufficient SNR (e.g. at b_{min}). At low SNR (e.g. b_{max}), the summed raw spectra with corrections derived from MP-PCA is closely matching to the one reconstructed from the input B_0 drift values, yet with a smaller amplitude than the summed spectra with corrections from the raw data. Denoising before B_0 drift correction led to a better accuracy of the B0 drift estimates with respect to the input drifts (right panel) at b_{max}, and a worse accuracy at b_{min}. $RMSE_{method} = \sqrt{\frac{1}{NS}\sum_{i=1}^{NS}(B_{0,corr,method} - B_{0,input})^2}$.

the scan could be reduced without a significant compromise in accuracy and precision of metabolite concentration and D_{intra}, yielded worse or at best similar accuracy and precision for D_{intra} as the full raw data (NS = 100) but also as half the raw data (NS = 50) depending on the metabolite.
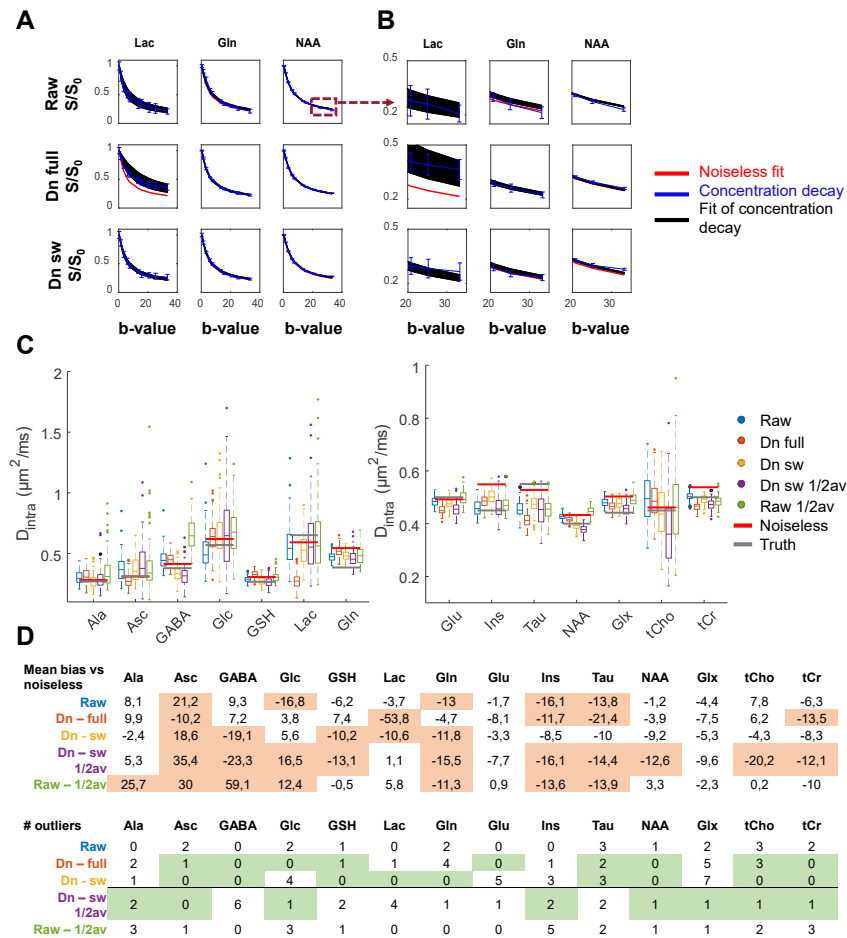
Figure 6.10: A: Representative concentration decay curves for three metabolites: Lac, Gln, NAA, normalized to the concentration at the lowest b-value. Overlaid curves are: mean and SD of concentrations across MC iterations (blue), Callaghan model fit using the mean D_{intra} estimated across MC iterations (black) and Callaghan model fit of the quantified noiseless concentration decay (red). **B**: Zoom-in of panel **A** for b-values between 20 and 33 ms/μm^2. **C**: Estimated metabolite D_{intra} from Callaghan's model using raw or denoised data, for various denoising strategies. The values labelled as "truth" represent the diffusion coefficients given as input in the simulations, and the values labelled as "noiseless" represent the LCModel concentrations fit from the noiseless data. **D**: % bias on D_{intra} and number of outliers between all methods and the noiseless fit ((D_{method}-$D_{noiseless}$)/$D_{noiseless}$). The D_{intra} that differ from the noiseless values by more than ±10% bias are highlighted in orange. The cases where denoising reduces or equalizes the number of outliers found with their raw data counterparts (raw or raw ½ av) are highlighted in green. Some metabolite-dependant bias on the concentrations and on D_{intra} estimates is either introduced or reduced compared to the raw data after denoising.

6.3.2 In vivo rodent data

The same analyses were performed on in vivo data from four animals and MP-PCA denoising effects were compared to the ones observed in simulations.
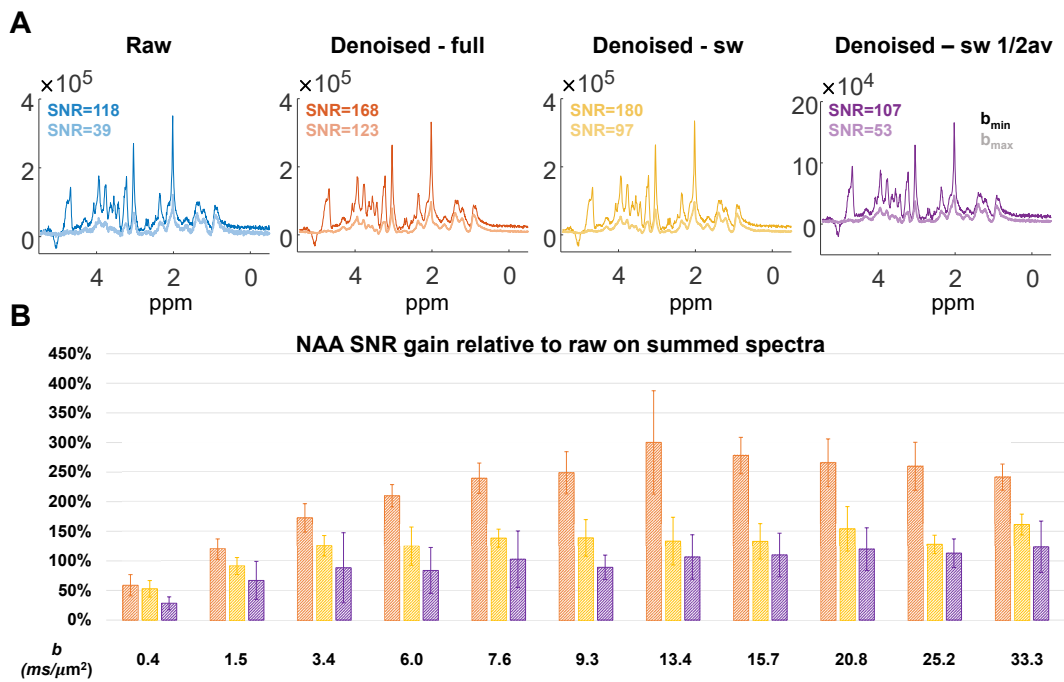
Figure 6.11: In vivo rodent data - spectral quality and apparent SNR gain, before versus after denoising. **A**: Representative summed spectra for one animal, at low (dark colors) and high (light colors) b-values, based on raw and denoised data, with strategies 1 to 3. NAA singlet SNR is displayed for each case. **B**: Relative apparent SNR gain from the denoising strategies 1 to 3, expressed in % increase compared to the raw data SNR, with mean and SD across animals. Orange: strategy 1, yellow: strategy 2, purple: strategy 3. Increased apparent spectral SNR was observed in vivo.

Apparent SNR

The summed spectra for the two extreme b-values before and after denoising using all three strategies are shown in **Figure 6.11A**. Denoising improved the apparent SNR at all b-values, yet to a smaller extent compared to simulations (**Figure 6.11B**): on average, the SNR gain is 59% at b_{min} and 241% at b_{max} for strategy 1 and 53% at b_{min} and 161% at b_{max} for strategy 2. The apparent SNR gain follows a similar b-value dependence to the one in simulations, with a maximum for a central b-value for strategy 1 and a constant gain for strategy 2.

Noise properties

For strategies 1 and 2, the noise level on in vivo data after denoising was non-uniform across shells, both on the sum and on the single shots (**Figure 6.12A**), and strategy 2 attenuated this effect: on the summed spectra: $\frac{\sigma_{b_{min}}}{\sigma_{bmax}} = 2.49$ for strategy 1 and $\frac{\sigma_{b_{min}}}{\sigma_{bmax}} = 1.87$ for strategy 2. A rank P = 12 for strategy 1 and P ∈ [4, 12] for strategy 2 was selected by the MP fit (**Figure 6.12B**),
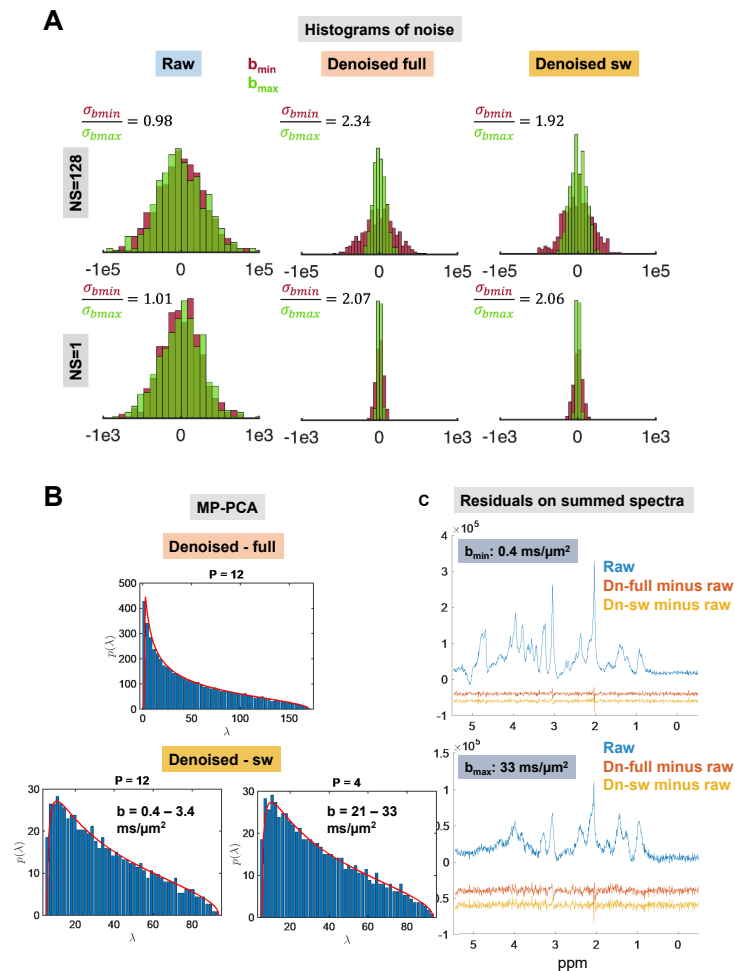
Figure 6.12: In vivo rodent data - MP-PCA denoising performance using strategy 1 and strategy 2. **A**: Histograms of spectral noise for one example animal in the 8.2-10.9 ppm noise-only region, for a single shot (bottom) and for the sum of the 128 shots (top), before and after each denoising strategy, for the smallest (red) and highest (green) b-values. The ratio of the experimental noise level at b_{min} over b_{max} is displayed in each case, averaged over the four animals. Standard deviations across animals associated to the mean ratios displayed: for NS = 100, 0.04 (raw), 0.28 (dn full), 0.25 (dn sw), and for NS = 1, 0.06 (raw), 0.44 (dn full), 0.65 (dn sw). **B**: MP fit for both strategies. **C**: Residuals between the denoised and raw spectra at the two extreme b-values, after summation of the 128 shots available, shifted downwards for display. The same trends as the ones for simulations can be observed: heterogeneous noise level across shells, increase in apparent SNR with no structure in spectral residuals after denoising, with strategy 2 mitigating some effects of strategy 1.

which was consistent among rats (strategy 1: P = 11.5±0.58, strategy 2: P_{bmin} = 11.25±0.5 and P_{bmax} = 3.5±1) and similar to the ranks found in simulations (**Figure 6.6B**). Similarly to the effect observed in simulations, the noise level distribution in a noise-only spectral region

within one shell remained Gaussian after denoising.
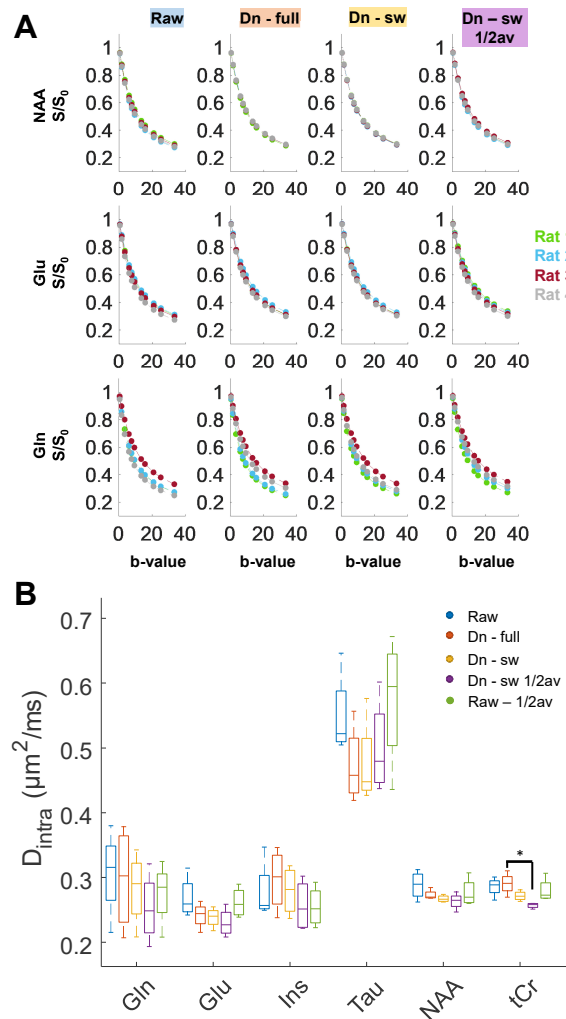
Figure 6.13: In vivo rodent data - concentration decays after quantification with LCModel, and resulting D_{intra} fit, for raw and denoised data with the three strategies. **A**: Representative decays across b-values for three metabolites: NAA, Glu, Gln, for each animal (circles), with concentrations normalized to the lowest b-value, and individual fits of Callaghan's model (solid line). **B**: Estimated D_{intra} from Callaghan's model for a few metabolites, for all strategies. Raw and denoised data provide similar estimates for most metabolites.

The spectral residuals for both strategies showed no distinct structure around metabolite frequencies (**Figure 6.12C**), suggestive of a homogeneous denoising in the spectra.

Estimation of metabolite concentrations as a function of b-value

All denoising strategies yielded similar concentrations and reduced ESFU compared to the raw data for the 6 quantified metabolites at b_{min} and b_{max} (**Appendix**). Similar trends to those identified in simulations are observed between estimates of D_{intra} from raw and denoised data (**Figure 6.13**). In the multiple comparison post-hoc test, only tCr D_{intra} showed a significant difference between strategy 1 and 3. For the high-concentrated metabolites (Glu, NAA and tCr), strategy 2 reduced the variability of D_{intra} estimates across animals, as compared to that from the raw data.

6.3.3   In vivo human data

The Connectom gradients allowed to reach strong diffusion weighting, making the human dMRS b-value range and the data quality comparable to the rodent ones. **Figure 6.14A** shows representative spectra at increasing b-values for one volunteer's dataset. The NAA spectral SNR decays with increasing b-values for the raw data, as expected (**Figure 6.14B**). In the case of strategy 1, the apparent spectral SNR is higher after denoising at all b-values and reaches a maximum for $b \approx 3$ ms/μm^2, an effect which is mitigated by strategy 2. There is hardly any structure in the spectral residuals for either strategy (**Figure 6.14C**). As observed in the simulations and in the rodent data, the denoising effect is stronger at b_{max} compared to b_{min}. The concentrations (**Appendix**) and the D_{intra} estimates (**Figure 6.14E**) show no significant difference between the raw and denoised data, confirming the observation made in rodent dMRS data. The fit error (root mean square error between the fit and the experimental decay) is reduced after denoising for tNAA, tCho and tCr, with strategies 1 and 2.

6.4   Discussion

The aim of this work was to evaluate the performance of MP-PCA denoising on synthetic and experimental datasets of single-voxel diffusion-weighted ^{1}H-MRS comprising spectra at multiple diffusion-weightings (b-values), as compared to conventional averaging across each b-value. We investigated three denoising strategies, comparing their impact on the data structure (apparent SNR increase, spectral residuals, noise correlation), and evaluating their potential for improved diffusion coefficient estimates. Similar characteristics of the denoised spectra were observed between simulations and in vivo data (similar SNR on the raw data between simulations, rodent and human data, noise ratios between first and last shells, apparent SNR gain and evolution as a function of b-value, spectral residuals) thus ensuring that conclusions drawn from simulations with respect to the ground truth are relevant for the in vivo datasets.
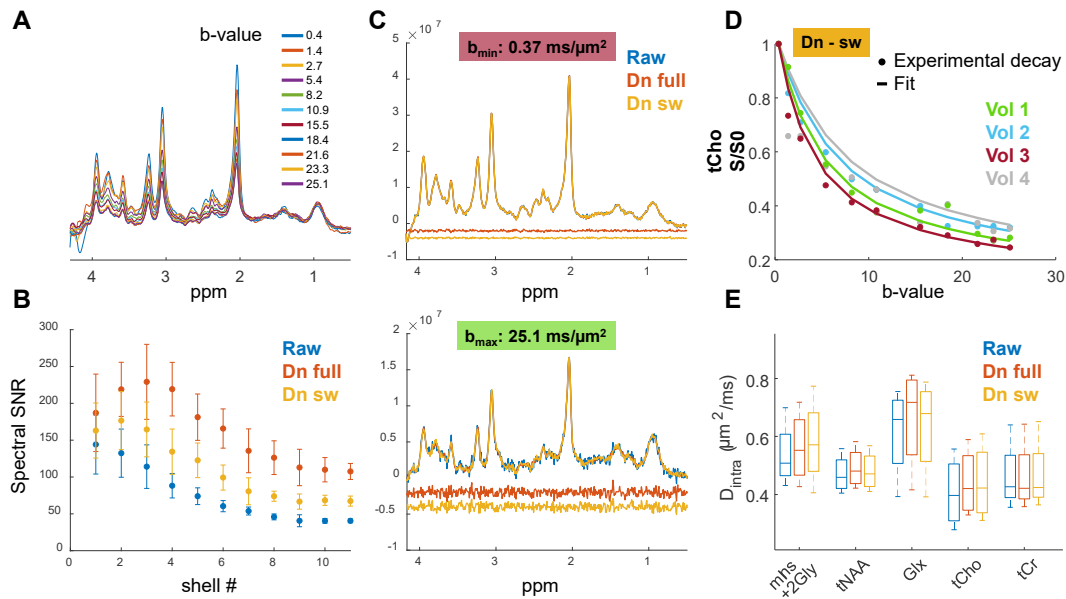
Figure 6.14: In vivo human data - effects of denoising in terms of apparent spectral SNR, residuals, fit and D_{intra} estimation. **A**: Representative diffusion-weighted raw spectra for one volunteer (LB = 2 Hz). **B**: Evolution of (apparent) spectral SNR as a function of the b-value, mean and standard deviation across the 4 volunteers. **C**: Overlap of raw, denoised full (strategy 1) and denoised with a sliding window (strategy 2) spectra and residues shifted downwards for display. **D**: Representative experimental decays across b-values for tCho with strategy 2 (circles), with concentrations normalized to the lowest b-value, and individual fits of Callaghan's model for all volunteers (solid line). **E**: Estimated median and population variance for D_{intra} from the Callaghan's model for a few metabolites for the raw data and the two denoising strategies. The fit error (root mean square error between the fit and the experimental decay) was reduced after denoising for tNAA, tCho and tCr, with both strategy 1 (median RMSE normalized to the one of raw, for tNAA: 0.91 [range 0.79-0.93], for tCho: 0.84 [range 0.64-0.99] and for tCr: 0.90 [range 0.88-1.01]) and strategy 2 (for tNAA: 0.90 [range 0.87-1.02], for tCho: 0.92 [range 0.73-1.09] and for tCr: 0.89 [range 0.78-0.95]). Denoising improves apparent SNR, yields no spectral residual and the same D_{intra} estimates for raw and denoised.

6.4.1 Increased apparent spectral SNR

Simulations revealed that denoising all DW-spectra together significantly improved apparent spectral SNR for each b-value compared to averaging (**Figure 6.4** and **Figure 6.6** for simulations and **Figure 6.11** for in vivo rodent data and **Figure 6.14** for human data). Remarkably, denoising also provided the following two valuable features vs averaging.

First, the correction for B_0 drifts between individual shots of high b-value shells was more reliable after denoising especially at low SNR (**Figure 6.9**). Whether a stronger apodization or spectral registration at high b-values could mimic the benefit of denoising prior to B_0 drift

correction should be further tested with multiple datasets. Interestingly, the correction for phase drifts did not improve after denoising. From this perspective, denoising could be used to determine the optimal frequency drift corrections on individual spectra, and apply it to raw spectra, as previously described in a simpler spectral pattern [287].

Second, the individual spectra after denoising displayed dramatically higher apparent SNR than raw spectra, even at the highest b-value. This single-shot SNR increase, however, results from a correlation with spectra from other shells. Whether this improvement on single shots may benefit other applications where averaging multiple spectra is detrimental, such as functional MRS, where it could provide a boost in temporal resolution, should be the subject of future work.

Figure 6.3 also provides a perspective: a reduction in voxel size could be acceptable (reduced SNR by a factor 2 to 3 while preserving the number of shots yielding to a similar rank and fit RMSE). This could help improving spatial resolution with little penalty in quantification.

6.4.2   Strategy 1 versus strategy 2

For large heterogeneities across the dataset to be denoised, such as the extreme case of very low and very high b-values (in our case b $\approx$ 0.4 and up to b $\approx$ 30 ms/μm^2), more leakage from high to low-SNR data is expected after denoising, which may bias high b-values concentration estimates.

Two approaches can, however, mitigate this effect.

The first approach is to denoise using a sliding-window along b-values, so that the spectra used in each denoising matrix are more similar to each other in terms of SNR. Here we tried a sliding window of three b-values (effectively leading to 3×2×NS rows, accounting for real and imaginary parts of the signal, where NS is the number of shots acquired for each b-value). While this approach resulted in a more limited noise reduction, especially at high b-values (apparent SNR increase compared to raw of 575% for strategy 1 and 265% for strategy 2 at b_{max} in simulations, 241% for strategy 1 and 161% for strategy 2 at b_{max} in rodents and 166% for strategy 1 and 66% for strategy 2 at b_{max} in humans), it preserved noise variance better across b-values. The apparent SNR increase is higher in simulations compared to in vivo data, possibly owing to sources of non-Gaussian noise or distortions present in raw in vivo spectra and absent in simulations. Additionally, in human data, motion and spurious echoe artefacts at low b-values (even after cutting out the water region) are more prominent than in rodent data. These variations will not be captured in the noise principal components, thus increasing the selected rank and leading to a smaller denoising effect. The number of components retained (P) as signal-carrying decreased across blocks, both in simulations and

in vivo (**Figure 6.6C** for simulations, **Figure 6.11B** for rodent data and from P_{bmin} = 71.0±9.6 to P_{bmax} = 7.3±2.1 for human data). One reason is that at high b-values, the variance created by the actual (low SNR) signal is close to the noise floor. An additional hypothesis is that sources of structural/physiological noise in the spectra (e.g. frequency drifts) are more discernible at low b-value than at high b-value and contribute to signal-carrying components. Possibly also, in the shells containing the highest b-values, the variations in the input data are more Gaussian-distributed than the ones observed in the shells containing the lowest b-values. This may further improve the separation of the signal from the artefacts and the noise.

The second mitigating approach, which remains to be tested, could be to diversify the dMRS acquisition scheme not only into multiple b-values, but also directions and diffusion times instead of plain repetitions. While working with only a small range of b-values (with similar SNR) – as for the sliding window above - the denoising matrix construct could nonetheless collect multiple directions and diffusion times. This would also enable to generate large matrices, improving the MP-PCA performance by fulfilling the asymptotic condition of the random matrix theory.

6.4.3 Assessment of denoising quality

One important aspect of MP-PCA denoising is the assumption of Gaussian, constant and uncorrelated entry noise. This assumption can be easily violated for MR imaging in clinical setups where multi-channel receiver coils are recombined using sum-of-squares algorithms, following which the magnitude of the complex signal is retained. In contrast, our in vivo preclinical setup was ideal to fulfil this criterion, as the receiver coil was a quadrature circuit whose signals were recombined physically prior to amplification. Each channel (real and imaginary) of the complex signal retained Gaussian noise properties. Despite the apparent SNR increase and homogenous residuals within each shot, some noise correlation within (**Figure 6.7**) and across shells ("noise decay", **Figure 6.6A** and **Figure 6.12A**) introduced by MP-PCA were identified in the current study. Consequently, noise estimation with a prior of uncorrelated Gaussian noise should be avoided in denoised spectra, as well as quality assessment based on noise amplitude, such as CRLB or the fit quality number (FQN) [30]. A bootstrapping approach for the estimation of metabolites concentration uncertainty has been recently proposed [266], where multiple fits of the same spectrum corrupted by correlated noise estimated from the denoised data, are performed.

6.4.4 Noise properties

Spectral residuals: When comparing denoising to averaging on a single-shell without distortions (**Figure 6.2**), we observed no patterns in the spectral residuals and their distribution

was Gaussian. For the multi-shell case, hardly any pattern was observed with the exception of small artefacts (spikes), likely due to a B_0-drift correction mismatch between raw and denoised data (**Figure 6.6D** for simulations, **Figure 6.12C**). Remarkably, these artefacts are not present in human data (**Figure 6.14C**) where the B_0-drift correction was performed before denoising.

Uniform noise level across spectral points: In the entire study (single-shell, multi-shell, simulations and in vivo data), the noise in a noise-only region on single shots was Gaussian-distributed after denoising. When investigating the variance on each spectral point across MC iterations, the authors of ref. [266], who investigated different low-rank denoising methods for MRSI data, reported a non-uniform variance. Concretely, the standard deviation of the spectrum across MC iterations is higher in the metabolite region of the spectrum and smaller in the noise region. In the present study, in the case of an input matrix with only one signal information (single-shell), which is not centered (see **Theory** section), and when a rank P = 1 is manually selected, a non-uniform variance on spectral points is also observed. When the matrix is not centered, the only singular value selected will be an estimate of the mean of the input matrix, which might be biased. Remarkably, no non-uniform variance across spectral points was observed in our work when denoising a matrix comprised of multi-shell data, even without centering, with any of the strategies. The high number of principal components selected, P $\approx$ 11 - 12, probably mitigates this effect.

Non-uniform noise level across b-values: In the present work, the noise level was b-value dependent after MP-PCA denoising (less noise in the high b-value spectra), an effect which was reduced by using a sliding-window across b-values. The evolution of the spectral SNR after denoising with strategy 1 is very similar between simulations, rodent data and human data, reaching a maximum value for intermediate b-values, b $\approx$ 7.6 ms/μm^2 for the simulations (**Figure 6.6C**), b $\approx$ 13.4 ms/μm^2 for in vivo rodent data (**Figure 6.11B**), and b $\approx$ 3 ms/μm^2 for in vivo human data (**Figure 6.14B**). **Figure 6.8** gives a tentative explanation of this effect. After MP-PCA, the time evolution of the spectral points in a noise-only region will be reconstructed from one of the first signal-carrying singular vectors in the shot dimension (U_1 in **Figure 6.8B**), representing the overall decay of metabolites across b-values (strongest contribution to the variance). Consequently, the noise points will decay with increasing b-values. Due to the initial positive/negative distribution of these noise points (**Figure 6.8D-E**), the noise level (standard deviation of the noise points across a spectral region) will decrease at intermediate b-values and increase again at higher b-values. Meanwhile, the NAA concentration decay is similar for raw and denoised data, which results in a maximum apparent SNR at intermediate b-values. With a similar argument in the other dimension, the first signal-carrying singular vectors in the spectral dimension will represent high SNR spectra (V_1 in **Figure 6.8B**). The closer the metabolite information to the noise level, the more likely it will be reconstructed from a linear combination of high SNR spectral information, and even more so when P is small.

This observation challenges the use of MP-PCA denoising for extracting low-concentrated metabolites information from the noise floor using the entire range of b-values. The sliding window approach can however mitigate these effects, as shown throughout the present work.

The number of principal components retained with strategy 1 was $\approx 11 - 12$ for simulations and in vivo data, which was also the rank found when using optimal shrinkage of the principal components [280]. The high number of components was mostly due to the B_0 drift distortions which were not corrected for prior to denoising, to the random water residual, and to possible sources of non-Gaussian noise in in vivo data. Structural noise, retained as signal component, which has a larger impact on low-b spectra (in particular the water residual which is completely suppressed at high b-values) may therefore serendipitously limit the impact of noise reduction across shells.

6.4.5   Estimation of diffusion coefficients

From the perspective of metabolite quantification, MP-PCA denoising reduced the concentration ESFU (**Appendix**). After denoising, the ESFU are not equivalent to the Cramer Rao Lower Bounds, representing the lower bounds of the fitting error, and which are based on a correct model and Gaussian uncorrelated noise, a prior which may be violated after denoising. Simulations showed that denoising based on the full range of b-values could also introduce bias for some metabolite concentration decays, such as lactate (**Figure 6.10A-B**), and an over-estimation of the concentrations at high b-values compared to the same concentrations on the raw data (**Appendix**). Interestingly, this over-estimation is not systematic anymore when comparing denoised vs noiseless data: although beyond the scope of this work, this observation highlights some systematic underestimation of concentrations with LCModel for raw data with realistic SNR and Lorentzian broadening, as shown in a MRS fitting challenge [283]. The sliding-window approach (strategy 2) introduced less bias on metabolite concentrations at high b-values than the full-range denoising and the raw data for high-concentrated metabolites, in addition to better preserving the noise structure. The observations made on the accuracy and precision of metabolite quantification could not be directly transposed to the estimations of the free diffusion coefficients D_{intra}. Overall, the sliding window-denoising followed the raw data estimates for most metabolites: whether or not bias (>10%) existed in the raw data estimates, the same was observed for strategy 2. The only exceptions are GABA, GSH, Lac, for which more bias was introduced with strategy 2 and Glc, Ins, Tau for which less bias was introduced with strategy 2. However, this performance may depend on the underlying diffusivity values chosen in our simulations.

In simulations, the variability across MC iterations was also reduced after denoising (when compared to the raw data with the same number of shots) for all metabolites (**Figure 6.10C**).

Remarkably, in rodent data, MP-PCA denoising also contributed to reducing the variability in metabolite concentration decay curves across the different rats (which were all part of a homogeneous control group) for some metabolites (NAA, tCr, Glu on **Figure 6.13**). The estimated metabolite diffusivities were systematically lower with MP-PCA denoising vs raw data, though the ground truth is not known in this case. This could reflect the systematic underestimation of the raw data concentrations found in simulations (mentioned above), yielding lower concentration values at the tail of the curve and thus a higher estimated diffusivity. For human data, the datasets were not fitted individually in ref [250], owing to their low SNR, but after doing a cohort average. The present study shows the feasibility of individual volunteer fitting, yet no difference in D_{intra} between the raw and denoised data with any strategy and no reduction in the group variability across volunteers was observed, possibly owing to the high P. Though, the difference between the diffusion decay fitted with Callaghan's model and the experimental data tended to be reduced after denoising.

It should also be noted that Callaghan's model of randomly-oriented sticks may not be well-suited to describe the diffusion of certain metabolites in vivo, e.g. if they are also extracellular and/or if the radius of the dendrites cannot be assumed to be effectively zero. For human data, in addition, there is substantial contribution of white matter where the randomly oriented stick model may not apply for the current case where only one arbitrary diffusion direction was acquired.

Simultaneous spectral and diffusion modelling [250, 288, 289, 290]– though possibly more challenging - may also offer increased fit stability, but may not readily be combined with MP-PCA denoising given the noise correlation between shells. A sliding-window approach along the spectral dimension instead of the diffusion-weighting dimension could also be considered. This would however lead to issues in LCModel quantification, and multiple resonances of the same metabolite (thus sharing common features) could be denoised separately, thereby decreasing the redundancy. Finally, the strong spectral overlap of some metabolite resonances also prevents the selection of a denoising window which could contain only one metabolite.

6.5   Conclusion

Overall, we have shown that MP-PCA denoising improves apparent SNR and B_0 drift correction and thus spectral averaging. For highly concentrated metabolites, which are the ones typically considered in dMRS studies, we have shown that denoising improves the within-group homogeneity of estimated diffusivities with little penalty to the diffusivity estimates – future work could focus on testing whether the between-group differences are thus reinforced by comparing a control to a patient group. However, for low-concentrated metabolites, we have also shown that denoising biases their estimated diffusivity due to signal leakage

from the high-concentrated metabolites. In agreement with previous studies, we suggest that PCA-denoising for diffusion MRS should be used with caution and we recommend that all effects should be tested in simulations prior to drawing conclusions on in vivo data. Uniform variance along the spectrum was preserved due to the matrix centering and the selection of a high rank P by the MP fit (with uncorrected B_0 drift prior to denoising), but noise correlation across rows were introduced as a consequence of the rank truncation, which should prevent the use of the term CRLB after denoising. We recommend the use of an across-shell sliding window denoising approach (i.e. denoising more self-similar matrices) to mitigate the b-value dependent noise level post-denoising. For dMRS acquisitions that include multiple diffusion times and diffusion directions, it remains to be established whether signal can be separated from noise more efficiently due to higher self-similarity of different measures.

6.6 Perspectives

As perspectives to this study, we envision to:

- test the method on different types of input data, including preclinical FID MRSI with Brayan Alves from our group and sparse ^{13}C MRS from Roland Kreis' group. The latter is a follow up of my secondment in his lab in Spring 2022, in the context of my PhD funding (European Union's Horizon 2020 research and innovation program under the Marie Sklodowska-Curie grant agreement No 813120 (INSPiRE-MED)).

- further investigate the limits of applicability of the methods on MRS data, depending on the type of input data, both theoretically and with simulations. This reflexion emerged from the following observations:

  1. on our very simple preliminary simulation framework containing metabolites only (no slowly decaying macromolecules, no water residual, no distortions), and thus poorly representing the complexity of the in vivo data (having more sources of non-Gaussian structure), the meaningful variance (e.g., distribution of diffusion coefficients) of the input data was not well preserved after MP-PCA, and that

  2. different groups working on denoising MR spectra with statistical approaches came up with different observations , very likely attributed to the different nature of their respective input data [266, 291, 292, 278].

For the reasons listed above, we would like to organize a working group on the topic, also involving groups working on denoising MRS with machine learning, to come up with an unified view and general recommendations of applicability of denoising for MRS.

6.7 Appendix

6.7.1 Appendix 1: concentration tables

Table 6.2: Concentrations and relative estimated spectral fit uncertainty (ESFU) for simulations (mean over MC iterations) at the lowest and highest b-values, for every method and every reliably quantified metabolite. The concentrations that differ from the noiseless values by more than ±10% are highlighted in orange (bias: (Concmethod-Concnoiseless)/Concnoiseless). In the ESFU tables, the values above 0.2 are highlighted in grey (fit quality). Denoising expectedly reduces the ESFUs but does not overall improve the quantification bias compared to raw data.

Simulations													
Conc (arbitrary units)							ESFU (relative LCModel SD)						
b-value (ms/µm²)	0.4						b-value (ms/µm²)	0.4					
Quantification	Raw	Raw ½	Dn – strategy 1	Dn – strategy 2	Dn – strategy 3	Noiseless	Quantification	Raw	Raw ½	Dn – strategy 1	Dn – strategy 2	Dn – strategy 3	Noiseless
Ala	0.675	0.663	0.669	0.683	0.696	0.64	Ala	0.086	0.136	0.04	0.041	0.055	0.02
Asc	0.847	0.865	0.937	0.96	0.905	0.979	Asc	0.134	0.202	0.055	0.057	0.086	0.03
GABA	1.351	1.292	1.302	1.315	1.349	1.299	GABA	0.058	0.089	0.03	0.03	0.04	0.02
Glc	1.424	1.61	1.376	1.359	1.346	1.41	Glc	0.103	0.12	0.055	0.059	0.08	0.03
GSH	1.349	1.358	1.364	1.36	1.35	1.361	GSH	0.04	0.06	0.02	0.02	0.03	0.01
Lac	0.67	0.683	0.577	0.623	0.638	0.669	Lac	0.084	0.128	0.043	0.042	0.059	0.02
Gln	2.495	2.531	2.403	2.385	2.41	2.386	Gln	0.033	0.05	0.02	0.02	0.023	0.01
Glu	8.942	8.876	8.856	8.837	8.679	9.157	Glu	0.01	0.02	0.01	0.01	0.01	0
Ins	5.226	5.388	5.105	5.164	5.141	5.343	Ins	0.02	0.021	0.01	0.01	0.015	0.01
Tau	3.726	3.787	3.552	3.637	3.667	3.914	Tau	0.03	0.036	0.02	0.02	0.02	0.01
NAA	7.704	7.603	7.651	7.643	7.586	7.8	NAA	0.01	0.02	0.01	0.01	0.01	0
Glu+Gln	11.437	11.407	11.26	11.223	11.089	11.543	Glu+Gln	0.01	0.02	0.01	0.01	0.01	0
GPC+PCho	0.891	0.803	0.868	0.872	0.854	0.849	GPC+PCho	0.073	0.105	0.034	0.036	0.05	0.02
Cr+PCr	7.142	7.138	7.093	7.108	7.002	7.457	Cr+PCr	0.01	0.013	0.01	0.01	0.01	0

Conc (arbitrary units)							ESFU (relative LCModel SD)						
b-value (ms/µm²)	33						b-value (ms/µm²)	33					
Quantification	Raw	Raw ½	Dn – strategy 1	Dn – strategy 2	Dn – strategy 3	Noiseless	Quantification	Raw	Raw ½	Dn – strategy 1	Dn – strategy 2	Dn – strategy 3	Noiseless
Ala	0.211	0.181	0.213	0.239	0.24	0.19	Ala	0.278	0.8	0.056	0.072	0.112	0.04
Asc	0.208	0.247	0.339	0.257	0.242	0.269	Asc	0.724	1.625	0.067	0.238	0.452	0.05
GABA	0.247	0.15	0.33	0.394	0.4	0.327	GABA	0.257	0.68	0.048	0.059	0.086	0.03
Glc	0.301	0.251	0.249	0.266	0.26	0.281	Glc	0.304	0.416	0.133	0.195	0.581	0.07
GSH	0.364	0.355	0.417	0.438	0.447	0.384	GSH	0.128	0.195	0.03	0.039	0.054	0.02
Lac	0.163	0.171	0.2	0.16	0.158	0.15	Lac	0.385	0.776	0.057	0.106	0.193	0.05
Gln	0.533	0.566	0.538	0.56	0.569	0.464	Gln	0.144	0.212	0.03	0.042	0.062	0.02
Glu	2.089	2.007	2.163	2.259	2.252	2.171	Glu	0.042	0.07	0.01	0.019	0.02	0.01
Ins	1.176	1.194	1.201	1.235	1.255	1.099	Ins	0.058	0.087	0.02	0.028	0.034	0.01
Tau	0.919	0.914	0.926	0.945	0.961	0.904	Tau	0.08	0.124	0.022	0.03	0.043	0.02
NAA	1.784	1.671	1.994	2.11	2.074	1.914	NAA	0.033	0.053	0.01	0.017	0.02	0.01
Glu+Gln	2.622	2.574	2.701	2.819	2.822	2.643	Glu+Gln	0.041	0.064	0.01	0.016	0.02	0.01
GPC+PCho	0.203	0.188	0.201	0.229	0.247	0.203	GPC+PCho	0.275	0.375	0.064	0.089	0.127	0.04
Cr+PCr	1.691	1.722	1.712	1.765	1.749	1.643	Cr+PCr	0.031	0.048	0.01	0.011	0.02	0.01

6.7.2 Appendix 2: MRS in MRS table

Table 6.3: Concentrations and estimated spectral fit uncertainty (ESFU) for in vivo rodent data (mean over animals) at the lowest and highest b-values, for every method and every reliably quantified metabolite. In the ESFU tables, the values above 0.2 are highlighted in grey (fit quality). Denoising expectedly reduces the ESFUs. Metabolite concentrations at all b-values are referenced to the water signal at b=0.4 ms/µm^2. They are therefore overestimated even at low b-values because of a faster water diffusivity compared to metabolites. This referencing neither affects the decay of metabolites relative to the first value, nor the difference between the different metabolites' decay because the same water file was used for every metabolite and every b-value.

In vivo rodent *data*											

Conc (arbitrary units)						ESFU (relative LCModel SD)					
b-value (ms/µm²)	0.4					b-value (ms/µm²)	0.4				
Quantification	Raw	Raw ½	Dn – strategy 1	Dn – strategy 2	Dn – strategy 3	Quantification	Raw	Raw ½	Dn – strategy 1	Dn – strategy 2	Dn – strategy 3
Gln	5.098	4.791	5.027	5.038	4.857	Gln	0.045	0.058	0.035	0.035	0.048
Glu	14.895	14.443	14.83	14.906	14.495	Glu	0.02	0.025	0.02	0.02	0.023
Ins	9.134	8.911	9.259	9.233	8.953	Ins	0.025	0.033	0.02	0.02	0.028
Tau	9.507	9.631	9.182	9.238	9.507	Tau	0.028	0.033	0.02	0.02	0.028
NAA	7.434	7.288	7.369	7.406	7.299	NAA	0.013	0.018	0.01	0.01	0.015
Cr+PCr	13.424	13.163	13.547	13.474	13.18	Cr+PCr	0.01	0.015	0.01	0.01	0.013

Conc (arbitrary units)						ESFU (relative LCModel SD)					
b-value (ms/µm²)	33					b-value (ms/µm²)	33				
Quantification	Raw	Raw ½	Dn – strategy 1	Dn – strategy 2	Dn – strategy 3	Quantification	Raw	Raw ½	Dn – strategy 1	Dn – strategy 2	Dn – strategy 3
Gln	1.025	1.082	1.293	1.393	1.399	Gln	0.2	0.23	0.065	0.068	0.08
Glu	4.39	4.528	4.905	5.44	5.049	Glu	0.053	0.065	0.023	0.023	0.03
Ins	1.936	2.22	2.462	2.64	2.581	Ins	0.095	0.1	0.035	0.04	0.048
Tau	1.17	1.141	1.554	1.771	1.661	Tau	0.188	0.203	0.065	0.06	0.078
NAA	2.105	2.293	2.201	2.511	2.341	NAA	0.04	0.045	0.023	0.023	0.025
Cr+PCr	3.488	3.739	3.934	4.356	4.132	Cr+PCr	0.04	0.048	0.015	0.02	0.023

Table 6.4: Concentrations and estimated spectral fit uncertainty (ESFU) for in vivo human data (mean over volunteers) at the lowest and highest b-values, for every method and every reliably quantified metabolite. In the ESFU tables, no values above 0.2 are found (fit quality). Denoising expectedly reduces the ESFUs. Metabolite concentrations at all b-values are referenced to an arbitrary value.

In vivo human *data*							
Conc (arbitrary units)				ESFU (relative LCModel SD)			
b-value (ms/µm²)	0.37			b-value (ms/µm²)	0.37		
Quantification	Raw	Dn – strategy 1	Dn – strategy 2	Quantification	Raw	Dn – strategy 1	Dn – strategy 2
mIns+2Gly	5.6975	5.7225	5.695	mIns+2Gly	0.0575	0.06	0.06
tNAA	7.9425	7.9175	7.9175	tNAA	0.03	0.03	0.03
Glx	12.825	12.825	12.825	Glx	0.08	0.08	0.08
tCho	1.341	1.3265	1.339	tCho	0.055	0.055	0.055
Cr+PCr	6.1725	6.135	6.1675	Cr+PCr	0.035	0.035	0.035

Conc (arbitrary units)				ESFU (relative LCModel SD)			
b-value (ms/µm²)	25.1			b-value (ms/µm²)	25.1		
Quantification	Raw	Dn – strategy 1	Dn – strategy 2	Quantification	Raw	Dn – strategy 1	Dn – strategy 2
mIns+2Gly	1.6875	1.7575	1.69	mIns+2Gly	0.0625	0.0475	0.0525
tNAA	2.3125	2.265	2.275	tNAA	0.035	0.0275	0.03
Glx	3.555	3.3425	3.5375	Glx	0.09	0.08	0.08
tCho	0.4105	0.38125	0.38875	tCho	0.055	0.0475	0.0475
Cr+PCr	1.8525	1.81	1.775	Cr+PCr	0.04	0.03	0.035

Table 6.5: MRSinMRS checklist from Lin et al. « Minimum Reporting Standards for in Vivo Magnetic Resonance Spectroscopy (MRSinMRS): Experts' Consensus Recommendations ».

1. Hardware	Simulations	9.4T rodent data	3T human data
a. Field strength [T]	9.4T	9.4T	3T
b. Manufacturer	N/A	Varian	Siemens
c. Model (software version if available)	N/A	Direct Drive Console	MAGNETOM Skyra Connectom A (Version VD11D)
d. RF coils: nuclei (transmit/receive), number of channels, type, body part	N/A	Homemade quadrature 2 loops surface coil	32 channel head coil
e. Additional hardware	N/A	Gradient strength: 400 mT/m	Gradient strength: 300 mT/m

2. Acquisition	Simulations	9.4T rodent data	3T human data
a. Pulse sequence	SPECIAL	Diffusion-weighted STEAM	Diffusion-weighted STEAM
b. Volume of Interest (VOI) locations	N/A	Full brain	Occipito-parietal cortex
c. Nominal VOI size [cm^3, mm^3]	N/A	162-245 μL,	23±2 cm^3
d. Repetition Time (TR), Echo Time (TE), mixing time (TM)	TE: 2.8 ms	TE: 15 ms, TM: 112 ms, TR: 4000 ms	TE: 30 ms, TM: 65 ms, TRmin: 1800 ms (ECG-triggered)
e. Total number of Excitations or acquisitions per spectrum	100 shots generated per b-value, 10 b-values from 0.4 to 33.3 ms/μm^2	128 shots per b-value, 11 b-values from 0.4 to 33.3 ms/μm^2	64 shots per b-value with metabolite cycling, 32 2-shot metabolite spectra per b-value, 11 b-values from 0.37 to 25.1 ms/μm^2
f. Additional sequence parameters (spectral width in Hz, number of spectral points, frequency offsets)		5000 Hz, 4096 points, Duration of diffusion gradients: 6 ms	4000 Hz, 4096 points, Duration of diffusion gradients: 8.8 ms, ramp time 1.7 ms
g. Water Suppression Method	N/A	VAPOR	Metabolite Cycling
h. Shimming Method, reference peak, and thresholds for "acceptance of shim" chosen	Signals generated with: 0.2 Hz L and 1.8 Hz G broadening on the simulated basis set, then an extra 5 Hz L broadening	FASTMAP, target LW: 18-21 Hz	Manufacturer's built-in automatic shimming tool (advanced mode), water linewidth < 6 Hz
i. Triggering or motion correction method	N/A	None	ECG-triggered

3. Data analysis methods and outputs	Simulations	9.4T rodent data	3T human data
a. Analysis software	LCModel v6.3	LCModel v6.3	LCModel v6.3
b. Processing steps deviating from quoted reference or product	EC, Phase, frequency drifts correction before quantification	EC, Phase, frequency drifts correction before quantification	EC, Phase, frequency drifts and motion correction before quantification
c. Output measure	Concentrations in arbitrary units (e.g. absolute concentration, institutional units, ratio)	Concentrations in arbitrary units	Concentrations in arbitrary units
d. Quantification references and assumptions, fitting model assumptions	The basis set includes a (rodent) in vivo acquired MM spectrum	The basis set includes an in vivo acquired MM spectrum	The basis set includes an in vivo acquired MM spectrum
	NUNFIL 2048, NRATIO 12*, NOMIT 7: lipids, Gua, Ser, -CrCh2, Fit region: 0.2-4.3 ppm, DKNTMN 0.25, *The effect of NRATIO was tested in a Monte Carlo simulation study and no significant difference was found in the diffusion coefficients with or without soft constraints	NUNFIL 2048, NRATIO 12*, NOMIT 7: lipids, Gua, Ser, -CrCh2, Fit region: 0.2-4.3 ppm, DKNTMN 0.25, *The effect of NRATIO was tested in a Monte Carlo simulation study and no significant difference was found in the diffusion coefficients with or without soft constraints	NUNFIL 2048, NRATIO 0, NOMIT 7: lipids, Gua, Ser, -CrCh2, Fit region: 0.2-4.3 ppm, DKNTMN 0.25

4. Data Quality	Simulations	9.4T rodent data	3T human data
a. Reported variables	SNR: definition given at the beginning of the method section, evaluated throughout the manuscript	SNR: definition given at the beginning of the method section, evaluated throughout the manuscript	SNR: definition given at the beginning of the method section, evaluated throughout the manuscript
(SNR, Linewidth (with reference peaks))	LW: not evaluated	LW: not evaluated	LW: not evaluated
b. Data exclusion criteria	N/A	None	Inclusion criteria: High SNR and low signal drop of 0.9 ppm MM peak to allow for individual fitting
c. Quality measures of postprocessing Model fitting (e.g. CRLB, goodness of fit, SD of residual)	Bias versus noiseless, ground truth, SD across MC iterations, LCModel SD%	SD across animals, LCModel SD%	SD across volunteers, LCModel SD%
d. Sample Spectrum	**Figure 6.2**	**Figure 6.11**	**Figure 6.14**

Study of metabolism with PET Part III imaging

7 Application of FDG-PET in HE

Abstract

Type C hepatic encephalopathy (HE) is a severe neuropsychiatric disorder occurring as a consequence of chronic liver disease. Alterations in energy metabolism have been suggested in type C HE, but in vivo studies on this matter remain sparse and have reported conflicting results. Here, we propose a novel preclinical ^{18}F-FDG PET quantification method where an image-derived input function (IDIF) was used to compute regional, steady state maps of the cerebral metabolic rate of glucose (CMR_{glc}). PET CMR_{glc} maps were then registered to an atlas and the mean CMR_{glc} from two regions of interest, the hippocampus and the cerebellum, were associated to localized ^{1}H MR spectroscopy acquisitions in the same regions. A 2-fold lower brain glucose uptake, concomitant with an increase in brain glutamine and a decrease in the main osmolytes was observed in the hippocampus and in the cerebellum. This study provides for the first time local and quantitative information on both brain glucose uptake and neurometabolic profile alterations in a rat model of type C HE, and constitutes an important step towards new insights into energy metabolism in the pathophysiology of HE. On the methodological stand point, the use of an IDIF made the quantitative PET measurement non-invasive and compatible with longitudinal studies. Moreover, the standardized uptake value, a more common metric in preclinical PET studies, would have failed to detect such differences between the BDL and sham groups, emphasizing the importance of PET quantification methods that account for systemic metabolism differences.

Publications

This chapter has been published as:

[140]: **J. Mosso**, T. Yin, C. Poitry-Yamate, D. Simicic, M. Lepore, V. A. McLin, O. Braissant, C. Cudalbu, and B. Lanz, "PET CMRglc mapping and 1H-MRS show altered glucose uptake and neurometabolic profiles in BDL rats," *Analytical Biochemistry*, vol. 647, p. 114606, June 2022.

Contributions

I implemented PET and MRS data analysis and initiated a quantification framework for the CMR_{glc} based on Bernard Lanz's method from ref. [293]. The PET and MRS acquisitions were performed before the beginning of my PhD by Bernard Lanz, Cristina Cudalbu, Carole Poitry-Yamate, Corina Berset and Mario Lepore. I wrote the first draft of the manuscript, which was reviewed by all the co-authors.

7.1 Context

In the previous parts of this thesis, brain metabolism in hepatic encephalopathy was studied with ^{1}H MR spectroscopy. The first use of ^{1}H MRS in patients with HE dates back to 1990 [143], where the authors measured alterations of brain metabolism concomitant with the liver disease, namely increased brain Gln and compensatory decreased osmolytes. Since then, ^{1}H MRS has been able to probe alterations in concentrations of a larger range of metabolites involved in neurotransmission, oxidative stress and energy metabolism [136]. However, glucose (Glc), a central player in the study of energy metabolism and the main source of energy for the brain, is hard to measure with traditional ^{1}H MRS sequences due to its low concentration and its overlap with other metabolites even at high magnetic fields. In addition, ^{1}H MRS informs only on steady state pools of metabolites and not on dynamic processes. Because mounting evidence suggests that energy metabolism might be impaired in HE (see details in the introduction chapter), appropriate non invasive imaging modalities to follow the dynamic fate of glucose were needed. Autoradiography and positron emission tomography (PET) methods have emerged as such candidates. ^{18}F-fluorodeoxyglucose (FDG) PET probes the transport of glucose into the cell and the first step of glycolysis (conversion into FDG 6-phosphate (FDG-6P)). **It holds the promise of informing on glucose uptake in the HE brain, on grounds that ^{1}H MRS is unable to explore.**

Moreover, in line with the ^{1}H MRS studies of microstructure and metabolism presented in the previous parts of this thesis, establishing quantitative, and not only semi-quantitative, imaging methods appeared fundamental. A semi-quantitative method will attribute a relative order between observations on an arbitrary scale, whereas a quantitative method will provide independent numbers to observations in a standard unit independent from the measurement approach. For example, PET data can be analysed semi-quantitatively, where the PET image is normalized to global factors (weight of the animal, injected dose) or referenced to another brain region, or fully-quantitatively, where a quantitative value is given to a process through metabolic modelling. Only the extraction of quantitative features from an imaging modality allows one to compare two groups accurately (a disease and a control group), two methodologies (fluxes derived from PET and ^{13}C MRS for example), the results from two different sites or from two operators. The PET project presented in this chapter was elaborated with this idea in mind. **Retrospectively, we observed that the application of ^{18}F-FDG PET in BDL animals was able to fully demonstrate the importance of quantitative imaging, where the semi-quantitative approach failed to probe the same results**.

In this chapter, the first application of ^{18}F-FDG PET combined with ^{1}H MRS on adult BDL rats will be presented, yielding important conclusions on brain energy metabolism in HE and on the necessity of quantitative PET analysis. We believe that the quantitative approach

developed in preclinical settings could have broader applications than HE, for which the non-invasive measurement of the input function presented in this chapter is crucial.

7.2 Positron emission tomography (PET)

The basic concepts

Contrary to MR, PET is an ionizing imaging technique. It utilizes ionizing radiation (β and γ), capable of removing electrons and creating ions in the matter that it travels through, which can be hazardous to life. PET relies on the β decay of radioisotopes caused by weak nuclear interactions, where a positron (β^+) and a neutrino (ν_e) are created following the conversion of a proton into a neutron [294]. Unlike in NMR where Zeeman splitting acts on the nuclear ground state, the β decay corresponds to a transition of much higher energies from the excited to the nuclear ground state. Typically, a radioisotope used in biomedical imaging is a β^+ emitter whose excited state can be maintained for a time sufficiently long that it can be measured and sufficiently short that radioactive material does not survive in nature for too long (the radioactive half-life, i.e. the time it takes for the population of radioisotopes to be decreased by 2, if for example 109 min for ^{18}F).

The emitted positron will then diffuse through matter (≈ 1 mm for ^{18}F, known as positron range). In practise, this diffusion limits the resolution of the PET image. During its travel, the positron will enter in collision with surrounding atoms and lose most of its kinetic energy, to finally be annihilated by an electron. Assuming its kinetic energy before the collision is negligible, the conservation of energy and momentum shows that 2 γ photons are produced, in almost opposite direction and with an energy of 511 keV:

$$m_e c^2 + m_p c^2 = 2 m_e c^2 = 2 E_{\text{ph}} = 2 \times 511 \text{ keV} \tag{7.1}$$

where m_e is the mass of the electron, m_p the mass of the positron and E_{ph} the energy of each emitted photons.

The PET scanner will detect the coincidence of the two γ photons emitted for each annihilation and reconstruct the source object following computed tomography principles. In practice, the γ photons travelling through matter are attenuated by Compton and photoelectric effects before reaching the detectors. Compton inelastic scattering dominates at the energies involved in PET imaging, and energy windows are used during the photon detection to filter out scattered coincidences with lower energy. Because of the simultaneous detection of photon pairs in opposite directions, the attenuation in the object will only depend on the dimension of the object on that direction and not on the exact position of the annihilation point. This is the reason why attenuation correction can easily be performed for PET measurements,

with for example a CT scan prior to the PET scan. Moreover, the directionality is given by the line between the two detectors simultaneously detecting a photon, and there is no need for collimation like in single-photon emission computed tomography (SPECT) imaging. The attribution of the correct position of the annihilation point is however influenced by the detection of additional unwanted coincidences (scattered, random, multiple), the detectors efficiency and the ring geometry [295].

In medical imaging applications, a radiotracer is injected in the body and its metabolic fate followed dynamically. It is a metabolic substrate to which a positron-emitting radioisotope is bound. It is injected in the body in trace amounts (typically in picomolar concentrations), in order not to disturb endogenous metabolism and avoid strong radioactive dose deposition. The radiotracer will compete with the endogenous molecule for metabolic conversion or protein binding for example. PET imaging is very sensitive (trace amounts of radiotracer create a high imaging contrast) but the spatial resolution is much lower than in MRI and is limited by the positron range on preclinical scanners and by the large ring diameter on human scanners.

^{18}F-FDG PET

^{18}F-FDG PET experiments allow one to investigate glucose uptake in vivo. ^{18}F-FDG will compete with glucose, its endogenous counterpart, for uptake in cells. ^{18}F-FDG has the distinctive feature to be converted into ^{18}F-FDG-6P, but its molecular structure after phosphorylation prevents any further conversion into glycolysis. The PET signal, resulting from γ rays emitted after positron-electron annihilation from both ^{18}F-FDG and ^{18}F-FDG-6P, provides unique information on the first steps of glucose metabolism in living tissue.

Application of PET imaging in disease

PET imaging has been used in multiple diseases and with different tracers, a few examples are listed below and a more exhaustive review for neurology applications can be found here [296]. ^{18}F-FDG is by far the most widespread tracer. Cancerous cells present a higher rate of glycolysis and expression of GLUT transporters than healthy cells, resulting in an elevated ^{18}F-FDG PET signal in tumor regions. Tracing the evolution of the PET signal can be used for diagnosis, detection of recurrence and follow up in oncology [297]. Tau and amyloid-β PET tracers have been recently developed to study neurodegenerative conditions including Alzheimer's disease, where a higher Tau and amyloid-β PET signal have been correlated with memory loss and mild cognitive impairment [298]. ^{18}F-DOPA has been used in Parkinson's disease patients, showing an impaired function of dopaminergic neurons via the reduced decarboxylation rate of F-DOPA in the brain [299].

The quantitative versus semi-quantitative approaches

The quantification of the PET radioactivity density maps can be done in several ways. In clinical studies, the most common method is the standardized uptake value (SUV), where radioactivity density maps are normalized by weight of the patient and by the ^{18}F-FDG injected dose. However, the SUV, although already an advanced step as compared to a simple non-calibrated intensity image, does not take into account variations in the amount of tracer available for the organ of interest in terms of the arterial input function (AIF), the radio-tracer activity density in the plasma measured dynamically, which could vary due to systemic effects such as altered metabolism of other organs. The SUV is thus considered as a semi-quantitative metric. In 1977, Sokoloff et al. derived a fully quantitative calculation for preclinical autoradiography measurements using ^{14}C deoxyglucose [194], that can similarly be used for FDG PET studies. In his method, both the AIF and the competition for transport between glucose and ^{18}F-FDG (through the Lumped Constant (LC)) are taken into account, as well as the blood glycemia levels that influence the uptake of both substrates. However, technical challenges make it more difficult for clinical translation, mainly because the AIF needs to be acquired dynamically with multiple blood sampling and before the steady state acquisition on the brain.

In this thesis, we will show that a 3D quantitative metabolic mapping of the cerebral metabolic rate of glucose can be achieved with the preclinical PET scanner spatial resolution, using the approach by Sokoloff et al. and a minimally invasive measurement of the FDG input function from the PET image.

7.3 Introduction

The pathophysiology of type C HE and the conflicting results reported in literature with regards to energy metabolism alterations have been presented in the introduction chapters.

To the best of our knowledge, no ^{18}F-FDG PET studies on preclinical models of type C HE are available to date. While ^{1}H MRS provides a steady state information on metabolic pools, ^{18}F-FDG PET provides kinetic information on local brain glucose uptake. ^{18}F-FDG, an analog of glucose labelled with the positron-emitting ^{18}F, is transported across the blood-brain barrier and converted to ^{18}F-FDG6P (analog of glucose-6-phosphate (G6P)) and no further metabolized through the glycolysis [300]. Therefore, the FDG PET signal at labelling steady-state reflects the very first two steps of glycolysis: glucose transport through the blood brain barrier (BBB) and phosphorylation into G6P. The SUV is routinely reported in PET studies, but it does not allow for a quantitative assessment of glucose cerebral metabolic rates, especially in pathological conditions with alterations of systemic metabolism. The derivation of the CMR_{glc} from labelling steady-state images is, on the contrary, a quantitative method introduced

by Sokoloff et al. [194] for 2-deoxy-D-[^{14}C] glucose autoradiography studies, which can be extended to in vivo ^{18}F-FDG PET data and provides both a local and quantitative rate of glucose utilization in the tissue in a non-invasive way. Yet, it requires the dynamic measurement of the blood FDG activity (the AIF) from the time of the bolus injection up to the labelling steady-state measurement time frame [300]. The measurement of arterial input function can be particularly challenging in rodents and is often the more invasive part of the FDG-PET study. Following a recent strategy proposed by Lanz et al. [293], the AIF can be measured prior to the brain acquisition from the PET image of the vena cava where the FDG bolus is observed. In doing so, difficulties linked to manual and multiple blood samplings can be circumvented. By combining this dynamic measurement of the AIF with a static PET measurement on the brain at labelling steady-state, the CMR$_{glc}$ can be derived from the sole PET scan for each animal with minimal invasiveness.

Here we propose a novel ^{18}F-FDG PET quantification method to perform a spatial mapping of glucose uptake, where CMR$_{glc}$ maps computed with the image-derived AIF were co-registered to a rat brain atlas. In addition, we combined the CMR$_{glc}$ maps with in vivo ^{1}H MRS at 9.4T in the hippocampus and cerebellum and showed regional alterations of brain glucose uptake in the BDL rat model of type C HE concomitant with neurometabolic pools' changes. Taken together, ^{1}H MRS and quantitative ^{18}F-FDG PET bring a new insight on brain energy metabolism in HE.

7.4 Methods

7.4.1 BDL rats

We used the bile duct ligated (BDL) rat model for chronic liver disease leading to type C HE, recognized by the International Society for Hepatic Encephalopathy and Nitrogen Metabolism (ISHEN) [135]. Male adult Wistar rats (N=18, Charles River Laboratories, France) underwent BDL (N=10, 175 ± 13 g at surgery) or sham surgery (N=8, 174 ± 14 g at surgery). Plasma bilirubin (Reflotron Plus analyzer, Roche, Switzerland) and blood ammonia (Integra 400 Plus, Roche, Switzerland) from the sublingual vein were measured at week 6 post-surgery in BDL rats to follow the disease progression. Ammonia was also measured at week 0. For all experiments, rats were under isoflurane anaesthesia (1.5-2% in a mixture of 50%/50% air/O$_2$ for MRS and 1-2% in 100% O$_2$ for PET) with the breathing rate maintained between 60 and 80 resp/minute (SA Instruments, USA). Body temperature was kept between 37.5°C and 38.5°C using a water bath system. All experiments were approved by the Committee on Animal Experimentation for the Canton de Vaud, Switzerland (VD3022.1).

7.4.2 ^{1}H MRS

^{1}H MRS experiments were performed on an actively shielded 9.4 Tesla horizontal magnet (Magnex Scientific, UK), 31-cm inner diameter bore, with a Direct Drive console (Varian Inc., USA) and a home-made transmit/receive quadrature surface radio-frequency coil. Anatomical T_2-weighted images were acquired in the axial plane to position the volumes of interest (VOIs) for ^{1}H MRS scans using a multislice turbo-spin-echo sequence (repetition time (TR)/effective echo time (TE_{eff}) = 4000/52 ms, echo train length = 8, field of view (FOV) = 23 × 23 mm^2, slice thickness = 1 mm, 15 slices, matrix size = 256 × 256, 1 average). The SPECIAL [21] sequence was used for localized spectroscopy with TE = 2.8 ms, TR = 4 s, 160 averages (10 blocks of 16 averages), a 5 kHz spectral width and 4096 spectral points. ^{1}H MRS acquisitions were performed on BDL rats before surgery (week 0) and at 6 weeks post-surgery on two brain regions, hippocampus (week 0: N=4, week 6: N=9) and cerebellum (week 0: N=3, week 6: N=4), with a voxel size of 2.8 × 2 × 2 mm^3 and 2.5 × 2.5 × 2.5 mm^3 (*x,y,z* on **Figure 7.4**), respectively. VAPOR [210] scheme was used for water suppression and FASTMAP [301] for shimming (target water linewidth in the hippocampus: 9-10 Hz, in the cerebellum: 14-17 Hz). Frequency drift and phase corrections between blocks were applied prior to absolute quantification of metabolites with LCModel [302] (version 6.2). An in vitro acquired metabolite basis set and the spectrum of macromolecules measured in vivo [303, 34] were used for LCModel quantification. The water signal from the same voxel was used as internal reference and the metabolite concentrations were derived from the ratio of peak areas, assuming that the water concentration in the voxel was 44.4 M. An exclusion criterion for individual metabolite concentrations based on relative Cramer Rao Lower Bounds (rejected if CRB% > 35%) was used. In addition, metabolites were not reported if more than 75% of quantified concentrations over the investigated group were rejected. Since ^{1}H MRS acquisitions were performed at week 0, each animal served as its own control for ^{1}H MRS results at week 6.

7.4.3 ^{18}F-FDG PET

PET acquisitions on BDL (N=10) and sham (N=8) rats at week 6 post-surgery were conducted on a small animal avalanche photodiode detector-based LabPET-4 scanner, with 250-650 keV energy window and 22.2 ns coincidence time window (Advanced Molecular Imaging, Canada). The acquisitions for each individual rat were performed and reconstructed in two steps:

Step (1) - a 45-min dynamic acquisition on the thoracic region of the animal to extract the image-derived input function from the vena cava, followed by,

Step (2) - a 15-min static acquisition at labelling steady-state with the rat brain in the FOV of the PET scanner, to further calculate glucose cerebral metabolic rate [194] maps of the brain.

For step (1), a 60 mm-diameter cylindrical FOV in the coronal plane and 36.6 mm in the axial direction (31 slices of 1.18 mm thickness) was positioned on the thoracic region of the rat and a bolus of ^{18}F-FDG (67.6±11.9 MBq) was injected in the tail vein, followed by a saline chase. Coincidence data were acquired in list mode to allow for a flexible reconstruction of time frames. Dynamic radioactivity density maps were quantified in Bq/mL using the LabPET-4 built-in calibration method and reconstructed using the iterative MLEM algorithm (5 iterations), with a time resolution enabling a good characterization of the bolus input function (24×5 s, 6×30 s, 5×120 s, 6×300 s) [293]. The inferior vena cava was then identified from the maximum intensity projection (MIP) images during the FDG bolus passage, using the PMOD software environment (PMOD Technologies Ltd.). The AIF was then extracted from the dynamic PET images from step (1) by averaging the activity in Bq/mL of 4 voxels over 4 successive axial slices (total volume: 4.7 mm^3) on the vena cava where the flow of ^{18}F-FDG was observed.

Following step (1), a 10 to 15 min-static acquisition on the brain was performed for step (2) ($0.5 \times 0.5 \times 1.18$ mm^3 standard voxel size, 60 mm-diameter coronal FOV, 31 axial slices of 1.18 mm thickness) and the quantified images in Bq/mL were reconstructed with a 15-iteration maximum likelihood expectation maximization (MLEM) algorithm [304].

During post processing, the AIF curve from step (1) was first corrected for radioactivity decay and blood versus plasma tracer content [305]. It was then extrapolated from the end of dynamic acquisition up to the central time of the static acquisition used in step (2) based on a bi-exponential fit started at t = 2 min (i.e. in the decaying phase of the AIF following the chase). In the calculation of the CMR$_{glc}$, trapezoidal integration of the extrapolated AIF curve was used. Brain images were corrected for radioactivity decay from the start of the vena cava acquisition (step (1)).

Finally, 3D maps of CMR$_{glc}$ were reconstructed following the 2-deoxy-D-[^{14}C]glucose quantification method of Sokoloff et al. [194]. In this method, the CMR$_{glc}$ is obtained from a three-compartment model, represented in **Figure 7.1**: a pool 1 of plasma Glc and ^{18}F-FDG, a pool 2 of intracellular Glc and ^{18}F-FDG, and a pool 3 of intracellular G6P and ^{18}F-FDG6P. The following 4 hypotheses were made. First, the static measurement is performed at a sufficiently late time point and in a homogeneous region such that the kinetic rates, the transport rates, the Glc plasma concentration, all intracellular concentrations and the CMR$_{glc}$ rate are constant. In our extension of this method to 3D CMR$_{glc}$ maps from static FDG-PET images, this assumption of homogeneous region applies to the reconstructed voxel. Second, the ^{18}F-FDG and ^{18}F-FDG6P concentrations are present in tracer amounts compared to their non-radioactive counterpart. Third, the hydrolysis of G6P to Glc and ^{18}F-FD6P to ^{18}F-FDG can be neglected compared to the reverse phosphorylation step. Forth, all brain regions receive a similar amount of tracer and Glc, and are homogenous in terms of transport and kinetic rates.

From these hypotheses, the CMR_{glc} value was derived, describing the rate of G6P utilization in the tissue [194]:

$$\text{CMR}_{\text{glc}} = \frac{C_i^*(T) - k_1^* e^{-(k_2^* + k_3^*)T} \int_0^T C_p^* e^{+(k_2^* + k_3^*)t} \text{dt}}{LC \times \left[\int_0^T \frac{C_p^*(t)}{C_p} dt - e^{-(k_2^* + k_3^*)T} \int_0^T \frac{C_p^*(t)}{C_p} e^{+(k_2^* + k_3^*)t} \text{dt} \right]} \tag{7.2}$$

where C_i^* is the summed concentration of intracellular radioactive compounds (^{18}F-FDG6P and ^{18}F-FDG) i.e. the quantity measured at steady state in a PET experiment, T the central time of the steady state static acquisition after the bolus injection, k_1^* the kinetic rate of ^{18}F-FDG transport from pool 1 to pool 2 through the BBB, k_2^* the reverse ^{18}F-FDG transport rate from pool 2 to pool 1, k_3^* the ^{18}F-FDG phosphorylation rate into ^{18}F-FDG6P, C_p^* the time-dependent plasma ^{18}F-FDG concentration and C_p the constant plasma Glc concentration. It is assumed that the chemical reaction between FDG and FDG6P is at equilibrium and that partial volume effect (additional radioactivity measured from the blood vessels in the tissue) is negligible when T is large.
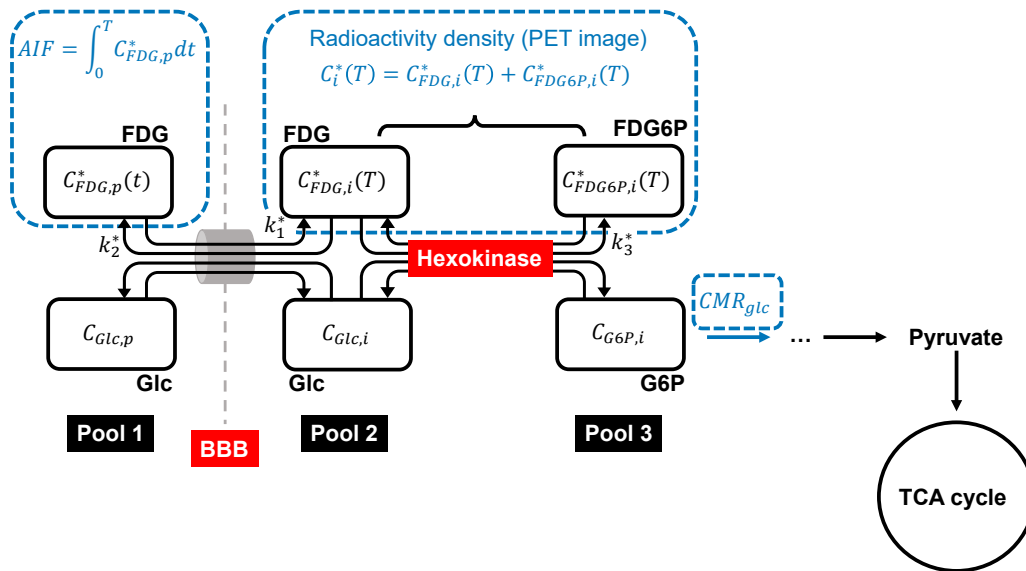
Figure 7.1: Three-compartment model of glucose and FDG metabolism used to compute CMR_{glc} values: the kinetic constants, k, and the pool concentrations, C, a denoted with a * when related to the radiolabeled compounds.

If T is large enough (experimentally, 45 min), the equation (1) can be approximated by:

$$\text{CMR}_{\text{glc}} = \frac{C_i^*(T) \times C_p}{LC \times \int_0^T C_p^*(t)\text{dt}} \tag{7.3}$$

, where $\int_0^T C_p^*(t)dt$ is the integral of the AIF from step (1) of the in vivo acquisition and $C_i^*(T)$ the steady-state brain radioactivity density, as measured from the PET images from step (2). LC is Lumped Constant, which accounts for the competition between Glc and ^{18}F-FDG at the transport and phosphorylation steps, as both substrates use the same BBB transporters [306] and are phosphorylated by the hexokinase [307]. In our study, the Lumped Constant (LC) was set to 0.71, as done previously in rat brain studies [308]. Glycemia C_p was measured at the end of step (2) in the tail vein. Since $C_i^*(T)$ is measured for each image voxel from the steady-state acquisition over the brain (step (2)), the derivation of the CMR$_{\text{glc}}$ results in a 3D metabolic CMR$_{\text{glc}}$ map with same nominal spatial resolution as the PET acquisition itself (i.e. $0.5 \times 0.5 \times 1.18$ mm^3), individually for each animal.

7.4.4 PET-atlas registration

Since PET images suffer from low spatial resolution and poor contrast, direct PET to atlas registration is challenging. To circumvent this limitation, the MRI anatomical images of one rat were used as an intermediate registration step (see the procedure described in **Figure 7.2**). The steady state CMR$_{\text{glc}}$ map from one animal with its corresponding MRI anatomical images were chosen as a reference pair. In step A, this reference CMR$_{\text{glc}}$ map was registered to its corresponding MRI image using mutual-information-based rigid transformation [309], and in step B, to the Waxholm Space Atlas [310] using affine and nonlinear symmetric deformable registration (SyN) through the Advanced Normalization Tools [311]. In step C, all other individual CMR$_{\text{glc}}$ maps were registered to the reference CMR$_{\text{glc}}$ map by applying rigid and seven-degrees of freedom similarity transformation with normalized gradient field similarity measure in MeVisLab [312]. Following step C, atlas labels were resampled to each individual PET space to perform a region of interest (ROI)-based analysis, where CMR$_{\text{glc}}$ maps were averaged over the hippocampus and the cerebellum regions, respectively.

7.4.5 Statistical analysis

All data are presented as mean ± standard deviations (SD) and assumed to be Gaussian-distributed. Variance equality was tested prior to any statistical test using a Fisher test (F-test of equality of variances). For plasma bilirubin and blood ammonia measurements, an unpaired Student's t-test between week 0 and 6 blood or plasma concentrations was performed. For brain volumes, the mean of the total brain volume covered by all atlas labels derived from the PET to altas registration was compared between sham and BDL rats using an unpaired
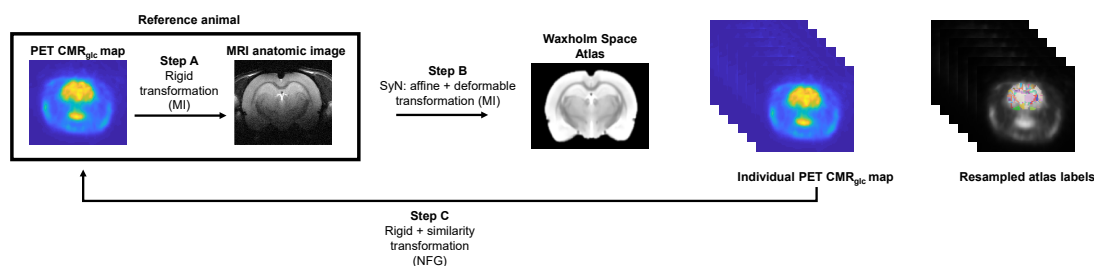
Figure 7.2: PET to atlas registration: the CMR_{glc} map of a reference animal was first registered to its corresponding MRI anatomical images, and then to the Waxholm Space Atlas [310]. Other CMR_{glc} maps were then aligned with the reference one to obtain segmentations for the cerebellum and hippocampus. SyN: nonlinear symmetric deformable registration, MI: mutual information, NFG: normalized field gradient

Student's t-test.

For ^{1}H MRS, only Asc concentrations in the hippocampus featured non-equal variances between week 0 and week 6. All metabolite mean concentrations ± SD at week 0 and week 6 were therefore compared using an unpaired Student's t-test, except for Asc concentrations in the hippocampus which was compared with a Welch's t-test, accounting for unequal variances.

For all metabolites where both brain regions displayed significant changes between week 0 and 6 (Gln, Glu and Ins+Tau+tCr+tCho), the impact of the brain region on concentration changes over the weeks was tested through the interaction of the week factor and the brain region factor in a two-way ANOVA (Prism 5.03, Graphpad, La Jolla CA US).

For ^{18}F-FDG PET, CMR_{glc} variances between sham and BDL rats for each brain region were found equal, thus mean CMR_{glc} ± SD were compared using a Student's t-test. We also checked that the standard error on the mean CMR_{glc} over the region of interest was smaller than the SD in the mean CMR_{glc} between animals, retrospectively ensuring that using the SD was meaningful.

The following statistical significance values were used: * $p < 0.05$, ** $p < 0.01$, *** $p < 0.001$, **** $p < 0.0001$.

7.5 Results

7.5.1 Biochemical measurements

Plasma bilirubin (<0.5 mg/dL at week 0 [136] to 8.07±2.03 mg/dL at week 6, N=11,****) and blood ammonia (89±43 μM at week 0, N=4 to 127±25 μM at week 6, N=4, non-significant) increased in all BDL rats, confirming the induced chronic liver disease (**Figure 7.3**).
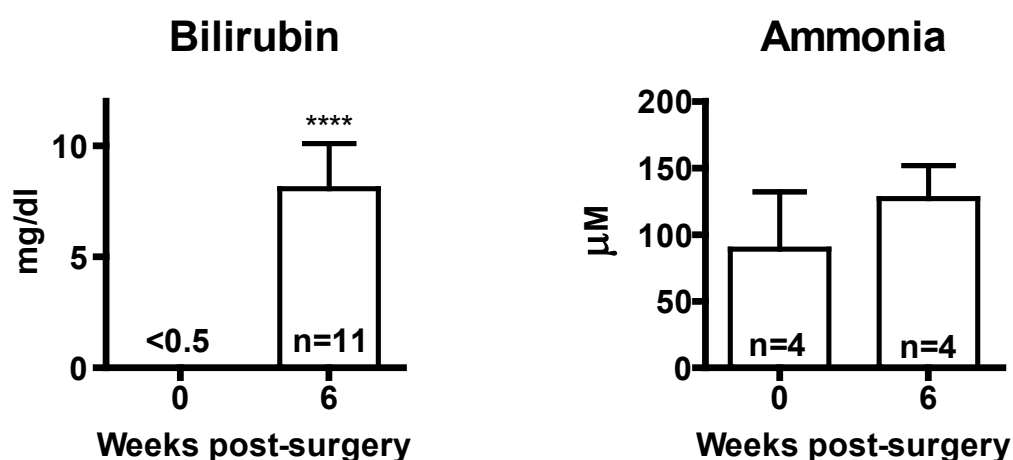
Figure 7.3: Evolution of plasma bilirubin and blood ammonia in BDL rats over weeks post-surgery.

7.5.2 ^{1}H MRS - impaired neurometabolic profiles in BDL rats

Representative spectra acquired in BDL rats at week 0 and 6 in both brain regions are shown in **Figure 7.4**. The ultra-short TE allowed the detection of 15 brain metabolites: ascorbate (Asc), glycerophosphocholine (GPC), phosphocholine (PCho), creatine (Cr), phosphocreatine (PCr), GABA, glutamine (Gln), glutamate (Glu), glutathione (GSH), myoinositol (Ins), lactate (Lac), N-acetylaspartate (NAA), Nacetylaspartylglutamate (NAAG), phosphoethanolamine (PE) and taurine (Tau). In the hippocampus, the group analysis showed a strong increase of Gln between week 0 and 6 (+73%,***), and a decrease of Glu (-13%,**), Tau (-20%,**), Ins (-11%, *), total creatine (Creatine+Phosphocreatine, tCr) (-10%,****) and Asc (-17%,**). In the cerebellum, the group analysis showed an increase of Gln, which was even stronger than the one in the hippocampus (+114%,***, with a 1.6-fold significant difference in % change between the two brain regions,*), a decrease of Glu (-22%,**) and Tau (-37%,**), but no significant difference was observed for tCr, Ins and Asc. GABA also showed a significant decrease in the cerebellum (-43%,* $p = 0.04$). Additionally, the main metabolites playing a role in osmoregulation (tCr, tCho, Ins, Tau) were summed to evaluate the osmoregulatory response to the Gln-induced osmotic stress and a significant decrease was observed in the hippocampus (-13%,***) and in the cerebellum (-15%,*), as shown in **Figure 7.6C**. All other individual metabolites that were reliably quantified (GSH, Lac, PE, total *N*-acetylaspartate (tNAA), and total choline (tCho)) showed no significant difference between week 0 and 6 in any of the two brain regions. Alanine (Ala), aspartate (Asp), scyllo-inositol (Scyllo), β-hydroxybutyrate (bHB) and glucose (Glc) were present in the basis set but were excluded from the analysis.
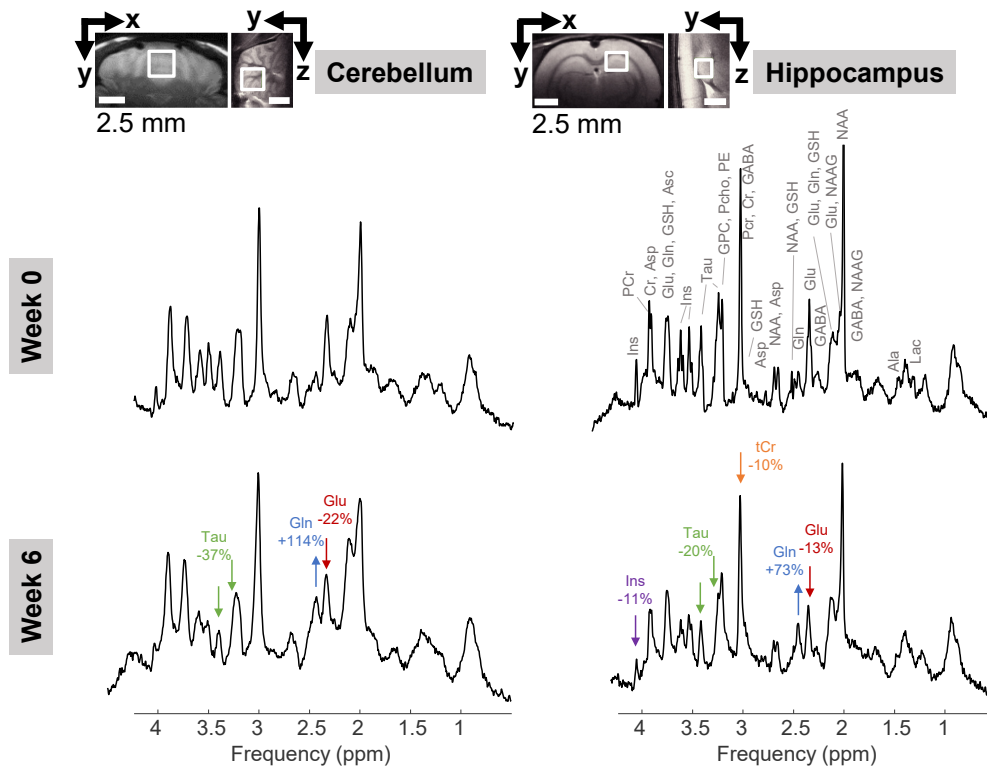
Figure 7.4: ^{1}H MRS spectra acquired at 9.4T in the hippocampus and cerebellum of BDL rats at week 0 and 6 post-surgery. Arrows show significant differences observed between week 0 and week 6 for each brain region, and point solely to non-overlapping (or least-overlapping) peaks for the displayed metabolites. The two voxels on anatomical T$_2$-weighted images are shown at the top, where (*x,y,z*) are the MRI gradient directions.

7.5.3 ^{18}F-FDG - impaired glucose uptake in BDL rats

The image-derived AIF was reliably measured for each rat from the radiotracer bolus observed in the vena cava during the 45-min dynamic acquisition. **Figure 7.5A** shows a representative AIF prior to correction for blood/plasma FDG content, as well as the chosen VOI over the vena cava based on the maximum intensity projection image. The higher temporal resolution at the beginning of the AIF acquisition allowed for accurate mathematical integration of the input function in the period when the bolus and the chase induced a fast variation of blood FDG activity. The CMR$_{glc}$ derivation from the step (2) PET acquisition over the brain at steady-state enabled the reconstruction of high resolution 3D metabolic maps for individual animals with the same spatial resolution as the reconstructed PET images. A typically two-fold lower CMR$_{glc}$ was observed in BDL versus sham rats on all axial slices (**Figure 7.5B** shows an example of CMR$_{glc}$ maps obtained on one BDL and one sham rat).
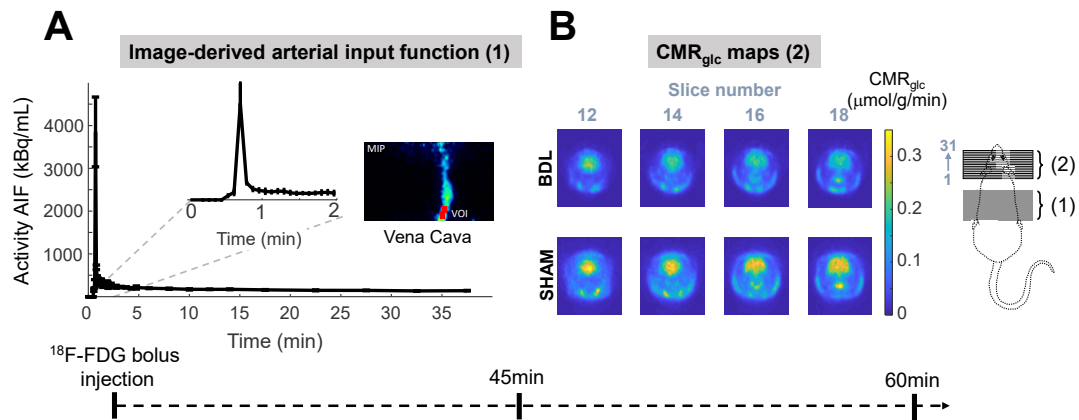
Figure 7.5: ^{18}F-FDG PET arterial input function and CMR$_{glc}$ maps acquired in BDL and sham rats. **A**: Representative arterial input function curve before correction for blood/plasma content [305], with corresponding VOI in the vena cava. **B**: Typical CMR$_{glc}$ maps in a BDL and a sham rat for four central slices. The rightmost part of the figure shows the position of the PET scanner FOV for the two acquisitions and the slices order. The bottommost part of the figure shows the time repartition of the two acquisitions after injection of the radiotracer.

PET to atlas registration through MRI anatomic images enabled a ROI-specific measure of glucose uptake and a quantitative comparison between PET and ^{1}H MRS data in the hippocampus and the cerebellum. **Figure 7.6A** shows the atlas labels for the two brain regions. A significant 2.66-fold and 2.53-fold smaller CMR$_{glc}$ in BDL rats compared to sham rats (Figure 7.6B) was measured respectively in the cerebellum (sham: 0.337 ± 0.064 μmol/g/min, BDL: 0.127 ± 0.052 μmol/g/min,****) and in the hippocampus (sham: 0.348 ± 0.068 μmol/g/min , BDL: 0.138 ± 0.063 μmol/g/min,****). The proposed co-registration provided quantitative metrics to the differences observed globally in the axial slices of the CMR$_{glc}$ maps (**Figure 7.5B**).

Figure 7.6C summarizes the ^{1}H MRS results presented in **Figure 7.4**, together with the colocalized PET results presented in **Figure 7.5**, allowing to draw an overall picture of glucose uptake and neurometabolic profiles alterations happening in BDL rats at week 6 in both brain regions. The BDL rats showed a smaller CMR$_{glc}$ (i.e. smaller glucose uptake) in both regions, an increase in glutamine (cerebellum: +114%, hippocampus: +73%), decrease in Glu (cerebellum: -22%, hippocampus: -13%) and main osmolytes (cerebellum: -15%, hippocampus: -13%), compared to control rats, together with a decrease in some low concentrated metabolites (Asc in the hippocampus (-17%), and in GABA in the cerebellum (-22%). Additionally, Gln increase was significantly stronger in the cerebellum compared to the hippocampus (week 0 to 6 % change), and Glu, Tau and CMR$_{glc}$ show a stronger decrease (although not statistically significant) in the cerebellum.
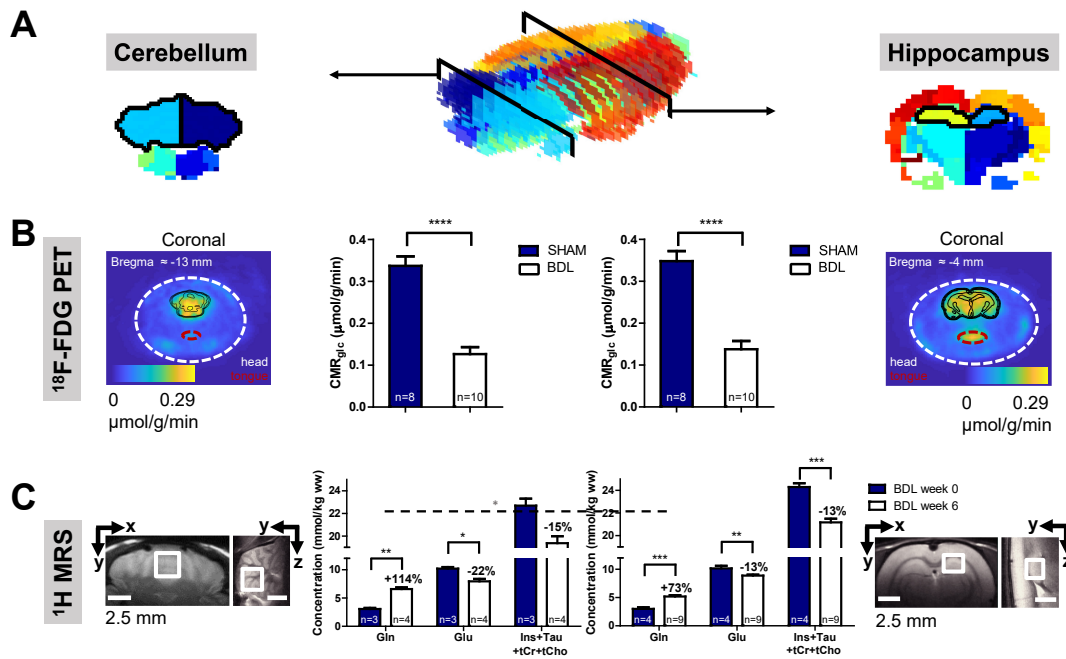
Figure 7.6: Atlas-based co-localization of ^{1}H MRS and ^{18}F-FDG PET. **A**: Atlas regions highlighted by solid lines. **B**: ^{18}F-FDG PET CMR$_{glc}$ values averaged over the atlas labels of the cerebellum and hippocampus. **C**: ^{1}H MRS metabolites quantifications in a voxel localized in the cerebellum and in the hippocampus. Low concentrated metabolites (Asc, GABA) are not displayed.

7.6   Discussion

The present study proposes a new quantification method to extract quantitative information on glucose metabolic rate from the raw PET image. This was made possible by using for the first time the combination of the image-derived AIF [293] measurement and the derivation of CMR$_{glc}$ maps from Sokoloff et al. [194], associated with the registration of PET images to a rat brain atlas through MRI T$_2$-weighted anatomic acquisitions. This new approach rendered the 3D PET image fully quantitative and provided an easier experimental implementation with minimal invasiveness of the AIF acquisition as compared with the standard technique employing repeated manual blood samplings. Consequently, we also report here the first in vivo study in BDL rats using both ^{18}F-FDG PET and ^{1}H MRS to map brain glucose uptake concomitant with other brain metabolites alterations, bringing a new insight into brain energy metabolism in HE.

7.6.1 Consequences of ammonia load on neurometabolic profiles in BDL rats

The increase in Gln and decrease in osmolytes (Ins, Tau, tCr) observed in the present study are in agreement with a previously published study in the hippocampus of BDL rats [136]. Very interestingly, this important finding was observed here using even fewer animals. Ins, tCr and Tau have been suggested as regulators of cellular volume during induced swelling [313, 314], here caused by the Gln load in the astrocytes, and where an efflux could help restoring the osmotic balance.

A primary explanation for decreased Glu in the two brain regions analyzed in this study arises from its excessive use, together with ammonia, for GS-mediated Gln production [136, 315]. In addition, altered neurotransmission, both glutamatergic[316] and GABAergic [317, 318], has also been proposed as a consequence of chronic hyperammonemia, which could reflect the decrease in Glu observed in both regions and the decrease of GABA in the cerebellum.

The benefit of the spectral separation of Gln/Glu with ^{1}H MRS spectroscopy at 9.4T confirms its importance in the context of HE. Indeed, the combined reduction of Glu and increase in Gln concentrations could partially compensate each other when only measuring Glx, the sum of Glu and Gln, a common limitation in ^{1}H MRS at lower fields. In addition, the cerebellum appears more vulnerable to metabolic changes compared to the hippocampus in BDL rats, confirming previously reported work in this rat model [201].

The Asc decrease in the hippocampus of BDL rats measured in this study is in line with another ^{1}H MRS study reported previously in BDL rats [136]. Of note, Asc absolute concentrations should be interpreted with care, as it is a low-concentrated and overlapping metabolite, but its relative decrease between week 0 and 6 is informative. Asc is playing an antioxidant role, therefore its decrease is usually linked to the oxidative stress occurring in the pathogenesis of HE [166] and is also in agreement with one of our previous studies where EPR was used as complementary technique to validate the ^{1}H MRS changes [319].

7.6.2 Impaired energy metabolism in BDL rats

Our present findings suggest an altered energy metabolism in BDL rats measured with ^{18}F-FDG PET, in agreement with a Glc hypometabolism observed in a patient with decompensated cirrhosis using FDG PET [183]. In contrast, a previous longitudinal study using ^{1}H MRS and ^{31}P MRS on BDL rats has reported no change in the steady state concentrations of energy metabolites (i.e. Adenosine triphosphate (ATP), tCr, Lac, while Glc was not reported after week 4) before week 8 post-surgery, with only Adenosine diphosphate (ADP) showing a significant decrease at week 8 post-BDL [188]. This discrepancy can be explained by the different nature of MRS and PET measurements and the complementary information that they provide. While

^{1}H MRS measures metabolic pool sizes and reflects the equilibrium changes of biochemical reactions, PET is a kinetic probe that informs on glucose metabolic fluxes. Additionally, it has been shown that brain tissue Glc measured by ^{1}H MRS tends to reflect the concentrations of plasma Glc if the later varies sufficiently slowly [320, 321], thus informing on Glc homeostasis rather than its metabolism. Glc pools are also challenging to measure using ^{1}H MRS because Glc is strongly overlapping with other metabolites on the upfield region of the spectra and with the water residual on the downfield region. Finally, ADP and ATP pools could remain constant if alternative substrate to glucose (such as Lac [190] or ketone bodies [322]) were to be used in the TCA cycle, but more exploratory work in BDL rats is required to test this hypothesis, as well as its link with a potential impairment of the Gln/Glu cycle [189].

7.6.3 CMR_{glc} versus standardized uptake value (SUV)

Previously published ^{18}F-FDG PET studies in HE [177, 178, 323] in patients and preclinical models show little or no impairment in glucose uptake, whereas we observed a strong difference between BDL and sham rats. In addition to the expected difference in HE type (chronic or acute, minimal or overt) and disease characteristics between human and animal studies, we believe that this discrepancy is mainly due to the method used to quantify ^{18}F-FDG PET data.

While most studies use the SUV (in g/mL, defined as the ratio between the quantified radioactivity density maps of the brain in Bq/mL and the fraction of the injected dose (Bq) over the weight of the animal (g)), the CMR_{glc} is rarely exploited. The SUV is widely used for its robustness and simplicity but is only a semi-quantitative approach, reflecting the normalized density of the tracer distribution in the brain. Its normalization is derived from a macroscopic information (fraction of the injected FDG dose over the weight of the animal) that may overlook subtler changes in the physiology of the animal.

To illustrate this point, the comparison between the CMR_{glc} and the SUV for both groups for the hippocampus and cerebellum is shown in **Figure 7.8A** and **B**. **Figure 7.8C** shows the normalization terms involved in the CMR_{glc} formula (integral of the AIF and final blood glycemia – C_p) and in the SUV formula (injected dose of FDG and weight of the animal). No difference between BDL and sham rats in either of the two investigated brain regions can be detected with the SUV (**Figure 7.8A** and **B**, hippocampus – BDL: 2.03±0.15 g/mL, sham: 2.23±0.48 g/mL, cerebellum - BDL: 2.17±0.34 g/mL, sham: 1.92±0.53 g/mL). Indeed, the difference in its macroscopic normalization factors (injected dose and weight) is not statistically significant between BDL and sham rats (**Figure 7.8C**, weight - BDL: 328±45 g, sham: 363±31 g, dose – BDL: 70.51±10.82 MBq, sham: 63.85±12.77 MBq), leading to no difference in the SUV. However, the CMR_{glc} normalization factors (AIF curves and final glycemia) both

display a difference between the groups, the latter being significant (BDL: 3.3±1.5 mM, sham: 10.1±2.1 mM,****).

Interestingly, with the same injected dose of FDG in the tail vein for both groups, the average maximum value of the AIF curve from the BDL group is smaller than the one from the sham group. This observation suggests that the injected dose is not an accurate measure of the true tracer availability for the brain, since systemic effects, such as the metabolism of other organs, and particularly in this study, of the liver, might affect the FDG bolus on its way from the tail to the thoracic region where the AIF is measured, and to the brain. This physiological effect would have been overlooked using the SUV quantification. The same reasoning holds for the comparison between glycemia in the CMR_{glc} and the weight in the SUV. The latter is also a poor indicator of the physiology of the animal since BDL and sham rats have on average the same weight, but BDL rats have a much lower blood glycemia than the sham rats, which would have not been detected using the SUV.

Because the CMR_{glc} is derived from the kinetics of the 3-compartment model described in **Figure 7.1** and in equations 7.2 and 7.3, its expression involves local information on glucose uptake through the ratio between glycemia (C_p) and the total amount of tracer in the blood (the summed AIF) multiplied by the LC [194] (see equation 7.3). However, the need for a carefully-sampled AIF is often the main difficulty preventing its wider use in metabolic imaging studies. In rodent studies, the small blood volume is a strong limitation for repeated manual sampling. Many technical challenges are also linked to the use of continuous measurements with external blood counters which often result in non-negligible physiological effects on the animal. Additionally, both manual blood sampling and external counters require the cannulation of veins or arteries, often rendering the experiment terminal. On the contrary, the proposed approach with the image-derived AIF provides a practical alternative to the manual blood sampling or external blood counters. It renders similar results [293] with particularly high temporal resolution, makes the measurement less invasive and allows for longitudinal studies with the same animal.

To further ensure a fair comparison between the groups, brain volumes were compared between BDL and sham rats (**Figure 7.7**). No overall brain atrophy was observed in BDL rats compared to sham rats (BDL brain volume – 1959.4±41.0 mm^3, sham brain volume – 1939.2±48.6 mm^3), ensuring that a given amount of tracer/plasma Glc is used by the same amount of brain tissue between the two groups.

Finally, the LC in the CMR_{glc} formula also mirrors an important physiological aspect as it accounts for the competition between glucose and FDG and their respective affinity for blood brain barrier transporters and hexokinase, and it was shown earlier that glycemia values strongly vary between the groups. All kinetic constants from the 3-compartment model, both
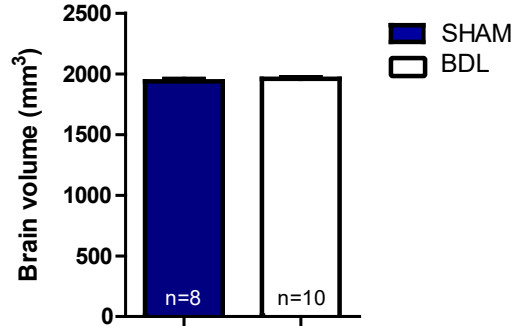
Figure 7.7: Brain volume comparison between BDL and sham rats, found by summing the voxels from all brain labels.

for enzyme-mediated transport through the BBB and the enzyme-mediated phosphorylation for both substrates are described by a Michaelis-Menten equation modified to account for competitive substrates and mutual inhibition [324]. This competition is formally contained in the Lumped Constant expression from Sokoloff et al. [194]:

$$LC = \frac{1}{\Phi} \times \frac{\frac{k_1^*}{(k_2^* + k_3^*)}}{\frac{k_1}{(k_2 + k_3)}} \times \frac{\frac{V_m^*}{K_m^*}}{\frac{V_m}{K_m}} \tag{7.4}$$

where Φ is the fraction of G6P that will be further metabolized in the glycolysis, the second fraction describing the ratio of kinetic constants of the radiotracer over the ones of natural Glc, and the last part of the fraction the ratio between Michaelis-Menten constants, $V_m^{(*)}$ the maximum velocity and $K_m^{(*)}$ Michaelis-Menten constants for the hexokinase reaction of either Glc or FDG. The LC constants were assumed identical for both groups. Importantly, this difference in blood glycemia and the resulting differential distribution of blood glucose versus FDG between groups would have been overlooked when analyzing the glucose uptake with the SUV approach, for which we observed no significant difference in animal weights between the two groups.

For all the reasons mentioned above, when practically feasible, we suggest using a quantitative approach for the analysis of FDG uptake which enables the determination of the CMR_{glc} in studies involving group comparison where the physiology of the animal could greatly vary.
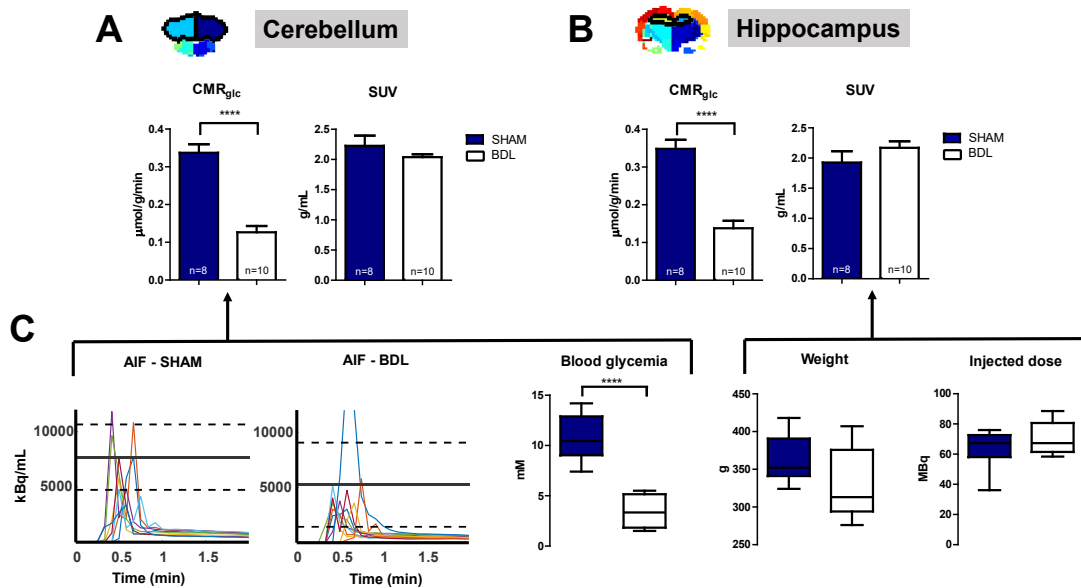
Figure 7.8: Comparison between two different metrics for PET data, the fully-quantitative CMR$_{glc}$ and the semi-quantitative SUV for the cerebellum (**A**) and the hippocampus (**B**) and their respective normalization terms (**C**). Individual arterial input function curves from each animal are displayed in the left part of panel **C**, the full line being the mean of the maximum of the AIF and the dashed line the corresponding mean±SD.

7.7 Conclusion

We reported the first dual ^{18}F-FDG PET and localized ^{1}H MRS in vivo study performed in a BDL rat model of type C HE, together with a quantitative and regional measurement of glucose uptake through the computation of CMR$_{glc}$ maps based on an image-derived AIF. A 2-fold lower glucose uptake was observed in the hippocampus and cerebellum of BDL versus sham rats using ^{18}F-FDG PET, concomitant with an increase in glutamine, a decrease in glutamate and in the osmolytes in both brain regions measured with ^{1}H MRS. This novel finding reopens the debate of energy failure in the pathophysiology of type C HE.

7.8 Perspectives

As perspectives to this study, we envision to:

- address the problem of varying glycemia over the time course of the PET experiment, both theoretically and experimentally. As a matter of fact, the derivation of the CMR$_{glc}$ based on Sokoloff et al. approach [194] relies on the hypothesis of a blood glycemia C_p constant over time (equation 7.3). However, we noticed that this hypothesis was partially

violated in our PET experiments. Glycemia was measured at the start of the scan (before the input function acquisition) and at the end (after the steady state brain acquisition). sham rats exhibit increased C_p between these two time points (percentage increase: +43.5±20.7%, N=8), and BDL rats decreased C_p (percentage decrease: -29.1±25.8%, N=10). For this reason, we would like to:

- derive an alternative to Sokoloff's CMR$_{\text{glc}}$ formula where C_p could vary with time. This requires an adjustment of the theory because Sokoloff's formula relies on Michaelis-Menten kinetic equations describing enzyme-catalysed reactions, with the hypothesis of constant concentration of substrate (C_p being the substrate for the transport through the BBB).

- conduct additional PET experiments where the glycemia would be stabilized experimentally by glucose or glucagon/insulin infusions during the PET scan. This is however much more challenging, first due to the requirement of multiple blood samplings and injections poorly tolerated by small animals, and second due to the radioactive environment to which the operator is exposed repeatedly.

- investigate the potential to reduce scan time for clinical translation of the CMR$_{\text{glc}}$ quantification with an IDIF. In the present study, the input function was sampled for 45 min. We would like to test whether one could afford to measure the IDIF for a few minutes only after the bolus, and extrapolate its (bi-exponential) decay up to the time of the steady-state acquisition in the brain without loosing accuracy on the CMR$_{\text{glc}}$ value. Doing so, patients could enter the PET scanner for a few minutes during the FDG injection and then go out and in again after ≈ 35-40 min to measure the steady state signal in the brain. This would improve patients comfort and hopefully promote clinical translation.

- compare different quantification methods of the PET data in the case where both the brain signal and the input function are acquired dynamically for an hour: Sokoloff's approach (which relies on the acquisition of only one steady state image ≈ 45 min after the injection, as presented in this chapter), the Patlak plot and the full compartmental modelling, the latter two requiring continuous (or multiple) sampling of both the steady-state brain image and the input function.

- implement a user-friendly toolbox with the quantification of PET data proposed in this chapter, together with improved PET-MR coregistration (for example based on a brain template from many animals used as reference). This could facilitate the translation of the method to other centres and other applications. This idea was started with a master student in Fall 2022, David Bekri, supervised jointly with Bernard Lanz.

Conclusions and outlook

Stepping back

The overall aims of this thesis work were to investigate in vivo some of the unexplored aspects of microstructure and metabolism alterations in the BDL rat model of type C HE, with the hope that these results will improve our understanding of the disease in humans and have direct clinical implications.

The state-of-the-art at the beginning of this thesis was as follows:

- Brain metabolism alterations in HE had been observed using ^{1}H MRS, but little information on glucose net rate to glycolysis had been reported unequivocally, neither in patients nor in animal models (conflicting results in literature).

- Microstructure alterations had been investigated ex vivo in type C HE, but never in vivo and the main hypothesis had been centred on edema and astrocytes swelling.

It is important to highlight that **1)** no clear conclusions on altered energy metabolism in BDL rats could have been drawn in this thesis without the development of the fully quantitative approach in the PET study (CMR$_{glc}$ versus SUV), and that **2)** no clear conclusions on specific microstructure alterations in BDL rats in vivo could have been drawn without the joint implementation and modelling of diffusion-weighted MRS and diffusion-weighted MRI. In addition to being non-cell specific, diffusion MRI observations have often limited the debate to the question of edema (vasogenic versus cytotoxic) in type C HE, before the emergence of more advanced biophysical models like the standard model. The latter provides a wide range of markers specific to different pathological mechanisms in the brain. In line with this observation, we have shown in this thesis that joint modelling of dMRI and dMRS can reorient the debate from edema to more complex multi-cellular microstructure alterations in HE. This is crucial especially in the chronic forms of the disease, where the changes are gradual and might not be associated with a measurable net change in water content, but instead with subtle changes of cellular morphology.

Overall, none of the insights regarding HE pathophysiology in BDL rats could have been made without an improvement of the state-of-the-art methodology available at the beginning of this thesis.

Did we improve our understanding of HE in rodents?

In this thesis, we proposed to use the yet unexploited potential of diffusion-weighted MRS for the study of HE. The measurement of the diffusion of metabolites informs on microstructure, as would the diffusion of water measured with diffusion-weighted MRI, but in a cell-specific

manner. Whereas the presence of water is ubiquitous (located in all compartments and exchanging between compartments), metabolites are mostly located in the intracellular space and have partial cell specificity. This allows one to alleviate the ambiguity of hypotheses explaining diffusion MRI results. We have shown that, analysed jointly, diffusion-weighted MRS and MRI at 14.1T probed increased metabolite diffusivities, as well as an increased intra-neurite and intra-axon water diffusivity in white and grey matter in the cerebellum of both a young and an adult rat model of type C HE compared to control rats. These results suggest an alteration of cell density and/or of neurite network complexity, confirmed ex vivo by histology, and preferential alterations of the intracellular space (more than of the extracellular space), and possibly of grey matter (more than of white matter) and of astrocytes (more than of neurons). Together, these results render dMRS a highly valuable tool to probe cell-specific microstructure in vivo.

Nonetheless, the higher specificity of diffusion-weighted MRS versus diffusion-weighted MRI coincides with a lower sensitivity. We have tried to alleviate these difficulties by improving the diffusion-weighted MRS acquisition. To do so, we developed a new diffusion-weighted MRS sequence (DW-SPECIAL) that enabled a better detection and subsequent estimation of the diffusion properties of metabolites with large J-couplings, such as glutamine, a metabolite of particular interest in the study of HE.

FDG-PET is a well-established and powerful technique to inform on the metabolic fate of glucose in the very first steps of glycolysis. It is widely used in the study of cancer where it can probe tumors having an abnormally high glucose consumption. Whereas it is often quantified using a semi-quantitative approach, we have shown that full-compartmental modelling of the FDG uptake, implemented here with little experimental penalty through the image-derived input function, is necessary to probe meaningful results in hepatic encephalopathy. With this improved methodology, we observed a 2-fold lower brain glucose uptake, concomitant with an increase in brain glutamine and a decrease in the main osmolytes, in the hippocampus and in the cerebellum of the bile-duct ligated rat model of type C HE.

The hot topic of denoising

The possibility to *denoise* datasets is very attractive in many fields of research. The current trend in medical imaging focuses on machine-learning based denoising algorithms, applied either on the input (improving the quality of an image/spectrum) or on the output (improving the classification of results, the identification of voxels). Interestingly, in the machine-learning field, there is a trend towards *explainable AI* [325] and *physics-informed AI* [326], and with this a wish to provide algorithms whose features are understandable by humans rather than being

'black boxes'. In this thesis, with a similar idea in mind, we were interested in investigating a transparent and well-established method for rank reduction in statistics, the principal component analysis. PCA was applied here on the input spectra, with an objective and user-independent rank selection, following a recent method proposed for diffusion-weighted MRI. Similarly to unsupervised learning for which no prior annotated inputs are required, PCA with a user-independent rank selection provides a more generalisable analysis framework than when the rank is selected empirically with prior knowledge of the content of the dataset (e.g., knowing the number of metabolites in the input spectra). Our main objective for this project was to thoroughly study the consequences of the method on the dataset properties and identify its limitations. We believe only a clear understanding of the range of applicability can promote a long-lasting implementation in the field. On simulated, in vivo rodent and human diffusion-weighted MRS data, we showed that MP-PCA denoising yielded an increased apparent SNR, a more accurate B_0 drift correction between shots, and similar estimates of metabolite concentrations and diffusivities compared to the raw data. However, it also introduced correlations in the noise level across shells, an effect which should be carefully considered and for which we provided a detailed description.

Moving forward

CMR$_{glc}$ with an imaged-derived input function - towards a broader application

We believe that the development of a non-invasive fully quantitative approach for preclinical PET studies can have a wider range of applications than HE. It would be especially important for diseases where systemic metabolism differ, like it is the case in HE, where the sick liver might shunt some of the FDG or impair blood flow to the brain. The same approach could also be used for tracers other than FDG, given that the equations governing their metabolic fate are known. In clinical settings, the semi-quantitative approaches still prevail because they are faster and less arduous for patients (the SUV quantification requires only a ≈ 15 min measurement). To compete with such implementations, fully quantitative approaches must be fast, with little additional effort from patients and from clinicians. With this idea in mind, future investigations could focus on the possibility to extrapolate the input function to reduce its acquisition time. Doing so, patients could enter the PET scanner for a few minutes during the FDG injection to measure the first points of the input function, and again later on for the brain acquisition, rather than staying inside the scanner for the entire duration in between.

GSH?

Glutathione, one of metabolites measured with ^{1}H MRS, could be an interesting target for future studies in HE, both with respect to metabolism and microstructure.

First, GSH is the major antioxydant metabolite in animal cells [327]. Decreased GSH levels in the cerebellum of young BDL rats have been observed with ^{1}H MRS in the present study, the first one to report a significant difference in brain GSH levels in BDL rats. Lower GSH levels lead to a limited power to scavenge reactive oxygen species and contribute to the development of oxidative stress, believed to play a major role in HE. The liver is the major producer of GSH [328], and its impaired function in HE may result in lower GSH production capacities. Finally, it is also acknowledged that female have a higher antioxidant power than males, and that GSH metabolism exhibit sexual dimorphism [329]. Interestingly, a recent study in female versus male BDL rats evidenced different responses to overt HE episodes depending on the sex of the animal, tentatively attributed to a difference response to oxidative stress [174]. The authors argued that female BDL rats were naturally protected against overt HE episodes thanks to their higher albumin (also an antioxydant produced by the liver) levels and lower levels of ROS markers compared to male BDL rats. In the light of this recent finding, future studies could explore whether GSH is also dysregulated in young male versus female BDL rats, and if this correlates with the disease status.

Second, GSH is much more concentrated in the astrocytes than in other mammalian cells [330, 331]. Because of the usual difficulties to quantify it with ^{1}H MRS, and even more so with ^{1}H dMRS, GSH has never been considered as a potential astrocytic marker for the purpose of measuring cell-specific microstructure with diffusion. We have shown in the present study that DW-SPECIAL enables an accurate quantification of low concentrated metabolites, including GSH. Studying the diffusion properties of GSH as a potential astrocytic marker could constitute a future step of the study, made possible with the implementation of DW-SPECIAL.

The naive view of metabolite compartmentation

One of the strongest assumptions underlying the modelling and conclusions derived from dMRS acquisitions is that *metabolites are cell-specific*, and consequently that their diffusion properties inform on cell-specific microstructure.

This simplistic assumption has been challenged by many authors [24]. Glutamine, for example, is assumed to be an astrocytic marker due to the exclusive location of glutamine synthetase, responsible for Gln synthesis, in the astrocytes. However, Gln is involved in a fast dynamic exchange with glutamate, also present in neurons, that could lessen the above statement. Moreover, oligodendrocytes also have high concentrations of glutamate and glutamine and are

often disregarded [224]. In addition, in pathological cases affecting many brain functions and cell types like HE, brain plasticity and compensation mechanisms may change the distribution of metabolites found in the healthy brain. Although hypotheses are required for any model, living matter should be seen as a complex system.

No method has yet successfully addressed the question of metabolite compartmentation, being very challenging to tackle in vivo, if at all feasible. Whether dMRS applied in controlled models can be used for that purpose or if another method could provide prior knowledge to diffusion studies remains to be investigated. Working on addressing this question, at least in the healthy brain, would be a significant step forward for the field of diffusion MRS.

Denoising - can the observations for MRS data be unified?

An important observation that emerged following our publication on MP-PCA denoising is the wide range of observations and opinions, sometimes contradictory, reported by different groups working on denoising MR spectra [266, 291, 292, 278]. This was the case both for denoising performed with machine-learning and with statistical approaches, and both when it was applied to single voxel and to multidimensional MRS datasets. This is particularly noteworthy because, on the contrary, MP-PCA denoising is more accepted and used in the field of dMRI, although MR images are a priori less suited for these methods because often featuring non-Gaussian noise [256, 275, 279, 332].

Is there a common denominator unifying our observations for MRS data? Could it be that the nature of the input dataset leads to a range of different conclusions? If this is indeed the case, we hope that in the near future we can gather people working in the field and together provide unified answers and recommendations to the community for the applicability of denoising for MRS.

How transferable are our results?

Another fundamental question to ask oneself when working on preclinical models of a disease is: *how transferable are our results?* Ideally, one would want to make sure that the results obtained during animal studies are applicable also to human populations, to pave the way for therapeutic solutions. The BDL rat model of type C HE has been acknowledged as an animal model representing well the manifestations of the disease in humans by the International Society for Hepatic Encephalopathy and Nitrogen Metabolism (ISHEN). As such, the most important findings related to brain metabolism (increased glutamine, decreased osmolytes) measured non-invasively with ^{1}H MRS in this rat model have been replicated in human studies.

There remain, however, unexplored aspects which prevent a complete translation. Among them, possible sex-differences in the response to HE of BDL animals have hardly been studied. To the best of my knowledge, the authors of ref. [174] were the first ones to do so, in 2022. In contrast, the studies presented in this thesis are applied on male BDL rats only. Doing so, our aim was to enable a direct comparison with published studies from other groups on BDL rats (mostly on male animals), and to ensure continuity in the results from our group.

Our results should thus be considered as providing partial conclusions on metabolism in BDL rats, until the potential sex-differences are studied. For a given metabolic biomarker, if no difference between male and female BDL rats were to be found, it would ensure that our claims are well applicable to the entire population. We can however argue that this is unlikely to be the case: first, in the light of the recent findings of ref. [174] (female BDL rats being naturally protected against overt episodes of HE versus male rats), second, because sex-differences have been suggested in children with biliary atresia [240], and third, given that metabolic differences between men and women are known to exist in different areas of research [333, 334, 335].

It appears very surprising to me that potential sex-differences in BDL rats have not triggered more interest in the community until recently. Indeed, one could also argue that the prevalence of decompensating events in cirrhotic patients is higher in men than women [336], hence the study of male animals. While this argument is in principle valid, potential protection mechanisms specific to women/female rats are then overlooked, with the risk of missing valuable information for future treatments. One could also argue against the inclusion of female animals *and* of sex as a biological variable because females are believed to be more variable than males due to hormones, or because it will double the sample size. Here again, both of these statements are incorrect (see refs. [337, 338] and [339]).

I would like to end this thesis here, with a personal thought. I do hope that the paradigm will fundamentally change. We have, with MRS, an extraordinarily powerful tool to study brain metabolism non-invasively. It is now time to include, in the big picture that we claim to provide, the even bigger picture that also captures the second half of humanity.

Bibliography

[1]   R. P. Feynman, F. L. Vernon, and R. W. Hellwarth, "Geometrical Representation of the Schrödinger Equation for Solving Maser Problems," *Journal of Applied Physics*, vol. 28, pp. 49–52, Jan. 1957.

[2]   M. H. Levitt, *Spin Dynamics: Basics of Nuclear Magnetic Resonance.* John Wiley & Sons, Nov. 2001.

[3]   J. Keeler, *Understanding NMR Spectroscopy.* John Wiley & Sons, Sept. 2011.

[4]   P. T. Callaghan, *Principles of Nuclear Magnetic Resonance Microscopy.* Clarendon Press, 1993.

[5]   R. A. d. Graaf, *In Vivo NMR Spectroscopy: Principles and Techniques.* John Wiley & Sons, Mar. 2013.

[6]   A. Abragam, *The Principles of Nuclear Magnetism.* Clarendon Press, 1961.

[7]   P. A. M. Dirac and R. H. Fowler, "The quantum theory of the electron," *Proceedings of the Royal Society of London. Series A, Containing Papers of a Mathematical and Physical Character*, vol. 117, pp. 610–624, Feb. 1928.

[8]   B. Lanz, A. Abaei, O. Braissant, I.-Y. Choi, C. Cudalbu, P.-G. Henry, R. Gruetter, F. Kara, K. Kantarci, P. Lee, N. W. Lutz, M. Marjańska, V. Mlynárik, V. Rasche, L. Xin, J. Valette, and t. E. W. G. o. M. r. s. i. t. r. Brain, "Magnetic resonance spectroscopy in the rodent brain: Experts' consensus recommendations," *NMR in Biomedicine*, vol. 34, no. 5, p. e4325, 2021.

[9]   F. Bloch and A. Siegert, "Magnetic Resonance for Nonrotating Fields," *Physical Review*, vol. 57, pp. 522–527, Mar. 1940.

[10] M. Garwood and L. DelaBarre, "The Return of the Frequency Sweep: Designing Adiabatic Pulses for Contemporary NMR," *Journal of Magnetic Resonance*, vol. 153, pp. 155–177, Dec. 2001.

[11] C. Graf, A. Rund, C. S. Aigner, and R. Stollberger, "Accuracy and performance analysis for Bloch and Bloch-McConnell simulation methods," *Journal of Magnetic Resonance*, vol. 329, p. 107011, Aug. 2021.

[12] D. J. Siminovitch, "Rotations in NMR: Part I. Euler–Rodrigues parameters and quaternions," *Concepts in Magnetic Resonance*, vol. 9, no. 3, pp. 149–171, 1997.

[13] H. Geen and R. Freeman, "Band-selective radiofrequency pulses," *Journal of Magnetic Resonance (1969)*, vol. 93, pp. 93–141, June 1991.

[14] N. Bloembergen, E. M. Purcell, and R. V. Pound, "Relaxation Effects in Nuclear Magnetic Resonance Absorption," *Physical Review*, vol. 73, pp. 679–712, Apr. 1948.

[15] D. K. Deelchand, P.-G. Henry, and M. Marjańska, "Effect of carr-purcell refocusing pulse trains on transverse relaxation times of metabolites in rat brain at 9.4 Tesla," *Magnetic Resonance in Medicine*, vol. 73, no. 1, pp. 13–20, 2015.

[16] D. K. Deelchand, E. J. Auerbach, and M. Marjańska, "Properties of Localization by Adiabatic SElective Refocusing (LASER) sequence," in *Proc. Intl. Soc. Mag. Reson. Med. 25*, 2017.

[17] J. Frahm, K.-D. Merboldt, and W. Hänicke, "Localized proton spectroscopy using stimulated echoes," *Journal of Magnetic Resonance (1969)*, vol. 72, pp. 502–508, May 1987.

[18] P. A. Bottomley, "Spatial localization in NMR spectroscopy in vivo," *Annals of the New York Academy of Sciences*, vol. 508, pp. 333–348, 1987.

[19] J. Slotboom, A. F. Mehlkopf, and W. M. M. J. Bovée, "A single-shot localization pulse sequence suited for coils with inhomogeneous RF fields using adiabatic slice-selective RF pulses," *Journal of Magnetic Resonance (1969)*, vol. 95, pp. 396–404, Nov. 1991.

Bibliography

[20] G. Öz, D. K. Deelchand, J. P. Wijnen, V. Mlynárik, L. Xin, R. Mekle, R. Noeske, T. W. Scheenen, I. Tkáč, and t. E. W. G. o. A. S. V. H. Mrs, "Advanced single voxel 1H magnetic resonance spectroscopy techniques in humans: Experts' consensus recommendations," *NMR in Biomedicine*, vol. 34, no. 5, p. e4236, 2021.

[21] V. Mlynárik, G. Gambarota, H. Frenkel, and R. Gruetter, "Localized short-echo-time proton MR spectroscopy with full signal-intensity acquisition," *Magnetic Resonance in Medicine*, vol. 56, no. 5, pp. 965–970, 2006.

[22] J. Pauly, D. Nishimura, and A. Macovski, "A k-space analysis of small-tip-angle excitation," *Journal of Magnetic Resonance (1969)*, vol. 81, pp. 43–56, Jan. 1989.

[23] C. Juchem, C. Cudalbu, R. A. de Graaf, R. Gruetter, A. Henning, H. P. Hetherington, and V. O. Boer, "B0 shimming for in vivo magnetic resonance spectroscopy: Experts' consensus recommendations," *NMR in Biomedicine*, vol. 34, no. 5, p. e4350, 2021.

[24] C. D. Rae, "A Guide to the Metabolic Pathways and Function of Metabolites Observed in Human Brain 1H Magnetic Resonance Spectra," *Neurochemical Research*, vol. 39, pp. 1–36, Jan. 2014.

[25] A. Covarrubias-Pinto, A. I. Acuña, F. A. Beltrán, L. Torres-Díaz, and M. A. Castro, "Old Things New View: Ascorbic Acid Protects the Brain in Neurodegenerative Disorders," *International Journal of Molecular Sciences*, vol. 16, pp. 28194–28217, Dec. 2015.

[26] M. Inazu, "Functional Expression of Choline Transporters in the Blood–Brain Barrier," *Nutrients*, vol. 11, p. 2265, Oct. 2019.

[27] J. Near, A. D. Harris, C. Juchem, R. Kreis, M. Marjańska, G. Öz, J. Slotboom, M. Wilson, and C. Gasparovic, "Preprocessing, analysis and quantification in single-voxel magnetic resonance spectroscopy: experts' consensus recommendations," *NMR in biomedicine*, vol. 34, p. e4257, May 2021.

[28] R. Simpson, G. A. Devenyi, P. Jezzard, T. J. Hennessy, and J. Near, "Advanced processing and simulation of MRS data using the FID appliance (FID-A)-An open source, MATLAB-based toolkit," *Magnetic Resonance in Medicine*, vol. 77, pp. 23–33, Jan. 2017.

[29] U. Klose, "In vivo proton spectroscopy in presence of eddy currents," *Magnetic Resonance in Medicine*, vol. 14, no. 1, pp. 26–30, 1990.

[30] R. Kreis, V. Boer, I.-Y. Choi, C. Cudalbu, R. A. d. Graaf, C. Gasparovic, A. Heerschap, M. Kriššák, B. Lanz, A. A. Maudsley, M. Meyerspeer, J. Near, G. Öz, S. Posse, J. Slotboom, M. Terpstra, I. Tkáč, M. Wilson, and W. Bogner, "Terminology and concepts for the characterization of in vivo MR spectroscopy methods and MR spectra: Background and experts' consensus recommendations," *NMR in Biomedicine*, vol. 34, no. 5, p. e4347, 2021.

[31] E. Bartholdi and R. R. Ernst, "Fourier spectroscopy and the causality principle," *Journal of Magnetic Resonance (1969)*, vol. 11, pp. 9–19, July 1973.

[32] J. Near, R. Edden, C. J. Evans, R. Paquin, A. Harris, and P. Jezzard, "Frequency and phase drift correction of magnetic resonance spectroscopy data by spectral registration in the time domain," *Magnetic Resonance in Medicine*, vol. 73, pp. 44–50, Jan. 2015.

[33] C. S. Bolliger, C. Boesch, and R. Kreis, "On the use of Cramér–Rao minimum variance bounds for the design of magnetic resonance spectroscopy experiments," *NeuroImage*, vol. 83, pp. 1031–1040, Dec. 2013.

[34] C. Cudalbu, K. L. Behar, P. K. Bhattacharyya, W. Bogner, T. Borbath, R. A. de Graaf, R. Gruetter, A. Henning, C. Juchem, R. Kreis, P. Lee, H. Lei, M. Marjańska, R. Mekle, S. Murali-Manohar, M. Považan, V. Rackayová, D. Simicic, J. Slotboom, B. J. Soher, Z. Starčuk, J. Starčuková, I. Tkáč, S. Williams, M. Wilson, A. M. Wright, L. Xin, and V. Mlynárik, "Contribution of macromolecules to brain 1 H MR spectra: Experts' consensus recommendations," *NMR in biomedicine*, vol. 34, p. e4393, May 2021.

[35] D. Simicic, V. Rackayova, L. Xin, I. Tkáč, T. Borbath, Z. Starcuk Jr, J. Starcukova, B. Lanz, and C. Cudalbu, "In vivo macromolecule signals in rat brain 1H-MR spectra at 9.4T: Parametrization, spline baseline estimation, and T2 relaxation times," *Magnetic Resonance in Medicine*, vol. 86, no. 5, pp. 2384–2401, 2021.

[36] M. Wilson, "Adaptive baseline fitting for MR spectroscopy analysis," *Magnetic Resonance in Medicine*, vol. 85, no. 1, pp. 13–29, 2021.

[37] P. Jones, Derek K., ed., *Diffusion MRI: Theory, Methods, and Applications*. Oxford University Press, Nov. 2010.

[38] E. L. Hahn, "Spin Echoes," *Physical Review*, vol. 80, pp. 580–594, Nov. 1950.

[39] E. O. Stejskal and J. E. Tanner, "Spin Diffusion Measurements: Spin Echoes in the Presence of a Time-Dependent Field Gradient," *The Journal of Chemical Physics*, vol. 42, pp. 288–292, Jan. 1965.

[40] D. Le Bihan, E. Breton, D. Lallemand, P. Grenier, E. Cabanis, and M. Laval-Jeantet, "MR imaging of intravoxel incoherent motions: application to diffusion and perfusion in neurologic disorders," *Radiology*, vol. 161, pp. 401–407, Nov. 1986.

[41] C. T. W. Moonen, P. C. M. V. Zijl, D. L. Bihan, and D. Despres, "In vivo nmr diffusion spectroscopy: 31p application to phosphorus metabolites in muscle," *Magnetic Resonance in Medicine*, vol. 13, no. 3, pp. 467–477, 1990.

[42] S. Posse, C. A. Cuenod, and D. Le Bihan, "Human brain: proton diffusion MR spectroscopy," *Radiology*, vol. 188, pp. 719–725, Sept. 1993.

[43] P. J. Basser, J. Mattiello, and D. LeBihan, "MR diffusion tensor spectroscopy and imaging," *Biophysical Journal*, vol. 66, pp. 259–267, Jan. 1994.

[44] P. J. Basser, J. Mattiello, and D. Lebihan, "Estimation of the Effective Self-Diffusion Tensor from the NMR Spin Echo," *Journal of Magnetic Resonance, Series B*, vol. 103, pp. 247–254, Mar. 1994.

[45] M. E. Moseley, Y. Cohen, J. Mintorovitch, L. Chileuitt, H. Shimizu, J. Kucharczyk, M. F. Wendland, and P. R. Weinstein, "Early detection of regional cerebral ischemia in cats: comparison of diffusion- and T2-weighted MRI and spectroscopy," *Magnetic Resonance in Medicine*, vol. 14, pp. 330–346, May 1990.

[46] W. A. Copen, L. H. Schwamm, R. G. González, O. Wu, C. B. Harmath, P. W. Schaefer, W. J. Koroshetz, and A. G. Sorensen, "Ischemic stroke: effects of etiology and patient age on the time course of the core apparent diffusion coefficient," *Radiology*, vol. 221, pp. 27–34, Oct. 2001.

[47] R. Guzman, A. Barth, K.-O. Lövblad, M. El-Koussy, J. Weis, G. Schroth, and R. W. Seiler, "Use of diffusion-weighted magnetic resonance imaging in differentiating purulent brain processes from cystic brain tumors," *Journal of Neurosurgery*, vol. 97, pp. 1101–1107, Nov. 2002.

[48] C.-H. Toh, M. Castillo, A. M.-C. Wong, K.-C. Wei, H.-F. Wong, S.-H. Ng, and Y.-L. Wan, "Primary cerebral lymphoma and glioblastoma multiforme: differences in diffusion characteristics evaluated with diffusion tensor imaging," *AJNR. American journal of neuroradiology*, vol. 29, pp. 471–475, Mar. 2008.

[49] D. Le Bihan, R. Turner, P. Douek, and N. Patronas, "Diffusion MR imaging: clinical applications," *AJR. American journal of roentgenology*, vol. 159, pp. 591–599, Sept. 1992.

[50] B. Issa, "In vivo measurement of the apparent diffusion coefficient in normal and malignant prostatic tissues using echo-planar imaging," *Journal of magnetic resonance imaging: JMRI*, vol. 16, pp. 196–200, Aug. 2002.

[51] P. S. Hüppi, S. E. Maier, S. Peled, G. P. Zientara, P. D. Barnes, F. A. Jolesz, and J. J. Volpe, "Microstructural development of human newborn cerebral white matter assessed in vivo by diffusion tensor magnetic resonance imaging," *Pediatric Research*, vol. 44, pp. 584–590, Oct. 1998.

[52] M. Wick, Y. Nagatomo, F. Prielmeier, and J. Frahm, "Alteration of intracellular metabolite diffusion in rat brain in vivo during ischemia and reperfusion," *Stroke*, vol. 26, pp. 1930–1933; discussion 1934, Oct. 1995.

[53] J. Pfeuffer, I. Tkác, and R. Gruetter, "Extracellular-intracellular distribution of glucose and lactate in the rat brain assessed noninvasively by diffusion-weighted 1H nuclear magnetic resonance spectroscopy in vivo," *Journal of Cerebral Blood Flow and Metabolism: Official Journal of the International Society of Cerebral Blood Flow and Metabolism*, vol. 20, pp. 736–746, Apr. 2000.

[54] I. Ronen, E. Ercan, and A. Webb, "Axonal and glial microstructural information obtained with diffusion-weighted magnetic resonance spectroscopy at 7T," *Frontiers in Integrative Neuroscience*, vol. 7, p. 13, 2013.

[55] M. Palombo, C. Ligneul, E. Hernandez-Garzon, and J. Valette, "Can we detect the effect of spines and leaflets on the diffusion of brain intracellular metabolites?," *NeuroImage*, vol. 182, pp. 283–293, Nov. 2018.

[56] J. Valette, C. Ligneul, C. Marchadour, C. Najac, and M. Palombo, "Brain Metabolite Diffusion from Ultra-Short to Ultra-Long Time Scales: What Do We Learn, Where Should We Go?," *Frontiers in Neuroscience*, vol. 12, p. 2, 2018.

[57] C. Najac, F. Branzoli, I. Ronen, and J. Valette, "Brain intracellular metabolites are freely diffusing along cell fibers in grey and white matter, as measured by diffusion-weighted MR spectroscopy in the human brain at 7 T," *Brain structure & function*, vol. 221, pp. 1245–1254, Apr. 2016.

[58] I. Ronen, M. Budde, E. Ercan, J. Annese, A. Techawiboonwong, and A. Webb, "Microstructural organization of axons in the human corpus callosum quantified by diffusion-weighted magnetic resonance spectroscopy of N-acetylaspartate and post-mortem histology," *Brain Structure and Function*, vol. 219, pp. 1773–1785, Sept. 2014.

[59] C. Ligneul, M. Palombo, E. Hernández-Garzón, M.-A. Carrillo-de Sauvage, J. Flament, P. Hantraye, E. Brouillet, G. Bonvento, C. Escartin, and J. Valette, "Diffusion-weighted magnetic resonance spectroscopy enables cell-specific monitoring of astrocyte reactivity in vivo," *NeuroImage*, vol. 191, pp. 457–469, May 2019.

[60] G. Genovese, M. Palombo, M. D. Santin, J. Valette, C. Ligneul, M.-S. Aigrot, N. Abdoulkader, D. Langui, A. Millecamps, A. Baron-Van Evercooren, B. Stankoff, S. Lehericy, A. Petiet, and F. Branzoli, "Inflammation-driven glial alterations in the cuprizone mouse model probed with diffusion-weighted magnetic resonance spectroscopy at 11.7 T," *NMR in Biomedicine*, vol. 34, no. 4, p. e4480, 2021.

[61] B. Bodini, F. Branzoli, E. Poirion, D. García-Lorenzo, M. Didier, E. Maillart, J. Socha, G. Bera, C. Lubetzki, I. Ronen, S. Lehericy, and B. Stankoff, "Dysregulation of energy metabolism in multiple sclerosis measured in vivo with diffusion-weighted spectroscopy," *Multiple Sclerosis (Houndmills, Basingstoke, England)*, vol. 24, pp. 313–321, Mar. 2018.

[62] X. Chen, X. Fan, X. Song, M. Gardner, F. Du, and D. Öngür, "White Matter Metabolite Relaxation and Diffusion Abnormalities in First-Episode Psychosis: A Longitudinal Study," *Schizophrenia Bulletin*, vol. 48, pp. 712–720, Jan. 2022.

[63] G. Genovese, B. Diaz-Fernandez, F.-X. Lejeune, I. Ronen, M. Marjańska, L. Yahia-Cherif, S. Lehéricy, F. Branzoli, and C. Rosso, "Longitudinal Monitoring of Microstructural Alterations in Cerebral Ischemia with in Vivo Diffusion-weighted MR Spectroscopy," *Radiology*, vol. 306, p. e220430, Mar. 2023.

[64] J. Valette, M. Chaumeil, M. Guillermier, G. Bloch, P. Hantraye, and V. Lebon, "Diffusion-weighted NMR spectroscopy allows probing of 13C labeling of glutamate inside distinct metabolic compartments in the brain," *Magnetic Resonance in Medicine*, vol. 60, no. 2, pp. 306–311, 2008.

[65] C. Najac, C. Marchadour, M. Guillermier, D. Houitte, V. Slavov, E. Brouillet, P. Hantraye, V. Lebon, and J. Valette, "Intracellular metabolites in the primate brain are primarily localized in long fibers rather than in cell bodies, as shown by diffusion-weighted magnetic resonance spectroscopy," *NeuroImage*, vol. 90, pp. 374–380, Apr. 2014.

[66] E. Mougel, S. Malaquin, M. Palombo, and J. Valette, "Probing lactate exchange in Gray Matter via time-dependent DW-MRS," in *Proc. Intl. Soc. Mag. Reson. Med. 31*, 2023.

[67] E. Mougel, J. Valette, and M. Palombo, "Investigating exchange, structural disorder and restriction in Gray Matter via water and metabolites diffusivity and kurtosis time-dependence," in *Proc. Intl. Soc. Mag. Reson. Med. 30*, 2022.

[68] A. Döring, F. Rösler, K. Simsek, M. Afzali, R. Kreis, D. K. Jones, J. Valette, and M. Palombo, "Time dependent diffusion and kurtosis of human brain metabolites," in *Proc. Intl. Soc. Mag. Reson. Med. 31*, 2023.

[69] P. T. Callaghan, K. W. Jolley, and J. Lelievre, "Diffusion of water in the endosperm tissue of wheat grains as studied by pulsed field gradient nuclear magnetic resonance.," *Biophysical Journal*, vol. 28, pp. 133–141, Oct. 1979.

[70] M. Palombo, N. Shemesh, I. Ronen, and J. Valette, "Insights into brain microstructure from in vivo DW-MRS," *NeuroImage*, vol. 182, pp. 97–116, 2018.

[71] S. N. Jespersen and D. Novikov, "Diffusion diffraction in disordered systems," in *Proc. Intl. Soc. Mag. Reson. Med. 31*, 2023.

[72] P. Linse and O. Soderman, "The Validity of the Short-Gradient-Pulse Approximation in NMR Studies of Restricted Diffusion. Simulations of Molecules Diffusing between Planes, in Cylinders and Spheres," *Journal of Magnetic Resonance, Series A*, vol. 116, pp. 77–86, Sept. 1995.

[73] C. Neuman, "Spin echo of spins diffusing in a bounded medium," *The Journal of Chemical Physics*, pp. 4508–4511, 1974.

[74] P. Vangelderen, D. Despres, P. C. M. Vanzijl, and C. T. W. Moonen, "Evaluation of Restricted Diffusion in Cylinders. Phosphocreatine in Rabbit Leg Muscle," *Journal of Magnetic Resonance, Series B*, vol. 103, pp. 255–260, Mar. 1994.

[75] P. T. Callaghan, "A Simple Matrix Formalism for Spin Echo Analysis of Restricted Diffusion under Generalized Gradient Waveforms," *Journal of Magnetic Resonance*, vol. 129, pp. 74–84, Nov. 1997.

[76] A. Ianuş, D. C. Alexander, and I. Drobnjak, "Microstructure Imaging Sequence Simulation Toolbox," in *Simulation and Synthesis in Medical Imaging* (S. A. Tsaftaris, A. Gooya, A. F. Frangi, and J. L. Prince, eds.), Lecture Notes in Computer Science, (Cham), pp. 34–44, Springer International Publishing, 2016.

[77] D. S. Novikov, E. Fieremans, S. N. Jespersen, and V. G. Kiselev, "Quantifying brain microstructure with diffusion MRI: Theory and parameter estimation," *NMR in Biomedicine*, vol. 32, no. 4, p. e3998, 2019.

[78] L. Avram, Y. Assaf, and Y. Cohen, "The effect of rotational angle and experimental parameters on the diffraction patterns and micro-structural information obtained from q-space diffusion NMR: implication for diffusion in white matter fibers," *Journal of Magnetic Resonance (San Diego, Calif.: 1997)*, vol. 169, pp. 30–38, July 2004.

[79] M. Nilsson, S. Lasič, I. Drobnjak, D. Topgaard, and C.-F. Westin, "Resolution limit of cylinder diameter estimation by diffusion MRI: The impact of gradient waveform and orientation dispersion," *NMR in Biomedicine*, vol. 30, no. 7, p. e3711, 2017.

[80] C. Ligneul, C. Najac, A. Döring, C. Beaulieu, F. Branzoli, W. T. Clarke, C. Cudalbu, G. Genovese, S. Jbabdi, I. Jelescu, D. Karampinos, R. Kreis, H. Lundell, M. Marjańska, H. E. Möller, J. Mosso, E. Mougel, S. Posse, S. Ruschke, K. Simsek, F. Szczepankiewicz, A. Tal, C. Tax, G. Oeltzschner, M. Palombo, I. Ronen, and J. Valette, "Diffusion-weighted MR spectroscopy: consensus, recommendations and resources from acquisition to modelling," May 2023. arXiv:2305.10829 [physics].

[81] J. E. Tanner, "Use of the Stimulated Echo in NMR Diffusion Studies," *The Journal of Chemical Physics*, vol. 52, pp. 2523–2526, Mar. 1970.

[82] C. Cudalbu, V. Mlynárik, L. Xin, and R. Gruetter, "Comparison of T1 relaxation times of the neurochemical profile in rat brain at 9.4 tesla and 14.1 tesla," *Magnetic Resonance in Medicine*, vol. 62, pp. 862–867, Oct. 2009.

[83] C. Ligneul, M. Palombo, and J. Valette, "Metabolite diffusion up to very high b in the mouse brain in vivo: Revisiting the potential correlation between relaxation and diffusion properties," *Magnetic Resonance in Medicine*, vol. 77, no. 4, pp. 1390–1398, 2017.

[84] N. Shemesh, J. T. Rosenberg, J.-N. Dumez, J. A. Muniz, S. C. Grant, and L. Frydman, "Metabolic properties in stroked rats revealed by relaxation-enhanced magnetic resonance spectroscopy at ultrahigh fields," *Nature Communications*, vol. 5, p. 4958, Sept. 2014.

[85] K. L. Behar and T. Ogino, "Characterization of macromolecule resonances in the 1H NMR spectrum of rat brain," *Magnetic Resonance in Medicine*, vol. 30, pp. 38–44, July 1993.

[86] N. Kunz, C. Cudalbu, V. Mlynarik, P. S. Hüppi, S. V. Sizonenko, and R. Gruetter, "Diffusion-weighted spectroscopy: a novel approach to determine macromolecule resonances in short-echo time 1H-MRS," *Magnetic Resonance in Medicine*, vol. 64, pp. 939–946, Oct. 2010.

[87] M. Palombo, C. Ligneul, and J. Valette, "Modeling diffusion of intracellular metabolites in the mouse brain up to very high diffusion-weighting: diffusion in long fibers (almost) accounts for non-monoexponential attenuation," *Magnetic resonance in medicine*, vol. 77, pp. 343–350, Jan. 2017.

[88] M. Palombo, C. Ligneul, C. Najac, J. Le Douce, J. Flament, C. Escartin, P. Hantraye, E. Brouillet, G. Bonvento, and J. Valette, "New paradigm to assess brain cell morphology by diffusion-weighted MR spectroscopy in vivo," *Proceedings of the National Academy of Sciences of the United States of America*, vol. 113, pp. 6671–6676, June 2016.

[89] D. S. Novikov and V. G. Kiselev, "Effective medium theory of a diffusion-weighted signal," *NMR in Biomedicine*, vol. 23, no. 7, pp. 682–697, 2010.

[90] C. Guglielmetti, J. Veraart, E. Roelant, Z. Mai, J. Daans, J. Van Audekerke, M. Naeyaert, G. Vanhoutte, R. Delgado y Palacios, J. Praet, E. Fieremans, P. Ponsaerts, J. Sijbers, A. Van der Linden, and M. Verhoye, "Diffusion kurtosis imaging probes cortical alterations and white matter pathology following cuprizone induced demyelination and spontaneous remyelination," *NeuroImage*, vol. 125, pp. 363–377, Jan. 2016.

[91] R. J. Sevick, F. Kanda, J. Mintorovitch, A. I. Arieff, J. Kucharczyk, J. S. Tsuruda, D. Norman, and M. E. Moseley, "Cytotoxic brain edema: assessment with diffusion-weighted MR imaging," *Radiology*, vol. 185, pp. 687–690, Dec. 1992.

[92] G. A. Lodygensky, T. West, M. Stump, D. M. Holtzman, T. E. Inder, and J. J. Neil, "In vivo MRI analysis of an inflammatory injury in the developing brain," *Brain, Behavior, and Immunity*, vol. 24, pp. 759–767, July 2010.

[93] M. D. Budde and J. A. Frank, "Neurite beading is sufficient to decrease the apparent diffusion coefficient after ischemic stroke," *Proceedings of the National Academy of Sciences of the United States of America*, vol. 107, pp. 14472–14477, Aug. 2010.

Bibliography

[94] H.-H. Lee, S. N. Jespersen, E. Fieremans, and D. S. Novikov, "The impact of realistic axonal shape on axon diameter estimation using diffusion MRI," *NeuroImage*, vol. 223, p. 117228, Dec. 2020.

[95] I. O. Jelescu, M. Zurek, K. V. Winters, J. Veraart, A. Rajaratnam, N. S. Kim, J. S. Babb, T. M. Shepherd, D. S. Novikov, S. G. Kim, and E. Fieremans, "In vivo quantification of demyelination and recovery using compartment-specific diffusion MRI metrics validated by electron microscopy," *NeuroImage*, vol. 132, pp. 104–114, May 2016.

[96] H. Benveniste, L. W. Hedlund, and G. A. Johnson, "Mechanism of detection of acute cerebral ischemia in rats by diffusion-weighted magnetic resonance microscopy," *Stroke*, vol. 23, pp. 746–754, May 1992.

[97] L. L. Latour, Y. Hasegawa, J. E. Formato, M. Fisher, and C. H. Sotak, "Spreading waves of decreased diffusion coefficient after cortical stimulation in the rat brain," *Magnetic Resonance in Medicine*, vol. 32, pp. 189–198, Aug. 1994.

[98] J. A. Goodman, J. J. H. Ackerman, and J. J. Neil, "Cs + ADC in rat brain decreases markedly at death," *Magnetic Resonance in Medicine*, vol. 59, pp. 65–72, Jan. 2008.

[99] I. O. Jelescu, L. Ciobanu, F. Geffroy, P. Marquet, and D. Le Bihan, "Effects of hypotonic stress and ouabain on the apparent diffusion coefficient of water at cellular and tissue levels in Aplysia," *NMR in biomedicine*, vol. 27, pp. 280–290, Mar. 2014.

[100] I. O. Jelescu and M. D. Budde, "Design and Validation of Diffusion MRI Models of White Matter," *Frontiers in Physics*, vol. 5, p. 61, 2017.

[101] M. Palombo, A. Ianus, M. Guerreri, D. Nunes, D. C. Alexander, N. Shemesh, and H. Zhang, "SANDI: A compartment-based model for non-invasive apparent soma and neurite imaging by diffusion MRI," *NeuroImage*, vol. 215, p. 116835, July 2020.

[102] E. Fieremans, J. H. Jensen, and J. A. Helpern, "White matter characterization with diffusional kurtosis imaging," *NeuroImage*, vol. 58, pp. 177–188, Sept. 2011.

[103] S. N. Jespersen, J. L. Olesen, B. Hansen, and N. Shemesh, "Diffusion time dependence of microstructural parameters in fixed spinal cord," *NeuroImage*, vol. 182, pp. 329–342, Nov. 2018.

[104] D. S. Novikov, J. Veraart, I. O. Jelescu, and E. Fieremans, "Rotationally-invariant mapping of scalar and orientational metrics of neuronal microstructure with diffusion MRI," *NeuroImage*, vol. 174, pp. 518–538, July 2018.

[105] C. Ingo, W. Brink, E. Ercan, A. G. Webb, and I. Ronen, "Studying neurons and glia non-invasively via anomalous subdiffusion of intracellular metabolites," *Brain Structure & Function*, vol. 223, pp. 3841–3854, Nov. 2018.

[106] N. Shemesh, J. T. Rosenberg, J.-N. Dumez, S. C. Grant, and L. Frydman, "Distinguishing neuronal from astrocytic subcellular microstructures using in vivo Double Diffusion Encoded 1H MRS at 21.1 T," *PloS One*, vol. 12, no. 10, p. e0185232, 2017.

[107] M. Vincent, M. Palombo, and J. Valette, "Revisiting double diffusion encoding MRS in the mouse brain at 11.7T: Which microstructural features are we sensitive to?," *Neuroimage*, vol. 207, Feb. 2020.

[108] E. Mougel, S. Malaquin, and J. Valette, "Assessing potential correlation between T2 relaxation and diffusion of lactate in the mouse brain," *Magnetic Resonance in Medicine*, vol. 88, no. 5, pp. 2277–2284, 2022.

[109] E. C. Parsons, M. D. Does, and J. C. Gore, "Temporal diffusion spectroscopy: theory and implementation in restricted systems using oscillating gradients," *Magnetic Resonance in Medicine*, vol. 55, pp. 75–84, Jan. 2006.

[110] M. D. Does, E. C. Parsons, and J. C. Gore, "Oscillating gradient measurements of water diffusion in normal and globally ischemic rat brain," *Magnetic Resonance in Medicine*, vol. 49, no. 2, pp. 206–215, 2003.

[111] J. Stepišnik, "Analysis of NMR self-diffusion measurements by a density matrix calculation," *Physica B+C*, vol. 104, pp. 350–364, Apr. 1981.

[112] C. Ligneul and J. Valette, "Probing metabolite diffusion at ultra-short time scales in the mouse brain using optimized oscillating gradients and "short"-echo-time diffusion-weighted MRS," *NMR in biomedicine*, vol. 30, no. 1, 2017.

[113] C. Marchadour, E. Brouillet, P. Hantraye, V. Lebon, and J. Valette, "Anomalous diffusion of brain metabolites evidenced by diffusion-weighted magnetic resonance spectroscopy in vivo," *Journal of Cerebral Blood Flow and Metabolism: Official Journal of the International Society of Cerebral Blood Flow and Metabolism*, vol. 32, pp. 2153–2160, Dec. 2012.

[114] P. P. Mitra, P. N. Sen, and L. M. Schwartz, "Short-time behavior of the diffusion coefficient as a geometrical probe of porous media," *Physical Review B*, vol. 47, pp. 8565–8574, Apr. 1993.

[115] D. M. Yang, J. E. Huettner, G. L. Bretthorst, J. J. Neil, J. R. Garbow, and J. J. Ackerman, "Intracellular water preexchange lifetime in neurons and astrocytes," *Magnetic Resonance in Medicine*, vol. 79, no. 3, pp. 1616–1627, 2018.

[116] I. O. Jelescu, A. de Skowronski, F. Geffroy, M. Palombo, and D. S. Novikov, "Neurite Exchange Imaging (NEXI): A minimal model of diffusion in gray matter with inter-compartment water exchange," *NeuroImage*, vol. 256, p. 119277, Aug. 2022.

[117] J. L. Olesen, L. Østergaard, N. Shemesh, and S. N. Jespersen, "Diffusion time dependence, power-law scaling, and exchange in gray matter," *NeuroImage*, vol. 251, p. 118976, May 2022.

[118] A. Chakwizira, C.-F. Westin, J. Brabec, S. Lasič, L. Knutsson, F. Szczepankiewicz, and M. Nilsson, "Diffusion MRI with pulsed and free gradient waveforms: Effects of restricted diffusion and exchange," *NMR in biomedicine*, vol. 36, p. e4827, Jan. 2023.

[119] N. Shemesh, E. Ozarslan, M. E. Komlosh, P. J. Basser, and Y. Cohen, "From single-pulsed field gradient to double-pulsed field gradient MR: gleaning new microstructural information and developing new forms of contrast in MRI," *NMR in biomedicine*, vol. 23, pp. 757–780, Aug. 2010.

[120] N. Weiss, R. Jalan, and D. Thabut, "Understanding hepatic encephalopathy," *Intensive Care Medicine*, vol. 44, pp. 231–234, Feb. 2018.

[121] C. F. Rose, P. Amodio, J. S. Bajaj, R. K. Dhiman, S. Montagnese, S. D. Taylor-Robinson, H. Vilstrup, and R. Jalan, "Hepatic encephalopathy: Novel insights into classification, pathophysiology and therapy," *Journal of Hepatology*, vol. 73, pp. 1526–1547, Dec. 2020.

[122] S. G. Sepanlou *et al.*, "The global, regional, and national burden of cirrhosis by cause in 195 countries and territories, 1990–2017: a systematic analysis for the Global Burden of Disease Study 2017," *The Lancet Gastroenterology & Hepatology*, vol. 5, pp. 245–266, Mar. 2020.

[123] H. Vilstrup, P. Amodio, J. Bajaj, J. Cordoba, P. Ferenci, K. D. Mullen, K. Weissenborn, and P. Wong, "Hepatic encephalopathy in chronic liver disease: 2014 Practice Guideline by the American Association for the Study of Liver Diseases and the European Association for the Study of the Liver," *Hepatology (Baltimore, Md.)*, vol. 60, pp. 715–735, Aug. 2014.

[124] A. Bahadori, B. Kuhlmann, D. Debray, S. Franchi-Abella, J. Wacker, M. Beghetti, B. E. Wildhaber, and V. A. McLin, "Presentation of Congenital Portosystemic Shunts in Children," *Children*, vol. 9, p. 243, Feb. 2022.

[125] C. Cudalbu, V. A. McLin, H. Lei, J. M. N. Duarte, A.-L. Rougemont, G. Oldani, S. Terraz, C. Toso, and R. Gruetter, "The C57BL/6J mouse exhibits sporadic congenital portosystemic shunts," *PloS One*, vol. 8, no. 7, p. e69782, 2013.

[126] S. Nardelli, O. Riggio, S. Gioia, M. Puzzono, G. Pelle, and L. Ridola, "Spontaneous porto-systemic shunts in liver cirrhosis: Clinical and therapeutical aspects," *World Journal of Gastroenterology*, vol. 26, pp. 1726–1732, Apr. 2020.

[127] M. A. Khan and F. Anjum, "Portal-Systemic Encephalopathy," in *StatPearls*, Treasure Island (FL): StatPearls Publishing, 2023.

[128] M. R. Kappus and J. S. Bajaj, "Covert Hepatic Encephalopathy: Not as Minimal as You Might Think," *Clinical Gastroenterology and Hepatology*, vol. 10, pp. 1208–1219, Nov. 2012.

[129] R. S. Rahimi, K. A. Brown, S. L. Flamm, and R. S. Brown, "Overt Hepatic Encephalopathy: Current Pharmacologic Treatments and Improving Clinical Outcomes," *The American Journal of Medicine*, vol. 134, pp. 1330–1338, Nov. 2021.

[130] K. R. Patidar, L. R. Thacker, J. B. Wade, R. K. Sterling, A. J. Sanyal, M. S. Siddiqui, S. C. Matherly, R. T. Stravitz, P. Puri, V. A. Luketic, M. Fuchs, M. B. White, N. A. Noble, A. B. Unser, H. Gilles, D. M. Heuman, and J. S. Bajaj, "Covert hepatic encephalopathy is independently associated with poor survival and increased risk of hospitalization," *The American Journal of Gastroenterology*, vol. 109, pp. 1757–1763, Nov. 2014.

[131] J. Bustamante, A. Rimola, P. J. Ventura, M. Navasa, I. Cirera, V. Reggiardo, and J. Rodés, "Prognostic significance of hepatic encephalopathy in patients with cirrhosis," *Journal of Hepatology*, vol. 30, pp. 890–895, May 1999.

[132] K. Pierzchala, A. Hadjihambi, J. Mosso, R. Jalan, C. F. Rose, and C. Cudalbu, "Lessons on brain edema in HE: from cellular to animal models and clinical studies," *Metabolic Brain Disease*, Aug. 2023.

Bibliography

[133] R. Jalan, S. W. M. Olde Damink, P. C. Hayes, N. E. P. Deutz, and A. Lee, "Pathogenesis of intracranial hypertension in acute liver failure: inflammation, ammonia and cerebral blood flow," *Journal of Hepatology*, vol. 41, pp. 613–620, Oct. 2004.

[134] A. J. C. Kerbert and R. Jalan, "Recent advances in understanding and managing hepatic encephalopathy in chronic liver disease," *F1000Research*, vol. 9, pp. F1000 Faculty Rev–312, Apr. 2020.

[135] S. DeMorrow, C. Cudalbu, N. Davies, A. R. Jayakumar, and C. F. Rose, "2021 ISHEN guidelines on animal models of hepatic encephalopathy," *Liver International: Official Journal of the International Association for the Study of the Liver*, vol. 41, pp. 1474–1488, July 2021.

[136] O. Braissant, V. Rackayová, K. Pierzchala, J. Grosse, V. A. McLin, and C. Cudalbu, "Longitudinal neurometabolic changes in the hippocampus of a rat model of chronic hepatic encephalopathy," *Journal of Hepatology*, vol. 71, pp. 505–515, Sept. 2019.

[137] V. Rackayova, O. Braissant, A.-L. Rougemont, C. Cudalbu, and V. A. McLin, "Longitudinal osmotic and neurometabolic changes in young rats with chronic cholestatic liver disease," *Scientific Reports*, vol. 10, p. 7536, May 2020.

[138] D. Simicic, V. Rackayova, O. Braissant, C. Toso, G. Oldani, D. Sessa, V. A. McLin, and C. Cudalbu, "Neurometabolic changes in a rat pup model of type C hepatic encephalopathy depend on age at liver disease onset," *Metabolic Brain Disease*, vol. 38, pp. 1999–2012, Aug. 2023.

[139] K. Pierzchala, D. Simicic, A. Sienkiewicz, D. Sessa, S. Mitrea, O. Braissant, V. A. McLin, R. Gruetter, and C. Cudalbu, "Central nervous system and systemic oxidative stress interplay with inflammation in a bile duct ligation rat model of type C hepatic encephalopathy," *Free Radical Biology and Medicine*, vol. 178, pp. 295–307, Jan. 2022.

[140] J. Mosso, T. Yin, C. Poitry-Yamate, D. Simicic, M. Lepore, V. A. McLin, O. Braissant, C. Cudalbu, and B. Lanz, "PET CMRglc mapping and 1H-MRS show altered glucose uptake and neurometabolic profiles in BDL rats," *Analytical Biochemistry*, vol. 647, p. 114606, June 2022.

[141] R. Leke, D. L. de Oliveira, B. H. M. Mussulini, M. S. Pereira, V. Kazlauckas, G. Mazzini, C. R. Hartmann, T. R. Silveira, M. Simonsen, L. K. Bak, H. S. Waagepetersen, S. Keiding, A. Schousboe, and L. V. Portela, "Impairment of the organization of locomotor and exploratory behaviors in bile duct-ligated rats," *PloS One*, vol. 7, no. 5, p. e36322, 2012.

[142] R. Leke, D. L. Oliveira, L. F. Forgiarini, T. D. C. Escobar, T. O. Hammes, F. S. Meyer, S. Keiding, T. R. Silveira, and A. Schousboe, "Impairment of short term memory in rats with hepatic encephalopathy due to bile duct ligation," *Metabolic Brain Disease*, vol. 28, pp. 187–192, June 2013.

[143] R. Kreis, N. Farrow, and B. Ross, "Diagnosis of hepatic encephalopathy by proton magnetic resonance spectroscopy," *The Lancet*, vol. 336, pp. 635–636, Sept. 1990.

[144] A. J. Cooper and F. Plum, "Biochemistry and physiology of brain ammonia," *Physiological Reviews*, vol. 67, pp. 440–519, Apr. 1987.

[145] C. R. Bosoi and C. F. Rose, "Identifying the direct effects of ammonia on the brain," *Metabolic Brain Disease*, vol. 24, pp. 95–102, Mar. 2009.

[146] J. Cordoba, "Hepatic Encephalopathy: From the Pathogenesis to the New Treatments," *ISRN hepatology*, vol. 2014, p. 236268, 2014.

[147] A. Martinez-Hernandez, K. P. Bell, and M. D. Norenberg, "Glutamine synthetase: glial localization in brain," *Science (New York, N.Y.)*, vol. 195, pp. 1356–1358, Mar. 1977.

[148] M. D. Norenberg, "Distribution of glutamine synthetase in the rat central nervous system," *The Journal of Histochemistry and Cytochemistry: Official Journal of the Histochemistry Society*, vol. 27, pp. 756–762, Mar. 1979.

[149] A. J. Montano-Loza, J. Meza-Junco, C. M. M. Prado, J. R. Lieffers, V. E. Baracos, V. G. Bain, and M. B. Sawyer, "Muscle wasting is associated with mortality in patients with cirrhosis," *Clinical Gastroenterology and Hepatology: The Official Clinical Practice Journal of the American Gastroenterological Association*, vol. 10, pp. 166–173, 173.e1, Feb. 2012.

[150] Y. H. Ju, M. Bhalla, S. J. Hyeon, J. E. Oh, S. Yoo, U. Chae, J. Kwon, W. Koh, J. Lim, Y. M. Park, J. Lee, I.-J. Cho, H. Lee, H. Ryu, and C. J. Lee, "Astrocytic urea cycle detoxifies Aβ-derived ammonia while impairing memory in Alzheimer's disease," *Cell Metabolism*, vol. 34, pp. 1104–1120.e8, Aug. 2022.

[151] T. H. Tranah, G. K. M. Vijay, J. M. Ryan, and D. L. Shawcross, "Systemic inflammation and ammonia in hepatic encephalopathy," *Metabolic Brain Disease*, vol. 28, pp. 1–5, Mar. 2013.

[152] W. Claeys, L. Van Hoecke, S. Lefere, A. Geerts, X. Verhelst, H. Van Vlierberghe, H. Degroote, L. Devisscher, R. E. Vandenbroucke, and C. Van Steenkiste, "The neurogliovascular unit in hepatic encephalopathy," *JHEP Reports*, vol. 3, p. 100352, Oct. 2021.

[153] R. A. Hawkins and J. Jessy, "Hyperammonaemia does not impair brain function in the absence of net glutamine synthesis.," *Biochemical Journal*, vol. 277, pp. 697–703, Aug. 1991.

[154] J. Albrecht and M. D. Norenberg, "Glutamine: a Trojan horse in ammonia neurotoxicity," *Hepatology (Baltimore, Md.)*, vol. 44, pp. 788–794, Oct. 2006.

[155] M. D. Norenberg, "The role of astrocytes in hepatic encephalopathy," *Neurochemical Pathology*, vol. 6, pp. 13–33, Feb. 1987.

[156] C. Cudalbu and S. D. Taylor-Robinson, "Brain Edema in Chronic Hepatic Encephalopathy," *Journal of Clinical and Experimental Hepatology*, vol. 9, pp. 362–382, May 2019.

[157] A. Lemberg and M. Alejandra Fernández, "Hepatic encephalopathy, ammonia, glutamate, glutamine and oxidative stress," *Annals of Hepatology*, vol. 8, pp. 95–102, Apr. 2009.

[158] S. Lores-Arnaiz, J. C. Perazzo, J. P. Prestifilippo, N. Lago, G. D'Amico, A. Czerniczyniec, J. Bustamante, A. Boveris, and A. Lemberg, "Hippocampal mitochondrial dysfunction with decreased mtNOS activity in prehepatic portal hypertensive rats," *Neurochemistry International*, vol. 47, pp. 362–368, Oct. 2005.

[159] J. C. Szerb and R. F. Butterworth, "Effect of ammonium ions on synaptic transmission in the mammalian central nervous system," *Progress in Neurobiology*, vol. 39, pp. 135–153, Aug. 1992.

[160] J. C. Lai and A. J. Cooper, "Brain alpha-ketoglutarate dehydrogenase complex: kinetic properties, regional distribution, and effects of inhibitors," *Journal of Neurochemistry*, vol. 47, pp. 1376–1386, Nov. 1986.

[161] A. Hadjihambi, N. Arias, M. Sheikh, and R. Jalan, "Hepatic encephalopathy: a critical current review," *Hepatology International*, vol. 12, pp. 135–147, Aug. 2017.

[162] L. Abenavoli, G. Fabiano, A. C. Procopio, I. Aquila, R. Pellicano, S. Barone, M. Morelli, and F. Luzza, "Hepatic Encephalopathy by Manganese Deposition: A Case Report and a Review of Literature," *Reviews on Recent Clinical Trials*, June 2022.

[163] Z. Chen, J. Ruan, D. Li, M. Wang, Z. Han, W. Qiu, and G. Wu, "The Role of Intestinal Bacteria and Gut–Brain Axis in Hepatic Encephalopathy," *Frontiers in Cellular and Infection Microbiology*, vol. 10, p. 595759, Jan. 2021.

[164] D. R. Aldridge, E. J. Tranah, and D. L. Shawcross, "Pathogenesis of hepatic encephalopathy: role of ammonia and systemic inflammation," *Journal of Clinical and Experimental Hepatology*, vol. 5, pp. S7–S20, Mar. 2015.

[165] R. F. Butterworth, "The liver-brain axis in liver failure: neuroinflammation and encephalopathy," *Nature Reviews. Gastroenterology & Hepatology*, vol. 10, pp. 522–528, Sept. 2013.

[166] C. R. Bosoi and C. F. Rose, "Oxidative stress: a systemic factor implicated in the pathogenesis of hepatic encephalopathy," *Metabolic Brain Disease*, vol. 28, pp. 175–178, June 2013.

[167] M. D. Norenberg, A. R. Jayakumar, and K. V. Rama Rao, "Oxidative Stress in the Pathogenesis of Hepatic Encephalopathy," *Metabolic Brain Disease*, vol. 19, pp. 313–329, Dec. 2004.

[168] D. Simicic, C. Cudalbu, and K. Pierzchala, "Overview of oxidative stress findings in hepatic encephalopathy: From cellular and ammonium-based animal models to human data," *Analytical Biochemistry*, vol. 654, p. 114795, Oct. 2022.

[169] C. R. Murthy, K. V. Rama Rao, G. Bai, and M. D. Norenberg, "Ammonia-induced production of free radicals in primary cultures of rat astrocytes," *Journal of Neuroscience Research*, vol. 66, pp. 282–288, Oct. 2001.

[170] A. R. Jayakumar, K. V. Rama Rao, A. Schousboe, and M. D. Norenberg, "Glutamine-induced free radical production in cultured astrocytes," *Glia*, vol. 46, pp. 296–301, May 2004.

[171] M. Bernardi, P. Angeli, J. Claria, R. Moreau, P. Gines, R. Jalan, P. Caraceni, J. Fernandez, A. L. Gerbes, A. J. O'Brien, J. Trebicka, T. Thevenot, and V. Arroyo, "Albumin in decompensated cirrhosis: new concepts and perspectives," *Gut*, vol. 69, pp. 1127–1138, June 2020.

[172] G. Aguilera, A. L. Colín-González, E. Rangel-López, A. Chavarría, and A. Santamaría, "Redox Signaling, Neuroinflammation, and Neurodegeneration," *Antioxidants & Redox Signaling*, vol. 28, pp. 1626–1651, June 2018.

Bibliography

[173] B. Görg, F. Schliess, and D. Häussinger, "Osmotic and oxidative/nitrosative stress in ammonia toxicity and hepatic encephalopathy," *Archives of Biochemistry and Biophysics*, vol. 536, pp. 158–163, Aug. 2013.

[174] M. Macedo de Oliveira, A. Monnet-Aimard, C. R. Bosoi, M. Tremblay, and C. F. Rose, "Sex is associated with differences in oxidative stress and susceptibility to severe hepatic encephalopathy in bile-duct ligated rats," *Journal of Neurochemistry*, vol. 162, no. 4, pp. 337–351, 2022.

[175] K. V. Rama Rao and M. D. Norenberg, "Brain energy metabolism and mitochondrial dysfunction in acute and chronic hepatic encephalopathy," *Neurochemistry International*, vol. 60, pp. 697–706, June 2012.

[176] A. S. Hazell and R. F. Butterworth, "Hepatic encephalopathy: An update of pathophysiologic mechanisms," *Proceedings of the Society for Experimental Biology and Medicine. Society for Experimental Biology and Medicine (New York, N.Y.)*, vol. 222, pp. 99–112, Nov. 1999.

[177] N. F. Cruz and T. E. Duffy, "Local Cerebral Glucose Metabolism in Rats with Chronic Portacaval Shunts," *Journal of Cerebral Blood Flow & Metabolism*, vol. 3, pp. 311–320, Sept. 1983.

[178] J. Jessy, M. R. DeJoseph, and R. A. Hawkins, "Hyperammonaemia depresses glucose consumption throughout the brain," *The Biochemical Journal*, vol. 277 (Pt 3), pp. 693–696, Aug. 1991.

[179] A. H. Lockwood, K. Weissenborn, M. Bokemeyer, U. Tietge, and W. Burchert, "Correlations Between Cerebral Glucose Metabolism and Neuropsychological Test Performance in Nonalcoholic Cirrhotics," *Metabolic Brain Disease*, vol. 17, pp. 29–40, Mar. 2002.

[180] A. H. Lockwood, E. W. H. Yap, H. M. Rhoades, and W.-H. Wong, "Altered Cerebral Blood Flow and Glucose Metabolism in Patients with Liver Disease and Minimal Encephalopathy," *Journal of Cerebral Blood Flow & Metabolism*, vol. 11, pp. 331–336, Mar. 1991.

[181] W. Zhang, N. Ning, X. Li, M. Li, X. Duan, Y. Guo, Y. Dang, Y. Li, J. Gao, J. Ye, and J. Yang, "Impaired brain glucose metabolism in cirrhosis without overt hepatic encephalopathy: a retrospective 18F-FDG PET/CT study," *Neuroreport*, vol. 30, pp. 776–782, Aug. 2019.

[182] R. E. O'Carroll, P. C. Hayes, K. P. Ebmeier, N. Dougall, C. Murray, J. J. Best, I. A. Bouchier, and G. M. Goodwin, "Regional cerebral blood flow and cognitive function in patients with chronic liver disease," *Lancet (London, England)*, vol. 337, pp. 1250–1253, May 1991.

[183] K. Vankadari, B. R. Mittal, R. Kumar, H. Singh, A. Bhattacharya, and R. K. Dhiman, "Detection of Hepatic Encephalopathy on 18F-FDG PET/CT Brain Images in a Patient With Decompensated Liver Cirrhosis," *Clinical Nuclear Medicine*, vol. 43, p. e486, Dec. 2018.

[184] G. Dam, S. Keiding, O. L. Munk, P. Ott, H. Vilstrup, L. K. Bak, H. S. Waagepetersen, A. Schousboe, and M. Sørensen, "Hepatic encephalopathy is associated with decreased cerebral oxygen metabolism and blood flow, not increased ammonia uptake," *Hepatology (Baltimore, Md.)*, vol. 57, pp. 258–265, Jan. 2013.

[185] A. Hadjihambi, C. Cudalbu, K. Pierzchala, D. Simicic, C. Donnelly, C. Konstantinou, N. Davies, A. Habtesion, A. V. Gourine, R. Jalan, and P. S. Hosford, "Abnormal brain oxygen homeostasis in an animal model of liver disease," *JHEP Reports*, vol. 4, p. 100509, Aug. 2022.

[186] M. Sørensen and H. Vilstrup, "Does ammonia really disrupt brain oxygen homeostasis?," *JHEP Reports*, vol. 5, p. 100616, Apr. 2023.

[187] P. S. Hosford, R. Jalan, and A. Hadjihambi, "Reply to: "Does ammonia really disrupt brain oxygen homeostasis?"," *JHEP Reports*, vol. 5, p. 100666, May 2023.

[188] V. Rackayova, O. Braissant, V. A. McLin, C. Berset, B. Lanz, and C. Cudalbu, "1H and 31P magnetic resonance spectroscopy in a rat model of chronic hepatic encephalopathy: in vivo longitudinal measurements of brain energy metabolism," *Metabolic Brain Disease*, vol. 31, no. 6, pp. 1303–1314, 2016.

[189] B. Lanz, V. Rackayova, O. Braissant, and C. Cudalbu, "MRS studies of neuroenergetics and glutamate/glutamine exchange in rats: Extensions to hyperammonemic models," *Analytical Biochemistry*, vol. 529, pp. 245–269, July 2017.

[190] C. R. Bosoi, C. Zwingmann, H. Marin, C. Parent-Robitaille, J. Huynh, M. Tremblay, and C. F. Rose, "Increased brain lactate is central to the development of brain edema in rats with chronic liver disease," *Journal of Hepatology*, vol. 60, pp. 554–560, Mar. 2014.

[191] B. Lanz, C. Cudalbu, V. McLin, M. Lepore, O. Braissant, and R. Gruetter, "In Vivo 13C MRS Investigation of Alterations in Cerebral Oxidative Metabolism in a Chronic Liver Disease Rat Model," in *Proc. Intl. Soc. Mag. Reson. Med. 21*, 2013.

240

[192] S. D. Taylor-Robinson, J. Sargentoni, R. J. Mallalieu, J. D. Bell, D. J. Bryant, G. A. Coutts, and M. Y. Morgan, "Cerebral phosphorus-31 magnetic resonance spectroscopy in patients with chronic hepatic encephalopathy," *Hepatology (Baltimore, Md.)*, vol. 20, pp. 1173–1178, Nov. 1994.

[193] S. D. Taylor-Robinson, J. Sargentoni, A. Oatridge, D. J. Bryant, J. V. Hajnal, C. D. Marcus, J. P. Seery, H. J. Hodgson, and N. M. deSouza, "MR imaging and spectroscopy of the basal ganglia in chronic liver disease: correlation of T1-weighted contrast measurements with abnormalities in proton and phosphorus-31 MR spectra," *Metabolic Brain Disease*, vol. 11, pp. 249–268, Sept. 1996.

[194] L. Sokoloff, M. Reivich, C. Kennedy, M. H. D. Rosiers, C. S. Patlak, K. D. Pettigrew, O. Sakurada, and M. Shinohara, "The [14c]deoxyglucose Method for the Measurement of Local Cerebral Glucose Utilization: Theory, Procedure, and Normal Values in the Conscious and Anesthetized Albino Rat," *Journal of Neurochemistry*, vol. 28, no. 5, pp. 897–916, 1977.

[195] D. D. You, G. S. Choi, J. M. Kim, C. H. D. Kwon, J. W. Joh, and S. K. Lee, "Long-term Outcomes for Liver Transplant Recipients in Terms of Hepatic Encephalopathy," *Transplantation Proceedings*, vol. 49, pp. 1425–1429, July 2017.

[196] E. U. Sotil, J. Gottstein, E. Ayala, C. Randolph, and A. T. Blei, "Impact of preoperative overt hepatic encephalopathy on neurocognitive function after liver transplantation," *Liver Transplantation: Official Publication of the American Association for the Study of Liver Diseases and the International Liver Transplantation Society*, vol. 15, pp. 184–192, Feb. 2009.

[197] D. Devictor, L. Desplanques, D. Debray, Y. Ozier, A.-M. Dubousset, J. Valayer, D. Houssin, O. Bernard, and G. Huault, "Emergency liver transplantation for fulminant liver failure in infants and children," *Hepatology*, vol. 16, no. 5, pp. 1156–1162, 1992.

[198] L. G. Sorensen, K. Neighbors, K. Martz, F. Zelko, J. C. Bucuvalas, and E. M. Alonso, "Longitudinal Study of Cognitive and Academic Outcomes after Pediatric Liver Transplantation," *The Journal of Pediatrics*, vol. 165, pp. 65–72.e2, July 2014.

[199] B. Hermann, M. Rudler, D. Galanaud, D. Thabut, and N. Weiss, "Magnetic resonance spectroscopy: A surrogate marker of hepatic encephalopathy?," *Journal of Hepatology*, vol. 71, pp. 1055–1057, Nov. 2019.

[200] V. A. McLin, O. Braissant, and C. Cudalbu, "Reply to: "Magnetic resonance spectroscopy: A surrogate marker of hepatic encephalopathy?"," *Journal of Hepatology*, vol. 71, p. 1057, Nov. 2019.

[201] D. Simicic, K. Pierzchala, V. Rackaova, O. Braissant, S.-O. Mitrea, D. Sessa, V. Mclin, and C. Cudalbu, "P: 33 In Vivo Longitudinal 1H MRS Study of Hippocampal, Cereberal and Striatal Metabolic Changes in the Adult Brain Using an Animal Model of Chronic Hepatic Encephalopathy," *The American Journal of Gastroenterology*, vol. 114, p. S17, Sept. 2019.

[202] J. Mosso, J. Valette, K. Pierzchala, D. Simicic, I. O. Jelescu, and C. Cudalbu, "Diffusion-weighted magnetic resonance spectroscopy in the cerebellum of a rat model of hepatic encephalopathy at 14.1T," in *Proc. Intl. Soc. Mag. Reson. Med. 29*, 2021.

[203] J. Mosso, M. Rey, D. Simicic, K. Pierzchala, I. O. Jelescu, and C. Cudalbu, "Diffusion MRI and MRS probe cerebellar microstructure alterations in the rat developing brain during hepatic encephalopathy," in *Proc. Intl. Soc. Mag. Reson. Med. 30*, 2022.

[204] J. Mosso, M. Chan, M. Rey, I. O. Jelescu, and C. Cudalbu, "Exploiting dual diffusion MRS and MRI acquisitions in the rat cerebellum at 14.1T: a measurement of intra-extracellular water exchange," in *Overcoming the barriers to clinical use*, 2022.

[205] S. Ackerman, *Discovering the Brain.* Washington (DC): National Academies Press (US), 1992.

[206] R. García-García, A. J. Cruz-Gómez, A. Mangas-Losada, A. Urios, C. Forn, D. Escudero-García, E. Kosenko, J. F. Ordoño, J. Tosca, R. Giner-Durán, M. A. Serra, C. Avila, V. Belloch, V. Felipo, and C. Montoliu, "Reduced resting state connectivity and gray matter volume correlate with cognitive impairment in minimal hepatic encephalopathy," *PLOS ONE*, vol. 12, p. e0186463, Oct. 2017.

[207] T. Balzano, J. Forteza, P. Molina, J. Giner, A. Monzó, J. Sancho-Jiménez, A. Urios, C. Montoliu, and V. Felipo, "The Cerebellum of Patients with Steatohepatitis Shows Lymphocyte Infiltration, Microglial Activation and Loss of Purkinje and Granular Neurons," *Scientific Reports*, vol. 8, p. 3004, Feb. 2018.

[208] B. Ahl, K. Weissenborn, J. van den Hoff, D. Fischer-Wasels, H. Köstler, H. Hecker, and W. Burchert, "Regional differences in cerebral blood flow and cerebral ammonia metabolism in patients with cirrhosis," *Hepatology*, vol. 40, no. 1, pp. 73–79, 2004.

[209] R. Kreis, "The trouble with quality filtering based on relative Cramér-Rao lower bounds," *Magnetic Resonance in Medicine*, vol. 75, no. 1, pp. 15–18, 2016.

[210] I. Tkác, Z. Starcuk, I. Y. Choi, and R. Gruetter, "In vivo 1H NMR spectroscopy of rat brain at 1 ms echo time," *Magnetic Resonance in Medicine*, vol. 41, pp. 649–656, Apr. 1999.

[211] V. Govindaraju, K. Young, and A. A. Maudsley, "Proton NMR chemical shifts and coupling constants for brain metabolites," *NMR in biomedicine*, vol. 13, pp. 129–153, May 2000.

[212] V. Govind, K. Young, and A. A. Maudsley, "Corrigendum: proton NMR chemical shifts and coupling constants for brain metabolites. Govindaraju V, Young K, Maudsley AA, NMR Biomed. 2000; 13: 129-153," *NMR in biomedicine*, vol. 28, pp. 923–924, July 2015.

[213] Z. Starčuk and J. Starčuková, "Quantum-mechanical simulations for in vivo MR spectroscopy: Principles and possibilities demonstrated with the program NMRScopeB," *Analytical Biochemistry*, vol. 529, pp. 79–97, July 2017.

[214] A. Naressi, C. Couturier, J. M. Devos, M. Janssen, C. Mangeat, R. d. Beer, and D. Graveron-Demilly, "Java-based graphical user interface for the MRUI quantitation package," *Magnetic Resonance Materials in Physics, Biology and Medicine*, vol. 12, p. 141, June 2001.

[215] D. Stefan, F. D. Cesare, A. Andrasescu, E. Popa, A. Lazariev, E. Vescovo, O. Strbak, S. Williams, Z. Starcuk, M. Cabanas, D. v. Ormondt, and D. Graveron-Demilly, "Quantitation of magnetic resonance spectroscopy signals: the jMRUI software package," *Measurement Science and Technology*, vol. 20, p. 104035, Sept. 2009.

[216] L. Vanhamme, n. van den Boogaart A, and n. Van Huffel S, "Improved method for accurate and efficient quantification of MRS data with use of prior knowledge," *Journal of Magnetic Resonance (San Diego, Calif.: 1997)*, vol. 129, pp. 35–43, Nov. 1997.

[217] B. Ades-Aron, J. Veraart, P. Kochunov, S. McGuire, P. Sherman, E. Kellner, D. S. Novikov, and E. Fieremans, "Evaluation of the accuracy and precision of the diffusion parameter EStImation with Gibbs and NoisE removal pipeline," *NeuroImage*, vol. 183, pp. 532–543, Dec. 2018.

[218] A. Daducci, E. Canales-Rodríguez, H. Zhang, T. Dyrby, D. Alexander, and J.-P. Thiran, "Accelerated Microstructure Imaging via Convex Optimization (AMICO) from diffusion MRI data," *NeuroImage*, vol. 105, Oct. 2014.

[219] S. Coelho, S. H. Baete, G. Lemberskiy, B. Ades-Aron, G. Barrol, J. Veraart, D. S. Novikov, and E. Fieremans, "Reproducibility of the Standard Model of diffusion in white matter on clinical MRI systems," *NeuroImage*, vol. 257, p. 119290, Aug. 2022.

[220] J. Levine, K. N. Chengappa, and R. Reddy, "Acute myo-inositol enhances swimming activity in goldfish (short communication)," *Journal of Neural Transmission (Vienna, Austria: 1996)*, vol. 106, no. 5-6, pp. 433–441, 1999.

[221] A. H. Sharp, P. S. McPherson, T. M. Dawson, C. Aoki, K. P. Campbell, and S. H. Snyder, "Differential immunohistochemical localization of inositol 1,4,5-trisphosphate- and ryanodine-sensitive Ca2+ release channels in rat brain," *The Journal of Neuroscience: The Official Journal of the Society for Neuroscience*, vol. 13, pp. 3051–3063, July 1993.

[222] I. Tkáč, R. Rao, M. K. Georgieff, and R. Gruetter, "Developmental and regional changes in the neurochemical profile of the rat brain determined by in vivo 1H NMR spectroscopy," *Magnetic Resonance in Medicine*, vol. 50, no. 1, pp. 24–32, 2003.

[223] A. Brand, C. Richter-Landsberg, and D. Leibfritz, "Multinuclear NMR studies on the energy metabolism of glial and neuronal cells," *Developmental Neuroscience*, vol. 15, no. 3-5, pp. 289–298, 1993.

[224] J. Urenjak, S. R. Williams, D. G. Gadian, and M. Noble, "Proton nuclear magnetic resonance spectroscopy unambiguously identifies different neural cell types," *The Journal of Neuroscience*, vol. 13, no. 3, pp. 981–989, 1993.

[225] J. L. Harris, I.-Y. Choi, and W. M. Brooks, "Probing astrocyte metabolism in vivo: proton magnetic resonance spectroscopy in the injured and aging brain," *Frontiers in Aging Neuroscience*, vol. 7, p. 202, 2015.

[226] L. Korbo, B. B. Andersen, O. Ladefoged, and A. Møller, "Total numbers of various cell types in rat cerebellar cortex estimated using an unbiased stereological method," *Brain Research*, vol. 609, pp. 262–268, Apr. 1993.

[227] A. Petzold, "Neurofilament phosphoforms: surrogate markers for axonal injury, degeneration and loss," *Journal of the Neurological Sciences*, vol. 233, pp. 183–198, June 2005.

[228] C. Barro, P. Benkert, G. Disanto, C. Tsagkas, M. Amann, Y. Naegelin, D. Leppert, C. Gobbi, C. Granziera, O. Yaldizli, Z. Michalak, J. Wuerfel, L. Kappos, K. Parmar, and J. Kuhle, "Serum neurofilament as a predictor of disease worsening and brain and spinal cord atrophy in multiple sclerosis," *Brain: A Journal of Neurology*, vol. 141, pp. 2382–2391, Aug. 2018.

[229] J. Kuhle, C. Barro, G. Disanto, A. Mathias, C. Soneson, G. Bonnier, O. Yaldizli, A. Regeniter, T. Derfuss, M. Canales, M. Schluep, R. Du Pasquier, G. Krueger, and C. Granziera, "Serum neurofilament light chain in early relapsing remitting MS is increased and correlates with CSF levels and with MRI measures of disease severity," *Multiple Sclerosis Journal*, vol. 22, pp. 1550–1559, Oct. 2016.

[230] M. Khalil, C. E. Teunissen, M. Otto, F. Piehl, M. P. Sormani, T. Gattringer, C. Barro, L. Kappos, M. Comabella, F. Fazekas, A. Petzold, K. Blennow, H. Zetterberg, and J. Kuhle, "Neurofilaments as biomarkers in neurological disorders," *Nature Reviews. Neurology*, vol. 14, pp. 577–589, Oct. 2018.

[231] J. Gaiottino, N. Norgren, R. Dobson, J. Topping, A. Nissim, A. Malaspina, J. P. Bestwick, A. U. Monsch, A. Regeniter, R. L. Lindberg, L. Kappos, D. Leppert, A. Petzold, G. Giovannoni, and J. Kuhle, "Increased neurofilament light chain blood levels in neurodegenerative neurological diseases," *PloS One*, vol. 8, no. 9, p. e75091, 2013.

[232] F. Santamaria, S. Wils, E. De Schutter, and G. J. Augustine, "Anomalous diffusion in Purkinje cell dendrites caused by spines," *Neuron*, vol. 52, pp. 635–648, Nov. 2006.

[233] F. Santamaria, S. Wils, E. De Schutter, and G. J. Augustine, "The diffusional properties of dendrites depend on the density of dendritic spines," *European Journal of Neuroscience*, vol. 34, no. 4, pp. 561–568, 2011.

[234] C. Cudalbu, P. Katarzyna, D. Simicic, G. Knott, S. Clerc-Rosset, B. Lanz, and I. Jelescu, "Diffusion of brain metabolites highlights altered brain microstructure in chronic hepatic encephalopathy," in *Proc. Intl. Soc. Mag. Reson. Med. 28*, 2020.

[235] M. Margoni, E. Pagani, P. Preziosa, M. Palombo, M. Gueye, M. Azzimonti, M. Filippi, and M. A. Rocca, "In vivo quantification of brain soma and neurite density abnormalities in multiple sclerosis," *Journal of Neurology*, vol. 270, pp. 433–445, Jan. 2023.

[236] Y. Diao and I. Jelescu, "Parameter estimation for WMTI-Watson model of white matter using encoder–decoder recurrent neural network," *Magnetic Resonance in Medicine*, vol. 89, no. 3, pp. 1193–1206, 2023.

[237] J. Kärger, "NMR self-diffusion studies in heterogeneous systems," *Advances in Colloid and Interface Science*, vol. 23, pp. 129–148, Aug. 1985.

[238] R. N. Henriques, M. Palombo, S. N. Jespersen, N. Shemesh, H. Lundell, and A. Ianuş, "Double diffusion encoding and applications for biomedical imaging," *Journal of Neuroscience Methods*, vol. 348, p. 108989, Jan. 2021.

[239] S. Malaquin and J. Valette, "How modeling lactate diffusion may inform on its cellular compartmentation? An initial study," in *Proc. Intl. Soc. Mag. Reson. Med. 30*, 2022.

[240] S. E. Caudle, J. M. Katzenstein, S. Karpen, and V. McLin, "Developmental assessment of infants with biliary atresia: differences between boys and girls," *Journal of Pediatric Gastroenterology and Nutrition*, vol. 55, pp. 384–389, Oct. 2012.

[241] D. Le Bihan, "Looking into the functional architecture of the brain with diffusion MRI," *Nature Reviews Neuroscience*, vol. 4, pp. 469–480, June 2003.

[242] K. Nicolay, K. P. Braun, R. A. Graaf, R. M. Dijkhuizen, and M. J. Kruiskamp, "Diffusion NMR spectroscopy," *NMR in biomedicine*, vol. 14, pp. 94–111, Apr. 2001.

[243] I. Ronen and J. Valette, "Diffusion-Weighted Magnetic Resonance Spectroscopy," in *eMagRes*, pp. 733–750, American Cancer Society, 2015.

[244] G. Genovese, M. Marjańska, E. J. Auerbach, L. Y. Cherif, I. Ronen, S. Lehéricy, and F. Branzoli, "In vivo diffusion-weighted MRS using semi-LASER in the human brain at 3 T: Methodological aspects and clinical feasibility," *NMR in biomedicine*, vol. 34, p. e4206, May 2021.

[245] G. Zeng, R. Penninkilampi, J. Chaganti, S. Montagnese, B. J. Brew, and M. Danta, "Meta-analysis of magnetic resonance spectroscopy in the diagnosis of hepatic encephalopathy," *Neurology*, vol. 94, pp. e1147–e1156, Mar. 2020.

[246] L. Xin, B. Schaller, V. Mlynarik, H. Lu, and R. Gruetter, "Proton T1 relaxation times of metabolites in human occipital white and gray matter at 7 T," *Magnetic Resonance in Medicine*, vol. 69, pp. 931–936, Apr. 2013.

Bibliography

[247] A. Lin, O. Andronesi, W. Bogner, I.-Y. Choi, E. Coello, C. Cudalbu, C. Juchem, G. J. Kemp, R. Kreis, M. Krššák, P. Lee, A. A. Maudsley, M. Meyerspeer, V. Mlynarik, J. Near, G. Öz, A. L. Peek, N. A. Puts, E.-M. Ratai, I. Tkáč, P. G. Mullins, and Experts' Working Group on Reporting Standards for MR Spectroscopy, "Minimum Reporting Standards for in vivo Magnetic Resonance Spectroscopy (MRSinMRS): Experts' consensus recommendations," *NMR in biomedicine*, vol. 34, p. e4484, May 2021.

[248] H. Lei, L. Xin, R. Gruetter, and V. Mlynárik, "Chapter 1.2 - Localized Single-Voxel Magnetic Resonance Spectroscopy, Water Suppression, and Novel Approaches for Ultrashort Echo-Time Measurements," in *Magnetic Resonance Spectroscopy* (C. Stagg and D. Rothman, eds.), pp. 15–30, San Diego: Academic Press, Jan. 2014.

[249] G. Oz and I. Tkáč, "Short-echo, single-shot, full-intensity proton magnetic resonance spectroscopy for neurochemical profiling at 4 T: validation in the cerebellum and brainstem," *Magnetic Resonance in Medicine*, vol. 65, pp. 901–910, Apr. 2011.

[250] K. Şimşek, A. Döring, A. Pampel, H. E. Möller, and R. Kreis, "Macromolecular background signal and non-Gaussian metabolite diffusion determined in human brain using ultra-high diffusion weighting," *Magnetic Resonance in Medicine*, vol. 88, no. 5, pp. 1962–1977, 2022.

[251] M. Marjańska, E. J. Auerbach, R. Valabrègue, P.-F. Van de Moortele, G. Adriany, and M. Garwood, "Localized 1H NMR spectroscopy in different regions of human brain in vivo at 7 T: T2 relaxation times and concentrations of cerebral metabolites," *NMR in biomedicine*, vol. 25, pp. 332–339, Feb. 2012.

[252] T. W. J. Scheenen, D. W. J. Klomp, J. P. Wijnen, and A. Heerschap, "Short echo time 1H-MRSI of the human brain at 3T with minimal chemical shift displacement errors using adiabatic refocusing pulses," *Magnetic Resonance in Medicine*, vol. 59, pp. 1–6, Jan. 2008.

[253] A. Döring, V. Adalid, C. Boesch, and R. Kreis, "Diffusion-weighted magnetic resonance spectroscopy boosted by simultaneously acquired water reference signals," *Magnetic Resonance in Medicine*, vol. 80, no. 6, pp. 2326–2338, 2018.

[254] C. Diez-Fernandez, D. Hertig, M. Loup, G. Diserens, H. Henry, P. Vermathen, J.-M. Nuoffer, J. Häberle, and O. Braissant, "Argininosuccinate neurotoxicity and prevention by creatine in argininosuccinate lyase deficiency: An in vitro study in rat three-dimensional organotypic brain cell cultures," *Journal of Inherited Metabolic Disease*, vol. 42, pp. 1077–1087, Nov. 2019.

[255] J. Mosso, D. Simicic, K. Şimşek, R. Kreis, C. Cudalbu, and I. O. Jelescu, "MP-PCA denoising for diffusion MRS data: promises and pitfalls," *NeuroImage*, vol. 263, p. 119634, Nov. 2022.

[256] J. Veraart, D. S. Novikov, D. Christiaens, B. Ades-aron, J. Sijbers, and E. Fieremans, "Denoising of diffusion MRI using random matrix theory," *NeuroImage*, vol. 142, pp. 394–406, Nov. 2016.

[257] J. Veraart, E. Fieremans, and D. S. Novikov, "Diffusion MRI noise mapping using random matrix theory," *Magnetic Resonance in Medicine*, vol. 76, no. 5, pp. 1582–1593, 2016.

[258] R. A. d. Graaf, K. P. J. Braun, and K. Nicolay, "Single-shot diffusion trace 1H NMR spectroscopy," *Magnetic Resonance in Medicine*, vol. 45, no. 5, pp. 741–748, 2001.

[259] V. Rackayova, C. Cudalbu, P. J. W. Pouwels, and O. Braissant, "Creatine in the central nervous system: From magnetic resonance spectroscopy to creatine deficiencies," *Analytical Biochemistry*, vol. 529, pp. 144–157, July 2017.

[260] A. Ebel, W. Dreher, and D. Leibfritz, "Effects of zero-filling and apodization on spectral integrals in discrete Fourier-transform spectroscopy of noisy data," *Journal of Magnetic Resonance (San Diego, Calif.: 1997)*, vol. 182, pp. 330–338, Oct. 2006.

[261] J. R. Brender, S. Kishimoto, H. Merkle, G. Reed, R. E. Hurd, A. P. Chen, J. H. Ardenkjaer-Larsen, J. Munasinghe, K. Saito, T. Seki, N. Oshima, K. Yamamoto, P. L. Choyke, J. Mitchell, and M. C. Krishna, "Dynamic Imaging of Glucose and Lactate Metabolism by 13C-MRS without Hyperpolarization," *Scientific Reports*, vol. 9, p. 3410, Mar. 2019.

[262] O. Ahmed, "New denoising scheme for magnetic resonance spectroscopy signals," *IEEE Transactions on Medical Imaging*, vol. 24, pp. 809–816, June 2005.

[263] M. Goryawala, M. Sullivan, and A. A. Maudsley, "Effects of apodization smoothing and denoising on spectral fitting," *Magnetic Resonance Imaging*, vol. 70, pp. 108–114, July 2020.

[264] A. Abdoli, R. Stoyanova, and A. A. Maudsley, "Denoising of MR spectroscopic imaging data using statistical selection of principal components," *Magma (New York, N.Y.)*, vol. 29, pp. 811–822, Dec. 2016.

[265] H. M. Nguyen, X. Peng, M. N. Do, and Z.-P. Liang, "Denoising MR Spectroscopic Imaging Data With Low-Rank Approximations," *IEEE transactions on bio-medical engineering*, vol. 60, pp. 78–89, Jan. 2013.

[266] W. T. Clarke and M. Chiew, "Uncertainty in denoising of MRSI using low-rank methods," *Magnetic Resonance in Medicine*, vol. 87, no. 2, pp. 574–588, 2022.

[267] A. Klauser, S. Courvoisier, J. Kasten, M. Kocher, M. Guerquin-Kern, D. Van De Ville, and F. Lazeyras, "Fast high-resolution brain metabolite mapping on a clinical 3T MRI by accelerated 1H-FID-MRSI and low-rank constrained reconstruction," *Magnetic Resonance in Medicine*, vol. 81, Dec. 2018.

[268] D. Simicic, J. Mosso, T. P. Lê, R. v. Heeswijk, I. O. Jelescu, and C. Cudalbu, "The impact of Marchenko-Pastur PCA denoising on high resolution MRSI in the rat brain at 9.4T," in *Proc. Intl. Soc. Mag. Reson. Med. 29*, 2021.

[269] F. Knoll, K. Bredies, T. Pock, and R. Stollberger, "Second Order Total Generalized Variation (TGV) for MRI," *Magnetic resonance in medicine : official journal of the Society of Magnetic Resonance in Medicine / Society of Magnetic Resonance in Medicine*, vol. 65, pp. 480–491, Feb. 2011.

[270] W. W. F. Pijnappel, A. van den Boogaart, R. de Beer, and D. van Ormondt, "SVD-based quantification of magnetic resonance signals," *Journal of Magnetic Resonance*, vol. 97, pp. 122–134, Jan. 1992.

[271] B. C. Rowland, L. Sreepada, and A. P. Lin, "A comparison of denoising methods in dynamic MRS using pseudo-synthetic data," tech. rep., Feb. 2021. Company: Cold Spring Harbor Laboratory Press Distributor: Cold Spring Harbor Laboratory Press Label: Cold Spring Harbor Laboratory Press Type: article.

[272] M. Doyle, B. L. Chapman, G. Blackwell, E. G. Walsh, and G. M. Pohost, "Adaptive Fourier threshold filtering: a method to reduce noise and incoherent artifacts in high resolution cardiac images," *Magnetic Resonance in Medicine*, vol. 31, pp. 546–550, May 1994.

[273] Y. Lei, B. Ji, T. Liu, W. J. Curran, H. Mao, and X. Yang, "Deep learning-based denoising for magnetic resonance spectroscopy signals," in *Medical Imaging 2021: Biomedical Applications in Molecular, Structural, and Functional Imaging*, vol. 11600, pp. 16–21, SPIE, Feb. 2021.

[274] M. Dziadosz, R. Rizzo, S. P. Kyathanahally, and R. Kreis, "Denoising 1H MR spectra in a time–frequency representation by deep learning," in *ESMRMB 38th Annual Scientific Meeting*, 2021.

[275] B. Ades-Aron, G. Lemberskiy, J. Veraart, J. Golfinos, E. Fieremans, D. S. Novikov, and T. Shepherd, "Improved Task-based Functional MRI Language Mapping in Patients with Brain Tumors through Marchenko-Pastur Principal Component Analysis Denoising," *Radiology*, vol. 298, pp. 365–373, Feb. 2021.

[276] Y. Diao, T. Yin, R. Gruetter, and I. O. Jelescu, "PIRACY: An Optimized Pipeline for Functional Connectivity Analysis in the Rat Brain," *Frontiers in Neuroscience*, vol. 15, p. 285, 2021.

[277] M. D. Does, J. L. Olesen, K. D. Harkins, T. Serradas-Duarte, D. F. Gochberg, S. N. Jespersen, and N. Shemesh, "Evaluation of principal component analysis image denoising on multi-exponential MRI relaxometry," *Magnetic Resonance in Medicine*, vol. 81, no. 6, pp. 3503–3514, 2019.

[278] M. Froeling, J. Prompers, D. Klomp, and T. Van der Velden, "PCA denoising and Wiener deconvolution of 31P 3D CSI data to enhance effective SNR and improve point spread function," *Magnetic Resonance in Medicine*, vol. 85, Feb. 2021.

[279] S. Moeller, P. K. Pisharady, S. Ramanna, C. Lenglet, X. Wu, L. Dowdle, E. Yacoub, K. Uğurbil, and M. Akçakaya, "NOise reduction with DIstribution Corrected (NORDIC) PCA in dMRI with complex-valued parameter-free locally low-rank processing," *NeuroImage*, vol. 226, p. 117539, Feb. 2021.

[280] M. Gavish and D. Donoho, "Optimal Shrinkage of Singular Values," *IEEE Transactions on Information Theory*, vol. 63, no. 4, pp. 2137–2152, 2017.

[281] I. M. Johnstone and D. Paul, "PCA in High Dimensions: An orientation," *Proceedings of the IEEE. Institute of Electrical and Electronics Engineers*, vol. 106, pp. 1277–1292, Aug. 2018.

[282] X. Ma, K. Uğurbil, and X. Wu, "Denoise magnitude diffusion magnetic resonance images via variance-stabilizing transformation and optimal singular-value manipulation," *NeuroImage*, vol. 215, p. 116852, July 2020.

[283] M. Marjańska, D. K. Deelchand, R. Kreis, and 2016 ISMRM MRS Study Group Fitting Challenge Team, "Results and interpretation of a fitting challenge for MR spectroscopy set up by the MRS study group of ISMRM," *Magnetic Resonance in Medicine*, vol. 87, pp. 11–32, Jan. 2022.

[284] R. Gruetter and I. Tkác, "Field mapping without reference scan using asymmetric echo-planar techniques," *Magnetic Resonance in Medicine*, vol. 43, pp. 319–323, Feb. 2000.

Bibliography

[285] G. Oz, I. Tkác, L. R. Charnas, I. Y. Choi, K. J. Bjoraker, E. G. Shapiro, and R. Gruetter, "Assessment of adrenoleukodystrophy lesions by high field MRS in non-sedated pediatric patients," *Neurology*, vol. 64, pp. 434–441, Feb. 2005.

[286] R. Stoyanova and T. Brown, "NMR spectral quantitation by principal component analysis - III. A generalized procedure for determination of lineshape variations," *Journal of magnetic resonance (San Diego, Calif. : 1997)*, vol. 154, pp. 163–75, Mar. 2002.

[287] T. Brown and R. Stoyanova, "NMR spectral quantitation by principal-component analysis. II. Determination of frequency and phase shifts.," *Journal of magnetic resonance. Series B*, 1996.

[288] V. Adalid, A. Döring, S. P. Kyathanahally, C. S. Bolliger, C. Boesch, and R. Kreis, "Fitting interrelated datasets: metabolite diffusion and general lineshapes," *Magma (New York, N.Y.)*, vol. 30, pp. 429–448, Oct. 2017.

[289] C. Najac, A. Döring, W. Clarke, G. Genovese, N. Just, R. Kreis, H. Lundell, J. Mosso, H. Mougel, G. Oeltzschner, M. Palombo, and C. Ligneul, "Differences in diffusion-weighted MRS processing and fitting pipelines, and their effect on tissue modeling: Results from a workshop challenge," in *Proc. Intl. Soc. Mag. Reson. Med. 30*, 2022.

[290] W. Clarke, C. Ligneul, M. Cottaar, and S. Jbabdi, "Dynamic fitting of functional MRS, diffusion weighted MRS, and edited MRS using a single interface," in *Proc. Intl. Soc. Mag. Reson. Med. 30*, 2022.

[291] M. Dziadosz, R. Rizzo, S. P. Kyathanahally, and R. Kreis, "Denoising single MR spectra by deep learning: Miracle or mirage?," *Magnetic Resonance in Medicine*, vol. 90, no. 5, pp. 1749–1761, 2023.

[292] N. V. Christensen, M. Vaeggemose, N. Bøgh, E. S. S. Hansen, J. L. Olesen, Y. Kim, D. B. Vigneron, J. W. Gordon, S. N. Jespersen, and C. Laustsen, "A user independent denoising method for x-nuclei MRI and MRS," *Magnetic Resonance in Medicine*, vol. n/a, no. n/a, 2023.

[293] B. Lanz, C. Poitry-Yamate, and R. Gruetter, "Image-derived input function from the vena cava for 18F-FDG PET studies in rats and mice," *Journal of Nuclear Medicine: Official Publication, Society of Nuclear Medicine*, vol. 55, pp. 1380–1388, Aug. 2014.

[294] B. Lanz, *Mathematical Modeling of Brain Energy Metabolism, Measured with PET and MRS in Rodents.* PhD thesis, EPFL, 2012.

[295] J. J. Vaquero and P. Kinahan, "Positron Emission Tomography: Current Challenges and Opportunities for Technological Advances in Clinical and Preclinical Imaging Systems," *Annual Review of Biomedical Engineering*, vol. 17, no. 1, pp. 385–414, 2015.

[296] Y. F. Tai and P. Piccini, "Applications of positron emission tomography (PET) in neurology," *Journal of Neurology, Neurosurgery, and Psychiatry*, vol. 75, pp. 669–676, May 2004.

[297] J. W. Fletcher, B. Djulbegovic, H. P. Soares, B. A. Siegel, V. J. Lowe, G. H. Lyman, R. E. Coleman, R. Wahl, J. C. Paschold, N. Avril, L. H. Einhorn, W. W. Suh, D. Samson, D. Delbeke, M. Gorman, and A. F. Shields, "Recommendations on the Use of 18F-FDG PET in Oncology," *Journal of Nuclear Medicine*, vol. 49, pp. 480–508, Mar. 2008.

[298] P. A. Rowley, A. A. Samsonov, T. J. Betthauser, A. Pirasteh, S. C. Johnson, and L. B. Eisenmenger, "Amyloid and Tau PET Imaging of Alzheimer Disease and Other Neurodegenerative Conditions," *Seminars in ultrasound, CT, and MR*, vol. 41, pp. 572–583, Dec. 2020.

[299] L. Wahl and C. Nahmias, "Modeling of Fluorine-18-6-Fluoro-L-Dopa in Humans," *Journal of Nuclear Medicine*, vol. 37, pp. 432–437, Mar. 1996.

[300] V. Berti, E. Vanzi, C. Polito, and A. Pupi, "Back to the future: the absolute quantification of cerebral metabolic rate of glucose," *Clinical and Translational Imaging*, vol. 1, pp. 289–296, Aug. 2013.

[301] R. Gruetter, "Automatic, localized in vivo adjustment of all first- and second-order shim coils," *Magnetic Resonance in Medicine*, vol. 29, pp. 804–811, June 1993.

[302] S. W. Provencher, "Estimation of metabolite concentrations from localized in vivo proton NMR spectra," *Magnetic Resonance in Medicine*, vol. 30, pp. 672–679, Dec. 1993.

[303] C. Cudalbu, V. Mlynárik, and R. Gruetter, "Handling macromolecule signals in the quantification of the neurochemical profile," *Journal of Alzheimer's disease: JAD*, vol. 31 Suppl 3, pp. S101–115, 2012.

[304] V. Selivanov, Y. Picard, J. Cadorette, S. Rodrigue, and R. Lecomte, "Detector response models for statistical iterative image reconstruction in high resolution PET," *Nuclear Science, IEEE Transactions on*, vol. 47, pp. 1168–1175, July 2000.

[305] H.-M. Wu, G. Sui, C.-C. Lee, M. L. Prins, W. Ladno, H.-D. Lin, A. S. Yu, M. E. Phelps, and S.-C. Huang, "In Vivo Quantitation of Glucose Metabolism in Mice Using Small-Animal PET and a Microfluidic Device," *Journal of Nuclear Medicine*, vol. 48, pp. 837–845, Jan. 2007.

[306] R. W. Horton, B. S. Meldrum, and H. S. Bachelard, "ENZYMIC AND CEREBRAL METABOLIC EFFECTS OF 2-DEOXY-d-GLUCOSE," *Journal of Neurochemistry*, vol. 21, no. 3, pp. 507–520, 1973.

[307] A. Sols and R. K. Crane, "Substrate specificity of brain hexokinase," *The Journal of Biological Chemistry*, vol. 210, pp. 581–595, Oct. 1954.

[308] J. Tokugawa, L. Ravasi, T. Nakayama, K. C. Schmidt, and L. Sokoloff, "Operational Lumped Constant for FDG in Normal Adult Male Rats," *Journal of Nuclear Medicine*, vol. 48, pp. 94–99, Jan. 2007.

[309] R. P. Woods, S. R. Cherry, and J. C. Mazziotta, "Rapid automated algorithm for aligning and reslicing PET images," *Journal of Computer Assisted Tomography*, vol. 16, no. 4, pp. 620–633, 1992.

[310] E. A. Papp, T. B. Leergaard, E. Calabrese, G. A. Johnson, and J. G. Bjaalie, "Waxholm Space atlas of the Sprague Dawley rat brain," *NeuroImage*, vol. 97, pp. 374–386, Aug. 2014.

[311] B. B. Avants, N. J. Tustison, G. Song, P. A. Cook, A. Klein, and J. C. Gee, "A reproducible evaluation of ANTs similarity metric performance in brain image registration," *NeuroImage*, vol. 54, pp. 2033–2044, Feb. 2011.

[312] T. Boehler, D. van Straaten, S. Wirtz, and H.-O. Peitgen, "A robust and extendible framework for medical image registration focused on rapid clinical application deployment," *Computers in Biology and Medicine*, vol. 41, pp. 340–349, June 2011.

[313] J. H. Bothwell, C. Rae, R. M. Dixon, P. Styles, and K. K. Bhakoo, "Hypo-osmotic swelling-activated release of organic osmolytes in brain slices: implications for brain oedema in vivo," *Journal of Neurochemistry*, vol. 77, no. 6, pp. 1632–1640, 2001.

[314] H. Pasantes-Morales and A. Schousboe, "Role of taurine in osmoregulation in brain cells: Mechanisms and functional implications," *Amino Acids*, vol. 12, pp. 281–292, Sept. 1997.

[315] E. Flatt, O. Braissant, S. Mitrea, D. Sessa, P. Mastromarino, R. Gruetter, V. A. McLin, and C. Cudalbu, "P: 37 Probiotics Combined With Rifaximin for the Treatment of Chronic Hepatic Encephalopathy: A Longitudinal In Vivo 1H-MRS Study of Brain Metabolism Using BDL Rats," *Official journal of the American College of Gastroenterology | ACG*, vol. 114, p. S19, Sept. 2019.

[316] P. Ott and H. Vilstrup, "Cerebral effects of ammonia in liver disease: current hypotheses," *Metabolic Brain Disease*, vol. 29, pp. 901–911, Dec. 2014.

[317] O. Cauli, M. T. Mansouri, A. Agusti, and V. Felipo, "Hyperammonemia increases GABAergic tone in the cerebellum but decreases it in the rat cortex," *Gastroenterology*, vol. 136, pp. 1359–1367, e1–2, Apr. 2009.

[318] V. Felipo, "Hepatic encephalopathy: effects of liver failure on brain function," *Nature Reviews Neuroscience*, vol. 14, pp. 851–858, Dec. 2013.

[319] K. Pierzchala, D. Simicic, V. Rackaova, D. Sessa, A. Sienkiewicz, O. Braissant, V. Mclin, R. Gruetter, and C. Cudalbu, "P: 68 Brain Regional Susceptibility to Oxidative Stress in a Rat Model of Chronic Hepatic Encephalopathy," *The American Journal of Gastroenterology*, vol. 114, pp. S33–S36, Sept. 2019.

[320] R. Gruetter, E. J. Novotny, S. D. Boulware, D. L. Rothman, and R. G. Shulman, "1H NMR Studies of Glucose Transport in the Human Brain," *Journal of Cerebral Blood Flow & Metabolism*, vol. 16, pp. 427–438, May 1996.

[321] R. Gruetter, K. Ugurbil, and E. R. Seaquist, "Steady-state cerebral glucose concentrations and transport in the human brain," *Journal of Neurochemistry*, vol. 70, pp. 397–408, Jan. 1998.

[322] L. Baker, B. Lanz, F. Andreola, J. Ampuero, A. Wijeyesekera, E. Holmes, and N. Deutz, "New technologies – new insights into the pathogenesis of hepatic encephalopathy," *Metabolic Brain Disease*, vol. 31, Dec. 2016.

[323] A. H. Lockwood, B. W. Murphy, K. Z. Donnelly, T. C. Mahl, and S. Perini, "Positron-emission tomographic localization of abnormalities of brain metabolism in patients with minimal hepatic encephalopathy," *Hepatology (Baltimore, Md.)*, vol. 18, pp. 1061–1068, Nov. 1993.

[324] M. Dixon and E. C. Webb, *Enzymes - 2nd Edition*. Academic Press, Jan. 1964.

[325] P. Linardatos, V. Papastefanopoulos, and S. Kotsiantis, "Explainable AI: A Review of Machine Learning Interpretability Methods," *Entropy (Basel, Switzerland)*, vol. 23, p. 18, Dec. 2020.

[326] G. E. Karniadakis, I. G. Kevrekidis, L. Lu, P. Perdikaris, S. Wang, and L. Yang, "Physics-informed machine learning," *Nature Reviews Physics*, vol. 3, pp. 422–440, June 2021.

Bibliography

[327] G. Wu, J. R. Lupton, N. D. Turner, Y.-Z. Fang, and S. Yang, "Glutathione Metabolism and Its Implications for Health," *The Journal of Nutrition*, vol. 134, pp. 489–492, Mar. 2004.

[328] O. W. Griffith, "Biologic and pharmacologic regulation of mammalian glutathione synthesis," *Free Radical Biology & Medicine*, vol. 27, pp. 922–935, Nov. 1999.

[329] L. Wang, Y. J. Ahn, and R. Asmis, "Sexual dimorphism in glutathione metabolism and glutathione-dependent responses," *Redox Biology*, vol. 31, p. 101410, Dec. 2019.

[330] S. P. Raps, J. C. Lai, L. Hertz, and A. J. Cooper, "Glutathione is present in high concentrations in cultured astrocytes but not in cultured neurons," *Brain Research*, vol. 493, pp. 398–401, July 1989.

[331] T. K. Makar, M. Nedergaard, A. Preuss, A. S. Gelbard, A. S. Perumal, and A. J. Cooper, "Vitamin E, ascorbate, glutathione, glutathione disulfide, and enzymes of glutathione metabolism in cultures of chick astrocytes and neurons: evidence that astrocytes play an important role in antioxidative processes in the brain," *Journal of Neurochemistry*, vol. 62, pp. 45–53, Jan. 1994.

[332] J. L. Olesen, A. Ianus, L. Østergaard, N. Shemesh, and S. N. Jespersen, "Tensor denoising of multidimensional MRI data," *Magnetic Resonance in Medicine*, vol. 89, pp. 1160–1172, Mar. 2023.

[333] R. M. Shansky and A. Z. Murphy, "Considering sex as a biological variable will require a global shift in science culture," *Nature Neuroscience*, vol. 24, pp. 457–464, Apr. 2021.

[334] J. S. Mogil, "Sex differences in pain and pain inhibition: multiple explanations of a controversial phenomenon," *Nature Reviews Neuroscience*, vol. 13, pp. 859–866, Dec. 2012.

[335] F. Mauvais-Jarvis, "Sex differences in metabolic homeostasis, diabetes, and obesity," *Biology of Sex Differences*, vol. 6, p. 14, Sept. 2015.

[336] J. B. Rubin, V. Sundaram, and J. C. Lai, "Gender differences among patients hospitalized with cirrhosis in the United States," *Journal of clinical gastroenterology*, vol. 54, pp. 83–89, Jan. 2020.

[337] J. B. Becker, B. J. Prendergast, and J. W. Liang, "Female rats are not more variable than male rats: a meta-analysis of neuroscience studies," *Biology of Sex Differences*, vol. 7, p. 34, July 2016.

[338] B. J. Prendergast, K. G. Onishi, and I. Zucker, "Female mice liberated for inclusion in neuroscience and biomedical research," *Neuroscience and Biobehavioral Reviews*, vol. 40, pp. 1–5, Mar. 2014.

[339] T. Buch, K. Moos, F. M. Ferreira, H. Fröhlich, C. Gebhard, and A. Tresch, "Benefits of a factorial design focusing on inclusion of female and male animals in one experiment," *Journal of Molecular Medicine*, vol. 97, pp. 871–877, June 2019.

Jessie Mosso

jessie.mosso@epfl.ch **–** Date of birth: July 2 1995
Residence: Switzerland - French citizenship
ORCID: https://orcid.org/0000-0001-6318-9507, Google Scholar: Jessie Mosso

Education

PhD – Ecole Polytechnique Fédérale de Lausanne (EPFL) - *Lausanne, Switzerland* *Center for Biomedical Imaging (CIBM) and Laboratory for Functional and Metabolic Imaging (LIFMET)* Physics doctoral program, EU Horizon 2020 - Marie Sklodowska-Curie 813120 (INSPiRE-MED) Thesis: New insights into rodent brain microstructure and metabolism in hepatic encephalopathy PhD supervisors: Dr Cristina Cudalbu and Pr. Rolf Gruetter	2019 - 2023
Master's degree – Neuroscience, Sorbonne Université - *Paris, France* Cognitive and behavioral neuroscience, neurological and psychiatric disorders, neuron-glia interactions, pharmacological approaches in neuroscience	2018 - 2019

Graduate engineering school's degree – ESPCI - *Paris, France*
Ecole **S**upérieure de **P**hysique et de **C**himie **I**ndustrielles de la ville de Paris (**ESPCI**): graduate engineering school of Physics, Chemistry and Biology and a founding member of a top French graduate network: the research-focused Paris Sciences et Lettres (PSL) (*www.parissciencesetlettres.org*)
     - Master-level diplôme d'ingénieur ESPCI Paris in January 2019
     - Advanced Master of Science and Technology in June 2019, Major: Physics
	2015 - 2019

Undergraduate preparatory course - *Orsay, France* French classes préparatoires aux grandes écoles, MPSI/MP* course Selective, intensive, high level preparation in Mathematics and Physics for the nationwide competitive entrance exams to French graduate schools	2013 - 2015
International Baccalaureate (OIB), Science major - *Luynes, France* Awarded with first class honors	2010 - 2013
CAE: Certificate of Advanced English, Cambridge exams	2012
IGCSEs: International General Certificate of Secondary Education in Mathematics and Human biology	2010

Experience

Teaching

- Teaching Assistant at EPFL, Switzerland Mechanics, Electromagnetism, Thermodynamics, Fundamentals of biomedical imaging	2019-2023
- Training of PhD students at EPFL: Brayan Alves and Jan Luxembourg	2021-2022
- Private tuition in Mathematics, Physics, Chemistry to high school and undergraduate students (4 hours a week)	2015-2018

Supervision of master students

- Supervision of 3 master students for semester projects at EPFL: Mickael Rey: "Combined DW-MRI and DW-MRS modelling for type C hepatic encephalopathy" Michael Chan: "Methods for time exchange estimation by diffusion MRI and diffusion MRS modelling for type C hepatic encephalopathy" David Bekri: "An innovative and interoperable toolbox for the co-registration of preclinical PET and MRI data"	2021-2022

Research intern – Ecole Normale Superieure (ENS) – *Paris, France* *Biomolecules structure and dynamics laboratory* Optimization of dissolution DNP methods to probe metabolic regulation of the pentose phosphate pathway, glycolysis and urea cycle in bacteria and neuroinflammatory cells' suspensions using hyperpolarized MRS (6 months)	2019

<u>Title</u>: Dynamic imaging of glucose metabolism in cell systems using dissolution dynamic nuclear polarization
<u>Supervisor</u>: Dr Daniel Abergel

Research intern – University of California, San Francisco (UCSF) – *San Francisco, United States*   2018
Chaumeil laboratory
Comparison of metabolic activity of neuroinflammatory cells and cancer cells in the context of brain tumors using hyperpolarized MRS in a bioreactor set-up (4 months)
<u>Title</u>: Hyperpolarized Magnetic Resonance Spectroscopy for the study of neuroinflammation in brain tumors
<u>Supervisor</u>: Pr. Myriam Chaumeil

Research intern - Institute of Myology - *Paris, France*   2017
Neuromuscular physiology laboratory – Pitié-Salpétrière Hospital
Design, testing and implementation of a new method to evaluate muscle cross-sectional area using bio impedance analysis, comparison with MRI T1-mapping standards (6 months)
<u>Title:</u> Evaluation of a leg muscle contractile cross-sectional area by bioimpedance analysis
<u>Supervisors</u>: Dr Jean-Yves Hogrel and Dr Damien Bachasson

Research projects
- <u>1st year project at ESPCI</u>: electrical bridge between neural cultures *in vitro* on gold electrodes   2015 - 2016
- <u>Prep classes project</u>: algorithm of neural networks (Python) for road signs detection   2014 - 2015
- <u>High school project</u>: memory and learning in mice, investigation in biochemistry and   2012 - 2013
  neurodegenerative diseases

Long term cultural exchange – *Melbourne, Australia*   2011
Geelong Grammar School, Science and English literature classes (4 months)

Scientific events organization

Local organizing committee – Magnetic Resonance Spectroscopy workshop - *Lausanne, Switzerland*   2022
"Overcoming the barriers to clinical use"
Organization of the workshop for 150 people at EPFL

Local organizing committee – INSPiRE-MED annual meeting - *Lausanne, Switzerland*   2022
Organization of the meeting for 50 people at EPFL

Volunteering

Volunteer work – Red Cross - *Paris, France*   2017 – 2019
Social actions in the Invalides National Institution (INI), looking after residents of a retirement home and a hospital, creating social link and physical support, organizing social events

Volunteer work – Humans for women (NGO) - *Paris, France*   2019
French private tuitions to exiled women (2 hours a week)
http://www.humansforwomen.org/

Languages and skills

English	Fluent – CAE level (2012)
	TOEFL – 105 (Listening: 25, Reading: 30, Writing: 27, Speaking: 23)
	TOEIC – 975 (Reading: 485/495, Listening: 490/495)
French	Mother tongue
Spanish	Basic skills
Computer skills	Expertise in Python and Matlab
	Expertise in Bruker MR sequence programming
	Basic skills in C and R-Studio
Trainings	Advanced Imaging Course (ParaVision) BRUKER
	ParaVision programming course BRUKER (Aquistion Parameters, Pulse Programming, Method Programming and Reconstruction Programming)
	English Academic Writing for Doctoral Students (Level C2)
	RESAL Module 1: Introductory Course in Laboratory Animal Science
	MINTT, EPFL: Management of Innovation and technology transfer

Scholarships and awards

Monahan Foundation Excellence Scholarship, US-France Fulbright commission	April 2019
Magma Cum Laude award, oral presentation, ISMRM	May 2021
ISMRM travel stipends	2020, 2021, 2022

Collaborators – PhD work

Dr Bernard Lanz (EPFL): PET, MR sequence design, metabolic modelling

Dr Katarzyna Pierzchala (EPFL): histology and biology of hepatic encephalopathy

Dr Julien Valette (CEA, Paris, France): diffusion-weighted MRS acquisitions

Pr. Ileana Jelescu (CHUV and UNIL, Lausanne, Switzerland): diffusion-weighted MRI acquisition and modelling, denoising

Pr. Olivier Braissant (UNIL, Lausanne, Switzerland) and Pr. Valérie A. McLin (UNIGE and HUG, Geneva, Switzerland): biology and clinical aspects of hepatic encephalopathy

Pr. Roland Kreis (University of Bern, Switzerland): MRS processing/denoising, diffusion-weighted MRS acquisitions

Invited talks

1. CIBM Breakfast and Science Seminar - *New insights into brain energy metabolism in type C hepatic encephalopathy: a dual 18F-FDG PET and 9.4T 1H MRS preclinical study*, August 2021

2. PET/MRI scientific interest group of the International Society of Blood Flow and Metabolism - *Quantitative FDG PET and 1H MRS reveal altered glucose uptake and neurometabolic profiles in BDL rats*, July 2022

3. Center for advanced imaging innovation and research, Radiology Department, New York University Langone Health, *Diffusion-Weighted MRS and 18F-FDG PET Probe Brain Microstructure and Energy Metabolism Alterations in a Rat Model of Hepatic Encephalopathy*, June 2023, post-doctoral interview

List of publications

Journal articles from PhD work - *published*:

1. **Jessie Mosso**, Dunja Simicic, Bernard Lanz, Rolf Gruetter, and Cristina Cudalbu. « Diffusion-weighted SPECIAL improves the detection of J-coupled metabolites at ultra high magnetic field ». *Magnetic Resonance in Medecine* 91 (2024):4-18. https://doi.org/10.1002/mrm.29805.

2. Clémence Ligneul, Chloé Najac, André Döring, Christian Beaulieu, Francesca Branzoli, William T. Clarke, Cristina Cudalbu, et al. « Diffusion-weighted MR spectroscopy: consensus, recommendations and resources from acquisition to modelling ». Accepted in *Magnetic Resonance in Medecine* (2024) https://doi.org/10.1002/mrm.29877.

3. Katarzyna Pierzchala, Anna Hadjihambi, **Jessie Mosso**, Rajiv Jalan, Christopher F. Rose, and Cristina Cudalbu. « Lessons on Brain Edema in HE: From Cellular to Animal Models and Clinical Studies ». *Metabolic Brain Disease* (2023). https://doi.org/10.1007/s11011-023-01269-5.

4. **Jessie Mosso**, Dunja Simicic, Kadir Şimşek, Roland Kreis, Cristina Cudalbu, and Ileana O. Jelescu. « MP-PCA Denoising for Diffusion MRS Data: Promises and Pitfalls ». *NeuroImage* 263 (2022): 119634. https://doi.org/10.1016/j.neuroimage.2022.119634.

5. **Jessie Mosso**, Ting Yin, Carole Poitry-Yamate, Dunja Simicic, Mario Lepore, Valérie A. McLin, Olivier Braissant, Cristina Cudalbu, and Bernard Lanz. « PET CMRglc Mapping and 1H-MRS Show Altered Glucose Uptake and Neurometabolic Profiles in BDL Rats ». *Analytical Biochemistry* 647 (2022): 114606. https://doi.org/10.1016/j.ab.2022.114606.

Journal articles anterior to PhD work - *published*:

1. Damien Bachasson, Alper Carras Ayaz, **Jessie Mosso**, Aurélie Canal, Jean-Marc Boisserie, Ericky Caldas, Olivier Benveniste, Harmen Reyngoudt, Benjamin Marty, Pierre G. Carlier, and Jean-Yves Hogrel. « Lean regional muscle volume estimates using explanatory

bioelectrical models in healthy subjects and patients with muscle wasting ». *Journal of Cachexia, Sarcopenia and Muscle* (2020). https://doi.org/10.1002/jcsm.12656

Journal articles from PhD work - *under review*:

1. Dunja Simicic, Brayan Alves, **Jessie Mosso**, Guillaume Briand, Thanh Phong Lê, Ruud B. van Heeswijk, Jana Starčuková, Bernard Lanz, Antoine Klauser, Bernhard Strasser, Wolfgang Bogner, Cristina Cudalbu. « Fast high-resolution metabolite mapping in the rat brain using 1H-FID-MRSI at 14.1T ». Under revision in *NMR in Biomedecine* (July 2023).

2. Brayan Alves, Dunja Simicic, **Jessie Mosso**, Thanh Phong Lê, Guillaume Briand, Wolfgang Bogner, Bernard Lanz, Bernhard Strasser, Antoine Klauser, Cristina Cudalbu. « Noise-reduction techniques for 1H-FID-MRSI at 14.1T: Monte-Carlo validation and in vivo application ». Under revision in *NMR in Biomedecine* (July 2023).

Journal articles from PhD work - *in preparation*:

1. **Jessie Mosso**, Michael Chan, Mickael Rey, Katarzyna Pierzchala, Dario Sessa, Dunja Simicic, Julien Valette, Ileana Jelescu, and Cristina Cudalbu. « Diffusion-weighted MRS and MRI probe brain cells alterations in the developing brain of a rat model of hepatic encephalopathy ».

2. **Jessie Mosso**, Guillaume Briand, Katarzyna Pierzchala, Dunja Simicic, Bernard Lanz, Ileana Jelescu, and Cristina Cudalbu. « Diffusion of brain metabolites highlights altered brain microstructure in chronic hepatic encephalopathy: a 9.4T preliminary study ».

Conference proceedings (7 oral presentations out of 9 first-author abstracts):

1. **Jessie Mosso**, Ting Yin, Carole Poitry-Yamate, Dunja Simicic, Mario Lepore, Valérie A. McLin, Olivier Braissant, Cristina Cudalbu, and Bernard Lanz. « A dual 9.4T 1H MRS and 18F-FDG PET study probes impaired neurometabolic profiles and brain glucose uptake in a rat model of type C hepatic encephalopathy ». Accepted – *ESMRMB*, 2023 **– oral**

2. **Jessie Mosso**, Dunja Simicic, Bernard Lanz, Rolf Gruetter, and Cristina Cudalbu. « DW-SPECIAL: a new sequence for rodent diffusion-weighted MRS at high magnetic field ». Accepted – *ESMRMB*, 2023 **– oral**

3. Brayan Alves, Dunja Simicic, **Jessie Mosso**, Thanh Phong Lê, Bernhard Strasser, Antoine

Klauser, and Cristina Cudalbu. « Effect of MP-PCA & Low Rank-TGV noise reduction techniques on preclinical 1H-MRSI: A study on in vivo metabolite concentrations distribution and Monte-Carlo simulations ». Accepted – *ESMRMB*, 2023

4. Katarzyna Pierzchala, **Jessie Mosso**, Dunja Simicic, Dario Sessa, Olivier Braissant, Valérie A. McLin, and Cristina Cudalbu. « Liver disfunction: An increasing risk of Alzheimer's disease? ». Accepted – *ESMRMB*, 2023

5. **Jessie Mosso**, Ting Yin, Carole Poitry-Yamate, Dunja Simicic, Mario Lepore, Valérie A. McLin, Olivier Braissant, Cristina Cudalbu, and Bernard Lanz. « New insights into brain energy metabolism in type C hepatic encephalopathy: a dual 18F-FDG PET and 9.4T 1H MRS preclinical study ». Accepted – *ISHEN*, 2023 **– oral**

6. **Jessie Mosso**, Dunja Simicic, Bernard Lanz, Rolf Gruetter, and Cristina Cudalbu. « Improved glutamine detection using diffusion-weighted SPECIAL at 14.1T ». *In Proc. Intl. Soc. Mag. Reson. Med. 31*, 2023.

7. **Jessie Mosso**, Mickaël Rey, Dunja Simicic, Katarzyna Pierzchala, Ileana O. Jelescu, and Cristina Cudalbu. « Diffusion MRI and MRS probe cerebellar microstructure alterations in the rat developing brain during hepatic encephalopathy ». *In Proc. Intl. Soc. Mag. Reson. Med. 30*, 2022. **– oral**

8. Chloé Najac, André Döring, William Clarke, Guglielmo Genovese, Natalie Just, Roland Kreis, Henrik Lundell, et al. « Differences in diffusion-weighted MRS processing and fitting pipelines, and their effect on tissue modeling: Results from a workshop challenge ». *In Proc. Intl. Soc. Mag. Reson. Med. 30*, 2022.

9. Dunja Simicic, Brayan Alves, **Jessie Mosso**, Thanh P. Lê, Ruud B. van Heeswijk, Jana Starcukova, Antoine Klauser, Bernhard Strasser, Wolfgang Bogner, and Cristina Cudalbu. « Fast high-resolution metabolite mapping on a preclinical 14.1T scanner using 1H-FIDMRSI». *Proc. Intl. Soc. Mag. Reson. Med. 30*, 2022. **– oral**

10. Brayan Alves, Dunja Simicic, **Jessie Mosso**, Ileana O. Jelescu, Cristina Cudalbu, et Antoine Klauser. « MP-PCA and Low-rank noise-reduction in 1H-FID-MRSI data in the rat brain at 14.1T ». *Proc. Intl. Soc. Mag. Reson. Med. 30*, 2022.

11. **Jessie Mosso**, Ting Yin, Carole Poitry-Yamate, Dunja Simicic, Mario Lepore, Valérie A. McLin, Olivier Braissant, Cristina Cudalbu, and Bernard Lanz. « Quantitative FDG-PET and 1H-MRS reveal altered glucose uptake and neurometabolic profiles in BDL rats », *Brain and Brain PET*, 2022. **– oral**

12. **Jessie Mosso**, Michael Chan, Mickael Rey, Ileana O. Jelescu, Cristina Cudalbu. «Exploiting dual diffusion MRS and MRI acquisitions in the rat cerebellum at 14.1 T: a measurement of intra-extracellular water exchange ». *MRS Workshop*, 2022

13. **Jessie Mosso**, Julien Valette, Katarzyna Pierzchala, Dunja Simicic, Ileana Ozana Jelescu, and Cristina Cudalbu. « Diffusion-weighted magnetic resonance spectroscopy in the cerebellum of a rat model of hepatic encephalopathy at 14.1T ». *Proc. Intl. Soc. Mag. Reson. Med. 29*, 2021 – **Magma Cum Laude award – oral**

14. Dunja Simicic, **Jessie Mosso**, Thanh P. Lê, Ruud van Heeswijk, Ileana O. Jelescu, and Cristina Cudalbu. « The impact of Marchenko-Pastur PCA denoising on high resolution MRSI in the rat brain at 9.4T ». *Proc. Intl. Soc. Mag. Reson. Med. 29*, 2021.

15. **Jessie Mosso**, Carole Poitry-Yamate, Dunja Simicic, Mario Lepore, Cristina Cudalbu, and Bernard Lanz. « Multimodal assessment of brain energy metabolism in a rat model of hepatic encephalopathy using 1H-MRS and 18F-FDG PET – a pilot study ». *Proc. Intl. Soc. Mag. Reson. Med. 28*, 2020. **– oral**

16. David Guarin, **Jessie Mosso**, Mathieu Baudin, Dennis Kurzbach, Emeric Miclet, Daniel Abergel. « Fluxomic studies by in cell and in vitro Dissolution-Dynamic Nuclear Polarization NMR. » *EUROISMAR*, 2019. https://conference.euroismar2019.org/event/1/contributions/150/

17. Damien Bachasson, **Jessie Mosso**, Benjamin Marty, Pierre Carlier, and Jean-Yves Hogrel. « Estimating thigh muscle volume using bioelectrical impedance analysis with reference to contractile muscle volume assessed by nuclear magnetic resonance imaging. » *World Muscle Society*, 2018. https://doi.org/10.1016/j.nmd.2018.06.409